

University of Warwick institutional repository: <http://go.warwick.ac.uk/wrap>

A Thesis Submitted for the Degree of PhD at the University of Warwick

<http://go.warwick.ac.uk/wrap/66290>

This thesis is made available online and is protected by original copyright.

Please scroll down to view the document itself.

Please refer to the repository record for this item for information to help you to cite it. Our policy information is available from the repository home page.



Advanced Applications of High Performance Fourier Transform Ion Cyclotron Resonance Mass Spectrometry

Juan Wei

A thesis submitted
for the degree of Doctor of Philosophy

Department of Chemistry
University of Warwick
August 2014

Acknowledgements

It is a great pleasure to express my deepest appreciation to all of my friends and family that supported me and all the people I met during my PhD.

I came into the mass spectrometry field as an amateur, and now I don't want to leave this field. I cannot make any of the progress without the support of my supervisor, Prof. Peter B. O'Connor, who helped me enormously in exploring the fascinating world of mass spectrometry. His wisdom, knowledge, passion to science, kindness, and American humour, impressed me through the three years. He is always ready to help and encourages me in doing research with lots of freedom. He is a purely scientist and definitely an extraordinary supervisor. Here, I would like to take this official opportunity to say thank you to him, and I am very proud to be his student.

Special thanks to Dr. Mark P. Barrow and Dr. Huilin Li for their patience and time in teaching me how to use the instrument and sharing their expertise. They have always been willing to listen to my problems and provide advises. Dr. Mark Barrow's endeavour in maintaining the instrument is greatly appreciated. My friend Huilin Li, who always follows her heart in pursuing her career and lifestyle, inspired me a lot.

I am deeply grateful to the former and present members in our group: Dr. David Kilgour, Dr. Maria van Agthoven, Dr. Andrea Lopez-Clavijo, Andrew Soulby, Chris Wootton, Dr. Pilar Perez-Hurtado, Dr. Rebecca Wills, Samantha Benson, Dr. Tzu-Yung Lin, and Dr. Yulin Qi. There were lots of useful and interesting discussions. I sincerely appreciate their support and kindness.

I would like to acknowledge our collaborators: Dr. Anthony Bristow, Prof. Oleg N. Antzutkin, Dr. Dinu Iuga, Prof. Steven Brown, Prof. Ray Dupree, Dr. Claire Eyers and Dr. Francesco Lanucara, for their efforts on the collaboration projects and insightful discussions.

I must thank the friends I met throughout the years for making my PhD life so enjoyable and unforgettable. A special thanks goes to Changhui the sweet girl who is always beside me. I also express my gratitude to all of my other friends in China.

My appreciation also goes to the Chancellor International Scholarship of the University of Warwick and the Department of Chemistry of the University of Warwick, for funding my PhD. Thanks to my advisory panels, Prof. Alison Rodger and Dr. Vas Stavros, for providing useful advises.

Finally, and most importantly, I am indebted to my beloved family, whose endless support and love have kept me motivated to finish. They are always proud of me, but actually they are my truly pride and joy. I would like to say a big thank you to my boyfriend, Aichun, whose encouragement helps me get through the toughest time. His company is very important and is greatly appreciated.

Juan Wei

11th August 2014

Coventry, UK

Declaration

I hereby declare that except where specific references are made to other sources, the thesis entitled 'Advanced applications of high performance Fourier transform ion cyclotron resonance mass spectrometry' is the original work of the named author. It has been composed by myself and has not been submitted, in whole or in part, for any other degree, diploma or other qualification.

Juan Wei

August 2014

Abstract

Fourier transform ion cyclotron resonance mass spectrometry (FTICR MS) displays its advances in obtaining high resolving power, high mass accuracy, and coupling with many different tandem mass spectrometry (MS/MS) techniques. In this thesis, the superior performance of FTICR MS was demonstrated by several different applications. The peak separation limit of the 12 T solariX FTICR instrument was challenged by measuring the isotopic fine structures of several ^{17}O enriched amyloid- β ($\text{A}\beta$) peptides (Chapter 2 and 3). A resolving power as high as 6 M was achieved at m/z 880, and peaks were assigned with mass uncertainty less than 70 ppb. The accurate measurement of ^{17}O labelling ratio is of value for estimating atomic distances by NMR experiments. Furthermore high mass accuracy and high resolution are proved vital for the confident assignment of peaks in a polymeric mixture due to the sample complexity and coexistence of different adducts (Chapter 4). On the other hand, one or more of the MS/MS techniques, collisionally activated dissociation (CAD), electron induced dissociation (EID), electron capture dissociation (ECD), and infrared multiphoton dissociation (IRMPD), were used to characterize the structures of chlorophyll-*a* (Chapter 6), pheophytin-*a* (Chapter 7), and d- α -tocopheryl polyethylene glycol succinate (TPGS), respectively, and diagnostic fragments are useful for their structural identification in the future. IRMPD was particularly efficient in fragmenting chlorophyll-*a* and pheophytin-*a* compared to EID and CAD. Based on the fragmentation pattern of TPGS attached with two different adducts (Li^+ , Na^+ , K^+ , Ag^+ , and H^+), investigating the influence of adducts in ECD and CAD processes are of benefit for understanding the fragmentation mechanisms when cation adducts are involved (Chapter 5). In an on-going project, FTICR also displays the capability to study intact proteins above 30 kDa (Chapter 8).

Table of Contents

Acknowledgements	ii
Declaration	iv
Abstract	v
List of Tables	xi
List of Schemes	xii
List of Figures	xiii
List of Abbreviations	xvi
Chapter 1 Introduction	1
1.1 Mass spectrometry	2
1.1.1 Ionization methods	2
1.1.2 Tandem mass spectrometry (MS/MS) techniques	6
1.1.3 Mass analyzers	15
1.2 Three important features of FTICR MS and the applications	30
1.2.1 High resolution	30
1.2.2 High mass accuracy	32
1.2.3 Flexible MS/MS	33
1.2.4 The 12 T solariX FTICR MS instrument	34
1.2.5 The important applications of FTICR MS and MS/MS	35
1.3 Content of the thesis	48
Chapter 2 Utilizing isotopic fine structure mass spectrometry to understand ¹⁷O labelled amyloid peptides	50
2.1 Introduction	50
2.1.1 Techniques to measure the isotopic abundance of elements ...	50
2.1.2 Utilizing isotopic fine structure mass spectrometry to aid the interpretation of NMR data of ¹⁷ O labelled amyloid beta peptides	52

2.1.3	Content of the chapter	54
2.2	Experimental section	54
2.2.1	Chemicals.....	54
2.2.2	Mass spectrometry experiments.....	55
2.3	Results and discussions	58
2.3.1	A β_{16-22} (C ₄₅ H ₆₇ O ₁₀ N ₈ ¹⁵ N) partialy labelled with ¹⁷ O.....	58
2.3.2	A β_{11-25} (C ₇₈ ¹³ C ₃ H ₁₁₉ O ₂₃ N ₂₀ ¹⁵ N) partialy labelled with ¹⁷ O	68
2.3.3	Fmoc-valine.....	74
2.4	Conclusions.....	76
Chapter 3 Utilizing isotopic fine structures to understand the Aβ_{37-42} (GG₃₈(¹⁷O)VVIA) and Aβ_{37-42} (GGV₃₉(¹⁵N)VIA) mixture		
		77
3.1	Introduction	77
3.2	Experimental section	78
3.2.1	Chemicals.....	78
3.2.2	Mass spectrometry experiments.....	78
3.3	Results and discussions	78
3.3.1	Isotopic fine structure measurement of A β_{37-42} mixtures	78
3.3.2	Isotopic fine structure measurement of ¹⁷ O labelled Fmoc-glycine	82
3.4	Conclusions.....	84
Chapter 4 D-α-tocopheryl polyethylene glycol 1000 succinate: A view from FTICR MS and tandem MS¹		
		86
4.1	Introduction	86
4.1.1	Methods to characterize synthetic polymers.....	86
4.1.2	D- α -tocopheryl polyethylene glycol 1000 succinate	89
4.1.3	Content of the chapter	90
4.2	Experimental section	91
4.2.1	Chemicals.....	91

4.2.2	Mass spectrometry experiments	91
4.3	Results and discussions	92
4.3.1	Full MS overview	92
4.3.2	MS/MS of [TPGS+nNa] ⁿ⁺	97
4.3.3	ECD/ECD MS ³	101
4.3.4	MS ² with different metallic-cation adducts	104
4.3.5	Variation of TPGS samples	106
4.4	Conclusions	113
Chapter 5 The competitive influence of Li⁺, Na⁺, K⁺, Ag⁺, and H⁺ on the fragmentation of TPGS²		114
5.1	Introduction	114
5.1.1	Investigation of the influence of metallic adduction on the fragmentation of polymers	114
5.1.2	Content of the chapter	117
5.2	Experimental section	118
5.2.1	Chemicals	118
5.2.2	Mass spectrometry experiments	118
5.3	Results and discussions	119
5.3.1	The influence of the metallic adduct on the fragmentation of TPGS in CAD	119
5.3.2	The influence of the metallic adduct on the fragmentation of TPGS in ECD	123
5.3.3	In comparison with protonation	128
5.4	Conclusions	131
Chapter 6 Structural characterization of chlorophyll-a³		132
6.1	Introduction	132
6.1.1	General characters of chlorophylls	132
6.1.2	MS analysis of chlorophylls and porphyrin derivatives	132

6.1.3	Content of the chapter	134
6.2	Experimental section	134
6.2.1	Chemicals.....	134
6.2.2	Mass spectrometry experiments.....	135
6.3	Results and discussions	136
6.3.1	Loss of the phytyl group	137
6.3.2	Cleavages from long aliphatic chains	138
6.3.3	Extensive cleavages.....	144
6.4	Conclusions.....	146
Chapter 7 Structural characterization of pheophytin-a.....		148
7.1	Background	148
7.2	Experimental section	150
7.3	Results and discussions	151
7.3.1	CAD spectra of pheophytin-a.....	153
7.3.2	IRMPD spectra of pheophytin-a.....	156
7.3.3	EID spectra of pheophytin-a	162
7.4	Conclusions.....	162
Chapter 8 Top-down analysis of p65 proteins.....		164
8.1	Introduction	164
8.1.1	Protein phosphorylation.....	164
8.1.2	Significance of p65/RelA	166
8.1.3	Top-down mass spectrometry in studying protein phosphorylation.....	167
8.1.4	Aims of the project.....	168
8.2	Experimental section	168
8.2.1	Sample preparation	168
8.2.2	Mass spectrometry experiments.....	169

8.3	Results and discussions	169
8.3.1	MS analysis	169
8.3.2	MS/MS sequencing	170
8.3.3	Phosphorylation investigation by MS	173
8.4	Conclusions.....	174
Chapter 9	Conclusions and future work	176
9.1	Conclusions.....	176
9.2	Future work	180
BIBLIOGRAPHY	184
Appendix A	(Supporting information for Chapter 2).....	208
Appendix B	(Supporting information for Chapter 3).....	219
Appendix C	(Supporting information for Chapter 4).....	225
Appendix D	(Supporting information for Chapter 5).....	246
Appendix E	(Supporting information for Chapter 6)	264
Appendix F	(Supporting information for Chapter 7)	272
Appendix G	(Supporting information for Chapter 8).....	279
Curriculum Vitae	280

List of Tables

Table 2.1 Isotopic masses and natural abundance of H, C, N, and O	53
Table 2.2 The mass list of proposed peaks in Figure 2.1	59
Table 2.3 The mass list of proposed peaks in Figure 2.7	71
Table 2.4 The abundance of ^{13}C , ^{16}O , ^{17}O , and ^{18}O in the Fmoc-valine, $\text{A}\beta_{16-22}$, and $\text{A}\beta_{11-25}$	75
Table 3.1 The mass list of proposed peaks in Figure 3.1	80
Table 4.1 The statistics of Mn , Mw , PD , and n	86
Table 4.2 The comparison of four batches of TPGS samples from two manufacturers, first measurement	109
Table 4.3 The comparison of four batches of TPGS samples from two manufacturers, second measurement.....	111
Table 6.1 Summary of fragments proposed cleavages from Chain A & B	140

List of Schemes

Scheme 4.1 Proposed structure of the fragment from cleavage at position 'a' in CAD.....	99
Scheme 4.2 CAD and ECD results of $[\text{TPGS}+3\text{Na}]^{3+}$, $[\text{TPGS}+3\text{Li}]^{3+}$, and $[\text{TPGS}+3\text{Ag}]^{3+}$	106
Scheme 5.1 CAD and ECD results of $[\text{TPGS}+2\text{Li}]^{2+}$, $[\text{TPGS}+2\text{Na}]^{2+}$, $[\text{TPGS}+2\text{K}]^{2+}$, and $[\text{TPGS}+2\text{Ag}]^{2+}$	121
Scheme 6.1 Labelling the proposed cleavages sites of chain A and B in ring IV&V	139
Scheme 7.1 Proposed mechanisms for the formation of peaks at m/z 593.2756 and m/z 533.2545	154
Scheme 8.1 Diagram shows the phosphorylation of serine, threonine, and tyrosine.....	165

List of Figures

Figure 1.1 Nomenclature for fragment ions used in mass spectrometry	7
Figure 1.2 The scheme of a quadrupole, adapted from http://www.files.chem.vt.edu/chem-ed/ms/quadrupo.html	16
Figure 1.3 A stable region of the Matthieu stability diagram	17
Figure 1.4 Several ICR cell geometries: (a) cubic cell, (b) cylindrical cell, and (c) infinity cell	19
Figure 1.5 Three ion motions in the ICR cell: cyclotron motion, magnetron motion, and trapping motion (Bruker Daltonics)	20
Figure 1.6 FTICR MS data process a) the raw time domain signal (transient); b) frequency spectrum; c) mass spectrum	24
Figure 1.7 A peak in a FTICR frequency spectrum displayed in dispersion mode ($D(\omega)$), absorption mode ($A(\omega)$), and magnitude mode ($M(\omega)$) ⁹⁸	26
Figure 1.9 Schematic of the 12 T solariX FTICR mass spectrometer (Bruker Daltonics)	34
Figure 2.1 An ultra high resolution FTICR mass spectrum of the singly-protonated $A\beta_{16-22}$ ($C_{45}H_{68}O_{10}N_8^{15}N$) in black, and the simulated spectra of $A\beta_{16-22}$ with natural abundance oxygen (the dashed blue line) and using the calculated ratio, $^{16}O: ^{17}O:$ $^{18}O = 34.4: 55.5: 10.1$ (the red line). The peak list is in Table 2.2	59
Figure 2.3 The separation of A+1 cluster of the singly-protonated $A\beta_{16-22}$ ($C_{45}H_{68}O_{10}N_8^{15}N$) with resolving power (R.P.) from 0.5 M to 5.0 M. The peaks labelled as ^{13}C and ^{17}O are the ^{13}C - ($C_{44}^{13}CH_{68}O_{10}N_8^{15}N$, m/z 896.508756) and ^{17}O - ($C_{45}H_{68}O_9^{17}ON_8^{15}N$, m/z 896.509618) substituted species, respectively	62
Figure 2.4 A dual nano-electrospray mass spectrum of the $A\beta_{16-22}$ sample with tuning mix as the internal calibrant, and peaks with asterisk are the peaks used in calibration. The spectrum on the top is the simulation of $A\beta_{16-22}$ of natural abundance oxygen	65
Figure 2.5 A CAD spectrum of the singly-charged $A\beta_{16-22}$. Insets on the top are the expanded regions of b_2 and b_3 ions (black) with the corresponding simulated spectra with natural abundance oxygen (blue) and using the calculated ratio, $^{16}O:$ $^{17}O: ^{18}O = 34.4: 55.5: 10.1$ (red)	66
Figure 2.6 The comparison of two mass spectra of $A\beta_{16-22}$ with different ion populations showing peak coalescence; at higher ion populations (b), the two peaks in the A+1 cluster, ^{13}C and ^{17}O substituted species, cannot be resolved despite having similar resolving power with (a)	68
Figure 2.7 An ultra high resolution FTICR mass spectrum of the doubly-charged $A\beta_{11-25}$ ($C_{78}^{13}C_3H_{121}O_{23}N_{20}^{15}N$) in black, and the simulated spectra of $A\beta_{11-25}$ with natural abundance oxygen (the dashed blue line) and using the calculated ratio, $^{16}O: ^{17}O: ^{18}O = 27.9: 56.8: 15.3$ (the red line). The peak list is in Table 2.3	70
Figure 2.9 The absorption mode mass spectrum of the $A\beta_{11-25}$ spectrum in Figure 2.7. Insets are the absorption- (bottom) and magnitude- (top) mode spectra of the expanded regions of A+1 and A+2 clusters, respectively	73

Figure 2.10 The structure of the Fmoc-valine with two oxygen atoms on the valine labelled	74
Figure 3.3 A FTICR mass spectrum of the Fmoc-glycine labelled with ^{17}O ; peaks labelled with ^{13}C , ^{17}O , $^{17}\text{O}^{13}\text{C}$, and $^{17}\text{O}_2$ are the corresponding ^{13}C -substituted, ^{17}O -substituted, $^{17}\text{O}^{13}\text{C}$ -substituted, and $^{17}\text{O}_2$ -substituted species respectively. The spectra in red are the simulation of Fmoc-glycine using the ratio $^{16}\text{O}:^{17}\text{O}:^{18}\text{O} = 41.299:58.700:0.001$. The peak list is in Table B.5.....	84
Figure 4.2 The full mass overview of TPGS sample. Detailed peak assignment is available in the Table C.1	93
Figure 4.3 ECD spectra of several pre-assigned groups: a) $[\text{M}+2\text{Na}+\text{H}]^{3+}$, b) $[\text{M}+2\text{Na}+\text{NH}_4]^{3+}$, and c) $[\text{M}+3\text{Na}]^{3+}$	94
Figure 4.4 A ECD spectrum of $[\text{M}+3\text{H}]^{3+}$; the fragment indicating α -tocopheryl is highlighted	95
Figure 4.5 The full mass overview of TPGS sample in ACN with Na_2SO_4 . Detailed peak assignment is available in Table C.2	97
Figure 4.6 CAD results of $[\text{TPGS}+n\text{Na}]^{n+}$ ($\text{C}_{87}\text{H}_{162}\text{O}_{32}\text{Na}_n$) $n=1, 2, 3$, and the collision energies used are: a) 50 V, b) 46 V, and c) 35 V. Detailed peak assignment is available in Table C.3.....	99
Figure 4.7 a): EID spectrum of $[\text{TPGS}+\text{Na}]^+$; b) and c) are ECD spectra of $[\text{TPGS}+2\text{Na}]^{2+}$ and $[\text{TPGS}+3\text{Na}]^{3+}$, respectively. Detailed peak assignment is available in the Table C.4	101
Figure 4.8 a): ECD spectrum of $[\text{M}+3\text{Na}]^{3+}$ as Figure 4.7c; b): In cell isolation of the doubly-charged fragment at m/z 643.3394; c): ECD/ECD MS ³ spectrum of isolated peaks. Detailed peak assignment is available in Table C.5.....	103
Figure 4.9 Zooming in peaks at m/z 665.352386 and m/z 643.339353 in the ECD spectrum of $[\text{TPGS}+3\text{Na}]^{3+}$ in Figure 4.7c.....	104
Figure 4.10 ESI-FTICR mass spectra of four batches of TPGS samples	107
Figure 4.11 CAD spectra of four batches of TPGS samples	108
Figure 4.12 ECD spectra of four batches of TPGS samples	108
Figure 5.1 Structure of TPGS_{27} (27 is the degree of polymerization)	117
Figure 5.2 CAD spectra of a): $[\text{TPGS}+2\text{Li}]^{2+}$, b): $[\text{TPGS}+2\text{Na}]^{2+}$, c): $[\text{TPGS}+2\text{K}]^{2+}$, and d): $[\text{TPGS}+2\text{Ag}]^{2+}$	120
Figure 5.3 CAD spectra of a): $[\text{TPGS}+\text{Li}+\text{Na}]^{2+}$, b): $[\text{TPGS}+\text{K}+\text{Li}]^{2+}$, c): $[\text{TPGS}+\text{Li}+\text{Ag}]^{2+}$, d): $[\text{TPGS}+\text{Na}+\text{Ag}]^{2+}$, e): $[\text{TPGS}+\text{K}+\text{Ag}]^{2+}$, and f): $[\text{TPGS}+\text{K}+\text{Na}]^{2+}$. 'nPEG' in the figure refers to loss of $n\text{C}_2\text{H}_4\text{O}$ units	122
Figure 5.4 ECD spectra of a) $[\text{TPGS}+2\text{Li}]^{2+}$, b) $[\text{TPGS}+2\text{Na}]^{2+}$, c) $[\text{TPGS}+2\text{K}]^{2+}$, and d) $[\text{TPGS}+2\text{Ag}]^{2+}$	124
Figure 5.5 ECD spectra of a) $[\text{TPGS}+\text{Li}+\text{Na}]^{2+}$, b) $[\text{TPGS}+\text{K}+\text{Li}]^{2+}$, c) $[\text{TPGS}+\text{Li}+\text{Ag}]^{2+}$, d) $[\text{TPGS}+\text{Na}+\text{Ag}]^{2+}$, e) $[\text{TPGS}+\text{K}+\text{Ag}]^{2+}$, and f) $[\text{TPGS}+\text{K}+\text{Na}]^{2+}$	126
Figure 5.6 CAD and ECD spectra of $[\text{M}+2\text{H}]^{2+}$, $[\text{M}+\text{H}+\text{Li}]^{2+}$, $[\text{M}+\text{H}+\text{Na}]^{2+}$, $[\text{M}+\text{H}+\text{K}]^{2+}$, and $[\text{M}+\text{H}+\text{Ag}]^{2+}$. 'nPEG' in the figure refers to loss of $n\text{C}_2\text{H}_4\text{O}$ units.	130
Figure 6.1 Structure of chlorophyll- <i>a</i>	133

Figure 6.2 Fragmentation of singly-charged chlorophyll-a under conditions of (a) optimized CAD 22 V; (b) IRMPD with pulse length of 0.9 s and 30% pulse power; (c) EID 12.2 V for 0.096 s	136
Figure 6.3 Expanded m/z region of 614-619 in Figure 6.2 (a) CAD; (b) IRMPD; (c) EID; (d) and (e) are simulations of $C_{35}H_{34}O_5N_4Mg$ and $C_{35}H_{35}O_5N_4Mg$, respectively. Inset on the left is the further zooming of m/z region of 615.2-615.3	138
Figure 6.5 Plotting of intensity changes of several radical ions according to the laser power in IRMPD	143
Figure 6.6 (I–V) Representative expanded spectra of several lower m/z regions (a) IRMPD; (b) EID; (c) and (d) are the corresponding simulations of the elemental compositions in the highlight regions respectively	145
Figure 7.1 Structure of pheophytin-a. Chain A, Chain B, and phytol group are illustrated.	149
Figure 7.2 List of the structural formulae of several derivatives of porphyrin and chlorophylls. Red boxes highlight the regions of difference among each structure.	150
Figure 7.3 MS spectra of chlorophyll-a in a) 50/50 (V/V) methanol/water and b) 50/50 (V/V) methanol/water with 1% Formic acid.....	152
Figure 7.4 a) CAD, b) IRMPD, c) EID MS/MS spectra of singly-charged pheophytin-a.....	153
Figure 7.5 The expanded regions from m/z 591-596 in Figure 7.4 a) CAD, b) IRMPD, c) EID MS/MS spectra of singly-charged pheophytin-a.....	156
Figure 7.6 Extensive fragmentation of pheophytin-a in IRMPD spectrum (70% laser power and 0.2 s pulse length). Peaks assignment is in Table F.1	158
Figure 7.7 IRMPD spectra of a): chlorophyll-a and b): pheophytin-a with 70% laser power and 0.5 s pulse length. Insets in the square are expanded regions from m/z 100-350. Peaks with asterisk are harmonics or noise.....	159
Figure 8.1 a): a nano-ESI spectrum of p65 sample showing its charge distribution; b): deconvolution spectrum of a).....	170
Figure 8.2 CAD results of the p65 ions, $[M+30H]^{30+}$, and the amino acid sequence of p65 showing b/y ions from cleavages from amide bonds in the backbone. Sites labelled with ‘*’ or ‘!’ are the detected ‘ b ’ ions either ~144.04 Da or ~126.03 Da heavier than the corresponding theoretical mass value.	172
Figure 8.4 MS spectra of a) phosphorylated p65 stimulated by Ikk β and b) non-phosphorylated p65	174

List of Abbreviations

A β	Amyloid beta
ACN	Acetonitrile
Ac	Acylation
APCI	Atmospheric pressure chemical ionization
CAD	Collisionally activated dissociation
CID	Collisionally induced dissociation
Chl	Chlorophyll
CEM	Chain ejection model
CRDS	Cavity ring-down spectroscopy
CRM	Charge residue model
Da	Daltons
DC	Direct current (<i>U</i>)
DTT	Dithiothreitol
ECD	Electron capture dissociation
EDD	Electron detachment dissociation
EI	Electron ionization

EID	Electron induced dissociation
EIEIO	Electron-induced excitation of ions from organics
ETD	Electron transfer dissociation
ESI	Electrospray ionization
ExD	Electron-based dissociation
FTICR	Fourier transform ion cyclotron resonance
FWHM	Full width at half maximum
Fmoc	Fluorenylmethyloxycarbonyl
GC-MS	Gas chromatography mass spectrometry
GC-C-IRMS	Gas chromatography-combustion isotope ratio mass spectrometry
Gly	Glycine
IA-ECD	Ion activated-electron capture dissociation
ICR	Ion cyclotron resonance
ICP MS	Inductively coupled plasma mass spectrometry
IEM	Ion evaporation model
IMS	Imaging mass spectrometry
IRMPD	Infrared multiphoton dissociation

IRMS	Isotope ratio mass spectrometry
IR-ECD	Infrared activated-electron capture dissociation
LC-MS	Liquid chromatography-mass spectrometry
MALDI	Matrix assisted laser desorption ionization
M_n	Number average molecular weight
M_w	Weight average molecular weight
MW	Molecular weight
MS	Mass spectrometry
MS/MS	Tandem mass spectrometry
MS^n	Multi stage tandem mass spectrometry
m/z	Mass to charge ratio
nESI	Nano-electrospray
NMR	Nuclear magnetic resonance
n	Repeat unit
ppm	Parts-per-million
PEG	Polyethylene glycol
QIT	Quadrupole ion trap
R.P.	Resolving power

REAPDOR	Rotational echo adiabatic passage double resonance
RF	Radio frequency (V)
PTMs	Posttranslational modifications
Ser	Serine
S/N	Signal to noise ratio
SORI	Sustained off resonance irradiation
T	Tesla
TOF	Time-of-flight
TPGS	D- α -tocopheryl polyethylene glycol succinate

Chapter 1 Introduction

Mass spectrometry (MS), has become a universal tool in daily analytical work as it brings many possibilities to research and shows great potential in solving analytical problems. Many exciting breakthroughs in the MS field has expanded the limits of the technique and greatly expanded the applications in many fields.

Although a mass spectrometer with a resolving power less than 10,000 is accepted in most daily analysis, many scientific challenges still demand far better mass spectrometry instruments, particularly for the separation and identification of complex mixtures, understanding macromolecules, and characterizing of molecular structures; moreover, some of these studies can only be accomplished by high performance mass spectrometry. Fourier transform ion cyclotron resonance (FTICR) mass spectrometer is widely recognized as the highest performance MS instrument,¹ not only because of the outstanding resolving power and mass accuracy, but also the extraordinary flexibility to couple with many tandem mass spectrometry (MS/MS) techniques on one instrument, and FTICR MS has shown great potential and displayed impressive performance in solving challenging analytical problems.

The current thesis focuses on applying the high performance features of FTICR MS, in terms of high resolving power, high mass accuracy, and flexible fragmentation ability, in the study of several important real samples to demonstrate the significance of high performance mass spectrometry in

practice. This chapter (chapter one) includes three parts. The first part (1.1) is a general introduction of mass spectrometry, including ionization methods (1.1.1), tandem mass spectrometry techniques (1.1.2), and mass analyzers, in particular the fundamental of FTICR MS (1.1.3). In the second part (1.2), the important features of FTICR MS are discussed in detail (1.2.1), and followed by a brief summary of the advanced applications of FTICR MS in recent years (1.2.2). Finally, an overview content of the thesis is listed in the third part (1.3).

1.1 Mass spectrometry

1.1.1 Ionization methods

Mass spectrometry measures the mass to charge ratio (m/z) of ions in the gas phase. In the early stage, electron impact (EI) was the most frequently used method to ionize molecules, and it is still the most important ionization source in gas chromatography-mass spectrometry, but it only shows high efficiency for ionizing molecules of high volatility and of small molecular weight, which greatly limits the application. In 1980s', the development of two ionization techniques, electrospray ionization (ESI)² and matrix-assisted laser desorption ionization (MALDI),^{3,4} enormously improved the ionization of large molecules and enriched the application of mass spectrometry, bringing biomolecular analysis into a new era. Different from EI, both ESI and MALDI are so called soft ionization methods, where intact molecules are ionized without producing extensive fragments, which is of great interest for many modern mass spectrometric studies.

Electrospray ionization (ESI)

In ESI, analytes in solution are directly converted into the gas phase ions, and analyzed. This revolutionary technique has a simple ionization process and facilitates the mass spectrometric investigation of a wide range of molecules. In 2002, John Fenn was awarded the Nobel prize in chemistry for his contributions in the discovery of the ESI source.²

In ESI, samples in solution are usually pumped through a capillary with a flow rate of 0.1 – 10 $\mu\text{L}/\text{min}$, and a high voltage (several kilovolts) is applied between the capillary and the inlet (orifice) of a mass spectrometer to provide the electric field gradient.⁵ When the high voltage is applied on the capillary, a Taylor cone will be formed at the tip of the capillary due to the accumulation of charges on the surface of the sample solution, and which will further generate micrometre-sized droplets rich in charges.⁶ These highly charged droplets will be evaporated, often assisted by heating and a counter flow of drying gas (N_2), and eventually turned into single ions suitable for the detection of the mass to charge ratio.⁷

Several mechanisms have been proposed for the formation of the gas phase ions, including the ion evaporation mode (IEM), the charged residue model (CRM), and the chain ejection model (CEM).^{7,8} The IEM is widely accepted for molecules of low molecular weight, and it suggests that during solvent evaporation the charge density of a droplet will increase gradually, due to the Columbic repulsion among charges in the droplet.⁹ When the barrier of surface tension is matched by the Columbic repulsion (the Rayleigh limit),¹⁰ the ejection of small ions from the droplet surface could happen

successively. The CRM¹¹ proposed that large globular species embedded in a droplet with solvent will eventually shrink into a single ion when the solvent totally evaporates and dries out. The CEM is very similar to IEM, but particularly relevant to polymer chains that are disordered, partially hydrophobic, and capable of binding excess charge carriers.⁷

As mentioned previously, the surface tension is a crucial factor influencing the efficiency of ionization; hence the choice of the solvent composition for ESI is important. Depending on different applications, various solvent systems could be selected, while the most common solvent for positive ESI experiments is a mixture of 50:50 methanol/acetonitrile and water, with a small amount of acid added to promote protonation.

Nano-electrospray (nESI) is a variety of ESI.¹² Instead of using a capillary of a diameter around 100 μm , nESI uses capillaries of a much smaller size tip (typically 1-5 μm), generating a flow rate of ~ 1 nL/min with solvent flow “pumped” only by capillary action, and the Taylor cone and plume become invisible because the droplets are in the 100 nm diameter range. In addition to using much smaller amount of samples, comparing to the traditional ESI source, nESI could improve the desolvation and ionization efficiency because droplets of smaller size are formed.

According to the proposed process of ion formation in ESI, it is rational that multiply-charged ions are usually produced and the same type of molecules could carry different numbers of charges or even different category of charge carriers, such as protons and sodium cations, showing peaks of different m/z on the mass spectrum. Even though, to some extent, multiple

charging makes the mass spectrum relatively complicated, this feature is of great benefit for analyzing molecules of high molecular weight.

Matrix-assisted laser desorption ionization (MALDI)

The MALDI source was first developed by Prof. Franz Hillenkamp and Prof. Michael Karas in 1985,¹³ and quickly became one of the most important ionization methods. In contrast to ESI, MALDI yields singly-charged ions in most cases so that the data interpretation is relatively easier, but may produce ions at very high m/z ($\geq 10,000$) which could be problematic for most modern mass analyzers. However, because MALDI is a pulsed ionization technique, it is particularly compatible with time-of-flight instruments (details will be discussed in section 1.1.3), which is also a mass analyzer suitable for analyzing big molecules.

In a MALDI experiment, the analyte is mixed with a selected matrix in a ratio of 1:50-1:5000 (analyte to matrix), and then is dried on a stainless steel MALDI target; afterwards, the target covered with crystal sample spots is inserted into the instrument and a laser, typically ultraviolet lasers of 337 nm (N_2) or 355 nm (Nd:YAG), will shoot on the pre-dried solid sample spot causing ionization. The process of how analyte ionization occurs in MALDI is still not fully understood, and one proposed mechanism is that analytes and matrixes are first evaporated by laser radiation generating ionized matrix ions and neutral analyte vapour, and then followed by proton transfer from the matrix ions to the analyte molecules forming ionized analytes. Karas and his colleagues recently experimentally demonstrated the presence of both the gas phase protonation and the Lucky Survivor pathways in MALDI.¹⁴ The

latter model, Lucky Survivor, suggests that the precharged analytes preserve the charges from solution, but are fully or partially neutralized by the corresponding counterions assisted by the protonated matrix molecules in ionization, generating singly-charged analytes.¹⁴

In addition to generating relatively simple mass spectra, several advantages make MALDI an extensively used source, for example, a higher tolerance for salt than ESI. Moreover, a wide variety of samples and a large range of masses can be effectively ionized using MALDI with a proper selection of the matrix.

1.1.2 Tandem mass spectrometry (MS/MS) techniques

To generate structural information, molecular dissociation is a crucial reaction in mass spectrometry. Various tandem mass spectrometry (MS/MS) techniques have been developed to break ions apart yielding fragment ions.

Collisionally activated dissociation (CAD)

The most important fragmentation technique so far is CAD (also known as collisionally induced dissociation, CID),^{15,16} which has been extensively applied in the structural characterization of proteins/peptides,¹⁷ polymers,¹⁸ and many other molecules.¹⁹ In CAD, the target ions are accelerated and collide with neutral species, such as Ar, N₂, or He, to increase the internal energy to dissociate. There are two kinds of CAD regimes depending on the energy used in accelerating target molecules: the low-energy CAD (1-100 eV) and the high-energy CAD (> 1 keV). In this thesis, the acronym 'CAD' normally refers to low-energy CAD.

Low-energy CAD is readily compatible with tandem quadrupoles and ion trapping instruments, and is the most common MS/MS technique. For low-energy CAD, the excitation is mostly vibrational and multiple collisions are dominant.²⁰ The internal energy gained in collisions is distributed randomly through the molecule, causing fragmentation via the lowest energy dissociation channel. In addition to bond cleavages, rearrangement is also possible and could be promoted by thermodynamically favourable structures. The optimization of the pressure and selection of the neutral gas can both have important impact on the fragmentation. CAD plays an important role in the structural study of peptides and proteins, where *b*- and *y*- type ions cleaving from the amide bond (CO-NH) are the main fragments (Figure 1.1).

21,22

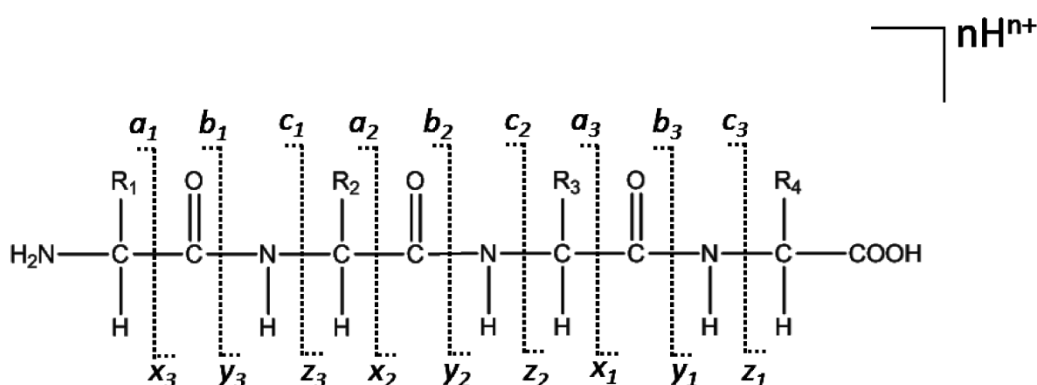


Figure 1.1 Nomenclature for fragment ions used in mass spectrometry

The low-energy CAD also occurs in the interface region of the ESI source and is known as in source CAD or nozzle/skimmer CAD,²³⁻²⁶ which is particularly useful to get rid of the noncovalent binding adducts when studying intact big molecules.^{24,25} Since there is no prior isolation, all of the ions could

be excited and fragmentation is feasible for labile compounds, but if extensive fragmentation occurs, it can be difficult or impossible to associate a particular fragment with a particular precursor.

In order to perform CAD in an ion cyclotron resonance cell (ICR cell, details see section 1.1.3), neutral gas has to be leak in, and ions trapped in the cell will be excited and undergo collisions. Depending on the frequency of the excitation waveform used, both on-resonance²⁷ and off-resonance²⁸ CAD can be implemented on FTICR instruments. Traditional on-resonance CAD has inherent disadvantages due to ion losses and low energy transfer efficiency. Two variations of on-resonance techniques have been demonstrated more efficient are: multiply excitation collision activation (MECA) by using low amplitude on-resonance excitation^{29,30} and very low energy (VLE)³¹ collision activation by periodically 180° phase shifting of the excitation waveform. Using sustained off-resonance irradiation (SORI) CAD,²⁸ ions are accelerated and decelerated by an excitation waveform with a frequency close to the cyclotron frequency of the targeted molecule, and the internal energy is accumulated. The efficiency of MECA, VLE, SORI, and traditional on-resonance CAD methods to fragment large multiply-charged ions were compared, and SORI technique is best in producing fragments with high efficiency and best resolution.³² However, with the development of hybrid-FTICR instruments, such as quadrupole-FTICR or linear ion trap-FTICR, more efficient CAD process could be achieved by collisions in front of the ion cyclotron cell.

Instead of introducing neutral gas, surface-induced dissociation (SID) is a MS/MS method where ions collide with a solid surface,^{33,34} and it shows

promising results for big molecules.³⁵ In practice, several experimental factors, such as surface composition, incidence angle, and collision energy, can have great effect on the fragmentation efficiency.³⁶ In addition to the expertise needed in tuning, modification is often required for most instruments to be compatible with a SID source, which restricts its application.

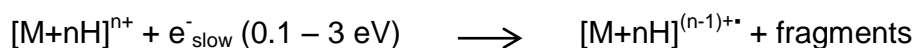
Infrared multiphoton dissociation (IRMPD)

IRMPD³⁷ is another ‘slow heating’ method³⁸ and has been primarily implemented in FTICR instruments, but has recently been also implemented on ion trap and orbitrap instruments.^{39,40} Typically, target ions are activated by a low-power (< 100 W) CO₂ laser (10.6 μm) for tens to hundreds of milliseconds. During the IRMPD process, ions absorb multiple photons from the IR radiation sequentially to enable vibrational excitation and produce fragments.⁴¹ Though similar fragmentation pathways with those from CAD are likely to occur in IRMPD, IRMPD displays advantages in investigating the lowest energy pathways and has been used in the study of peptides/proteins,^{22,39,42} oligosaccharide,⁴³⁻⁴⁵ lipid,⁴⁶ and some other small molecules.⁴⁶⁻⁵¹

Electron-based fragmentation techniques

Electron capture dissociation (ECD) results were initially observed in an ultraviolet photon dissociation experiment,⁵² and the ECD technique was further developed by McLafferty’s group.⁵³⁻⁵⁶ In ECD, multiply-charged ions are irradiated by low energy (0.1 – 3 eV) electrons, and then, fragmentation follows electron capture (Scheme 1.1). Different from the fragmentation methods described above, the ECD activation process is very fast⁵⁷ and the

ion excitation falls into the region of electronic excitation.⁵⁸ So far, ECD has been most successfully implemented in FTICR MS instruments, which are widely commercially available.



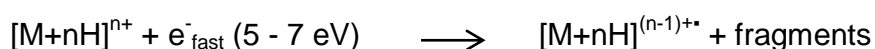
Scheme 1.1 Electron capture dissociation (ECD) process

Because of the complementary role of ECD in producing fragments, additional structural information could be formed, and it is emerging as one of the most important MS/MS techniques, which is extensively employed in the structural characterization of proteins and peptides. ECD generally produces more extensive backbone cleavages than CAD, and retains labile groups, thus, providing more sequence information.^{53,54,56,59} Instead of breaking the amide bond of proteins/peptides, ECD usually cleaves the N-C_α (NH-CHR) bond and produces c and z[•] fragments (Figure 1.1), and it is worthy to note that the disulfide bonds will be cleaved preferentially in ECD over the backbone. Several ECD mechanisms have been proposed. One of the early propositions is the ‘hot-hydrogen’ model,^{54,60} which is also called the Cornell mechanism. In the ‘hot hydrogen’ model, the electron capture happens at the protonated group, such as N-terminus and basic side chains, followed by the neutralization of the charge and a hydrogen migration from the electron capture site to a carbonyl oxygen of an adjacent amide bond, resulting in the dissociation of the N-C_α bond.⁵⁴ The hydrogen transfer in the ‘hot hydrogen’ process is not always feasible according to theoretical calculations,^{61,62} and another mechanism, the ‘amide super base’ mechanism (Utah-Washington

mechanism), has become more attractive.^{61,63,64} In the later model, the electron is captured by the carbonyl oxygen, forming an anion radical, which can exothermically abstract a proton from the nearby group and induce bond cleavages.

One advantage of ECD over CAD and the other 'slow heating' MS/MS techniques in studying biomolecules is that it generates far fewer side-chain cleavages. Information like posttranslational modifications (PTMs) is more likely to be traced. ECD is thus becoming one of the most useful tools in top-down proteomics, in particular to identify and locate PTMs. Whereas, sometimes, using ECD to fragment proteins could be problematic due to the folding structure and intramolecular noncovalent interactions, pre-unfolding strategies such as irradiating with IR laser (IR-ECD),⁶⁵ or colliding with background gas²⁵ can be helpful, and these strategies are so-called activated-ion ECD (AI-ECD) in general.^{65,66}

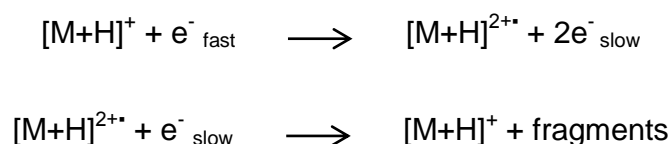
Upon increasing the electron energy to 5 - 7 eV, both electronic excitation and vibrational excitation could happen and induce dissociation, which is named hot ECD.^{58,67} For proteins or peptides, hot ECD can yield *c/z*·, *b/y* fragments, as well as some secondary fragmentation. Though spectra interpretation is normally more complicated compared to low energy ECD, the sequence coverage is likely to be improved by using hot ECD, and some side chain cleavages may provide useful structural information, such as distinguishing leucine from isoleucine.⁶⁷



Scheme 1.2 Hot electron capture dissociation (hot ECD) process

Electron induced dissociation (EID)

Though ECD was found as a valuable complementary MS/MS technique in producing fragments, it is not suitable for singly-charged ions due to neutralization and can have poor fragmentation efficiency on species with a low charge state. This limitation, however, can be overcome by utilizing high energy electrons (10-25 eV), and several terms have been used for this concept, including electronic excitation dissociation (EED)⁶⁸ introduced by Roman Zubarev and electron induced dissociation (EID),⁶⁹ where the latter term is more widely accepted. One difference between these terms is that the presence of the radical dication ($[M+H]^{2+•}$) has been reported in EED, but it is not necessary in EID.^{69,70} Moreover, Zubarev's group reported another technique, electron ionization dissociation,⁷¹ which uses electrons of an energy higher than the ionization threshold of the cation (typically above 15 eV) to produce hydrogen deficient species, generating both odd-electron and even-electron fragmentation.



Scheme 1.3 Electron induced dissociation (EID) process

Dating back to 1980s, Cody and Freiser first reported an electron-based fragmentation method referred to electron-induced excitation of ions from organics (EIEIO),^{72,73} in which the singly-charged parent ions were irradiated by electrons to generate fragments, but whether electron capture was

involved is not clear. Though the early research did not define the level of the electron energy carefully, choosing the electron energy and the irradiation time were proved to be crucial. Later on, in most of the EID experiments, neutralization is found to be the dominant process when the electron energy is lower than 10 eV,^{70,74} in contrast, fragmentation becomes feasible by increasing electron energy to 10-25 eV. In addition to CAD, EID is demonstrated to be of particular interest in the structural characterization of many singly- or doubly- charged molecules.^{48,75-79}

There are also some electron-based fragmentation methods specific for negative ions, including electron detached dissociation (EDD), and negative electron capture dissociation (NECD), which are not discussed herein.

ECD has mostly been implemented on FTICR MS instruments, and the development of electron transfer dissociation (ETD)⁸⁰ enabled more mass spectrometers access to ECD-like dissociation providing a comprehensive MS/MS method.⁸¹⁻⁸³ Since a binding energy has to be crossed when an electron leaves the anion, in compared to ECD, a slightly lower energy (~0.6 eV) is released in ETD after electron transfer, so that some different fragmentation patterns might be produced.⁸⁴



Scheme 1.4 Electron transfer dissociation (ETD) process

The essential difference between ‘slow heating’ dissociation methods and electron-based dissociation methods is the time-scale of ion activation and whether odd-electron fragmentation is involved. In ‘slow heating’ methods, ions are normally activated or irradiated in a time-scale of microseconds to seconds,⁸⁵ and energy accumulated in the activation can be redistributed through molecular vibration. In contrast, electron capture or transfer is a crucial step in electron-based MS/MS methods, and radical ions are formed and dissociated. The ‘stabilization time’ of a positive ion capturing an electron is of the order 10^{-16} - 10^{-15} s.⁵⁷ This time-scale is faster than vibrational motion of a molecule, 10^{-12} - 10^{-14} s, and electronic excitation is induced. However, it has to be noted that even though the electron activation process seems very fast, the rate of successive dissociation processes may highly depend on the structure of a molecule. For example, computational calculation shows that the rate of peptide ketyl radicals dissociation is above 10^5 s⁻¹ if there is no hydrogen bonding, but the cleavage of hydrogen bonds is the rate-determining step.⁶²

So far, most investigations of fragmentation mechanisms focus on the dissociation of peptides. For ‘slow heating’ methods, the ‘mobile proton’ model is widely accepted,⁸⁶⁻⁸⁸ where protons migrate along the peptide backbones induce adjacent bond cleavages. As discussed above, two mechanisms are proposed for ECD. The recent calculation (‘Utah-Washington mechanism’) suggests that an electron is guided to SS σ^* or amide π^* through a Rydberg orbital centred on a positively charged site, causing fragmentation.⁸⁹ In addition, another mechanism, the free radical reaction cascade, evoked by the observation of multiple bond cleavages from

doubly-charged cyclic peptides, is intriguing.⁵⁹ The unexpected amino acid losses, from doubly-charged cyclic peptides, suggested that the C $_{\alpha}$ radical can migrate and promote multiple backbone cleavages, and thus, extensive secondary fragmentation argues that free radical rearrangements generally follow the formation of the C $_{\alpha}$ radical. In brief, the even-electron fragmentation (CAD, IRMPD, etc) and odd-electron fragmentation (ECD, ETD, EID, etc) are two complementary strategies and are likely inducing fragments through different mechanisms, but more solid experimental study is necessary to deeply understand the mechanisms proposed for any particular molecules.

1.1.3 Mass analyzers

Quadrupole

The quadrupole analyzer (Figure 1.2) is undoubtedly one of the most important mass analyzers, and can be used for ion selection, ion scanning, and ion focusing (the latter can also be achieved with multipoles). In addition to these features, quadrupoles also have advantages such as high sensitivity, low acceleration voltage, and low cost.⁹⁰ Resolving power ~ 1000 and mass accuracy ~ 100 ppm are achievable for modern quadrupole instruments.

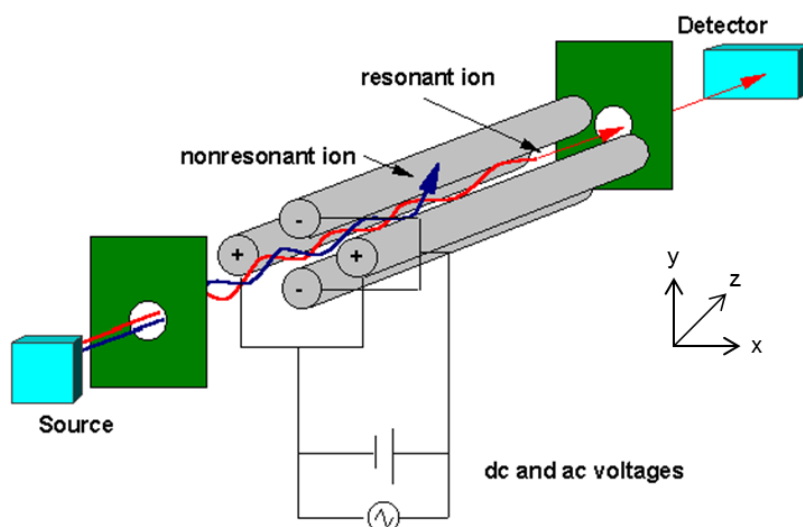


Figure 1.2 The scheme of a quadrupole, adapted from <http://www.files.chem.vt.edu/chem-ed/ms/quadrupo.html>

A quadrupole is composed of four parallel cylindrical or hyperbolical rods (Figure 1.2), and opposite pairs of rods are connected together and a voltage is implied consisting of a DC voltage (U) and a RF voltage (V). The total voltage (ϕ) on each rod will be:

$$\phi = \pm(U + V \cos \omega t) , \quad \text{Equation (1.1)}$$

ω is the RF frequency Ions injected into the quadrupole along the axial direction (z direction in Figure 1.2) will be repelled or attracted by the rods with the same sign or the rods with the opposite sign, respectively. Since the sign of the potential on the two pairs of rods switches periodically, the route of ions will be zigzag (ion oscillation), so that only those ions having stable motions in both x and y directions can pass through successfully and be

detected. The stability of ion motion can be determined by the Mathieu equation, which involves two values, a and q :

$$a = \frac{8eU}{mr_0^2\omega^2}, \quad \text{Equation (1.2)}$$

$$q = \frac{4eV}{mr_0^2\omega^2}, \quad \text{Equation (1.3)}$$

where r_0 is the half distance between two opposing rods. A stability diagram with a versus q can be plotted and is particularly useful in designing the voltage scheme including U and V in practice. Figure 1.3 shows one stable region of the best interest for normal quadrupole experiments. Since the RF frequency, ω , and r_0 are generally constants, values of a and q are directly related to the voltages (U and V) and the m/z .

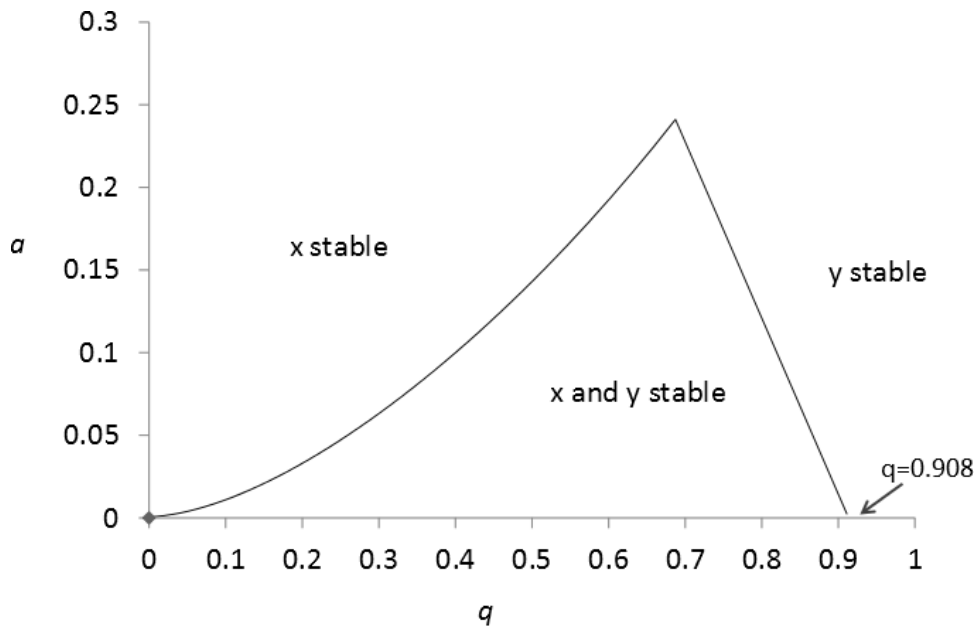


Figure 1.3 A stable region of the Mathieu stability diagram

Fourier transform ion cyclotron resonance mass spectrometry (FTICR MS)

Comisarow and Marshall introduced the Fourier transform into the ion cyclotron resonance (ICR) experiment in 1974.⁹¹ Since then, FTICR MS has been extensively investigated and applied, and several distinct features of FTICR have made it an unrivalled mass spectrometry technique. In a FTICR MS experiment, ions confined in a ICR cell (Figure 1.4) by an electric field and magnetic field will rotate circularly in the x/y plane and oscillate in the z direction (Figure 1.5);⁹² the m/z of an ion could then be determined by measuring its cyclotron frequency. This process is discussed in detail below.

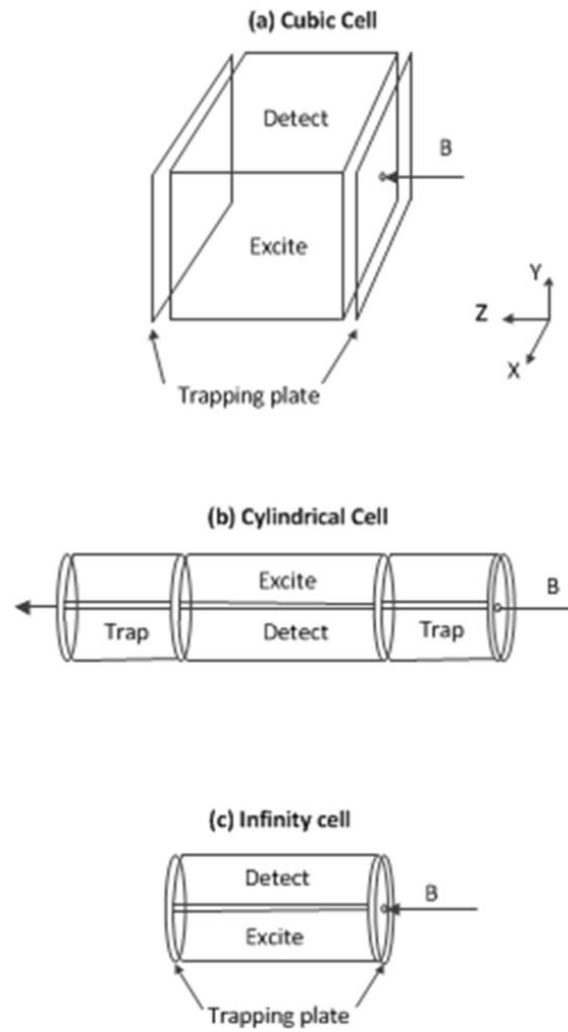


Figure 1.4 Several ICR cell geometries: (a) cubic cell, (b) cylindrical cell, and (c) infinity cell

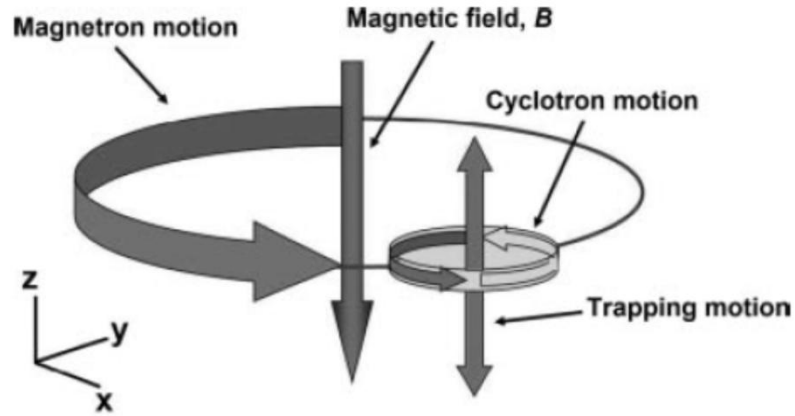


Figure 1.5 Three ion motions in the ICR cell: cyclotron motion, magnetron motion, and trapping motion (Bruker Daltonics)

Ion cyclotron motion

The superconducting magnet is most commonly used in providing a spatially uniform magnetic field B in the z -axis (axial) of an ICR cell (Figure 1.4). Ideally, without the electric field and collisions, the charged particles in the cell will simply undergo circular rotation in the x/y plane (the plane perpendicular to B) driven by an inward Lorentz force. If the ion has a velocity of v_{xy} in the x/y plane rotating with a circle of radius, r , then it should be described by Equation (1.4):

$$m \frac{v_{xy}^2}{r} = qBv_{xy}. \quad \text{Equation (1.4)}$$

Because the angular velocity ω_c and the velocity v_{xy} can be converted by

$$v_{xy} = \omega_c r. \quad \text{Equation (1.5)}$$

Replacing of v_{xy} by ω_c in Equation(1.4) will have

$$\omega_c = \frac{qB}{m}, \quad \text{Equation (1.6)}$$

and the cyclotron frequency of the ion, f_c

$$f_c = \frac{qB}{2\pi m}. \quad \text{Equation (1.7)}$$

(f_c in Hz; q in C; B in tesla; m in kg)

As $q = ez$, Equation (1.7) indicates that, under a stable magnetic field, the cyclotron frequency of an ion is directly related to its m/z regardless of its position and velocity, which is a big advantage of FTICR MS and greatly facilitates ultra-high resolution ($\geq 1M$) detection.

Trapping motion

As mentioned above, the Lorentz force confines ions in the x/y plane; however, without restraints in the z direction, ions could still be lost easily due to the axial velocity (z-axis). To solve the problem, an electric well is introduced by applying a small voltage on two trapping plates, mounted on both sides of the ICR cell either perpendicular to the z-axis (like Figure 1.4 a/c) or like in Figure 1.4b, which will leave ions oscillating back and forth along the z direction and can effectively prevent most of the ions escaping from the ICR cell. The angular frequency of the ion's trapping motion, ω_z , is described as:

$$\omega_z = \sqrt{\frac{2qV_T\alpha}{ma^2}}, \quad \text{Equation (1.8)}$$

in which α is the trapping scale factor depending on the geometry of the cell and a is the distance between two trapping plates.¹

Magnetron motion

Introduction of the trapping potential also creates an outward-directed electric force ($\frac{qV_T\alpha r}{a^2}$) opposite to the inward-directed Lorentz force which pushes ions away from the centre of the cell, so instead of Equation (1.4), the force on the ion in the x/y plane becomes:

$$m\omega^2 r = qB\omega r - \frac{qV_T\alpha r}{a^2}, \quad \text{Equation (1.9)}$$

and solving this quadratic equation in ω , will result in a reduction of the cyclotron frequency of the ion, ω_+ , and another motion called magnetron motion having a frequency of ω_- :

$$\omega_+ = \frac{\omega_c}{2} + \sqrt{\left(\frac{\omega_c}{2}\right)^2 - \frac{\omega_z^2}{2}}, \quad \text{Equation (1.10)}$$

$$\omega_- = \frac{\omega_c}{2} - \sqrt{\left(\frac{\omega_c}{2}\right)^2 - \frac{\omega_z^2}{2}}, \quad \text{Equation (1.11)}$$

where ω_c and ω_z are the unperturbed cyclotron frequency and the trapping frequency as defined above. In general, the cyclotron frequency is in the range of hundreds of kHz to MHz; the magnetron frequency (1-100 Hz) is usually much smaller than the cyclotron frequency, and the trapping frequency is typically a few kHz (less than 10 kHz). For example, at 12 T, with a trapping voltage of 1 V, an ion of m/z 1000 in an infinity cell ($a = 5$ cm) will have a reduced cyclotron frequency of 191.0 kHz, a magnetron frequency of 15.1 Hz, and a trapping frequency of 2.4 kHz. Hence, the magnetron motion and trapping motion can be ignored in most occasions.

Excitation and detection

Ions trapped in the cell usually have a small amount of kinetic energy (less than 1 eV),⁹³ so the initial radii of ions (a few micrometres) are typically much smaller than the radius of the cell (a few centimetres). Thus, excitation is required to increase the radius of the ion, to generate a detectable signal. Since the cyclotron radius is proportional to the v_{xy} of the ion when the cyclotron frequency is relatively constant, a spatially uniform electric field oscillating sinusoidally with time can be used for acceleration, and ions of the same frequency with the excitation frequency will be accelerated to a larger orbit becoming detectable. The post-excitation radius is decided by the duration of the excitation, T_{excite} , the peak to peak voltage difference between the two excitation plates, V_{p-p} , the distance between the two plates, d , and the magnetic field, B .

$$r = \frac{V_{p-p} T_{excite}}{2dB} \quad \text{Equation (1.12)}$$

Therefore, as long as the duration and the magnitude of the excitation are consistent, all of the ions can be excited to the same orbit without discrimination. Additionally, the initially randomly positioned ions with the same m/z are synchronized and become coherent after the excitation. The excited ion packets of individual m/z value will oscillate with the same cyclotron radius but different velocities; thus, these packets could be separated eventually and be detected. The non-destructive detection is realized by tracking the ion image current⁹⁴ induced by the moving ions, and a time domain will be recorded which could be further applied on Fourier transform to generate the frequency spectrum and eventually the mass

spectrum. A scheme in Figure 1.6 illustrates how a FTICR mass spectrum is generated from the image current.

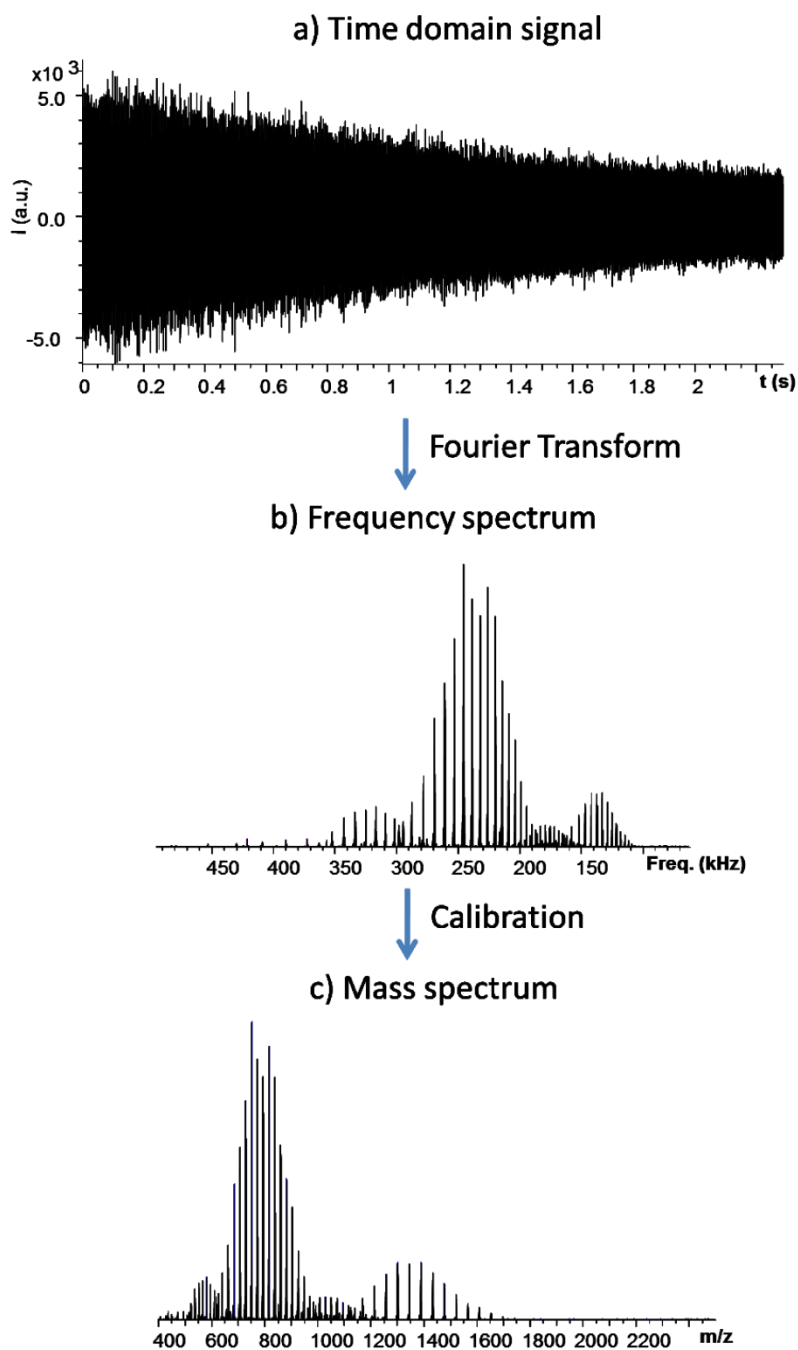


Figure 1.6 FTICR MS data process a) the raw time domain signal (transient); b) frequency spectrum; c) mass spectrum

The broadband excitation (a wide range of m/z) is usually achieved by frequency-sweep excitation (Chirp),⁹⁵ or stored waveform inverse Fourier transform (SWIFT) excitation,⁹⁶ where the latter one has a more uniform excitation power across the desired excitation range, and, ideally, ions through the selected m/z range will be excited to the same radius successively. In addition, excitation could also be used to select ions of a single m/z value by ejecting all other ions, and the selected ions can be subsequently excited and fragmented.

The time domain signal is a function of time which could be described as Equation (1.13).

$$f(t) = e^{-t/\tau} \cos(\omega t + \Phi) \quad \text{Equation (1.13)}$$

τ is the damping constant, ω is the frequency, and Φ is the phase angle.

By applying Fourier transform, Equation (1.14), on the time domain signal in Figure 1.6a, the corresponding frequency spectrum (Figure 1.6b) is generated and will be further calibrated to a mass spectrum (Figure 1.6c) by applying a calibration equation between the observed frequency and m/z .⁹⁷

$$f(\omega) = \int_{-\infty}^{\infty} f(t) e^{-i\omega t} dt \quad \text{Equation (1.14)}$$

The frequency domain is composed of two components differing by 90° in phase, absorption ($A(\omega)$) and dispersion ($D(\omega)$) (Figure 1.7), which are the projections of $f(\omega)$ in the real and imaginary axes. The absorption spectrum and the dispersion spectrum contain both positive and negative peaks, so in practice, the absolute value magnitude spectrum ($M(\omega)$) is generally used in FT-MS field.

$$M(\omega) = \sqrt{[A(\omega)]^2 + [D(\omega)]^2}$$

Equation (1.15)

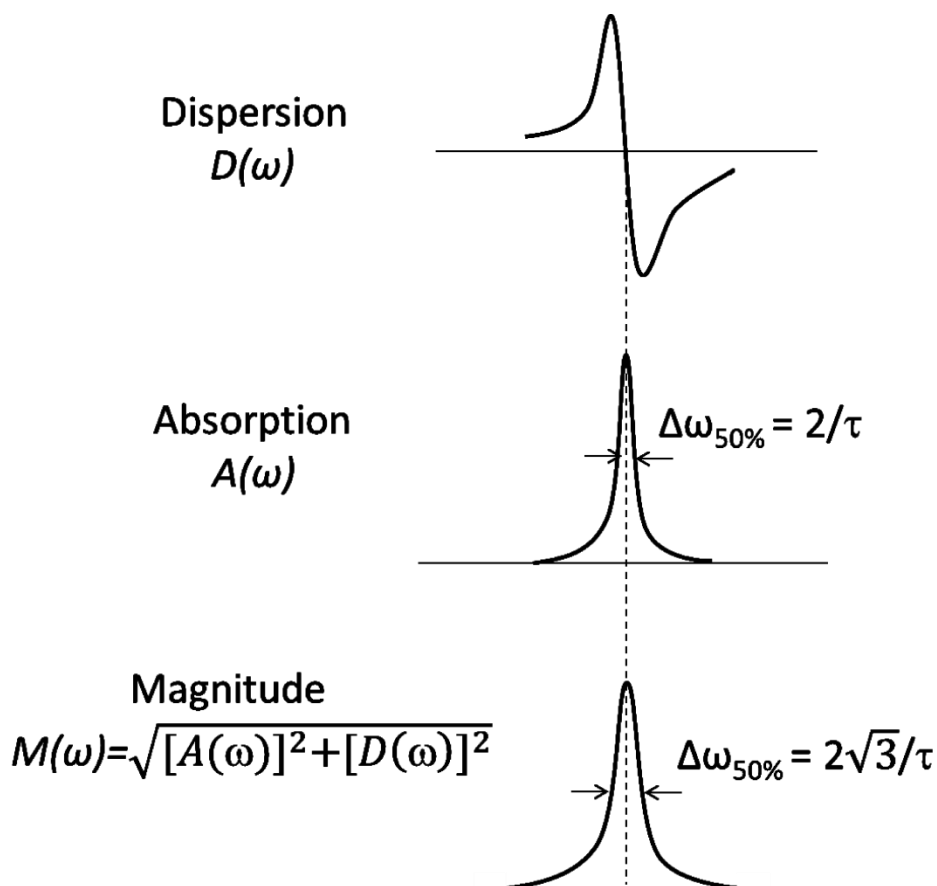


Figure 1.7 A peak in a FTICR frequency spectrum displayed in dispersion mode ($D(\omega)$), absorption mode ($A(\omega)$), and magnitude mode ($M(\omega)$)⁹⁸

Figure 1.7 shows the peak in magnitude mode is broader than the peak in absorption mode. Although the resolution difference also depends on the peak shape, spectra in absorption mode typically have a higher resolution, approximately 1.7-2 times, than the ones in magnitude mode. In order to display mass spectra in absorption mode, a phase correction is necessary. Three problems, however, make the phase correction complicated: 1)

different m/z accumulates different phase because ions are excited sequentially; 2) the time delay between excitation and detection allows additional phase accumulation; 3) to find the correct phase angle for peaks having a phase shift beyond 2π .^{98,99} Recently, O'Connor's group developed a method to find the right phase angle for each peak in a wide range of m/z by applying quadratic least square fitting, and this method has been successfully implemented for many different spectra obtained from different FTICR instruments.¹⁰⁰⁻¹⁰⁴

Though FTICR MS has advantages to obtain ultra-high resolution, Equation (1.16) displays that the length of time domain transient depends on the data set and the highest frequency in practice.

$$T=D/S \quad \text{Equation (1.16)}$$

Where T is the length of the transient, D is the number of data points, and S is the sampling frequency (at least 2 times of the highest frequency), respectively. The relationship between resolution and the length of the transient will be discussed in section 1.2.1, and T is proportional to the resolving power. Therefore, when D is constant, lowering the sampling frequency will allow a longer transient, which can be realized by using heterodyne (narrowband) detection. Heterodyne detection is done by mixing $f(t)$ with a reference signal. Based on the trigonometric product-to-sum formula ($\cos\omega_1 \cdot \cos\omega_2 = [\cos(\omega_1 + \omega_2) + \cos(\omega_1 - \omega_2)]/2$), by choosing a frequency of interest (ω_1) and a reference frequency (ω_2), $(\omega_1 - \omega_2)$ could be used to recover the information of ω_1 and ω_2 with a low sampling frequency as shown in Figure 1.8.

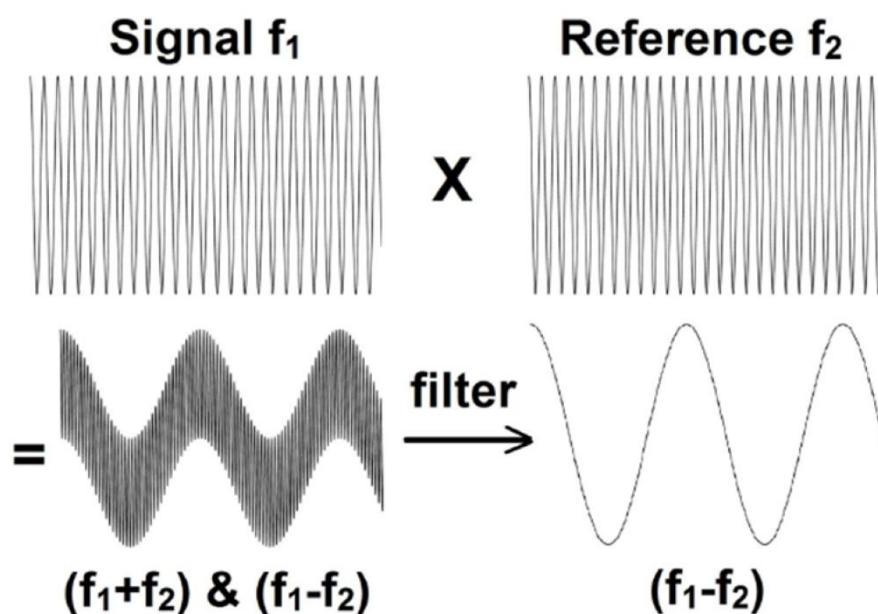


Figure 1.8 A diagram shows the principle of heterodyne detection by choosing a reference frequency $f_2=2\pi\omega_2$ which is close to the signal frequency, $f_1=2\pi\omega_1$, and (f_1-f_2) is finally detected.^{93,98,99} Adapted from Qi, Y.; O'Connor, P.B. Data processing in Fourier transform ion cyclotron resonance mass spectrometry, *Mass Spectrom. Rev.* 2014, 33, 333-352.⁹⁹

Apodization

After Fourier transform, the lineshape of peaks in a frequency/mass spectrum depends on the transient length, T , and the damping constant, τ . The peak shape shows as a sinc function when $T \ll \tau$, while if the time domain signal damps much faster than the acquisition time, $T \gg \tau$, a Lorentzian peak shape appears to fit better.⁹⁸ In practice, the peak shape is quite often a combination of sinc function and Lorentzian function. Sometimes the wiggles from the sinc function peak shape could distort the detection of some small peaks adjacent to big peaks; so, to solve this problem, an additionally function can be multiplied with the time domain signal before

Fourier transform, which is called apodization. A large variety of functions could be useful for presenting mass spectra, such as Gaussian and Hamming.¹⁰⁵ Apodization is useful to smooth the peak shape but at a cost of resolution, which could also smooth out real peak spacing, so special attention has to be taken to apply apodization.

Harmonics

Some artifacts could also be detected and displayed as peaks in the mass spectrum. One important category of artifacts is harmonics, which have frequencies equal to n ($n=1, 2, 3, \dots$) times ω (the frequency of a real peak). Since harmonics peaks appear at a higher frequency and lower m/z in comparison to the real peak, harmonics peaks have a higher resolving power than the corresponding real peak (the resolving power is inversely proportional to m/z), but they could also complicate the mass spectrum. Odd-harmonics ($3\omega, 5\omega, 7\omega, \dots$) are typically detected due to the saturation of the amplifier or overloading to analogy-to-digital converter, while the even-harmonics are mostly produced by misalignment of the ICR cell with the magnetic field, misbalance of the detector amplifiers, or large magnetron radius.^{99,106}

The key component of a FTICR MS instrument is the ICR cell, where all of the above events are performed. So far a large variety of cell geometries have been developed; cubic cell¹⁰⁷ and cylindrical cell¹⁰⁸ are the two most basic designs (Figure 1.4). Lots of progresses have been achieved to reach a more perfect quadrupolar electrostatic trapping potential and a spatially uniform excitation potential.¹⁰⁸⁻¹¹¹

1.2 Three important features of FTICR MS and the applications

FTICR mass spectrometry is a sophisticated state-of-art technique, and notably, three advantages make it unrivalled, which are high resolution, high mass accuracy, and wide accessibility to different MS/MS methods. Even though having the highest performance, FTICR is not yet as widely available as many of the other instruments due to the cost and requirement for delicate tuning; however, the three features or one of them could be necessary in some applications. Moreover, high resolution and high mass accuracy are always crucial to improve the confidence of the result and to achieve high quality of MS data, which are further demonstrated through this thesis.

1.2.1 High resolution

In general, the resolution of a peak at one m/z in a FTICR mass spectrum depends on the separation of the ion packets of different m/z values in the cell, coherence of the ions of the same m/z value, and stability of the ion frequency during detection; in FTICR, high resolution is achieved by improving all of these aspects.

First, the initial cyclotron velocity of an ion can be derived from Equation (1.5) and (1.6):

$$v_{xy} = \frac{qB_0r}{m} , \quad \text{Equation (1.17)}$$

so, at 12 T, an ion of m/z 1000 orbiting at a radius of 5 mm will have an instantaneous cyclotron velocity of 60,000 m/s; additionally, the velocity can be further increased after the excitation due to a larger cyclotron radius. Moreover, in a FTICR instrument, ions can stay relative stable in the cell for

seconds or even tens of seconds before collapse, which greatly facilitates a high resolution. Therefore, a mass spectrum is obtained from ions, which have, typically, travelled hundreds of kilometres in the cell. In comparison with another type of high performance mass analyzer, Time-of-flight (TOF), which has a flight tube at most several metres long, the superior capability of FTICR in providing high resolution is obvious.

On the other hand, in order to achieve a high resolution, each ion packet should orbit coherently without interfering with closely-spaced ion packets. Moreover, it is also crucial that the three frequencies (trapping frequency, magnetron frequency, and cyclotron frequency) of the ions of the same m/z keep consistent. The ion coherence is first realized by excitation; during the period of detection, the magnetic field, electric field, and the pressure in the cell become vital for a stable ion packet and a constant ion frequency. The superconducting magnet extensively used in FTICR MS is usually very stable, so that frequency drift caused by the magnetic field can be generally ignored. To minimize the collisions between neutral particles and the analytes, which is another adverse aspect can distort the resolution, the cell is kept in ultra-high vacuum ($\leq 10^{-10}$ mbar). In comparison, generating a homogeneous electric field in the cell is most problematic, which becomes the key factor limiting the performance of a FTICR mass spectrometer, because it is hard to have both uniform excitation potential and uniform trapping potential through the cell; however, designs have been developed to obtain a desired electric field.¹⁰⁸⁻¹¹⁰ Moreover, collisions with neutral ions still occur. Then it is reasonable that the time domain signal damps with time in practice. Thus, potentially, the longer the ions are kept with a stable cyclotron motion (T_{acq}),

the higher resolution will be, where the theoretical resolving power (R) could be roughly estimated by Equation (1.18):⁹³

$$R \approx \frac{qB_0T_{acq}}{2m} . \quad \text{Equation (1.18)}$$

In a mass spectrum, the resolving power of one specific peak is calculated from $m/\Delta m_{50\%}$, where m is the m/z value and $\Delta m_{50\%}$ is the full peak width at half maximum height (FWHM).

1.2.2 High mass accuracy

To some extent, mass accuracy is related to the resolution, because low mass accuracy due to frequency shift may often be accompanied by a low resolution. In a FTICR experiment, the experimental m/z value, however, depends more heavily on the cell parameters and the ion population in the cell. For example, it is shown clearly in Equation (1.10) that the reduced cyclotron frequency of an ion varies according to the trapping voltage in the cell. Fortunately, calibration,¹¹² in particular internal calibration, could lessen the impacts from instrument tuning and the number of ions in the cell, improving the mass accuracy. Lower than 5 ppm (part per million) mass accuracy is commonly obtained by external calibration,¹¹³ and internal calibration could further improve the accuracy to sub-ppm.

Due to the Coulomb force between ions, one side effect of charged particles orbiting in a confined small space deteriorating both resolution and mass accuracy is called the space-charge effect,¹¹³⁻¹¹⁷ which is particularly severe for ions having similar frequencies and is very sensitive to the ion

number. Where ions of similar masses merge into one ion packet and show as one peak in a mass spectrum is known as peak coalescence.^{118,119}

Another merit of FTICR over other mass analyzers is that the mass detection in FTICR is independent of the kinetic energy of the ions according to Equation (1.7) and Equation (1.10), which is a big advantage in obtaining high resolution and high mass accuracy.

The mass accuracy of peaks in a mass spectrum is quite often calculated in part per million unit (ppm) using the following equation.¹²⁰

$$\text{mass accuracy (ppm)} = \frac{(\text{Experimental } m/z - \text{Theoretical } m/z) \times 1000\,000}{\text{Theoretical } m/z}$$

1.2.3 Flexible MS/MS

In section 1.2, several most important fragmentation techniques are summarized. Because some of those MS/MS methods produce cleavages by different mechanisms, complementary structural information could be obtained by using different methods. Therefore, in practice, combining structural information from different MS/MS methods has many benefits. One advantage of FTICR is its capability to apply with a large variety of fragmentation techniques, such as CAD, IRMPD, ECD, and ETD, which makes FTICR MS/MS a superior technique in structural characterization. As noted above, ions can be trapped in an ICR cell stably for seconds, which enables the ions to be irradiated by lasers or electrons for a certain length of period to produce fragmentation.

1.2.4 The 12 T solariX FTICR MS instrument

The Bruker 12 T solariX FTICR MS instrument used for most of the work in this thesis has the configuration in 9, which is a hybrid mass spectrometer consisting of a quadrupole (Q) and a hexapole (collision cell) in front of the ICR infinity cell. Ions of a selected range of m/z can be isolated in the quadrupole before being sent into the cell and then accumulated or/and fragmented with the neutral gas (CAD) in the collision cell. Though in cell isolation and SORI CAD are also possible, the isolation is improved by introducing the quadrupole and CAD in the collision cell is more efficient than CAD in the ICR cell. Moreover, coupling a quadrupole to a FTICR mass analyzer makes multiply tandem mass spectrometry (MS^n) experiments more versatile. An electron gun and an infrared laser mounted at the end of the instrument are used for the electron-based fragmentation and IRMPD experiments, respectively. A wide variety of ionization sources including electrospray, nano-electrospray, and MALDI are accessible in our lab.

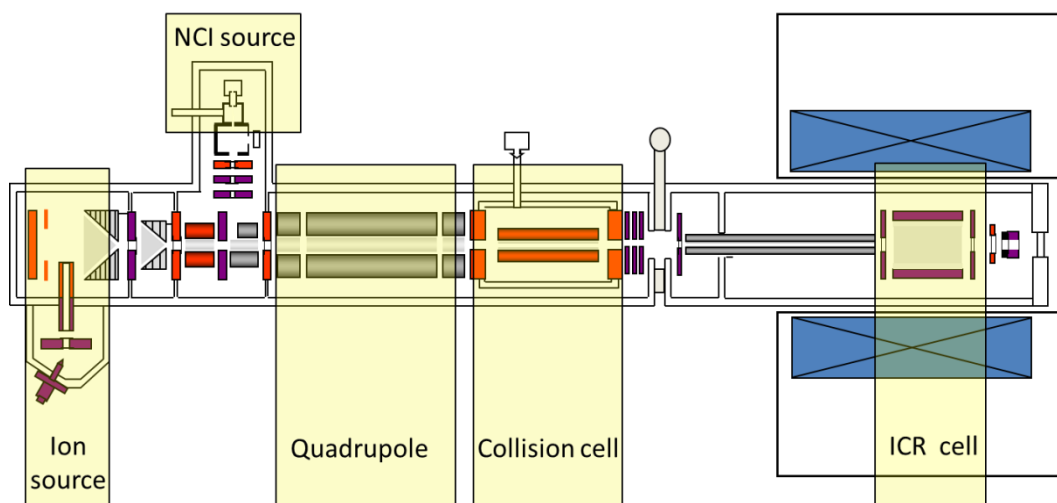


Figure 1.9 Schematic of the 12 T solariX FTICR mass spectrometer (Bruker Daltonics)

1.2.5 The important applications of FTICR MS and MS/MS

The purpose of this section is to summarize some recent advances in using FTICR to pursue the ultimate ability of MS, and in particular to highlight the applications in obtaining fine structures, characterizing the structure of both big and small molecules, analyzing complex mixtures, as well as one of the most hot topics, top-down proteomics.

Fine structure

For most atoms in nature, in addition to the most abundant isotope of each element (primarily ^{12}C , ^{14}N , ^{16}O , and ^1H for organic compounds), the remaining isotopes (e.g., ^{13}C , ^{15}N , ^{17}O , ^2H) are present in a lower or minor abundance. Thus, in a mass spectrum, every monoisotopic assignment is accompanied with various possible isotopic combinations, positioned approximately 1 Da apart (defined as A, A+1, A+2, ...).¹²¹ Except for carbon-12, no other elemental atom has an exact whole number mass value, so each isotopic peak holds its specific accurate mass (H: 1.007825, ^{14}N : 14.003074, ^{16}O : 15.994915). Therefore, apart from the monoisotopic peak (A), every isotopic cluster (A+1, A+2, ...) consists of several peaks, where each of them represents the simple sum of every individual isotopic atom and its integer quantity. These species differ from each other by typically a few mDa, and the resolved peaks are termed the isotopic fine structure.¹²¹ In principle, all of the fine structures can be separated if the resolution is sufficiently high (typically requiring resolving power of 1-5 M at m/z 1000 depending on the isotope), but it remains a challenging task for most modern mass

spectrometers, and there will always be an upper mass limit beyond which the isotopic fine structure cannot be resolved.

As each of the isotopic clusters contains multiple peaks representing all the possible combinations, such as the A+2 peak may either include two ^{13}C atoms or two ^2H atoms or one ^{34}S , the complexity of the fine structure will increase dramatically with the molecular weight and the increase in variety of atoms in the elemental composition. Moreover, peak coalescence is more likely to occur for big molecules.^{118,119} So far, most of the ultra-high resolution isotopic fine structure separations have been achieved using FTICR MS on molecules smaller than 1500 Da,¹²²⁻¹²⁸ and are particularly focused on the determination of the elemental composition.^{103,121,124,125,129-131} Two closely-spaced peptides (monoisotopic mass ~904) having a mass difference of 0.000 45 Da, less than the weight of one electron, were separated under a resolving power of ~3.3 M by a 9.4 T FTICR instrument with a large-diameter Penning trap.¹²² This achievement reveals the limitations of present proteomics research carried out on mass spectrometers with resolving power less than 10,000, where multiple peptides having similar masses could be assigned incorrectly, and demonstrates the possibility of more confident analysis using higher resolution MS.

Although fine separation is difficult for big molecules (>10 kDa) under present technical conditions, utilizing isotope depletion has proved to be an effective strategy to simplify the isotopic pattern. The isotopic fine structure of a isotopic ^{13}C , ^{15}N doubly depleted tumour suppressor protein, p16 (15.8 kDa), was detected without peak coalescence by Shi et al. using a 9.4 T FTICR instrument, which enabled the number of sulfur atoms to be counted solely

from the abundance of the resolved ^{34}S peak.¹²¹ To our knowledge, this protein (p16) is so far the biggest molecule published when the isotopic fine structure has been resolved by mass spectrometry, where an average experimental mass resolving power of 8.0 M was reached using heterodyne mode detection. To avoid frequency shift and obtain a better signal-to-noise ratio, several spectra were aligned before frequency domain coaddition.

Even though it is almost always challenging to detect the fine structure of a molecule, ultra-high resolution becomes more feasible with the development of new techniques in recent years. With decent tuning, LTQ-Orbitrap also showed its capability for small molecule isotopic distribution analysis.¹²⁴ At 7 T, the recently released dynamically harmonized ion cyclotron resonance cell succeeded in measuring the isotopic fine structures of reserpine (*MW*: 608 Da) and substance P (*MW*: 1347 Da),¹²³ with a resolving power of ~ 4.0 M and with mass error less than 200 ppb, which promises new capabilities. Most recently, using the same type of cell and a 4.7 T magnet, the fine structure of substance P was obtained with a resolving power of 12 M at m/z 675.¹³² Undoubtedly, the ability to detect molecular isotopic fine structure by ultra-high resolution mass spectrometry greatly extends the understanding of molecules and provides more possibilities for scientific research.

Complex mixtures

The high resolution and high mass accuracy of FTICR MS also make compounds identification in complex samples feasible. The compositions of a variety of complex organic mixtures have been investigated by FTICR MS, and several most extraordinary achievements in this area are bottom-up

proteomics, petroleomics, imaging mass spectrometry (IMS), and polymer analysis.

Bottom-up proteomics

In bottom-up proteomics, digested peptides are more readily detected and sequenced by MS compared to intact proteins in top-down approach, but the complexity can increase dramatically, where tens of thousands of peptides with a large dynamic range (ratio of the highest abundance species to the lowest abundance species) may have to be analyzed in one spectrum or in a few spectra. Both high resolution and high mass accuracy are essential in this case. To provide high confidence to a proteomics study, a maximum mass deviation of ~100 ppb is required for the identification of small tryptic peptides.¹³³ Working on collagen digests, the collagen peptide deamination was monitored using FTICR MS, where the mass difference of the ^{12}C peak of the deamidated peptide and the ^{13}C -substituted peak of the non-deamidated form is 19 mDa.¹³⁴ To improve the confidence of bottom-up analysis, incorporating with accurate mass measurement of FTICR MS can also provide more sequence information. The PTMs of a pilin protein, PilE (~17 kD), was fully characterized by using high resolution FTICR MS and quadrupole TOF MS/MS, where multiple modifications including glycerophosphorylation, disulfide bond, deamidation, N-terminal methylation, and glycosylation were identified.^{135,136}

Petroleomics

Within a dynamic range around 10,000, petroleum including crude oils and coals is recognized as an extremely compositionally complex organic

mixture,¹³⁷ which makes its MS analysis a hugely challenging task even with an ultra-high performance instrument. Understanding these extreme samples highly depends on the performance of the instrument, where resolution, sensitivity, and dynamic range are all necessary. So far, tens of thousands of species with mass measurement accuracy in the ppb range can be identified in a single mass spectrum.¹³⁸ Utilizing a 14.5 T FTICR mass spectrometer, up to 50,000 peaks from a Middle Eastern light crude oil sample were resolved across a $340 < m/z < 1500$ range, where 35 resolved elemental compositions presented in a single Da.¹³⁹ Later on, with a resolving power of more than 1.3 M, 244 components in the same single nominal mass can be resolved.¹⁴⁰ Incorporating FTICR mass spectrometry with liquid chromatography (LC) enables analysis of petroleum heavy ends.¹⁴⁰⁻¹⁴² By analyzing the fractionated heavy crude oil samples, about twice as many compounds were obtained in comparison with unfractionated ones.¹⁴²

Synthetic polymers

Though MALDI-TOF is still the most important MS strategy used in studying synthetic polymers, following advances in polymer science, a higher performance mass analyzer could be of particular interest for some challenging problems. With increasing complexity and diversity of structures of polymers, different MS/MS techniques may be required in the structural characterization. FTICR MS and MS/MS is emerging as an alternative and valuable tool in polymer research,¹⁴³⁻¹⁴⁶ to determine the mass distribution and absolute molar masses,¹⁴⁷ end-groups and polymerization mechanisms,¹⁴⁸ structures and compositions.^{55,145} Combining LC-ion trap (IT) /MS and FTICR MS/MS, the end-group study of methacrylic polymers was

investigated, where the remarkable mass accuracy and resolution of a FTICR MS instrument demonstrated its utility in studying complex synthetic polymer systems.¹⁴⁸ By using FTICR MS with both ECD and CAD, Kaczorowska and Cooper reported the structural characterization of polyphosphoesters, and their MS/MS degradation pathways were discussed.¹⁴⁹ Most recently, a better understanding of the composition and variability of two commonly used polymeric excipients, Gelucire 44/14 and polysorbate 80, between batches were achieved aided by the high mass accuracy of FTICR MS.¹⁴⁴

Imaging mass spectrometry (IMS)

High-resolution IMS is another fascinating breakthrough drawing widely attention in MS field in the past decade, as it provides new insights of changes in molecular level in tissues and pathologies. The driving force of the rise of IMS research is the potential to discover new diagnostic/prognostic biomarkers and its capability to simultaneously trace the spatial distributions of various molecules of interest in tissues without labels.¹⁵⁰ Though MALDI-TOF has become a routine technique in MS imaging study, the promising ability of FTICR in compound identification has been shown in many research areas, including drugs, metabolites, peptides, and proteins.¹⁵¹⁻¹⁵⁴ A better performance mass analyzer can significantly improve the spatial definition.

Metabolomics

Beyond the mixtures discussed above, a high performance mass spectrometer is also mandatory in the analysis of many other complex samples, e.g. biofluids, because of the complexity and the isobaric (compounds with the same nominal mass but different exact mass)

interference, and non-targeted metabolomics is one of the challenging subjects.¹⁵⁵⁻¹⁵⁷ Assisted by the high mass accuracy and high resolution of FTICR MS, the elemental composition of a molecule could be determined. Moreover, if the isotopic fine structures can be resolved, matching the isotopic peaks in the fine structure with the theoretical simulation is particularly useful for unambiguous assignment.^{126,158,159} MS/MS is also available to provide structural information. Using LC-FTICR MS, ³²S-containing metabolites in onion bulbs were assigned by the theoretical mass difference between ³²S-monoisotopic ions and their ³⁴S counterparts, and then the carbon number and elemental composition can be identified by comparing ¹²C- and ¹³C-based MS and MS/MS spectra.¹³⁰ Introducing isotopically-labelled standard is also useful for quantitative metabolomics studies.¹⁵⁹ Additionally, the development of comprehensive metabolomics database further improves the metabolomics study by MS.^{160,161}

Tandem mass spectrometry in structural characterization of small molecules

When analyzing unknown compounds without regular patterns like proteins/peptides using MS, there are two most important requirements in selecting a mass spectrometer. The first one is mass accuracy which is also a major index to assess a mass spectrometer; it is proven to be vital for the identification of unknown compounds and providing a reliable result. If intent to find the detail structural information, an effective MS/MS method is undoubtedly significant. As discussed in section 1.1.2, contemporary MS/MS can be achieved in numerous ways such as CAD, ECD, EDD, EID, and IRMPD. High performance FTICR mass spectrometry, which is available with

almost all of these MS/MS events, serves itself as a key tool in structural elucidation of small molecules.

Even though some MS/MS methods are more popular and ubiquitous than the others, none of them is universal. Thus, for different types of compounds or even an individual compound, a combination of different MS/MS strategies is often required to provide abundant structural information. CAD and IRMPD can be readily implemented on both singly and multiply-charged compounds. In contrast, the other popular fragmentation technique, ECD, only behaves efficiently on multiply-charged ions.¹⁶² Fortunately, EID has been demonstrated to be a complementary MS/MS method in obtaining structural information for both singly- and multiply-charged species,^{70,78,79} which is particularly beneficial in pharmaceutical research and metabolism study. Structures of a series of singly-charged organic molecules of pharmaceutical interest were characterized by EID as well as CAD, and EID was proved to provide a much greater depth of information.⁷⁸ Among 33 molecules employed in this study, much more product ions were generated from EID tandem MS/MS compared to CAD, with very little overlap between these two techniques.⁷⁸ Later on the achievement of rapid EID in LC time-scale further highlighted its ability in analyzing complex real-world samples.⁷⁵ In Wills' work on polyketides, two isomers, lasalocid A and iso-lasalocid A, were distinguished with sub-ppm accuracy aided by a FTICR CAD/EID MS³ experiment.¹⁶³

With the advances of MS/MS techniques, in addition to protein/peptide analysis, applications in oligosaccharides,^{19,164,165} lipid,¹⁶⁶ nucleotide,¹⁶⁷ etc. have developed enormously; some of the research has been reviewed

recently elsewhere.¹⁶⁸⁻¹⁷¹ One similar character between these categories of compounds is that the analysis strategy of any specific molecule in each group may be easily implemented to a series of analogues of different modification/decoration; however, none of the investigations would be feasible without a high performance instrument. The large diversity and some polymorphic structural features of oligosaccharides and lipids made their characterization historical challenges. To fully characterize oligosaccharides, including the sequence of oligomeric chain, linkage and branching information, a mass spectrometer with high resolution, high mass accuracy, and effective MS/MS access is necessary.¹⁷⁰ The traditional low-energy CAD of oligosaccharides produce mostly glycosidic fragments, whereas cross-ring cleavages are generally absent.¹⁹ Comparatively, another 'slow-heating' method, IRMPD, was suggested to provide more sequence information.^{19,43} Meanwhile, electron-based MS/MS techniques, electron activated dissociation with vary energy level (ECD at low energies, hot-ECD at intermediate energies, and electronic excitation dissociation at high energies), ETD, EDD, have shown great promises in yielding structural information including linkage and branching detail.^{164,165}

Top-down mass spectrometry analysis

A significant iconic achievement of the high performance MS is the top-down approach for protein analysis, originated from McLafferty's group in 1999.¹⁷² Although the bottom-up strategy is still more widely applied,¹⁷³ it is limited by the lack of ability to provide full scan view of the targeted protein as only a small fraction of the tryptic peptides is normally detected. Without prior digestion, top-down MS enables the whole protein been analyzed directly,

where intact protein ions can also be further isolated and fragmented subsequently to yield the information of both molecular and fragment ions, providing an extensive molecular connectivity information.¹⁷²⁻¹⁷⁶ To date, top-down MS has been employed in a wide range of research, in particular characterizing various modifications,¹⁷⁷⁻¹⁸⁵ identification and quantification proteomics,¹⁸⁶⁻¹⁸⁹ as well as understanding intact proteins within complexes.¹⁹⁰⁻¹⁹²

Proteins are converted to mature form through a completed sequence of post-translational processing and 'decoration' events.¹⁹³ The original and also one of the most essential roles of top-down MS is to study the primary structure of proteins, including amino acid sequencing, isoform identification, PTMs and protein-ligand binding site. Flexible MS/MS approaches are particularly useful to achieve these goals, so high performance MS, such as FTICR, is usually necessary in top-down research. The sequence polymorphisms of intact proteins from human saliva were studied using a FTICR mass spectrometer,^{188,194} and some isoforms arising from single nucleotide polymorphisms (SNPs) were identified. Seven human salivary cystatin variants (~14 kDa), including S, S1, S2, SA, SN, C, and D, were assigned from the masses of precursor and product ions at a tolerance of 10 ppm.¹⁹⁴ The structural diversity of some abundant salivary proteins was further investigated by combining different fragmentation modes, CAD, IRMPD, and ECD. Seventeen major proteins were analyzed, and two isoforms of protein II-2 of a mass difference less than 1 Da were determined unambiguously.¹⁸⁸ Four new sequence variants of PDC-109 from bovine seminal plasma were identified by top-down FTICR MS in addition to the

previously known variants.¹⁹⁵ FTICR armed with ECD also succeeded in precisely mapping the positions of five disulfide bonds in human salivary α -amylase (~ 56 kDa) using top-down strategy in conjugation with complete and partial reduction by tris (2-carboxyethyl) phosphine.¹⁹¹ A truncation of N-terminal 15 amino acid residues and the formation of pyroglutamic acid at the new N-terminal were identified in the protein.

Incorporated with ECD in particular, top-down strategy has special advantages in locating the covalent PTMs as well as the labile noncovalent protein-ligand binding sites, by preferentially cleaving the protein backbone.^{56,196,197} This methodology was recently applied for mapping the modification of platinum anticancer drugs on calmodulin¹⁷⁸ and also used to track the location of a hexapeptide binding ligand on the p53-inhibitor protein anterior gradient-2.¹⁹⁸ A factor that decides whether noncovalent protein-ligand binding will survive in tandem MS is the relative stability of the gas phase complexes. By coupling a FTICR MS with CAD and ECD MS/MS, the native state ATP-protein binding complexes were explored.^{184,199} The result suggested that the higher charged complexes generated by supercharging agents produced more fragments that retain the ligand, which can facilitate ligand binding research in the future. Despite the low stoichiometry of some variants, Kelleher's group has dedicated effort to the comprehensive study of PTMs of histone proteins from cell lysate in the past years.^{185,200-202} Various histone family members with different degree of modifications including phosphorylation, methylation, and acetylation were separated and precisely identified. Thus, the PTMs relevant biological activities of these histone isoforms has been discussed further.²⁰³

The impact of high performance mass spectrometry on the analysis of intact proteins and protein assemblies is dramatic. The efficiency of macromolecule analysis has been significantly improved during last decade, though it is still challenging for proteins larger than 100 kDa. Until now, there were only a few proteins exceeding 100 kDa been baseline unit mass resolved. With a substantial redesigned 9.4 T FTICR mass spectrometer, a 20 s time-domain signal with resolving power of ~420,000 has been achieved for an intact 147.7 kDa monoclonal antibody (mAb), where the highest magnitude isotopic peak differs from the predicted value by -1 Da.²⁰⁴ In the past few years, Michael Gross's group made exciting progress in using native ESI and ECD FTICR MS to study intact protein complexes.^{205,206} The remarkable performance of this approach was tested by three protein assemblies larger than MDa, yeast alcohol dehydrogenase (147 kDa), concanavalin A (103 kDa), and a photosynthetic protein complex (FMO 140 kDa),²⁰⁵⁻²⁰⁷ and paved its way for more tough challenges. In this approach, not only the noncovalent metal-binding sites and assembly stoichiometry information could be obtained, but also more significantly, the flexible regions which can be fragmented and sequenced by MS/MS (ECD or activated-ion ECD in this case) correlated well with the data from X-ray crystallography. Most recently, Li in Loo's group reported isotopic resolution of a 158 kDa protein complex, tetrameric aldolase, with an average absolute deviation of 0.36 ppm, which is the largest molecule isotopically resolved to date, and partially sequencing was realized by native top-down ECD.²⁰⁸

Two-dimensional FTICR MS (2D FTICR MS)

One distinct capability of FTICR MS is to implement two-dimensional mass spectrometry, where ions will be detected and fragmented without isolation in the ICR cell, so that a 2D mass spectrum contains the information of all of the ions detected in MS and their fragments. Potentially, 2D FTICR MS has advantages in providing more information of complex mixtures, because species of low abundance are fragmented without discrimination, and the ion loss during isolation is also minimized. The crucial part for the final success of 2D MS analysis is to change the pulse sequence to control the speed and the position of ions in the cell. Figure 1.10 shows a typical pulse sequence of a 2D FTICR MS experiment.^{209,210} In the excitation pulse (P_1), all of the ions in the cell will be excited to the same radius, and after spinning for a period of t_1 , the ions could be de-excited by another pulse (P_2). The ions which have returned to the center of the cell can be fragmented efficiently and detected successively. Therefore, by manipulate the time t_1 , all ions will be fragmented and detected sequentially. In-cell CAD, IRMPD, and ECD are all available fragmentation methods compatible in 2D experiments.²¹⁰⁻²¹⁴

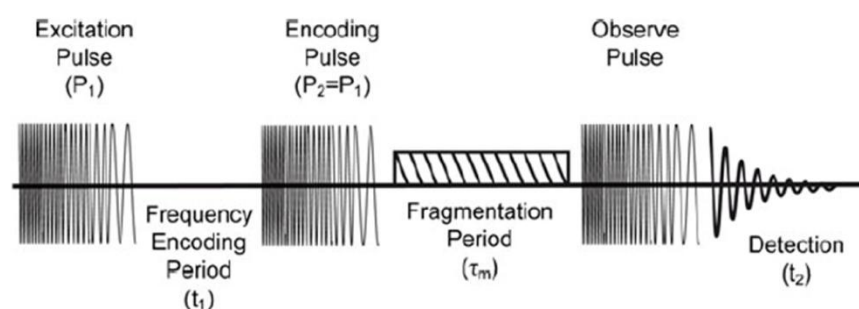


Figure 1.10 Pulse sequence for a two-dimensional FTICR MS experiment.^{209,210}

1.3 Content of the thesis

The thrust of the thesis is to utilize the advantages, in particular three advanced features, high resolution, high mass accuracy, and flexible tandem mass spectrometry techniques, of FTICR MS to investigate some molecules of great interest in science and/or industry.

In the second chapter, the separation limit of a 12 T solariX FTICR instrument is challenged by measuring the isotopic fine structures of two ^{17}O enriched amyloid- β ($\text{A}\beta$) peptides, $\text{Ac-A}\beta_{16-22}\text{-NH}_2$ (MW : 894.498124 Da) and $\text{A}\beta_{11-25}$ (MW : 1757.885869 Da). In the third chapter, $\text{A}\beta_{37-42}$ peptides labelled with either ^{17}O on Gly38 ($\text{GG}_{38}(^{17}\text{O})\text{VVIA}$, MW : 515.315166 Da) or ^{15}N on Val39 ($\text{GGV}_{39}(^{15}\text{N})\text{VIA}$, MW : 515.307984 Da) are analyzed with ultra-high resolution, so that the ratio of ^{17}O could be estimated by the isotopic fine structure to assist the NMR data interpretation. In the fourth chapter, all of the three advanced features of FTICR MS are utilized to provide a confident analysis of the composition of TPGS samples and the structure of the TPGS molecule, a widely used polymeric excipient in the drug industry. Following on observations from the MS/MS experiments of TPGS attached with different metallic adducts in Chapter 4, the competitive influence of several popular adducts on the fragmentation of TPGS is studied, and some trends are summarized, which is useful for understanding the mechanisms of CAD and ECD processes. Aided by the availability to different fragmentation techniques of FTICR MS, the MS/MS fragmentation, including CAD, EID, and IRMPD, of chlorophyll-*a* and its Mg^{2+} depleted species, pheophytin-*a*, are investigated respectively in Chapter 6 and 7. In an on-going project, a top-down MS strategy is used to study a protein of a molecular weight of 35 kDa, p65

(C₁₅₂₆H₂₄₁₉N₄₅₆O₄₆₀S₁₃), and FTICR MS displays the ability to analyze big molecules (≥ 30 kDa). Chapter 9 is the conclusions and future work.

Chapter 2 Utilizing isotopic fine structure mass spectrometry to understand ^{17}O labelled amyloid peptides

2.1 Introduction

2.1.1 Techniques to measure the isotopic abundance of elements

Isotope ratio measurements are a very important field directly related to the fundamentals of atomic physics. Back to 1913, J. J. Thomson first demonstrated the presence of isotopes of elements by showing that neon is composed of two isotopes, ^{20}Ne and ^{22}Ne ,²¹⁵ and which experiment is also recognized as the first example of mass spectrometry. Over the years, mass spectrometry has developed enormously, and becomes a routine technique used for a vast amount of applications. Even though the isotope ratio measurement is no longer the most hot-topic in the mass spectrometry field, it still has irreplaceable importance for a number of different applications, such as monitoring the isotope variation in nature and tracing experiments using enriched isotopes.²¹⁶ So far, two predominant techniques used for the precise isotope ratio measurement are isotope ratio mass spectrometry (IRMS) and inductively coupled plasma mass spectrometry (ICP-MS).²¹⁷

Traditionally, magnetic sector analyzers are used in IRMS, and are quite often coupled with a gas chromatography (GC) -combustion interface, known as GC-C-IRMS. GC-C-IRMS is in particular useful for accurately measuring the isotopic abundance of ^2H , ^{13}C , ^{15}N , and ^{18}O in small organic molecules. GC-C-IRMS is able to determine the ratio of $^{13}\text{C}/^{12}\text{C}$ with a precision of 0.03% on average;²¹⁸ a similar level of precision could be achieved for $^2\text{H}/\text{H}$, $^{15}\text{N}/^{14}\text{N}$,

and $^{18}\text{O}/^{16}\text{O}$, but which is more challenging due to very low abundance of ^2H , ^{15}N , and ^{18}O in nature. In practice, small and volatile molecules, such as amino acids or small metabolites are more suitable for IRMS experiments; otherwise, derivatization will be needed. Moreover, a reference is necessary to ensure a high precision. On the other hand, ICP-MS mainly focuses on determining the isotopic abundance of chemical elements in inorganic compounds, where the precision can be pushed to be as low as 0.005%.^{216,219} Most recently, a spectroscopy technique called cavity ring-down spectroscopy (CRDS) emerges as an alternative choice of IRMS for isotopic analysis of small organic molecules. CRDS has displayed promising roles in characterizing the isotopic abundance of ^2H , ^{13}C , ^{17}O and ^{18}O .²²⁰⁻²²² Although the precision of CRDS is inferior to GC-C-IRMS, CRDS instruments cost less and are more compact.²²²

Using high resolution isotopic fine structures to determine the isotope ratio has been available for a long time, but it is not extensively applied due to two main reasons. One reason is the limited accessibility to high performance mass spectrometers and expertise of tuning, and the other is the low natural abundance of many isotopes. To measure the subtle difference in the isotopic abundance precisely is challenging for most modern mass spectrometers. However, the ultra-high resolution isotopic fine structure of molecules has been demonstrated to be of great interest in determining the elemental composition of molecules less than 1500 Da,^{103,121-131} where most of which were achieved using FTICR MS. Isotopic fine structures have also been used in monitoring the hydrogen/deuterium exchange of a peptide by the unambiguous separation of the ^2H - and ^{13}C - substituted peaks.¹²⁸

2.1.2 Utilizing isotopic fine structure mass spectrometry to aid the interpretation of NMR data of ^{17}O labelled amyloid beta peptides

The well-known amyloid beta ($\text{A}\beta$) peptides are the major components of the amyloid plaque filaments associated with Alzheimer's disease.²²³⁻²²⁵ Different polymorphs of amyloid fibrils and, in particular, the aggregation of $\text{A}\beta$ peptides (oligomers) are key toxic species implicated in Alzheimer's disease.^{225,226} Most importantly, different inter- and/or intra- molecular hydrogen bonding is recognized as a key factor in influencing the structural variety.^{227,228} Recently, a novel solid-state NMR strategy that applied the REAPDOR methodology was demonstrated²²⁹ and succeeded in assigning the specific $^{17}\text{O} \cdots \text{H}-^{15}\text{N}$ hydrogen bonding in $\text{A}\beta$ peptides.²³⁰ By measuring the $^{15}\text{N}-^{17}\text{O}$ dipolar coupling between the carbonyl oxygen and the amide nitrogen atoms, illustrated as $\text{C}=\text{O} \cdots \text{H}-^{15}\text{N}$, the distance between the nuclei can be determined and the result could be correlated with the presence of intra- and /or inter- molecular interactions due to hydrogen bonding. The $^{15}\text{N}\{^{17}\text{O}\}$ REAPDOR method has the advantage of measuring the shorter nitrogen-oxygen distances as opposed to longer indirect carbon-carbon or carbon-nitrogen distances in traditional $^{13}\text{C}-^{13}\text{C}$ or $^{13}\text{C}-^{15}\text{N}$ NMR methods.²³⁰⁻²³² Molecules labelled with ^{15}N and ^{17}O are necessary for this measurement because of their low natural abundances (0.37% for ^{15}N and 0.04% for ^{17}O , see Table 2.1), and the enrichment ratio will be crucial for the interpretation of the NMR coupling constant and interatomic distances. Although there are a few accurate methods to determine $^{17}\text{O}/^{18}\text{O}$ enrichment values,^{220,221,233} in this experiment, the important value is the ^{17}O enrichment of one specific oxygen atom within an otherwise normal peptide. Most methods one could consider

to accurately determine this value would require chemistry such as acid hydrolysis or enzymatic digestion to cleave the peptide into individual amino acids and afterwards measure the ^{17}O enrichment of the individual amino acid, but such strategies run a strong risk of scrambling the ^{17}O labelling position and thus invalidating the measured ^{17}O enrichment information, and such methods generally will also dilute the signal by inclusion of the oxygen atoms from other unlabelled amino acids.

Table 2.1 Isotopic masses and natural abundance of H, C, N, and O^{234,235}

Isotope	Mass (Da)	Natural abundance
^1H	1.007825	99.99%
^2H	2.014102	0.01%
^{12}C	12.000000	98.93%
^{13}C	13.003355	1.07%
^{14}N	14.003074	99.63%
^{15}N	15.000109	0.37%
^{16}O	15.994915	99.76%
^{17}O	16.999132	0.04%
^{18}O	17.999160	0.21%

The two samples studied in this chapter are Ac-A β_{16-22} -NH₂ (N-acetyl-KLV₁₈(^{17}O)FF₂₀(^{15}N)AE-NH₂, abbreviated as A β_{16-22} hereafter) and A β_{11-25} (EVHHQKL₁₈(^{17}O)FFA₂₁(U- ^{13}C , ^{15}N)EDVG). Since ^{15}N is labelled (> 99%) on Phe20 for A β_{16-22} or on Ala21 for A β_{11-25} , and similarly ^{13}C is labelled (> 99%) on Ala21 for A β_{11-25} , the formulae of the two peptides are written as C₄₅H₆₇O₁₀N₈ ^{15}N (MW: 894.498124 Da) and C₇₈ $^{13}\text{C}_3$ H₁₁₉O₂₃N₂₀ ^{15}N (MW: 1757.885869 Da), respectively. In order to calculate the ratio of ^{17}O labelling,

the two peaks corresponding to ^{13}C -substituted and ^{17}O -substituted peptides in the A+1 cluster (second isotopic cluster) must be fully resolved for both peptides, where the mass difference (Δm) between $^{13}\text{C}^{16}\text{O}$ and $^{12}\text{C}^{17}\text{O}$ is 0.000863 Da. Theoretically, for a singly-charged $\text{A}\beta_{16-22}$, baseline separation of the two closely-spaced species, ^{13}C - and ^{17}O - substituted peaks, requires a resolving power of approximately 3.0 M ($3m/\Delta m$ corresponding to the approximate baseline separation of two closely-spaced peaks), and the resolving power required for $\text{A}\beta_{11-25}$ is higher (~ 6.0 M) because of its higher mass.

2.1.3 Content of the chapter

In this chapter, the isotopic fine structures of ^{17}O enriched $\text{A}\beta_{16-22}$ and $\text{A}\beta_{11-25}$ were measured, and the ^{13}C -substituted and the ^{17}O -substituted peaks were baseline-resolved by a 12 T solarix FTICR MS instrument with average resolving power ≥ 5.0 M. The results enable the ratio of ^{17}O enrichment to be estimated with 2.1% and 5.2% uncertainties for the $\text{A}\beta_{16-22}$ and $\text{A}\beta_{11-25}$, respectively, according to the detection of the ^{13}C -species in the same peptide, which is crucial for interpreting the relationship between the experimental NMR signal and the inter/intra-atomic distance of interest. Additionally, the position of the ^{17}O labelling was located based on the fragmentation information generated by CAD.

2.2 Experimental section

2.2.1 Chemicals

The synthesis and preparation of $\text{Ac-A}\beta_{16-22}\text{-NH}_2$ (N-acety-KLV $_{18}$ (^{17}O)FF $_{20}$ (^{15}N)AE-NH $_2$) and $\text{A}\beta_{11-25}$ (EVHHQKLV $_{18}$ (^{17}O)FFA $_{21}$ (U- ^{13}C , ^{15}N)EDVG) were

described in detail elsewhere.²³⁰ For mass spectrometry experiments, the peptide samples were dissolved in 50:50 acetonitrile (VWR Co., Radnor, PA, USA) /water with 1% of formic acid (Sigma-Aldrich Co., St. Louis, MO, USA) to a concentration of ~1 μ M. Water was purified by a Millipore Direct-Q purification system (Merck Millipore, MA, USA). ESI tuning mix was purchased from Agilent Technologies (Product No: A182611, Agilent Technologies, USA) and was stored in 4°C fridge.

2.2.2 Mass spectrometry experiments

All mass spectrometry experiments were carried out on a Bruker 12 T solariX FTICR mass spectrometer (Bruker Daltonik, GmbH, Bremen, Germany) with a custom nano-electrospray ion source. ~5-10 μ L of sample was loaded into a glass capillary tip with a stainless steel wire inside to form the electrical connection.¹⁷⁹ Nano-electrospray ionization was generated by applying a voltage of 600-1200 V between the spraying needle and inlet capillary tip of the instrument. To remove undesired ions, the monoisotopic peak (A, m/z 895.505401 for singly-charged A β_{16-22} and m/z 879.950210 for doubly-charged A β_{11-25}) and several isotopic peak clusters of interest (A+1, A+2, and A+3) were isolated using a quadrupole with an isolation window of ± 7 Da, where the central m/z and the width of the window were optimized to ensure a good isolation. The embedded ^{13}C isotope distribution was used to evaluate the isolation. After accumulated in the collision cell for typically 1-20 milliseconds, those ions were cooled for 0.01 s in the collision cell before being sent to the ICR infinity cell.¹¹⁰ The front and end trapping voltages were set at 1.55 and 1.57 V or 1.75 and 1.77 V for the detection of A β_{16-22} or A β_{11-25} . The ion population in the cell was maintained as low as possible to reduce

peak coalescence and ion-ion interactions as a precondition for detection at sufficiently high resolution to separate the isotopic fine structure peaks, so the intensity of the base peak is usually kept at around 4×10^6 /scan. To enable a long transient, all of the ultra-high resolution spectra were detected in heterodyne mode,²³⁶ with a sampling frequency of 7-15 kHz and using 256 k or 128 k data points. The transient coherence was monitored to choose the optimal transient length.

For CAD experiments, the isolated parent ions using the quadrupole were then transferred to the collision cell for fragmentation using a collisional energy of 20-27 V, and fragments were detected in the ICR cell. Up to 20 scans were averaged for CAD experiments to achieve a desirable S/N and spectrum quality. Otherwise, all of the ultra-high resolution spectra were acquired as one scan and were presented in magnitude mode unless otherwise noted. For comparison, some spectra were manually phased to absorption mode using a previously reported method.¹⁰² The resolving power is calculated from $m/\Delta m_{50\%}$. Unapodized spectra were used in order to monitor the true separation of closely-spaced peaks, because apodization may smooth out the real peak spacing particularly when the two peaks are not fully resolved. All of the spectra were processed by DataAnalysis 4.0 software (Bruker Daltonik, GmbH, Bremen, Germany). The theoretical isotopic distribution was simulated either by IsoPro3.0²³⁷ (oxygen enriched) or DataAnalysis (natural abundance) using a resolving power similar to the experimental result. The simulation of oxygen enriched molecules was achieved by modifying the isotopic abundance of one atom in the IsoPro data base. Take $A\beta_{16-22}$ ($C_{45}H_{68}O_{10}N_8^{15}N$) as an example, if assuming that one of

the oxygen atoms (O^*) is enriched and contains 40% ^{16}O , 50% ^{17}O , and 10% ^{18}O , the simulation can be done by using the elemental composition: $C_{45}H_{68}O_9O^*N_8N^*$, where O^* has 40% ^{16}O , 50% ^{17}O , and 10% ^{18}O , and N^* has 100% ^{15}N .

In this research, the ion accumulation time, cooling time, and cell parameters are vital for the final success of obtaining a ultra-high resolution. Particularly, it is interesting that a relatively high trapping voltage (1 - 2 V) combined with a low excitation power (35.0 - 55.5 V_{pp}) was most effective in detecting isotopic fine structures in practice, which is contradictory to some previous ultra-high resolution studies carried out on FTICR instruments with different ICR cell geometries. For example, trapping voltages lower than 0.5 V during the detection were used in Marshall's work.^{121,122} Using a lower trapping voltage is of benefit to inhibit the space-charge effect by allowing the ions to spread out, thereby minimizing the effects of peak coalescence²³⁸ and peak broadening.²³⁹ However, the electric and magnetic field are both more homogenous in the center of the ICR cell, furthermore, a lower cyclotron radius means a lower spin-speed of the ion, minimizing ion collisions and thus retaining ion coherence longer. Regardless, it is crucial to control the ion number in the cell. The discrepancy between current research and previous reports is likely due to the use of different ICR cell geometries, and the Infinity cell¹¹⁰ appears to have a smaller 'sweet spot' with low electric field inhomogeneity compared to an open cylindrical cell. Further observation will be discussed in detail in 2.3.1.

2.3 Results and discussions

2.3.1 A β_{16-22} (C₄₅H₆₇O₁₀N₈¹⁵N) partially labelled with ¹⁷O

Figure 2.1 shows the high resolution fine structure of the singly-protonated A β_{16-22} (C₄₅H₆₈O₁₀N₈¹⁵N, MW: 895.505401 Da) including the baseline-resolved ¹³C-substituted (C₄₄¹³CH₆₈O₁₀N₈¹⁵N) and ¹⁷O-substituted (C₄₅H₆₈O₉¹⁷ON₈¹⁵N) peaks in the A+1 cluster. The m/z values of the peaks in Figure 2.1 are listed in Table 2.2 with the monoisotopic peak at m/z 895.505401 as the internal lock mass, and the overall mass uncertainty is ± 29 ppb. In comparison, the theoretical mass spectrum of the corresponding A β_{16-22} peptides with natural abundance oxygen is plotted in Figure 2.1 as a blue dashed line above the experimental spectrum. With an average experimental resolving power (abbreviated as R.P.) of ~ 4.94 M shown in Figure 2.1, the two peaks in the A+1 cluster are clearly resolved and a 0.000805 Da experimental mass difference is measured which is 57 μ Da different from the theoretical value (0.000862 Da). The time-domain transient length is 37.9 s. Although only a single transient was acquired, the experimental mass value was determined into the 5th digit past the decimal (0.01 ppm), remaining mass errors could be due to various factors, e.g. inhomogeneous electric and magnetic field, space-charge effect, and non-zero vacuum.

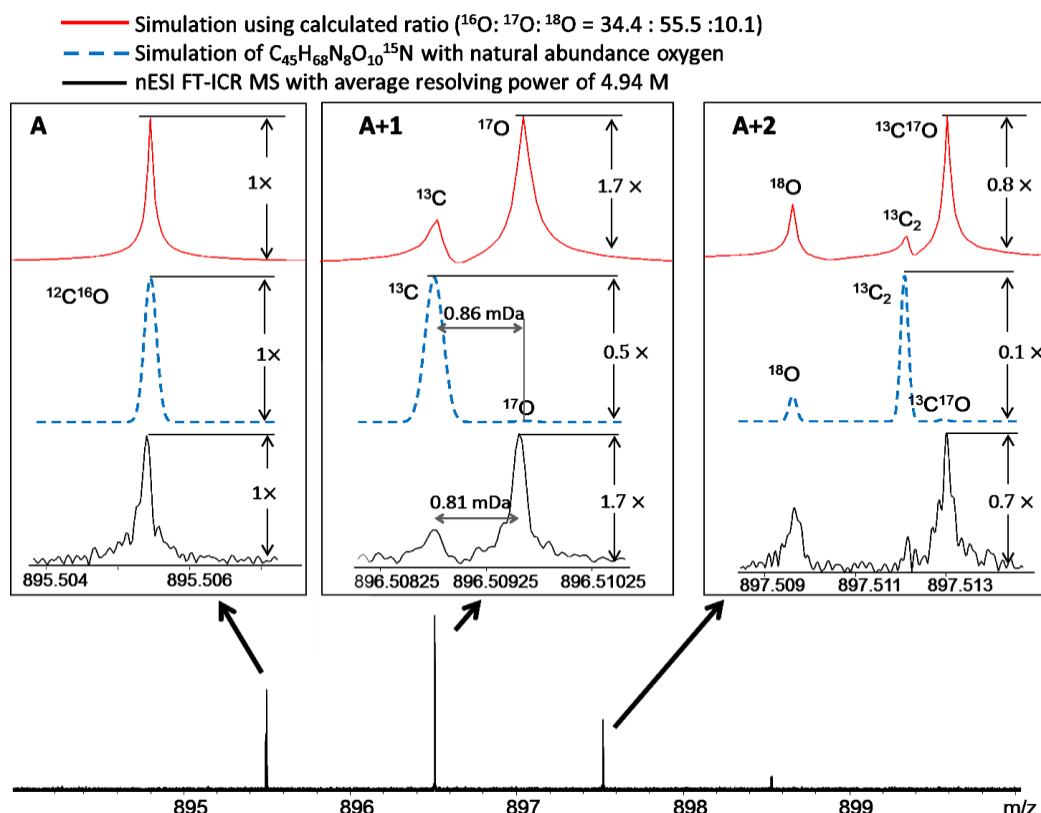


Figure 2.1 An ultra high resolution FTICR mass spectrum of the singly-protonated $\text{A}\beta_{16-22}$ ($\text{C}_{45}\text{H}_{68}\text{O}_{10}\text{N}_8^{15}\text{N}$) in black, and the simulated spectra of $\text{A}\beta_{16-22}$ with natural abundance oxygen (the dashed blue line) and using the calculated ratio, $^{16}\text{O} : ^{17}\text{O} : ^{18}\text{O} = 34.4 : 55.5 : 10.1$ (the red line). The peak list is in Table 2.2

Table 2.2 The mass list of proposed peaks in Figure 2.1

Isotope difference	Formula	Resolving power/M	Theoretical m/z	Experimental m/z	Error /ppm
	* $\text{C}_{45}\text{H}_{68}\text{N}_8^{15}\text{NO}_{10}$	5.66	895.505401	895.505401	----
^{13}C	$\text{C}_{44}^{13}\text{CH}_{68}\text{N}_8^{15}\text{NO}_{10}$	3.89	896.508756	896.508757	0.001
^{17}O	$\text{C}_{45}\text{H}_{68}\text{N}_8^{15}\text{NO}_9^{17}\text{O}$	5.65	896.509618	896.509561	-0.064
^{18}O	$\text{C}_{45}\text{H}_{68}\text{N}_8^{15}\text{NO}_9^{18}\text{O}$	2.63	897.509647	897.509649	0.002
$^{13}\text{C}_2$	$\text{C}_{43}^{13}\text{C}_2\text{H}_{68}\text{N}_8^{15}\text{NO}_{10}$	7.76	897.512110	897.512148	0.042
$^{13}\text{C}^{17}\text{O}$	$\text{C}_{44}^{13}\text{CH}_{68}\text{N}_8^{15}\text{NO}_9^{17}\text{O}$	4.04	897.512972	897.513005	0.037
	Average of the absolute value	4.94			0.029
	STDEV				0.042

* The peak used as the lock mass

The unambiguous sub-ppm assignment of the ^{13}C - ($\text{C}_{44}^{13}\text{H}_{68}\text{O}_{10}\text{N}_8^{15}\text{N}$) and ^{17}O - ($\text{C}_{45}\text{H}_{68}\text{O}_9^{17}\text{ON}_8^{15}\text{N}$) substituted species is further demonstrated by a spectrum averaged from a 10-scan acquisition (Figure 2.2), indicating that errors caused by space charge and other field inhomogeneities are lower than the peak width of an individual scan.

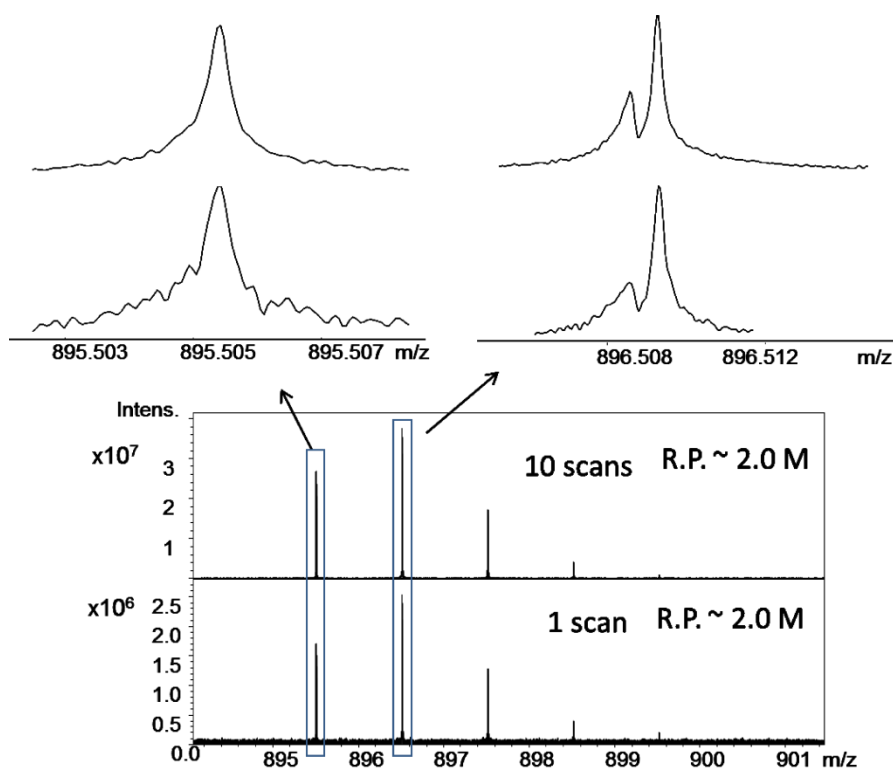


Figure 2.2 The comparison of two mass spectra of singly protonated $\text{A}\beta_{16-22}$ with different acquisition scans (10 scans and 1 scan) but the same resolving power (~ 2.0 M).

If the detection of the A+1 cluster with R.P. from 500,000 to 5,000,000 is tracked (shown in Figure 2.3), the identification of these two peaks becomes even more unambiguous. At a resolving power of 3 M, the fine structure is

already baseline-resolved, which agrees with the theoretical estimate that the baseline separation of the ^{13}C and ^{17}O species requires a R.P. of $\sim 3 \text{ M}$ ($3m/\Delta m$). On the other hand, at a R.P. of 500,000 (Figure 2.3e), which is still generally not achievable by other types of modern mass spectrometers, the peaks adjacent are completely overlapped.

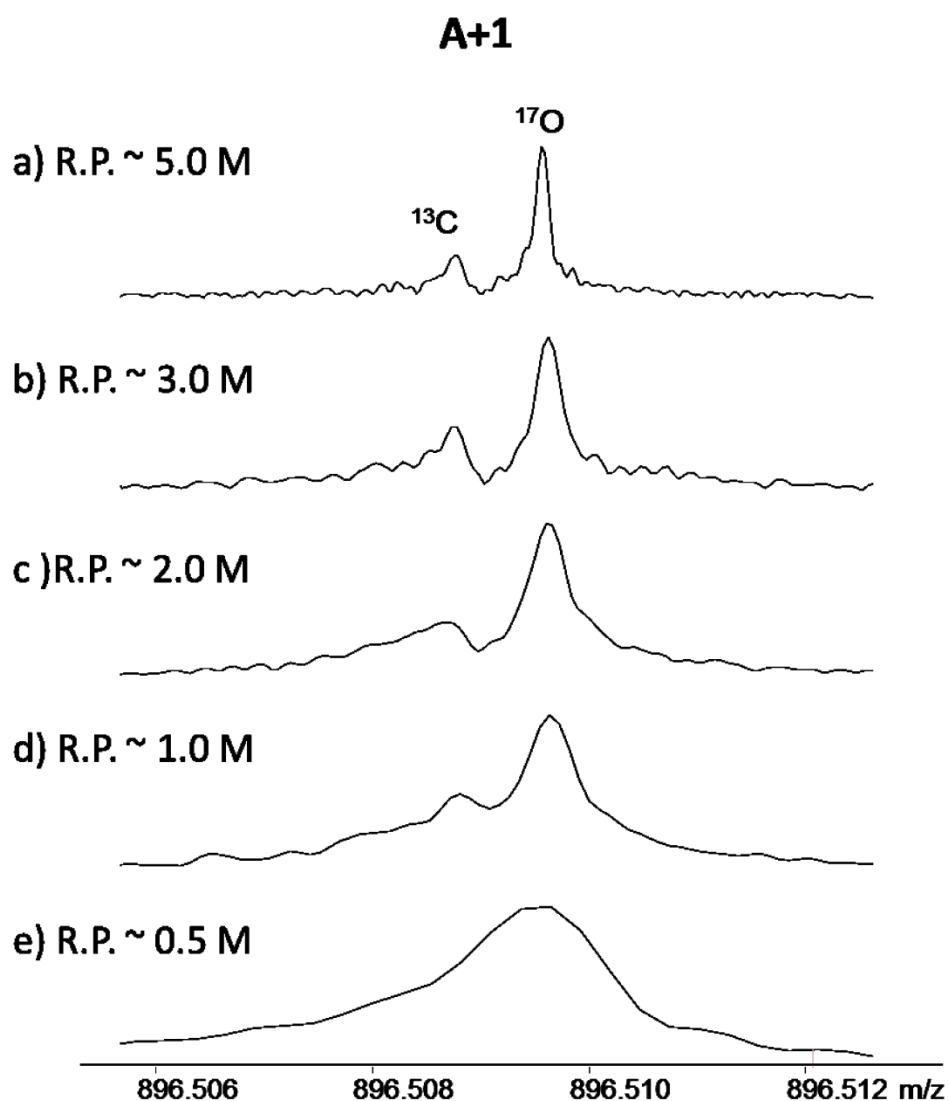


Figure 2.3 The separation of A+1 cluster of the singly-protonated $A\beta_{16-22}$ ($C_{45}H_{68}O_{10}N_8^{15}N$) with resolving power (R.P.) from 0.5 M to 5.0 M. The peaks labelled as ^{13}C and ^{17}O are the ^{13}C - ($C_{44}^{13}CH_{68}O_{10}N_8^{15}N$, m/z 896.508756) and ^{17}O - ($C_{45}H_{68}O_9^{17}ON_8^{15}N$, m/z 896.509618) substituted species, respectively

Aided by the fine separation, the ratio of ^{17}O abundance is able to be calculated by:

$$^{17}\text{O abundance} = \frac{I(^{12}\text{C}^{17}\text{O})}{I(^{12}\text{C}^{16}\text{O}) + I(^{12}\text{C}^{17}\text{O}) + I(^{12}\text{C}^{18}\text{O})}, \quad \text{Equation (2.1)}$$

where $I(^{12}\text{C}^{16}\text{O})$, $I(^{12}\text{C}^{17}\text{O})$, and $I(^{12}\text{C}^{18}\text{O})$ are the ion intensity of $^{12}\text{C}^{16}\text{O}$ -, $^{12}\text{C}^{17}\text{O}$ -, and $^{12}\text{C}^{18}\text{O}$ - substituted peaks. To minimize the influence of signal fluctuation, the results from six runs are averaged (see the Appendix A Table A.1), where the experimental ratios of the $^{12}\text{C}^{16}\text{O}$ -, the $^{12}\text{C}^{17}\text{O}$ -, and the $^{12}\text{C}^{18}\text{O}$ - peaks are $34.4 \pm 2.3\%$, $55.5 \pm 2.2\%$, and $10.1 \pm 1.3\%$, respectively (for these $x \pm \Delta x\%$, $\Delta x\%$ is defined as one standard deviation of the uncertainty in the calibration). In contrast, for the corresponding natural abundance oxygen $\text{A}\beta$ species, these numbers are 97.6%, 0.4%, and 2% correspondingly. Therefore, in addition to ^{17}O labelling, ^{18}O is also simultaneously detected to be about 8% enrichment for the $\text{A}\beta_{16-22}$ peptide. It is noted that, to estimate the accuracy and reliability of the result, the experimental ratio of ^{13}C was compared with the theoretical value. The consistency of these two numbers, 31.9% (experimental ratio of ^{13}C calculated according to Equation A1 in Table A.2) and 32.6% (theoretical ratio of ^{13}C), boosts the confidence of the result, and the uncertainty of the experiment is calculated from $\frac{31.9\% - 32.6\%}{32.6\%} \times 100\% \cong -2.1\%$ (Table 2.4). The simulated spectrum generated by using the calculated ratio ($^{16}\text{O}: ^{17}\text{O}: ^{18}\text{O} = 34.4: 55.5: 10.1$) is displayed on the top of Figure 2.1 in red, which matches well with the experimental spectrum on the bottom (black). Additionally, the abundance of each isotope is also calculated according to the peak area by equations A4-A7 in Table A.2, similar results are obtained (Table A.1 in the Appendix A). Since the calculation using the

peak area has a relatively higher standard deviation, Equation 1 utilizing the peak intensity is used. To double check the result, switching ^{12}C to ^{13}C , the ratio of ^{17}O enrichment is calculated by equation A8 in Table A.2, and a similar value is observed (data is not shown).

Due to protonation and multiple isotopic labelling, although unlikely, it is possible that the monoisotopic peak is mis-assigned without sufficient mass accuracy, which could result in mis-assignment of the fine structure peaks. To further check the peak assignment, a calibration standard, ESI tuning mix, was ionized together with the peptide analyte using a dual nano-electrospray setup (Figure A.1 in Appendix A) to calibrate the spectrum internally, rather than using a peak from the peptide as the lock mass. The result is shown in Figure 2.4 (peak list is available in Table A.3), and the mass of the monoisotopic peak at m/z 895.50539 differs from the assumed formula $\text{C}_{45}\text{H}_{68}\text{O}_{10}\text{N}_8^{15}\text{N}$ (m/z 895.50540) by 0.01 ppm. For example, if the ^{15}N and ^{17}O labelling on the $\text{A}\beta_{16-22}$ peptide was not clear, the errors for two possible formulae, $\text{C}_{45}\text{H}_{67}\text{O}_{10}\text{N}_7^{15}\text{N}_2$ (m/z 895.49461) or $\text{C}_{45}\text{H}_{68}\text{O}_9^{17}\text{O}\text{N}_9$ (m/z 895.51258), would be 12.05 ppm and -8.01 ppm, respectively. Hence, based on the high mass accuracy result, the single ^{15}N labelling on the $\text{A}\beta_{16-22}$ is also determined to be $> 99\%$ because the natural abundance species ($\text{C}_{45}\text{H}_{68}\text{O}_{10}\text{N}_9$) can be barely detected. As the dual nano-electrospray experiment is carried out in broadband mode having relatively lower mass resolution ($\sim 300,000$), most of the peaks in the isotopic fine structure cannot be resolved, and the peak merging could also distort the mass accuracy, such as the 2.98 ppm error of the peak at m/z 897.51029 in Table A.3, which was

caused by the merging of peaks for $C_{44}^{13}CH_{68}N_8^{15}NO_9^{17}O$ and $C_{43}^{13}C_2H_{68}N_8^{15}NO_{10}$.

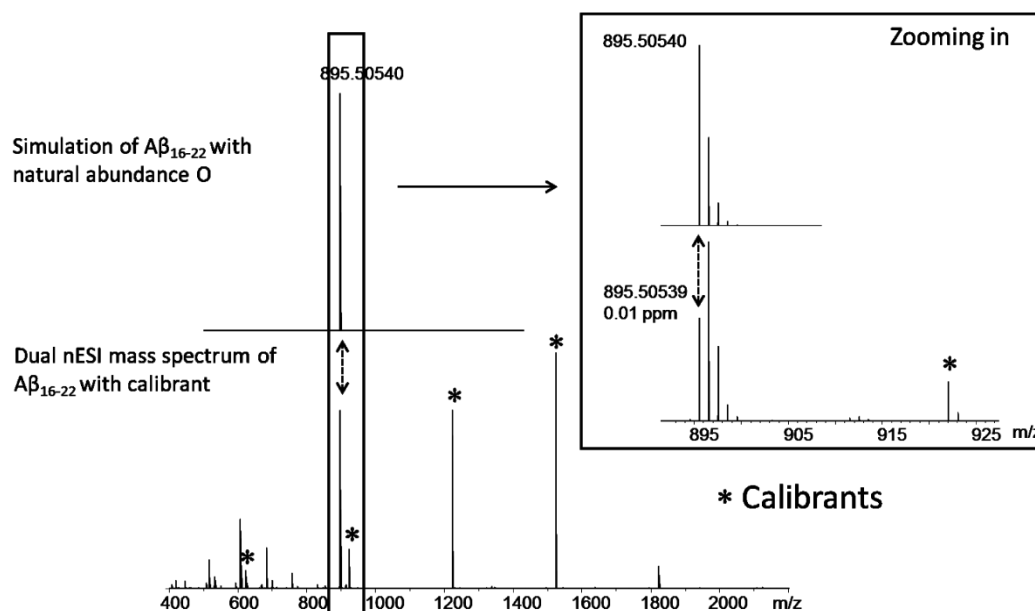


Figure 2.4 A dual nano-electrospray mass spectrum of the $A\beta_{16-22}$ sample with tuning mix as the internal calibrant, and peaks with asterisk are the peaks used in calibration. The spectrum on the top is the simulation of $A\beta_{16-22}$ of natural abundance oxygen

One key feature of a mass spectrometer is the ability to fragment ions of interest and generate structural information. Herein, CAD is applied to determine the ^{17}O labelled site. In this case, it is known that ^{17}O labelled valine was used in the synthesis of $Ac-A\beta_{16-22}-NH_2$ (N-acety-KLV $_{18}(^{17}O)$ FF $_{20}(^{15}N)$ AE- NH_2), and which is consistent with the CAD result in Figure 2.5 (peak list is in Table A.4). The isotopic distributions of the b_2 and b_3 ions clearly demonstrate that ^{17}O labelling is on the carbonyl oxygen of the valine,

because the difference between those two fragments is the valine amino acid residue, C_5H_9ON . Therefore, MS/MS approaches are proved useful to verify the stable isotope labelling site, and could be even more valuable if the labelling position is unknown.

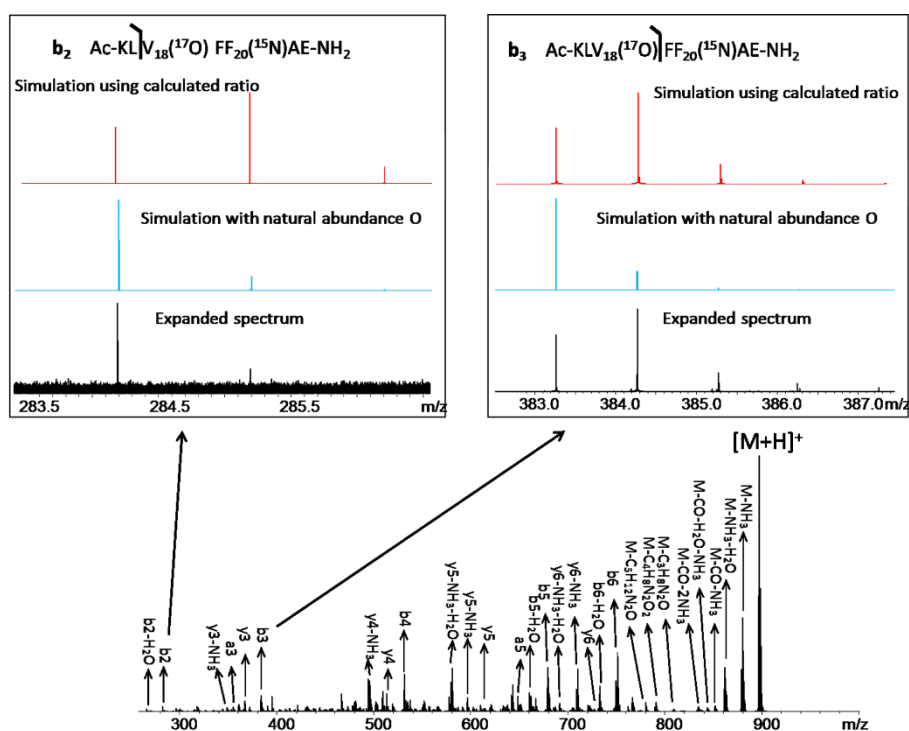


Figure 2.5 A CAD spectrum of the singly-charged Aβ₁₆₋₂₂. Insets on the top are the expanded regions of b_2 and b_3 ions (black) with the corresponding simulated spectra with natural abundance oxygen (blue) and using the calculated ratio, $^{16}O: ^{17}O: ^{18}O = 34.4: 55.5 : 10.1$ (red)

Additionally, the influence of ion population on the separation of closely-spaced peaks was studied, and peak coalescence was observed at a higher ion population (Figure 2.6). Peak coalescence is believed to be due to the

Coulomb repulsion between closely-spaced orbiting packets of ions, resulting in the merging of those two individual packets of ions, so that only one peak appears in the mass spectrum rather than two peaks.^{119,122,238,240} Peak coalescence occurs on ions of similar m/z and can be exaggerated by increasing ion population. Even though having very similar resolution, in Figure 2.6a, the ^{13}C and ^{17}O peaks in the $A+1$ isotopic cluster start showing up distinctly, while with approximately double the ion population, these two peaks are not separated at all in Figure 2.6b. This explains why the number of ions in the cell is minimized in the experiment.

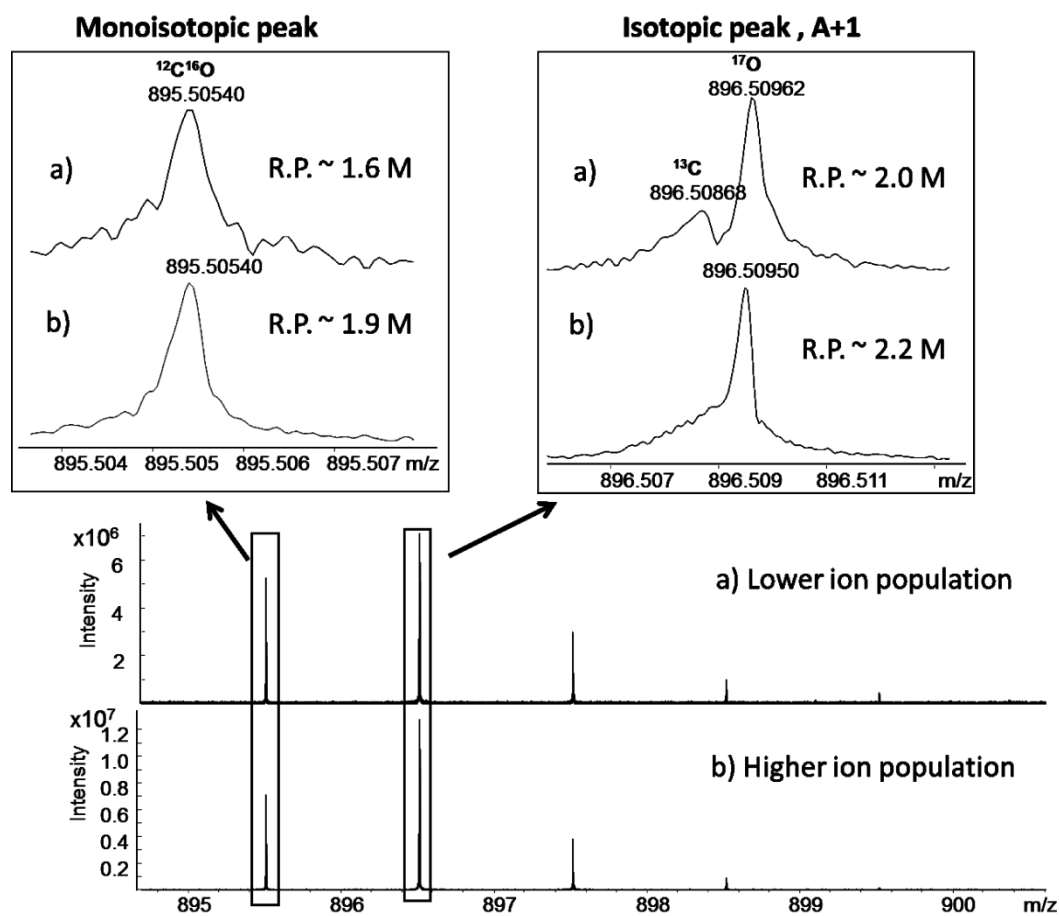


Figure 2.6 The comparison of two mass spectra of $A\beta_{16-22}$ with different ion populations showing peak coalescence; at higher ion populations (b), the two peaks in the A+1 cluster, ^{13}C and ^{17}O substituted species, cannot be resolved despite having similar resolving power with (a)

2.3.2 $A\beta_{11-25}$ ($\text{C}_{78}^{13}\text{C}_3\text{H}_{119}\text{O}_{23}\text{N}_{20}^{15}\text{N}$) partially labelled with ^{17}O

With increasing molecular weight, the complexity of elemental composition and the difficulty of isotopic fine structure measurement will increase dramatically. Moreover, the tendency for peak coalescence will grow as well.^{119,241} In this section, the $A\beta_{11-25}$ ions are investigated as a more challenging isotopic fine structure measurement, since its molecular weight

(MW: 1757.885869 Da) is almost twice as much as that of A β ₁₆₋₂₂ (MW: 894.498124 Da).

The doubly-charged A β ₁₁₋₂₅ ions are selected, having the monoisotopic peak at m/z 879.950210 (C₇₈¹³C₃H₁₂₁O₂₃N₂₀¹⁵N). The Δm between those two peaks of interest, the ¹³C peak (C₇₇¹³C₄H₁₂₁O₂₃N₂₀¹⁵N) and the ¹⁷O peak (C₇₈¹³C₃H₁₂₁O₂₂¹⁷O N₂₀¹⁵N), is still the same (0.000862 Da), but $\Delta m/z$ is half, or is 0.000431 in this case. Since a theoretical resolving power ≥ 6.0 M is required, despite a R.P. of ~ 8.0 M which has been achieved on bovine ubiquitin (8.6 kDa) using a 9.4 T home-built FTICR mass spectrometer in Marshall's group,¹²¹ this task is undoubtedly pushing the current limits. Figure 2.7 shows the ultra-high resolution fine structure detection of the A β ₁₁₋₂₅ with an average R.P. of 5.95 M and the corresponding peak list is summarized in Table 2.3. The resolution varies depending on the peak intensity and peak shape, and several peaks in the isotopic clusters have R.P. as high as 7.0 M. Additionally, using the monoisotopic peak as the internal lock mass, the average mass error for the 9 peaks observed in the isotopic clusters is 27 ppb (Table 2.3), and the ratio of ¹⁷O enrichment is also estimated by the result. The experimental results are 27.9 %, 56.8%, and 15.3% of the ¹²C ¹⁶O-, ¹²C ¹⁷O-, and ¹²C ¹⁸O- substituted peaks, respectively, which are slightly different from the values obtained for the A β ₁₆₋₂₂. Similarly, the accuracy of those values is checked by the experimental and theoretical ratios of ¹³C, and the two numbers are 45.8% and 48.2%, so there might be around 5.2% uncertainty for the experimental values.

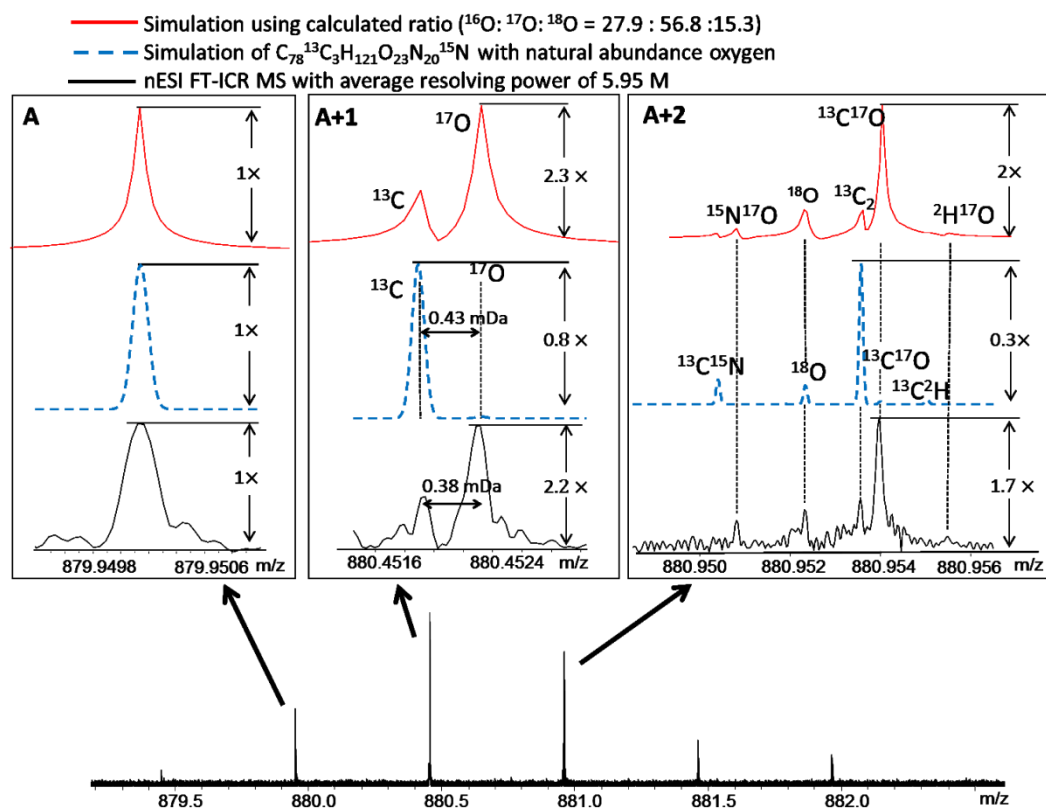


Figure 2.7 An ultra high resolution FTICR mass spectrum of the doubly-charged $\text{A}\beta_{11-25}$ ($\text{C}_{78}^{13}\text{C}_3\text{H}_{121}\text{O}_{23}\text{N}_{20}^{15}\text{N}$) in black, and the simulated spectra of $\text{A}\beta_{11-25}$ with natural abundance oxygen (the dashed blue line) and using the calculated ratio, $^{16}\text{O} : ^{17}\text{O} : ^{18}\text{O} = 27.9 : 56.8 : 15.3$ (the red line). The peak list is in Table 2.3

Table 2.3 The mass list of proposed peaks in Figure 2.7

Isotope difference	Formula	Resolving power /M	Theoretical m/z	Experimental m/z	Error/ppm
¹² C	C ₇₉ ¹³ C ₂ H ₁₂₁ O ₂₃ N ₂₀ ¹⁵ N	6.22	879.448533	879.448550	0.019
	*C ₇₈ ¹³ C ₃ H ₁₂₁ O ₂₃ N ₂₀ ¹⁵ N	7.20	879.950211	879.950210	----
¹³ C	C ₇₇ ¹³ C ₄ H ₁₂₁ O ₂₃ N ₂₀ ¹⁵ N	5.34	880.451888	880.451925	0.042
¹⁷ O	C ₇₈ ¹³ C ₃ H ₁₂₁ O ₂₂ N ₂₀ ¹⁵ N ¹⁷ O	7.18	880.452319	880.452298	-0.024
¹⁵ N ¹⁷ O	C ₇₈ ¹³ C ₃ H ₁₂₁ O ₂₂ N ₁₉ ¹⁵ N ₂ ¹⁷ O	7.01	880.950837	880.950818	-0.022
¹⁸ O	C ₇₈ ¹³ C ₃ H ₁₂₁ O ₂₂ N ₂₀ ¹⁵ N ¹⁸ O	6.48	880.952334	880.952327	-0.008
¹³ C ₂	C ₇₆ ¹³ C ₅ H ₁₂₁ O ₂₃ N ₂₀ ¹⁵ N	4.67	880.953566	880.953550	-0.018
¹³ C ¹⁷ O	C ₇₇ ¹³ C ₄ H ₁₂₁ O ₂₂ N ₂₀ ¹⁵ N ¹⁷ O	3.57	880.953997	880.953961	-0.041
² H ¹⁷ O	C ₇₈ ¹³ C ₃ H ₁₂₀ ² HO ₂₂ N ₂₀ ¹⁵ N ¹⁷ O	5.96	880.955458	880.955475	0.019
¹³ C ₂ ¹⁷ O	C ₇₆ ¹³ C ₅ H ₁₂₁ O ₂₂ N ₂₀ ¹⁵ N ¹⁷ O	5.85	881.455674	881.455631	-0.049
	Average of the absolute value	5.95			0.027
	STDEV				0.014

* The peak used as the lock mass

Finally, the ¹⁷O labelling is also located on the valine residue by the CAD result shown in Figure 2.8 and Table A.6 in Appendix A.

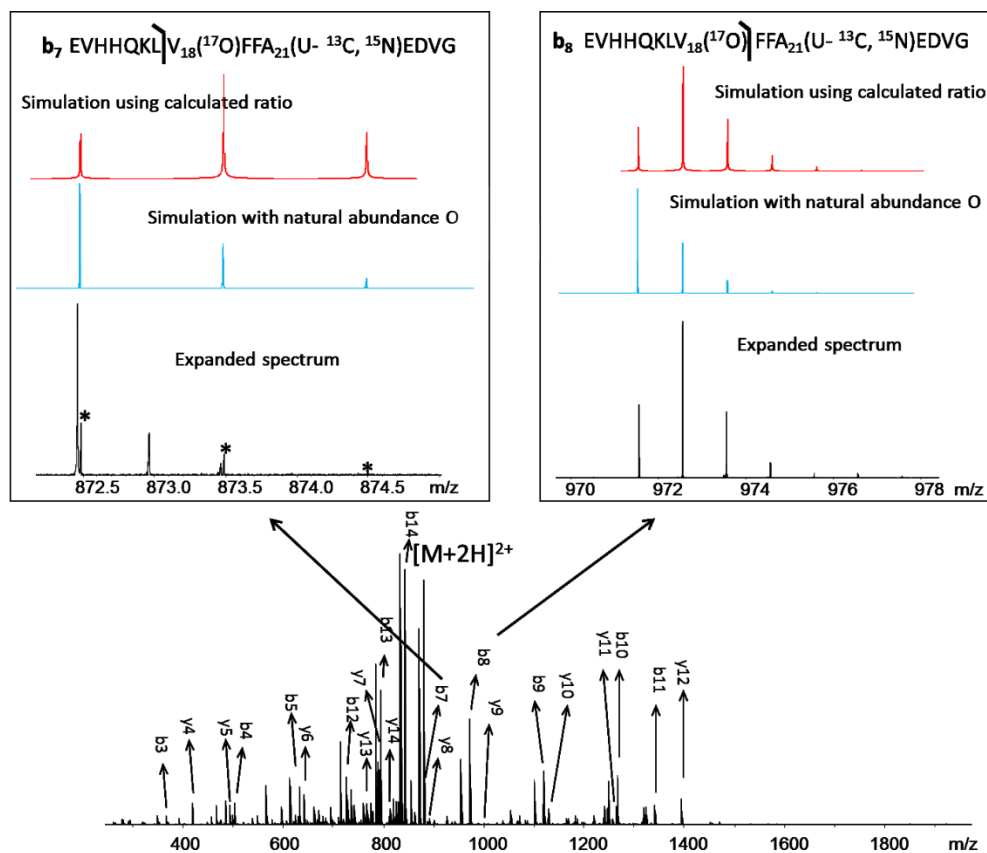


Figure 2.8 A CAD spectrum of the A β_{11-25} . Insets on the top are the expanded regions of b_7 and b_8 ions. Peaks labelled with asterisk are the isotopic distribution of b_7 ion.

The previously reported phase correction method can increase the resolving power of FTICR mass spectra by converting the traditional magnitude mode to absorption mode.^{102,104} For comparison, the spectrum in Figure 2.7 is phased to absorption mode¹⁰⁴ to check its influence on this narrowband (heterodyne mode) result. The phased spectrum is shown in Figure 2.9 and the peak list is in Table A.7. According to the result, an overall R.P. of 9.36 M was reached, which represents a 57% increase over that of

the magnitude mode (R.P. of 5.95 M in average). As the R.P. in the magnitude mode is already sufficient for separation (peaks in A+1 cluster) in this case, the peak separation is not heavily affected, and this is why most of the spectra in this thesis are kept in magnitude mode as the raw data generated from the instrument also makes the comparison with previous research more consistent. However, the result unambiguously demonstrated that absorption mode could be of great benefit for improving the resolution for narrowband FTICR mass spectra.

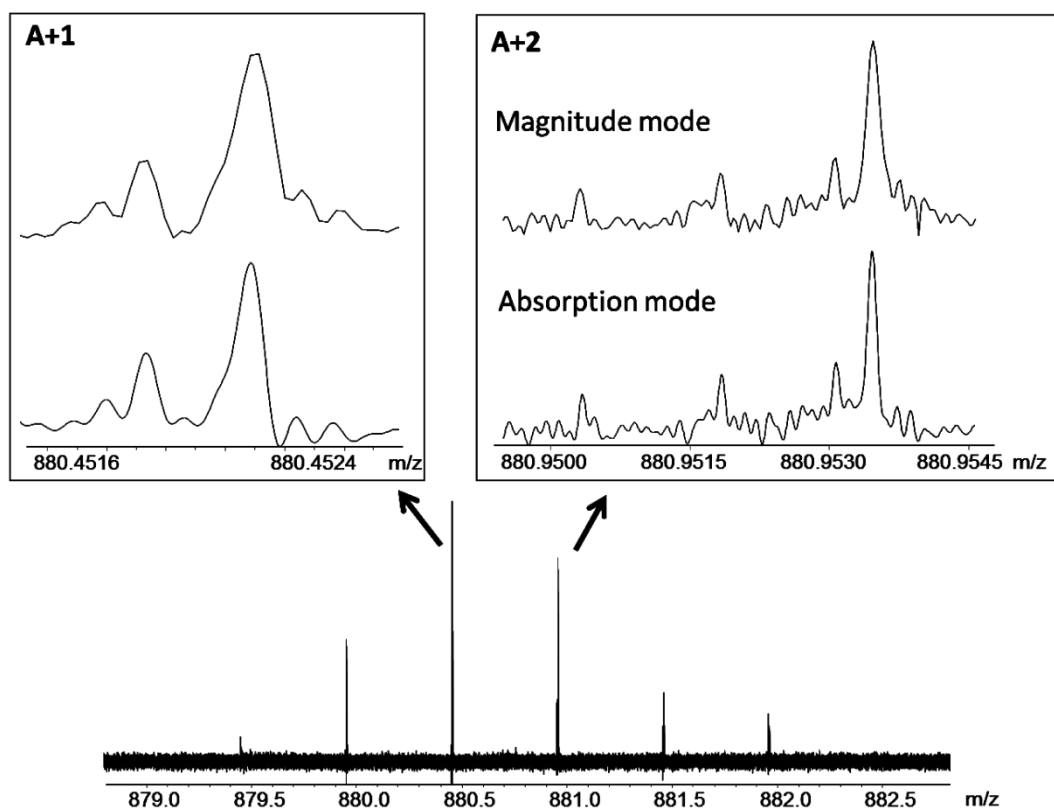


Figure 2.9 The absorption mode mass spectrum of the A β_{11-25} spectrum in Figure 2.7. Insets are the absorption- (bottom) and magnitude- (top) mode spectra of the expanded regions of A+1 and A+2 clusters, respectively

2.3.3 Fmoc-valine

Finally, the oxygen labelling ratio of the Fmoc-valine sample ($C_{20}H_{21}NO_4$, *MW*: 339.147058 Da, the structure is shown in Figure 2.10) used in synthesising the two peptides was measured and is estimated to have $27.3 \pm 0.9\%$, $59.4 \pm 0.4\%$, and $13.3 \pm 0.8\%$ for ^{16}O , ^{17}O , and ^{18}O , respectively (Figure 2.11 and Table A.8). Although the same ^{17}O labelled valine was used in the synthesis of both of the peptides, because the ^{17}O labelling on the two oxygen atoms of the carboxyl group could be exchanged back to ^{16}O during storage or reaction due to the ubiquitous present of ^{16}O in solution or atmosphere, the ^{17}O labelling value in the peptide products and the original amino acid used in the synthesis may not be exactly the same. Table 2.4 summarized the abundance of ^{13}C , ^{16}O , ^{17}O , and ^{18}O in the Fmoc-valine, $A\beta_{16-22}$, and $A\beta_{11-25}$, respectively, showing that the experimental ratios are consistent between the Fmoc-valine and the two peptides within the tolerance of the experimental uncertainty.

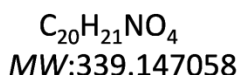
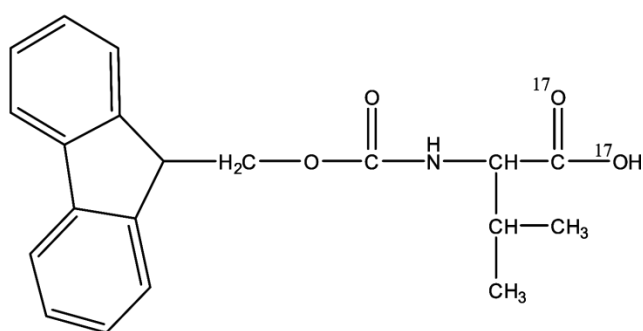


Figure 2.10 The structure of the Fmoc-valine with two oxygen atoms on the valine labelled

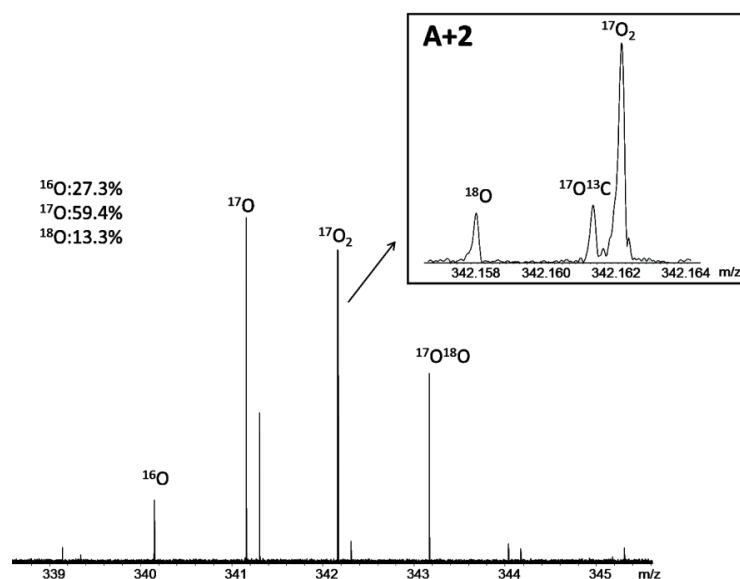


Figure 2.11 A FTICR mass spectrum of the Fmoc-valine labelled with ^{17}O and ^{18}O ; peaks labelled with ^{17}O , ^{18}O , $^{17}\text{O}_2$, $^{17}\text{O}^{13}\text{C}$, and $^{17}\text{O}^{18}\text{O}$ are the corresponding ^{17}O -substituted (m/z 341.158457), ^{18}O -substituted (m/z 342.158507), $^{17}\text{O}_2$ -substituted (m/z 342.162668), $^{17}\text{O}^{13}\text{C}$ -substituted (m/z 342.161883), and $^{17}\text{O}^{18}\text{O}$ -substituted (m/z 343.162733) species, respectively. The relative abundance of each oxygen isotope was calculated in Table A.8

Table 2.4 The abundance of ^{13}C , ^{16}O , ^{17}O , and ^{18}O in the Fmoc-valine, $\text{A}\beta_{16-22}$, and $\text{A}\beta_{11-25}$

O labelled samples	The ratio of $^{13}\text{C}/\%$		The experimental uncertainty/%	The experimental ratio/%		
	Theoretical	Experimental		^{16}O	^{17}O	^{18}O
Fmoc-Valine	17.8	17.3	-0.3	27.3±0.9	59.4±0.4	13.3±0.8
$\text{A}\beta_{16-22}$	32.7	31.9	-2.1	34.4±2.3	55.5±2.2	10.1±1.3
$\text{A}\beta_{11-25}$	45.8	48.2	+5.2	27.9±1.8	56.8±2.2	15.3±0.7

* The uncertainty of the experiment is calculated from $\frac{\text{The experimental ratio of } ^{13}\text{C} - \text{The theoretical ratio of } ^{13}\text{C}}{\text{The theoretical ratio of } ^{13}\text{C}} \times 100\%$

* For these $x \pm \Delta x\%$, $\Delta x\%$ is defined as one standard deviation of the uncertainty of the results from six runs (Fmoc-valine and $\text{A}\beta_{16-22}$), or three runs for $\text{A}\beta_{11-25}$.

*The experimental ratios are calculated by Equation A1 and equations in Table A.2

2.4 Conclusions

To meet the demand of ^{17}O related NMR research, the ratios of ^{17}O enrichment of two A β peptides, Ac-A β_{16-22} -NH $_2$ (MW: 894.498124 Da) and A β_{11-25} (MW: 1757.885869 Da), were quantified by their mass spectrometry isotopic fine structures in this study. Ultra-high resolving power ~ 6.0 M was achieved in a commercial 12 T FTICR mass spectrometer. A further 57% resolution increase was observed using absorption mode. The baseline separation of the ^{13}C and ^{17}O peaks and the isolation of whole isotopes of each peptide enable the calculation. Each resolved peak in the isotopic fine structure was compared with the theoretical simulation and was identified with mass uncertainty less than 70 ppb, where the overall average error was 27 ppb. CAD was utilized to determine the ^{17}O labelled site. This research expanded the application of isotopic fine structure mass spectrometry and demonstrated the unrivalled high resolution and high mass accuracy of FTICR instruments; additionally, this research also challenged the resolution limit of the 12 T FTICR mass spectrometer with an Infinity cell.

Chapter 3 Utilizing isotopic fine structures to understand the $A\beta_{37-42}$ ($GG_{38}(^{17}O)VVIA$) and $A\beta_{37-42}$ ($GGV_{39}(^{15}N)VIA$) mixture

3.1 Introduction

For the interest of NMR research, the isotopic fine structures of $A\beta_{16-22}$ and $A\beta_{11-25}$ labelled with ^{17}O and ^{15}N were obtained by ultra-high resolution in Chapter 2. In this chapter, a mixture including two $A\beta$ peptides, $A\beta_{37-42}$ partially labelled with ^{17}O on Gly38 ($GG_{38}(^{17}O)VVIA$) and $A\beta_{37-42}$ (^{15}N) fully labelled with ^{15}N on Val39 ($GGV_{39}(^{15}N)VIA$), is involved in measuring the ratio of ^{17}O in the $A\beta_{37-42}$. To be specific, the main components of the $A\beta_{37-42}$ mixture are $A\beta_{37-42}$ (^{15}N) with ^{15}N labelled ($\geq 99\%$) on Val39 ($C_{23}H_{42}N_5O_7^{15}N$, *MW*: 515.30853 Da), $A\beta_{37-42}$ ($C_{23}H_{42}N_6O_6^{17}O$, *MW*: 515.31572 Da) with X% labelled ^{17}O on Gly38, and the rest, approximately 1-X%, $A\beta_{37-42}$ with unlabelled ^{16}O ($C_{23}H_{42}N_6O_7$, *MW*: 514.31150 Da) which should also include a small portion of $A\beta_{37-42}$ (^{18}O) (natural abundance) in theory, where 'X' is the number to be detected. Theoretically, to fully resolve the singly protonated $A\beta_{37-42}$ (^{15}N) at m/z 516.315809 and ^{17}O -substituted $A\beta_{37-42}$ peak at m/z 516.322991 only requires a resolving power of $\sim 220,000$, while the challenging task is to fully separate the ^{13}C -substituted peak of $A\beta_{37-42}$ at m/z 516.322129 and the ^{17}O -substituted $A\beta_{37-42}$ at m/z 516.322991 which requires a resolving power of 1.8 M. Because several peaks closely-spaced are present, in practice, an even higher resolving power is necessary to ensure a

good separation. Moreover, without a decent separation, peak tailing and/or peak coalescence would distort the peak intensity and the measurement.

3.2 Experimental section

3.2.1 Chemicals

A β_{37-42} samples were dissolved in acetonitrile/water 50:50 with 0.1% of trifluoroacetic acid (Sigma-Aldrich Co., St. Louis, MO, USA) to a concentration of ~ 1 μ M. PEG400 was prepared in 50:50 acetonitrile/water, and Fmoc-glycine was in 50:50 acetonitrile/water with 0.1% of formic acid .

3.2.2 Mass spectrometry experiments

All mass spectrometry experiments were carried out on a Bruker 12 T solariX FTICR mass spectrometer (Bruker Daltonik, GmbH, Bremen, Germany) with a custom nano-electrospray ion source. The front and end trapping voltages were set at 1.30 and 1.20 V for the detection of A β_{37-42} , where heterodyne mode was used with a sampling frequency of 15 kHz and 256 k data points. Fmoc-glycine was detected in broadband mode using 16 M data points, and the spectrum of Fmoc-glycine was averaged from 10 scans.

3.3 Results and discussions

3.3.1 Isotopic fine structure measurement of A β_{37-42} mixtures

The peaks of interest are isolated in the quadrupole in front of the infinity ICR cell to remove undesired. With a resolving power of ~ 3.5 M, a mass spectrum of the mixture is shown in Figure 3.1, where the fine structures of the two A β_{37-42} peptides are well resolved and the corresponding peaks are listed in Table 3.1. In the expanded A+1 region, three peaks representing the

monoisotopic peak of $A\beta_{37-42}(^{15}\text{N})$ (shown as ^{15}N in Figure 3.1), the ^{13}C -substituted peak of $A\beta_{37-42}$ (shown as ^{13}C in Figure 3.1), and the ^{17}O -substituted peak of $A\beta_{37-42}$ (shown as ^{17}O in Figure 3.1), respectively, are detected and separated unambiguously. The experimental mass difference between the ^{13}C peak and the ^{17}O peak is 0.84 mDa, which agrees with the theoretical value, 0.86 mDa.

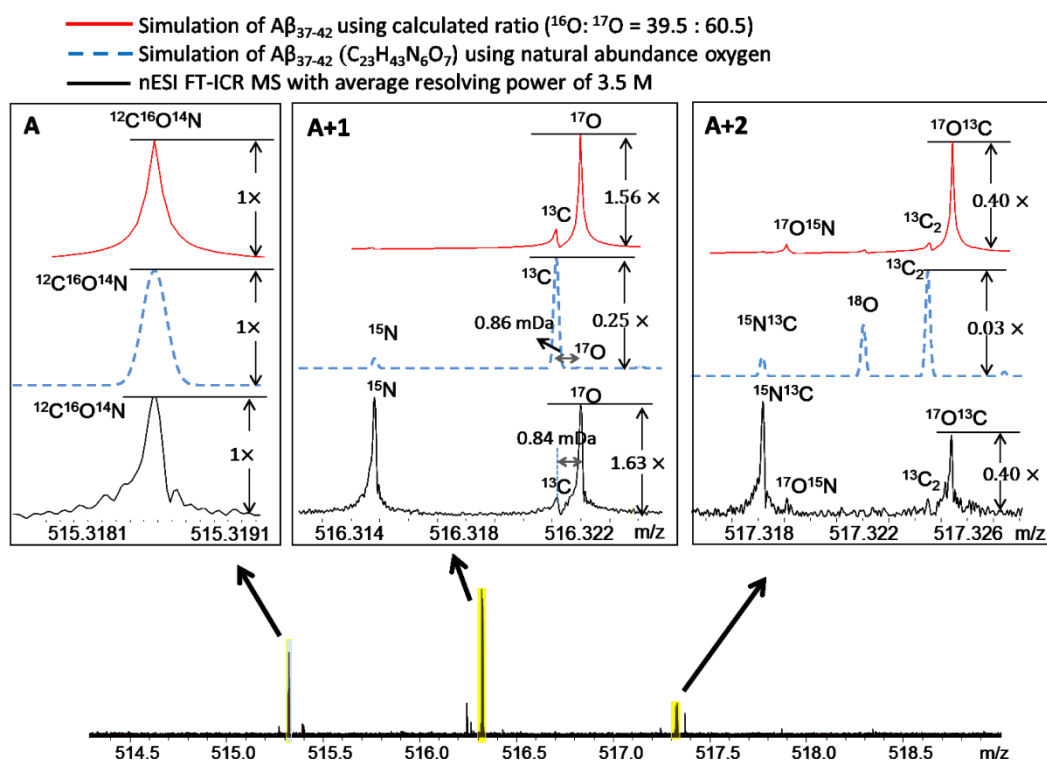


Figure 3.1 An ultra high resolution FTICR mass spectrum of the singly-protonated $A\beta_{37-42}$ ($\text{C}_{23}\text{H}_{42}\text{N}_6\text{O}_7$) in black, and the simulated spectra of $A\beta_{16-22}$ with natural abundance oxygen (the dashed blue line) and using the calculated ratio, $^{16}\text{O} : ^{17}\text{O} = 39.5 : 60.5$ (the red line). The peak list is in Table 3.1

Table 3.1 The mass list of proposed peaks in Figure 3.1

Formula	Resolving power /Million	Theoretical m/z	Experimental m/z	Error /ppm
*C ₂₃ H ₄₃ N ₆ O ₇	3.2	515.318774		-----
C ₂₃ H ₄₃ N ₅ ¹⁵ NO ₇	3.3	516.315809	516.315800	-0.02
C ₂₂ ¹³ CH ₄₃ N ₆ O ₇	2.3	516.322129	516.322143	0.03
C ₂₃ H ₄₃ N ₆ O ₆ ¹⁷ O	3.3	516.322991	516.322979	-0.02
C ₂₂ ¹³ CH ₄₃ N ₅ ¹⁵ NO ₇	3.4	517.319164	517.319183	0.04
C ₂₃ H ₄₃ N ₅ ¹⁵ NO ₆ ¹⁷ O	4.8	517.320026	517.320087	0.12
C ₂₂ ¹³ CH ₄₃ N ₆ O ₆ ¹⁷ O	3.6	517.326346	517.326374	0.05
C ₂₁ ¹³ C ₂ H ₄₃ N ₆ O ₇	4.3	517.325484	517.325489	0.01
Average of the absolute value	3.5			0.04
STDEV				0.05

* The peak used as the lock mass

The peak assignment and the low overall mass error, 40 ppb, in Table 3.1 are all based on assuming that the peak detected at around m/z 515.318 is the monoisotopic peak of A β ₃₇₋₄₂ (m/z 515.318177). The assumption, however, could be misleading due to limited knowledge of the mixture and the peak at around m/z 515.318; therefore, in order to double check the assignment, a calibration standard, polyethylene glycol with an average mass of 400 Da, is employed to calibrate the spectrum internally (Figure 3.2). Using the homemade dual nano-electrospray setup, the analyte and the calibration standard are ionized at the same time using two different capillaries, rather than mixing the two together. The result in Figure 3.2 is generated at a resolving power of 0.87 M using broadband detection, and an average mass accuracy of the assigned peaks is about 80 ppb (Table B.3), including a peak, C₂₂¹³CH₄₃N₆O₇, has a mass error of 430 ppb due to the interference of the peak closely-spaced without sufficient resolution.

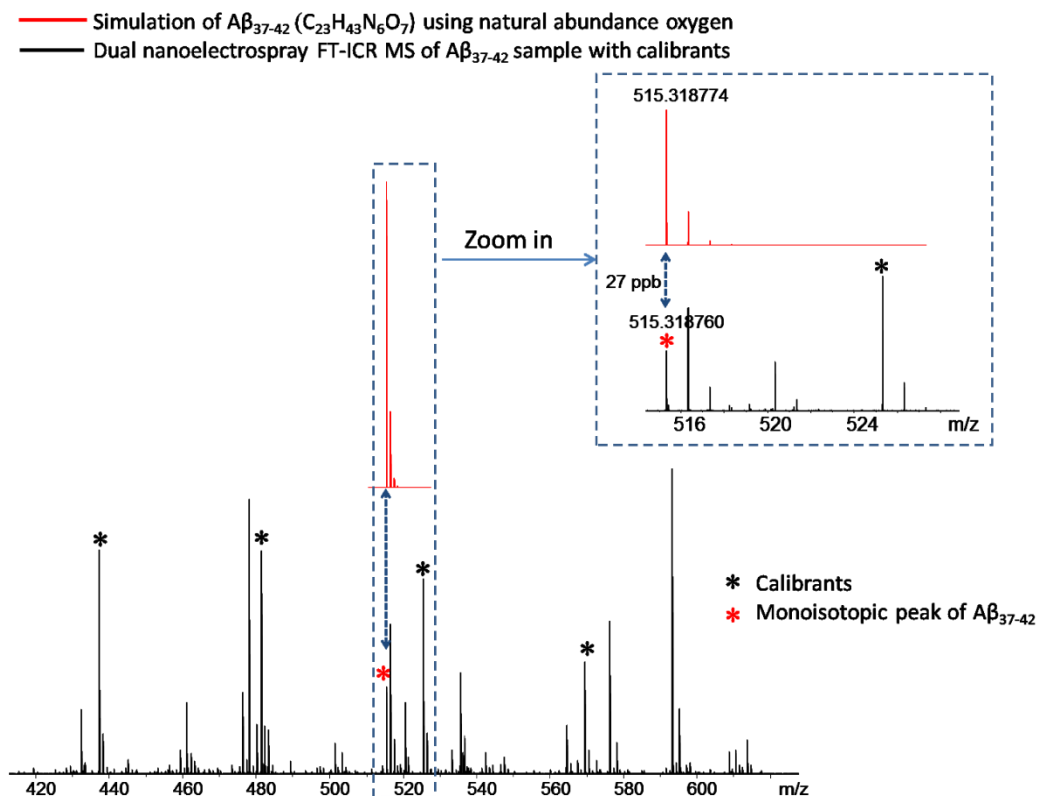


Figure 3.2 A dual nano-electrospray mass spectrum of the A β_{37-42} sample using PEG400 as the internal calibrant. Peaks with black asterisk and the peak labelled with red asterisk are the calibrants and the monoisotopic peak of A β_{37-42} , respectively. The spectrum on the top in red is the simulation using natural abundance oxygen. The peak list is in Table B.3

As the two peptides contain peaks of very similar m/z values and cyclotron frequencies, in the ultra-high resolution experiments, the number of ions in the cell was kept as low as possible to minimize the influence of space charge,^{114-116,242} so that, potentially, the influence of peak coalescence could be effectively inhibited. Aided by the fine separation in Figure 3.1, the ratio of ^{17}O abundance in A β_{37-42} is able to be calculated by Equation (3.1). It has to

be noted that the ^{18}O component is missing in the calculation compared to the Equation (2.1) in last chapter because no peaks correlated to ^{18}O substituted species are observed in Figure 3.1, which suggests ^{18}O is depleted in $\text{A}\beta_{37-42}$.

$$^{17}\text{O} \text{ abundance} = \frac{I(^{17}\text{O})}{I(^{17}\text{O}) + I(^{16}\text{O})}, \quad \text{Equation (3.1)}$$

where $I(^{16}\text{O})$ and $I(^{17}\text{O})$ are the intensity of the monoisotopic peak of $\text{A}\beta_{37-42}$ and the corresponding ^{17}O -substituted peak, respectively. To minimize the influence of signal fluctuation, the results from five runs are averaged (see the Table B.1), and the experimental ratios of the ^{16}O and ^{17}O are $39.5 \pm 1.7\%$, and $60.5 \pm 1.7\%$. Similarly, to check the accuracy of this measurement, the experimental ratio of ^{13}C in $\text{A}\beta_{37-42}$, 20.3%, is compared to the theoretical value, 19.9%, and the uncertainty of the experiment is calculated by $\frac{20.3\% - 19.9\%}{19.9\%} \times 100\% \cong 2.0\%$, which allows estimation of the uncertainty in measurement of the isotopic fine structure to be $\sim 2.0\%$.

Additionally, the relative ratio of the three composites in the mixture, ^{15}N labelled $\text{A}\beta_{37-42}$ (^{15}N) ($\text{GGV}_{39}(^{15}\text{N})\text{VIA}$), ^{17}O labelled $\text{A}\beta_{37-42}$ ($\text{GG}_{38}(^{17}\text{O})\text{VVIA}$), and $\text{A}\beta_{37-42}$ (GGVVIA), is obtained. The ratio of $\text{A}\beta_{37-42}$, ^{17}O labelled $\text{A}\beta_{37-42}$, and ^{15}N labelled $\text{A}\beta_{37-42}$ (^{15}N) averaged from five spectra is 1.00:1.88:1.54; if subtracting the natural ^{15}N component (2.2% in total) attributed to $\text{A}\beta_{37-42}$ (GGVVIA) in the $\text{A}\beta_{37-42}$ (^{15}N) monoisotopic peak, the ratio becomes 1.00:1.86:1.54.

3.3.2 Isotopic fine structure measurement of ^{17}O labelled Fmoc-glycine

Moreover, the isotopic fine structure of the ^{17}O labelled Fmoc-glycine ($\text{C}_{17}\text{H}_{15}\text{NO}_2^{17}\text{O}_2$, MW : 299.1085 Da) used in synthesising the $\text{GG}_{38}(^{17}\text{O})\text{VVIA}$

peptide is also detected (Figure 3.3, Table B.5) to determine the ^{17}O abundance. Because the two oxygen atoms in the carboxyl group of glycine should be equivalent and are both labelled with ^{17}O , the average abundance of the ^{17}O on one oxygen atom could be estimated using the following equation:

$$^{17}\text{O abundance} = \frac{I(^{16}\text{O}^{17}\text{O})/2 + I(^{17}\text{O}^{17}\text{O})}{I(^{16}\text{O}^{16}\text{O}) + I(^{16}\text{O}^{17}\text{O}) + I(^{17}\text{O}^{17}\text{O})}, \quad \text{Equation (3.2)}$$

$I(^{16}\text{O}^{16}\text{O})$, $I(^{17}\text{O}^{16}\text{O})$, and $I(^{17}\text{O}^{17}\text{O})$ are the peak intensity of $^{16}\text{O}^{16}\text{O}$ -, $^{17}\text{O}^{16}\text{O}$ -, and $^{17}\text{O}^{17}\text{O}$ -substituted Fmoc-glycine peaks (Figure 3.3). After peptide synthesis, only one of the two labelled oxygen atoms is retained in the peptide product. The ^{17}O abundance is estimated to be $58.7 \pm 0.5\%$ (averaged from five runs, Table B.4) in the Fmoc-glycine with an uncertainty of 0.6% estimated from the detection of the ^{13}C -species; this value is consistent with the corresponding ratio in $\text{GG}_{38}(^{17}\text{O})\text{VVIA}$ ($60.5 \pm 1.7\%$ averaged from five runs) if the experimental uncertainty is counted. The simulation spectrum in Figure 3.3 in red using a ratio of $^{16}\text{O}:^{17}\text{O}:^{18}\text{O} = 41.299:58.700:0.001$ matches well with the spectrum detected thus the results also show that there is a depletion of ^{18}O in the Fmoc-glycine. If the ^{18}O atom has natural abundance in the Fmoc-glycine, there would be a small peak of about half the height of the $^{13}\text{C}^{17}\text{O}$ peak at m/z 300.111630 in Figure 3.3. Even though the mass difference between the ^{13}C -substituted and the ^{17}O -substituted peaks is always the same, $\Delta m = 0.86$ mDa, comparatively, resolving the isotopic fine structure of amino acids is more feasible than distinguishing the isotopic fine structure of peptide because the frequency difference ($\Delta\omega$) is larger for smaller molecules. Moreover, the presence of

several peptides of similar masses in a mixture could further increase the difficulty of the fine separation in practice.

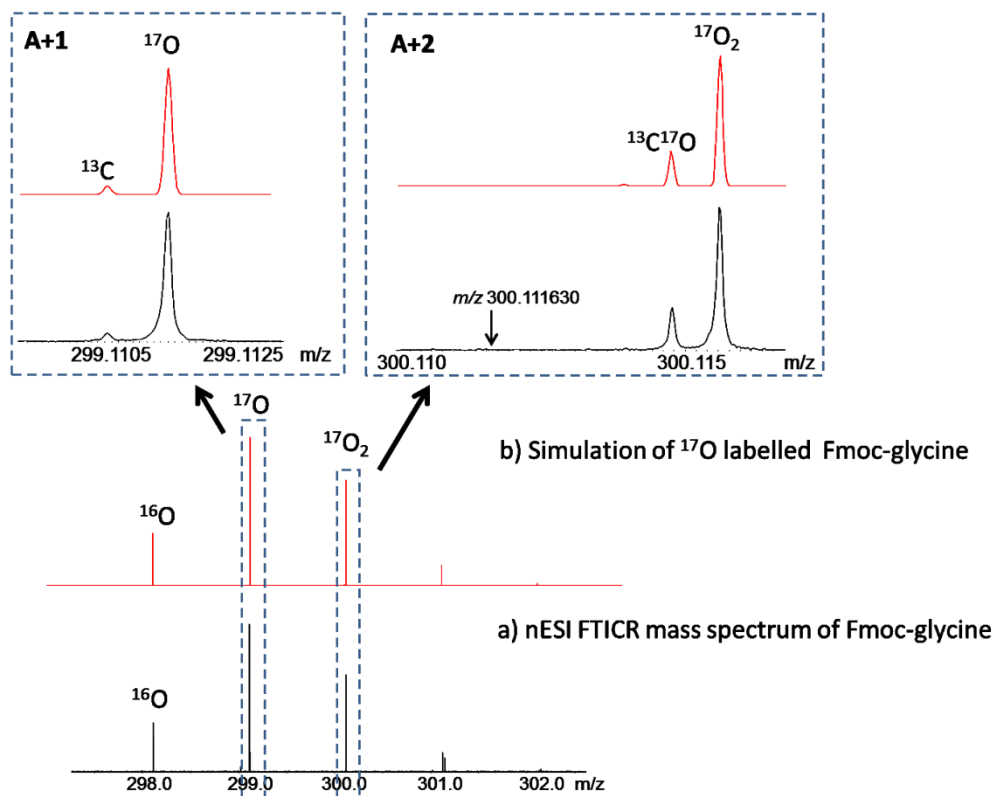


Figure 3.3 A FTICR mass spectrum of the Fmoc-glycine labelled with ^{17}O ; peaks labelled with ^{13}C , ^{17}O , $^{17}\text{O}^{13}\text{C}$, and $^{17}\text{O}_2$ are the corresponding ^{13}C -substituted, ^{17}O -substituted, $^{17}\text{O}^{13}\text{C}$ -substituted, and $^{17}\text{O}_2$ -substituted species respectively. The spectra in red are the simulation of Fmoc-glycine using the ratio $^{16}\text{O}:^{17}\text{O}:^{18}\text{O} = 41.299:58.700:0.001$. The peak list is in Table B.5

3.4 Conclusions

In conclusion, aided by the fine separation of peaks from ^{15}N labelled $\text{A}\beta_{37-42}$ (^{15}N) (GGV₃₉(^{15}N)VIA), ^{17}O labelled $\text{A}\beta_{37-42}$ (^{17}O) (GG₃₈(^{17}O)VVIA), and $\text{A}\beta_{37-42}$ (GGVVIA), in particular the well resolved ^{13}C -substituted peak of $\text{A}\beta_{37-42}$ at m/z 516.32213 and the ^{17}O -substituted peak of $\text{A}\beta_{37-42}$ at m/z 516.32299 with

a resolving power of ~ 3.5 M, the ^{17}O labelling ratio is estimated to be 60.5% with an uncertainty of $\sim 2\%$ according to the detection of the ^{13}C -species in the same peptide. The characterization of isotopic labelling of one atom in a peptide mixture without any extra separation/chemistry is of great benefit for some applications. Though the precision of the measurement in this report is still not comparable with some traditional techniques, such as isotope ratio mass spectrometry ($\sim 0.03\%$),²¹⁸ a calibration reference is not necessary for the current method, and this method does not require combustion or pyrolysis and also enables multi-element detection at the same time. The strategy can be easily adapted to qualitatively and quantitatively distinguish a species from its isotope labelled counterparts.

Chapter 4 D-α-tocopheryl polyethylene glycol 1000 succinate: A view from FTICR MS and tandem MS¹

4.1 Introduction

4.1.1 Methods to characterize synthetic polymers

Apart from mass spectrometry, several analytical methods have been traditionally applied for the characterization of the molar mass of synthetic polymers, which are briefly summarized in the next paragraph. Table 4.1 shows several important terms in determining the molar mass of synthetic polymers.

Table 4.1 The statistics of M_n , M_w , PD , and n

M_n	Number average molecular weight	$M_n = \frac{\sum_i (M_i \times I_i)}{\sum_i I_i}$
M_w	Weight average molecular weight	$M_w = \frac{\sum_i (M_i \times I_i) \times M_i}{\sum_i (M_i \times I_i)}$
PD	Polydispersity	M_w/M_n
N	Number of the repeat unit	$n = \frac{(M_n - M_{Endgroup})}{M_{Repeat unit}}$

M_i : mass of the molecule of repeat unit= i

I_i : the ion intensity of the molecule of repeat unit= i

$M_{Endgroup}$: mass of the end group

$M_{Repeatunit}$: mass of the repeat unit

¹This chapter has been partially adapted with permission from Wei, J.; Bristow, A.W.T.; McBride, E.; Kilgour, D.P.A.; O'Connor, P.B. D-α-tocopheryl polyethylene glycol 1000 succinate: A view from FTICR MS and tandem MS, *Anal. Chem.*, 2014, 86 (3), pp 1567–1574. Copyright 2014 American Chemical Society. Bristow, A.W.T. and McBride, E. supplied the TPGS samples. Wei, J. did all of the experiments and drafted the manuscript under the supervision of O'Connor P. B..

Light scattering is one of the most extensively used methods, which measures the molar mass according to the radius of gyration, but this method is limited by the requirement of a consistent and sterile background solution.^{143,243} Comparatively, the light scattering experiment is time consuming, and it is not suitable for small molecules because of the low scattering strength. Because the viscosity of a polymer solution is directly related to the molar mass of the solute, viscometry is another useful technique in polymer research. However, a calibration using molecular weight standards is required for viscometry experiments, and the accuracy of the measurement can be affected by various factors, such as the presence of copolymers and broad molecular weight distribution.¹⁴³ The most popular technique used currently is size exclusion chromatography (SEC). In SEC experiments, the larger molecules elute earlier from the column than the ones of smaller size, so that all of the analytes are separated by size. SEC is relatively simple and robust; along with advanced SEC data process systems, it is a routine analytical method in polymer research. Infrared (IR) and ultraviolet (UV) are both useful detectors that can be combined with SEC to determine the functional groups. Two main limitations of current SEC techniques are how to obtain a calibration curve with high accuracy and how to achieve a high resolution separation in a short time, additionally, analysis of complex polymers is still challenging. Nuclear magnetic resonance (NMR) has been demonstrated to be a very effective method to estimate the M_n by measuring the ratio of protons on the end-groups to protons on the polymer chain. One advantage of NMR over the former methods is that it is able to provide some structural details of the polymer. The estimation of M_n , however,

is based on a complete understanding of the monomer and end-groups of the polymer; moreover, it is difficult for NMR to deal with a complex mixture.

By measuring the m/z , modern mass spectrometry is a valuable tool to determine the molecular weight distribution, end groups and modifications, compositions of complex polymers, and even to obtain structural information. MS is a fast and robust method with high sensitivity, and which is also of high accuracy. Even though MALDI-TOF instruments incorporate many features beneficial for studying synthetic polymers, such as high mass range, good resolution, and generating relatively simple mass spectrum, FTICR MS has special interest for some applications.

Using high performance mass spectrometry for the study of synthetic polymers has grown sharply in the past decade following advances in polymerization methods. Especially with increasing complexity and diversity of structures, many polymeric materials are now requiring advanced structural investigations. A high performance mass spectrometry combined with MS/MS technique is a valuable tool in the study of polymer structures since it has been successfully used in obtaining structural information for many categories of compounds. Utilizing MS/MS in the structural characterization of synthetic polymers, however, is still underdeveloped, due to difficulties involved in fragmenting diverse, and often stable, polymer bonds between monomer units¹⁴⁵ and distinct data analysis strategies associated with different polymer classes.

4.1.2 D- α -tocopheryl polyethylene glycol 1000 succinate

D- α -tocopheryl polyethylene glycol 1000 succinate (TPGS) (chemical structure shown in Figure 4.1a) is an amphiphilic polymer frequently used in drug formulations, and was approved as a water-soluble alternative of vitamin E.²⁴⁴ TPGS contains a lipophilic head, the tocopheryl moiety, also known as vitamin E, and a polar polyethylene glycol (PEG, *Mn* 1000) tail, which are connected by a succinate diester linker. As a non-ionic surfactant, TPGS has drawn special attention in the drug industry as an emulsifier, stabilizer, and absorption/permeation enhancer, and it is also a drug solubilizer approved by the FDA.^{245,246} It was reported that TPGS is readily absorbed in the gastrointestinal tracts and can increase the oral bioavailability of some anti-cancer drugs by inhibiting P-glycoprotein.²⁴⁷ Another special interest of TPGS in drug delivery is to form TPGS based nanoparticles,²⁴⁵ micelles, or liposomes.²⁴⁸

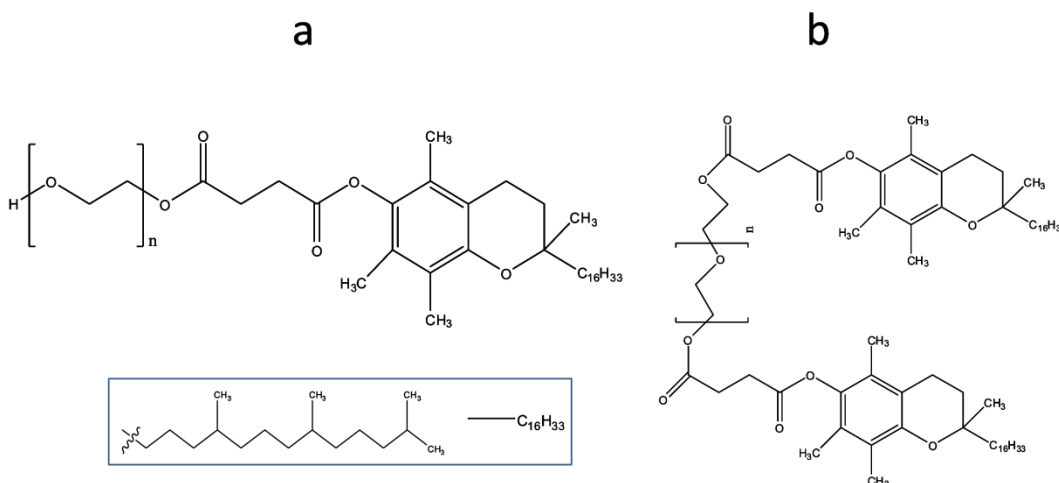


Figure 4.1 a): Structure of TPGS; b): Structure of Di-TPGS

TPGS is readily available from a wide range of suppliers and manufactures. In the literature, in addition to TPGS, several components including free PEG, Di-TPGS, and α -tocopheryl are reported to be present in some TPGS samples.²⁴⁹⁻²⁵¹ The main techniques currently used for the study of TPGS are NMR, FTIR, UV, and chromatography,^{250,252,253} but most of these methods struggle to provide an overview of component composition of a mixture, and are particularly challenging for structural characterization of low abundant components. Combining high performance liquid chromatography (HPLC) with mass spectrometry can provide some composition information; however, most of the literature has only focused on the information extracted from molecular mass values, without doing specific analysis of structural details using tandem mass spectrometry due to the limited performance of the mass spectrometer.

4.1.3 Content of the chapter

Differing compositions of the TPGS samples between batches are believed to result in variable performance of the formulated product. In this chapter, a high performance method using a FTICR mass spectrometer to study the composition and structure of TPGS was established, which could be used as a complementary tool in addition to those traditional techniques popular in polymer study. Utilizing FTICR MS with CAD and ECD/EID, MS/MS behaviours of TPGS under different fragmentation methods and adducts, particularly the influence of different metallic-cations (Li^+ , Na^+ , Ag^+), are discussed.

4.2 Experimental section

4.2.1 Chemicals

TPGS samples provided by AstraZeneca were dissolved in 50:50 methanol/water or 100% acetonitrile in a concentration of ~ 1 μ M before use. For different experiments, sodium sulfate, lithium chloride, or silver nitrate, (Fisher Scientific UK limited, UK) were added to a final concentration of 1 mM or 0.1% for formic acid (Sigma-Aldrich Co., St. Louis, MO, USA).

4.2.2 Mass spectrometry experiments

All mass spectrometry experiments were carried out on a Bruker 12 T solariX FTICR mass spectrometer (Bruker Daltonik, GmbH, Bremen, Germany) with an electrospray source and a homemade nano-electrospray ion source. For CAD, the parent ions were isolated in the quadrupole and then transferred to the collision cell for fragmentation using a collision energy which was optimized for each sample to provide an even spread of fragments, and fragments were finally detected in the ICR infinity cell.¹¹⁰ In the ECD/EID experiment, the isolated ions were accumulated externally in the collision cell and then transferred to the ICR cell. Trapped ions were then irradiated with electrons from a 1.5 A heated hollow cathode, and the bias voltages used for ECD and EID experiments were ~ 2 V and 12 V, respectively. For the ECD/ECD MS³ experiment, fragment ions of interest from ECD MS/MS were isolated in the ICR cell, and then activated with another ECD pulse. To achieve a desirable S/N and quality spectrum, up to 200 scans were averaged. All spectra were phased to absorption mode^{102,254} and processed by DataAnalysis 4.0 software.

4.3 Results and discussions

4.3.1 Full MS overview

For the initial study, the mass distribution of the TPGS sample was investigated by nano-electrospray FTICR MS, and the spectrum is shown in Figure 4.3. Several groups with different charge states are present. With the help of high mass accuracy, the formulae of these groups are assigned to free PEG and TPGS with different adduct combinations (Na^+ , NH_4^+ , H^+) and charge states. Proposed formulae are summarized in the Table C.1. An overall mass accuracy around 0.4 ppm is achieved, and the mass accuracy is generally better for peaks with higher S/N and lower m/z . The high resolution data available from the FTICR MS is particularly useful for assigning some of the closely-spaced species. For example, in the case of the expanded inset in Figure 4.2, these two groups of peaks (~20 mDa apart separated by a resolving power of 370,000) are assigned to TPGS with different adducts, $[\text{M}+2\text{Na}+\text{H}]^{3+}$, vs $[\text{M}+3\text{H}]^{3+}$ with different PEG units.

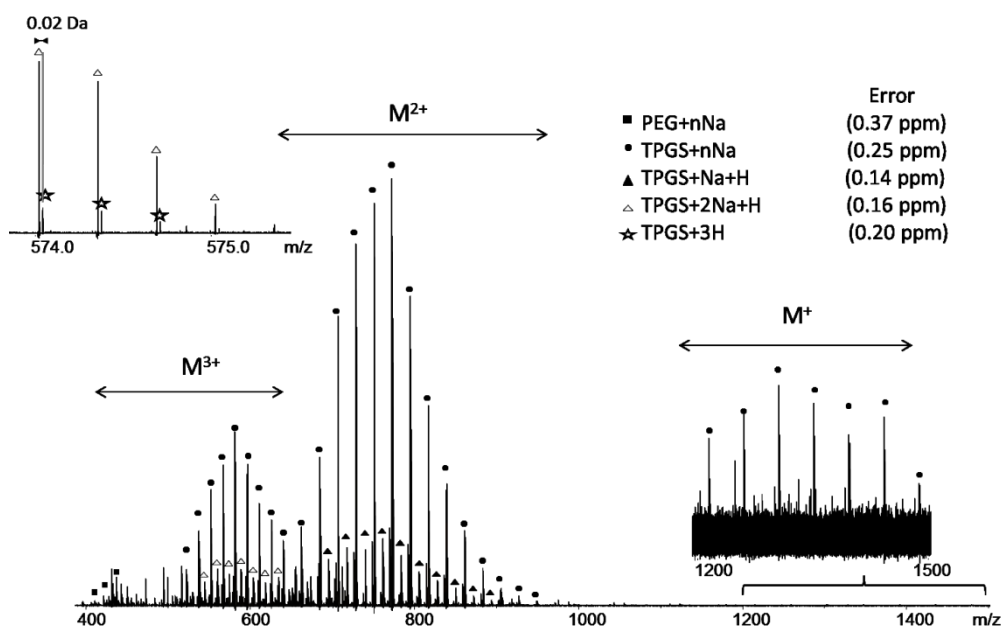


Figure 4.2 The full mass overview of TPGS sample. Detailed peak assignment is available in the Table C.1

As all of these formulae are proposed solely based on experimental m/z value and restricted by the elemental composition of TPGS, ECD MS/MS is implemented with several pre-assigned groups, $[M+3Na]^{3+}$, $[M+2Na+H]^{3+}$, $[M+2Na+NH_4]^{3+}$, and $[M+3H]^{3+}$, in order to check the assignments.

For the sodiated ions, after analyzing the ECD spectra of $[M+2Na+H]^{3+}$, $[M+2Na+NH_4]^{3+}$, and $[M+3Na]^{3+}$, the proposed formulae are consistent with the ECD results, where peaks losing H/ NH_4 /Na from the molecular ions respectively, are detected (Figure 4.3). Interestingly, the $[M+2Na+H]^{3+}$ and $[M+2Na+NH_4]^{3+}$ precursor ions readily lose H and NH_4 respectively from the charge-reduced radical cation to form $[M+2Na]^{2+}$. The same two precursors can lose Na to form $[M+Na+H]^{2+}$ and $[M+Na+NH_4]^{2+}$, but this fragmentation channel is less favorable, so these fragments are not abundant (Figure 4.3).

Furthermore, almost all fragments from all three precursors are sodiated species. For alkali metal adducts, previous research using CAD showed that smaller adduct ions such as Na^+ , were more strongly bond to PEG backbone than bigger adduct ions, such as K^+ or Cs^+ .²⁵³ In these ECD spectra, the increased loss of H^+ / NH_4^+ is more favourable compared to loss of Na^+ , but the previous research did not do the comparison for CAD, and additionally related research is discussed in Chapter 5. Looking into the fragments, most of them are from the same cleavage but with different numbers of PEG units, and the three precursors have very similar cleavage patterns. The interpretation of ECD fragments of $[\text{M}+3\text{Na}]^{3+}$ will be discussed in detail in the next section, 4.3.2.

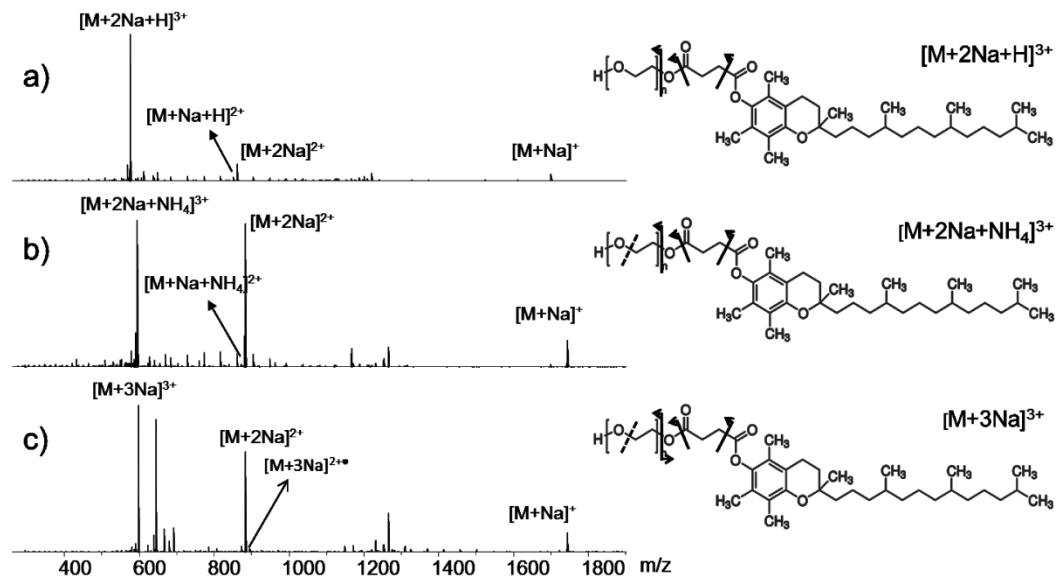


Figure 4.3 ECD spectra of several pre-assigned groups: a) $[\text{M}+2\text{Na}+\text{H}]^{3+}$, b) $[\text{M}+2\text{Na}+\text{NH}_4]^{3+}$, and c) $[\text{M}+3\text{Na}]^{3+}$

In contrast to the sodiated precursors discussed above, the ECD result of $[M+3H]^{3+}$ shows a difference. On the spectrum of $[M+3H]^{3+}$, a peak losing a proton or hydrogen only is not observed, but α -tocopheryl ($[C_{29}H_{49}O_2H]^+$ at m/z 430.38053) is present as the most abundant fragment under ECD. (see Figure 4.4) Comparing the results, the sodium cation is more likely to attach to the PEG group, while the proton seems to stay in the tocopheryl region.

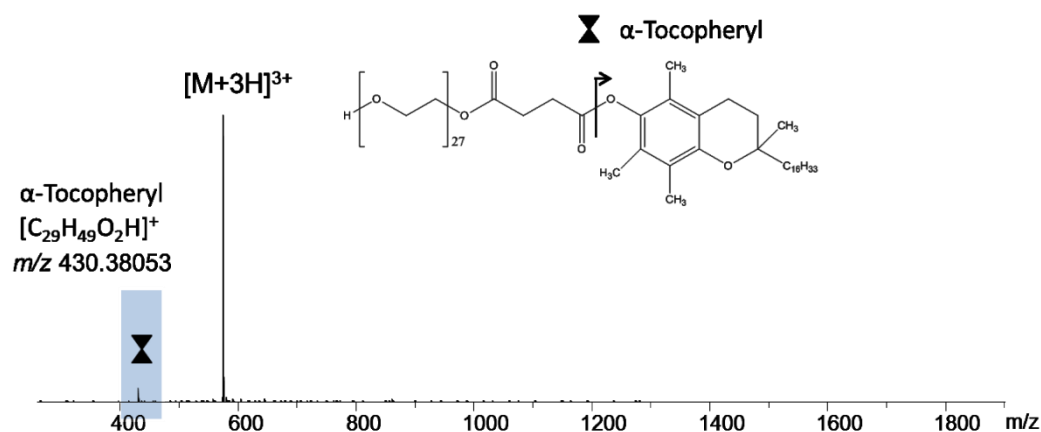


Figure 4.4 A ECD spectrum of $[M+3H]^{3+}$; the fragment indicating α -tocopheryl is highlighted

Intriguingly, in practice, it was found that the detection of Di-TPGS (structure shown in Figure 4.1b) can be greatly influenced by the solution used for ionization. As discussed above, only free PEG and TPGS appeared in the TPGS sample analyzed using methanol and water (50:50 V:V) as the solution, which is a routine solution used for electrospray. However, when switching the solution to 100% methanol or pure acetonitrile, in addition to the change of charge distributions of each series, Di-TPGS is also detected.

Figure 4.5 is the mass spectrum of the TPGS sample generated by using acetonitrile with saturated Na_2SO_4 as the solution. Aided by the peak assignment of Figure 4.2 and consistent high mass accuracy (see Table C.2), the peaks in Figure 4.5 are easily defined as PEG, TPGS, and Di-TPGS with different adducts and charge states, where the corresponding peak list can be found in Table C.2. Even though there are still some NH_4^+ and proton adducts, most of the abundant series in Figure 4.5 are sodiated. Actually, the ratio of organic solvent to water in the solution was also evaluated and pure methanol or acetonitrile was demonstrated to be the most suitable solution in the composition study of TPGS samples. In addition to a better solubility in pure organic solvent of Di-TPGS, using different percentage of organic solvent might also affect the ionization mechanism of Di-TPGS during spray. Comparing the structures of TPGS and Di-TPGS in the solution containing water, Di-TPGS could be much more folded than TPGS, since it has two long hydrophobic tails on both sides of its structure. Thus, during electrospray/nano-electrospray under this condition, while the chain ejection model (CEM) may be a more accurate model for TPGS ion formation, charged residue model (CRM) appears to be more suitable for Di-TPGS.⁷ Therefore, the lower CRM ion formation rate could inhibit the signal intensity of the folded Di-TPGS. On the other hand, once the solution is switched to pure organic solvent, the flexible Di-TPGS would have the same ionization mechanism as TPGS become detectable.

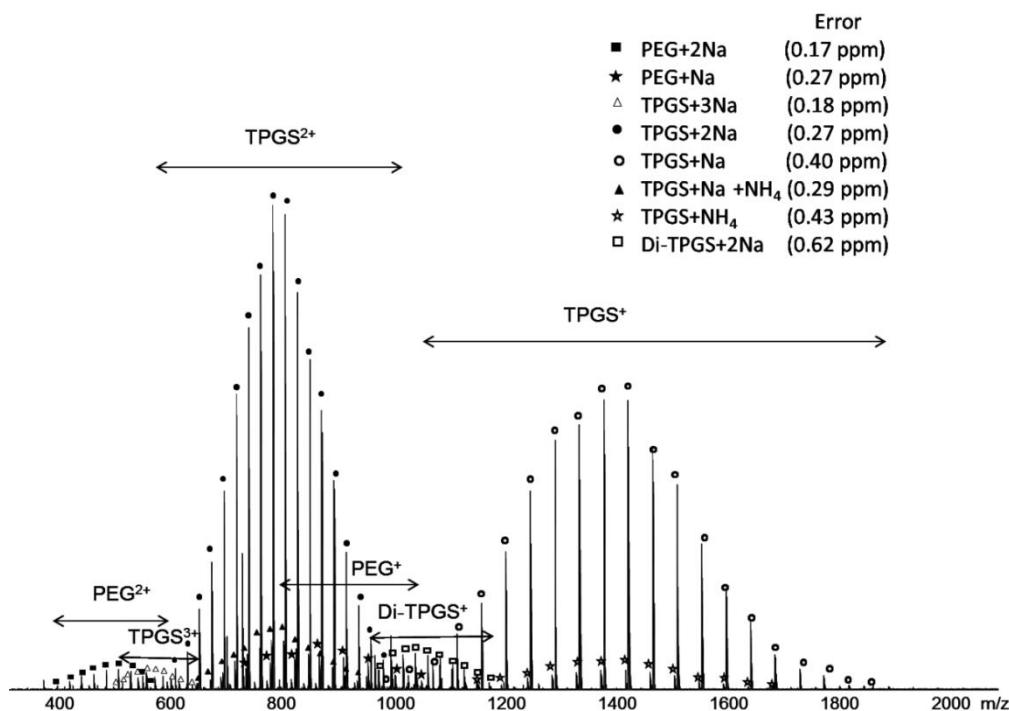


Figure 4.5 The full mass overview of TPGS sample in ACN with Na₂SO₄.

Detailed peak assignment is available in Table C.2

4.3.2 MS/MS of [TPGS+nNa]ⁿ⁺

For pharmaceutical applications, in addition to consistent composition between batches, a consistent structure is also essential. Use of FTICR MS high quality data to determine the composition of TPGS is discussed above. In this section, both CAD and electron-based fragmentation techniques (ECD/EID) are applied to investigate the fragments of TPGS. As sodium is a ubiquitous adduct for a PEGylated polymer, [TPGS+3Na]³⁺, [TPGS+2Na]²⁺, and [TPGS+Na]⁺ are selected respectively in this study. TPGS with 27 PEG units, having a formula of C₈₇H₁₆₂O₃₂Na_n (n=1, 2, 3) is selected for further fragmentation, based on peak intensity.

CAD spectra of TPGS with different numbers of sodium adducts, $[M+3Na]^{3+}$, $[M+2Na]^{2+}$, and $[M+Na]^+$, are presented in Figure 4.6. The first interesting result is that no fragment ions in the m/z range of 98 – 2000 are detected for the singly sodiated precursor, $[M+Na]^+$, even at higher fragmentation collision energy. It is worth noting that the fragmentation of such species would be difficult using MALDI MS/MS since only singly-charged ions would be generated; however, MALDI ionization is still the most commonly used ionization method for polymer study where the singly-charged ions provide for a simple mass distribution.²⁵⁵ Fortunately, with 2 or 3 sodium adducts, many cleavages are produced. (Figure 4.6b-c) Utilizing accurate mass, the elemental formulae of most fragments can be assigned, and peak assignments with an average of 0.3 ppm mass uncertainty are available in the Table C.3. For sodiated species, loss of the entire tocopheryl succinate ester (position 'f') and a cross-ring cleavage (position 'a') are more common. The cross-ring cleavage in position 'a' is intriguing, particularly as it is also the most abundant fragment in both $[M+3Na]^{3+}$ and $[M+2Na]^{2+}$ CAD spectra. The intensity of this peak is likely driven by the thermodynamic stability of a larger conjugated structure as in Scheme 4.1. A similar situation was reported in the work with chlorophyll-a (6.3.2),⁴⁸ where a frequent 2H abstraction leading to a larger conjugated structure was observed.

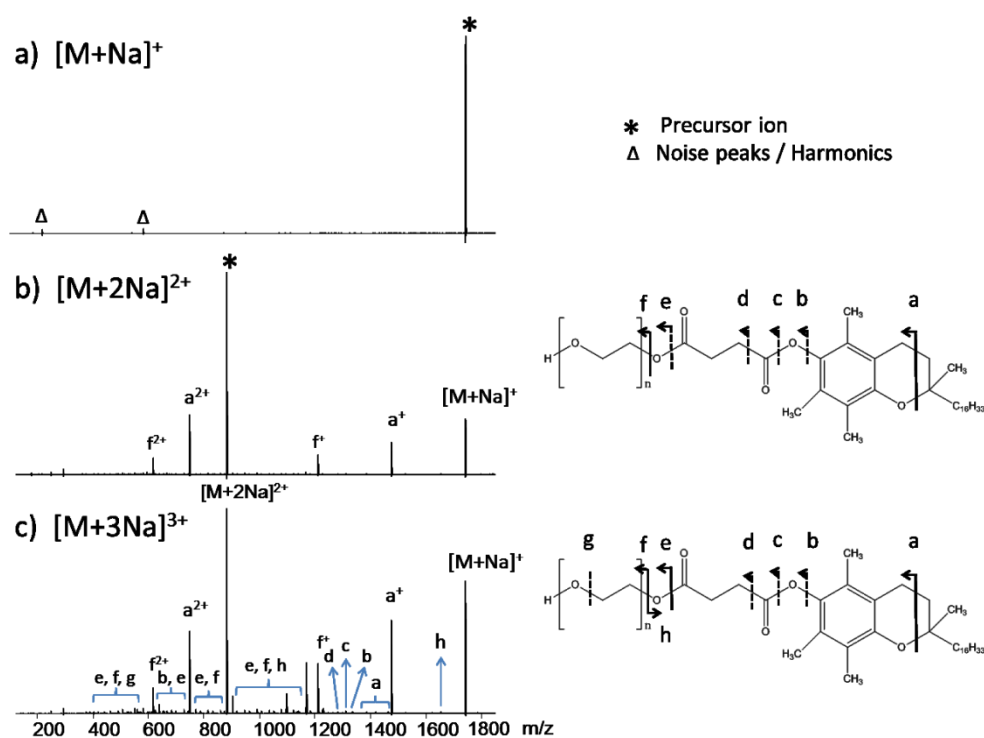
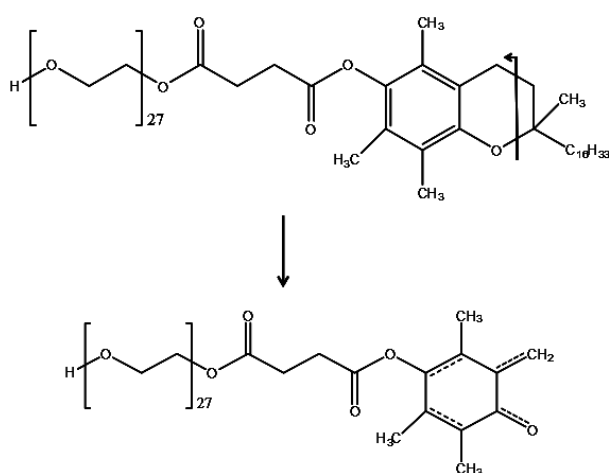


Figure 4.6 CAD results of $[TPGS+nNa]^{n+}$ ($C_{87}H_{162}O_{32}Na_n$) $n=1, 2, 3$, and the collision energies used are: a) 50 V, b) 46 V, and c) 35 V. Detailed peak assignment is available in Table C.3



Scheme 4.1 Proposed structure of the fragment from cleavage at position 'a' in CAD

In the ECD and EID results, similarly, no fragment ions were detected on the EID spectrum of $[M+Na]^+$, and more fragments are produced from the higher charge-state precursors (Figure 4.7). As discussed in 1.1.2, by utilizing a relatively higher energy, EID has demonstrated its complementary role in obtaining structural information of many singly-charged molecules.^{70,78,79,163} However, to our knowledge, there are few literature reports about using EID to investigate synthetic polymers.¹⁴³ Unfortunately, in this case, EID did not generate fragments. For higher charged precursors, more charge carriers and the Coulombic repulsion between the charges apparently contribute to the abundant fragment ions in the MS/MS spectra. Even though it generates fewer fragments than CAD, ECD does show different bond cleavage patterns. In contrast to cleavages 'a' and 'f' being dominated in CAD, cleavages next to the two carbonyl groups, at positions 'd' and 'e', produce the most intense fragments in ECD of $[M+3Na]^{3+}$ and $[M+2Na]^{2+}$. In terms of structural identification of TPGS, cleavages from positions 'a', 'f', 'd' and 'e' from CAD and ECD, provide useful, intense, diagnostic fragments.

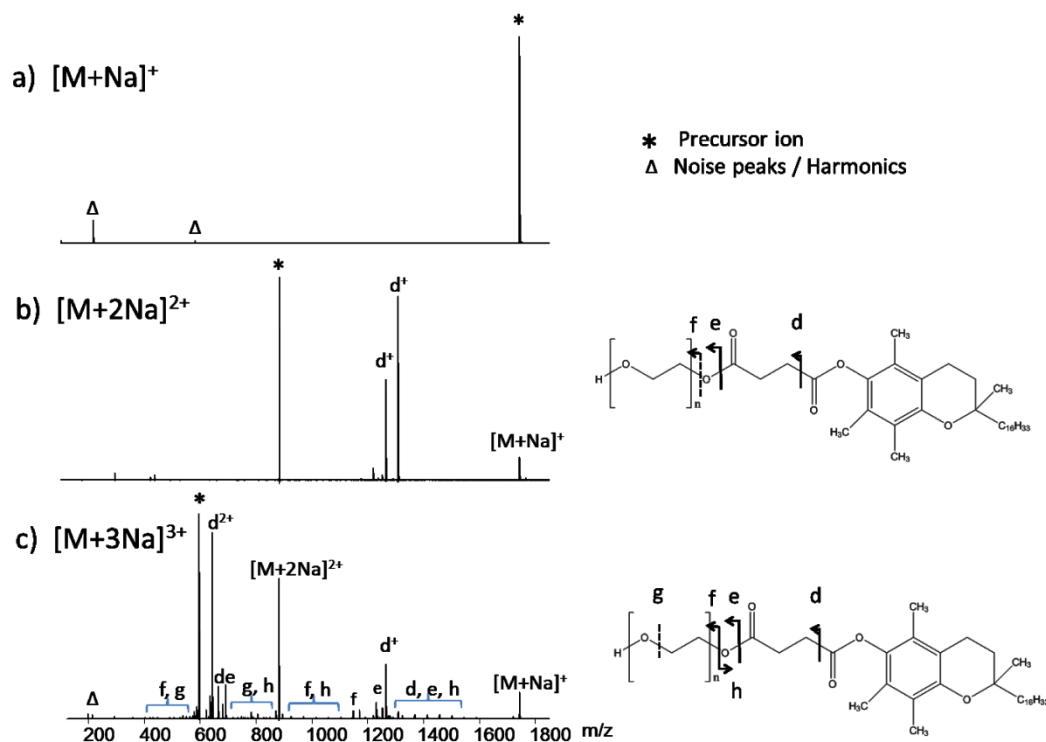


Figure 4.7 a): EID spectrum of $[TPGS+Na]^+$; b) and c) are ECD spectra of $[TPGS+2Na]^{2+}$ and $[TPGS+3Na]^{3+}$, respectively. Detailed peak assignment is available in the Table C.4

4.3.3 ECD/ECD MS³

In the ECD spectrum of $[M+3Na]^{3+}$ (Figure 4.7c), in addition to losing one sodium and two sodium cations, the charge-reduced species, $[M+3Na]^{2+\bullet}$, is detected. Regarding data analysis, apart from the restrictions of the formula of TPGS, the balance between elemental compositions, and the degree of unsaturation, one problem which makes the interpretation of these ECD results more complicated is that a singly-charged fragment can have either 1, 2, or 3 sodium adducts, and a doubly-charged ion may have 2 or 3 sodium adducts, because of charge reduction by electron capture. The high mass

accuracy is of great benefit in most situations, but tandem mass spectrometry is still useful for distinguishing some subtle features. Take the most abundant fragment, the doubly-charged ion at m/z 643.33935, as an example, the two most possible formulae are $[C_{57}H_{108}O_{28}Na_2]^{2+}$ (1.9 ppm) and $[C_{55}H_{109}O_{28}Na_3]^{2+}$ (0.04 ppm). If the doubly-charged fragment has two sodium adducts, the formula may indicate a cleavage from the aromatic ring in the α -tocopheryl part, with a loss of two PEG units. However, as the average mass accuracy for the ECD result is around 0.5 ppm (Table C.4), the formula with 3 sodium adducts seems more reasonable which implies a cleavage from position 'd' and with a loss of one PEG unit (C_2H_4O). To check this assignment, ECD/ECD MS³ is employed on the fragment ion at m/z 643.33935. Following ECD MS/MS of $[TPGS+3Na]^{3+}$, all other peaks except the one of interest, m/z 643.33935, are ejected from the cell, and then another ECD pulse is applied to the remaining ions. ECD/ECD MS³ process is shown in Figure 4.8. Several fragments are produced in Figure 4.8c, and the most useful one is the peak at m/z 1229.64615 with a formula of $C_{52}H_{104}O_{27}Na_3$ (-0.72 ppm), which shows a cleavage from position 'e' and with a loss of one PEG unit. The MS³ result clearly proves that the doubly-charged peak at m/z 643.33935 is from a cleavage at position 'd', with a loss of one PEG unit. Further scrutinizing of the ECD spectrum of $[M+3Na]^{3+}$, revealed a peak at m/z 665.35239 $[C_{57}H_{113}O_{29}Na_3]^{3+}$ (0.13 ppm) representing a direct cleavage from position 'd' without losing any PEG unit, which has much lower intensity than the peak at m/z 643.33935 (Figure 4.9). Interestingly, in the ECD spectrum of TPGS with 2 sodium adducts, $[TPGS+2Na]^{2+}$, the peak at m/z 1307.71559 $[C_{57}H_{113}O_{29}Na_2]^+$ which is from a direct cleavage at position 'd' without losing

any PEG unit is the most abundant fragment. Losing one PEG unit is favourable in the ECD process of $[\text{TPGS}+3\text{Na}]^{3+}$ but not for $[\text{TPGS}+2\text{Na}]^{2+}$, which is likely because of different structural conformations of TPGS with different numbers of sodium adducts. A loss of one PEG unit ($\text{C}_2\text{H}_4\text{O}$) from the molecular ion of $[\text{TPGS}+3\text{Na}]^{3+}$ is detected, though the intensity is low (Figure C.1).

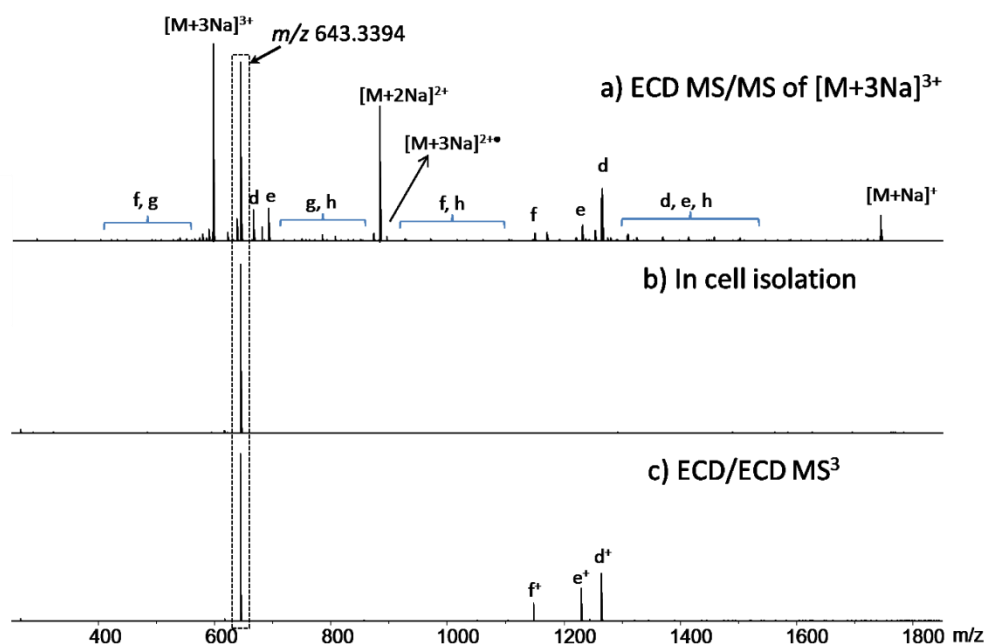


Figure 4.8 a): ECD spectrum of $[\text{M}+3\text{Na}]^{3+}$ as Figure 4.7c; b): In cell isolation of the doubly-charged fragment at m/z 643.3394; c): ECD/ECD MS^3 spectrum of isolated peaks. Detailed peak assignment is available in Table C.5

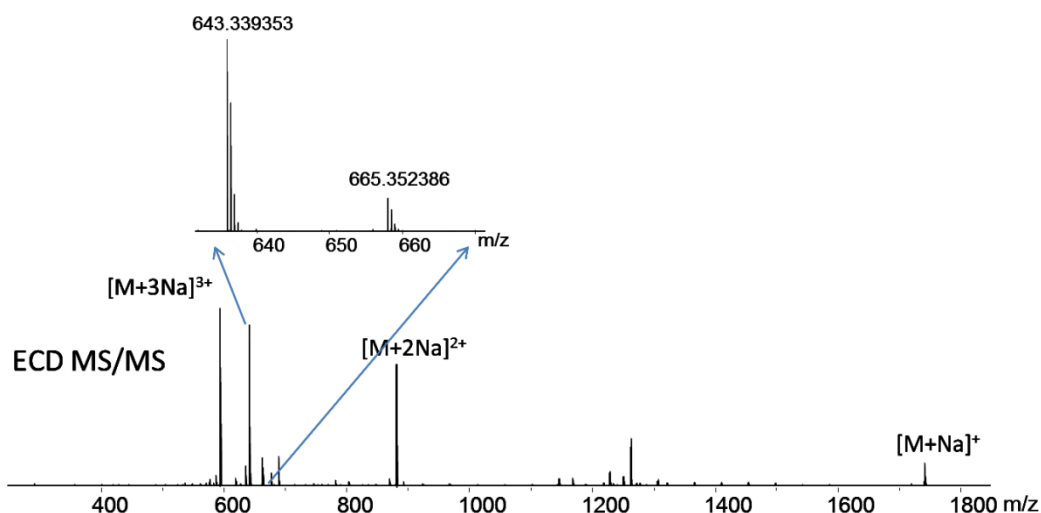


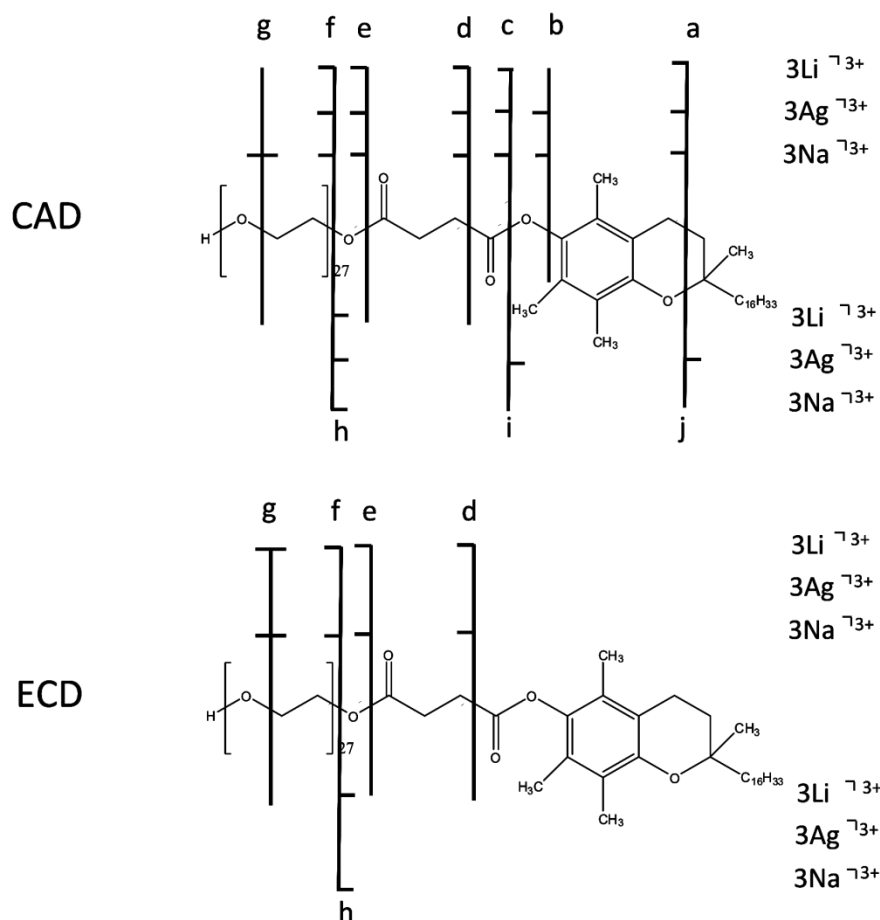
Figure 4.9 Zooming in peaks at m/z 665.352386 and m/z 643.339353 in the ECD spectrum of $[\text{TPGS}+3\text{Na}]^{3+}$ in Figure 4.7c

4.3.4 MS^2 with different metallic-cation adducts

It was reported that different ionization cations can cause complementary fragmentation patterns for multiply-charged polymers,¹⁴⁵ so the influence of several metallic-cationizing agents are investigated. Apart from sodium, lithium and silver are chosen for this study, since lithium is the most reactive metal and the smallest alkali metal, while silver typically bonds to a π bonded region. Ag^+ is also known to be of beneficial for ionizing and fragmenting polystyrene because of a possible binding to phenyl rings,^{256,257} which might be applicable for the chromanol ring in the tocopheryl region. Additionally, it was reported that Li and Ag cationization are facile methods for generating low energy CAD spectra of polyglycols.²⁵⁸

CAD and ECD results of $[\text{M}+3\text{Na}]^{3+}$, $[\text{M}+3\text{Li}]^{3+}$, and $[\text{M}+3\text{Ag}]^{3+}$ are compared in Scheme 4.2. TPGS with lithium cation adducts produces similar cleavages

to the one with sodium adduct in both CAD and ECD. Comparatively, TPGS with silver adducts also yields some similar cleavages in the CAD experiment, with more fragments in the tocopheryl side (positions 'i' and 'j'). In the ECD spectrum of $[\text{TPGS}+3\text{Ag}]^{3+}$, no cleavages from the TPGS are generated except for loss of the Ag^+ cation (see Figure C.2), though Ag has higher electron affinity than Li or Na. Additionally, one of the Ag^+ cations is likely to attach to the aromatic region via cation- π interaction. Since the ECD MS/MS spectrum only involved partial neutralization and loss of Ag^+ cation (Figure C.2), capture of the electron to neutralize the silver atom followed by loss of the resulting Ag^\bullet adduct is a likely pathway. In addition, since Na^+ is a common contaminant for polymers, in terms of structural characterization in practice, diagnostic peaks from CAD and ECD of $[\text{TPGS}+3\text{Na}]^{3+}/[\text{TPGS}+2\text{Na}]^{2+}$ are preferred for simplicity.



Scheme 4.2 CAD and ECD results of $[\text{TPGS}+3\text{Na}]^{3+}$, $[\text{TPGS}+3\text{Li}]^{3+}$, and $[\text{TPGS}+3\text{Ag}]^{3+}$

4.3.5 Variation of TPGS samples

Following the compositional and structural study using FTICR MS and MS/MS, the variety of four batches of TPGS samples from 2 different manufacturers (A and B) is investigated, where the four batches are labelled as A1, A2, B1, and B2, respectively. According to the mass spectrum of each batch (see Figure 4.10), the number average molecular weight (M_n), weight average molecular weight (M_w), repeat unit (n) (Table 4.1), and the relative intensity of TPGS, Di-TPGS and PEG (TPGS%, Di-TPGS %, and PEG%) can

be calculated and are summarized in Table 4.2. Table 4.2 shows that the polymerization extent of TPGS for the four samples is similar, with a repeat unit of 22 ± 1 (n). Moreover, the CAD and ECD spectra of $[\text{TPGS}_{27} + 2\text{Na}]^{2+}$ from the four samples (Figure 4.11 and Figure 4.12) are almost identical which argues for similar structures of TPGS between batches. Even though consistent structures of TPGS and similar compositions (TPGS, PEG, and Di-TPGS) between the four batches are observed, compared to batches B1 and B2, A1 and A2 contain more TPGS and less PEG based on the relative intensity of each series.

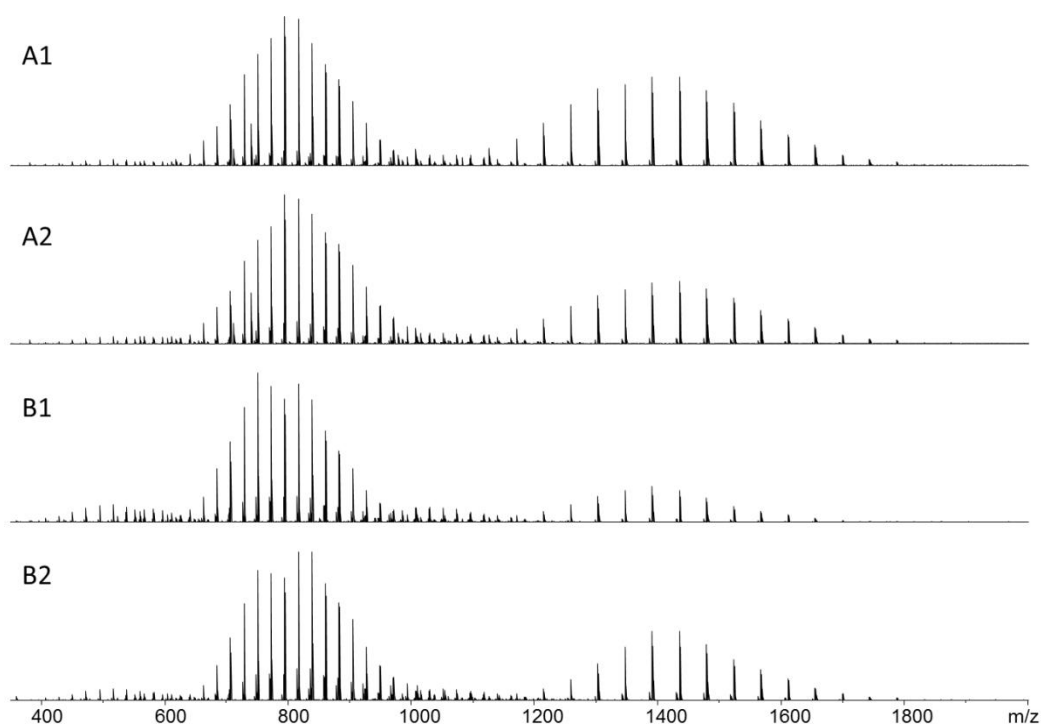


Figure 4.10 ESI-FTICR mass spectra of four batches of TPGS samples

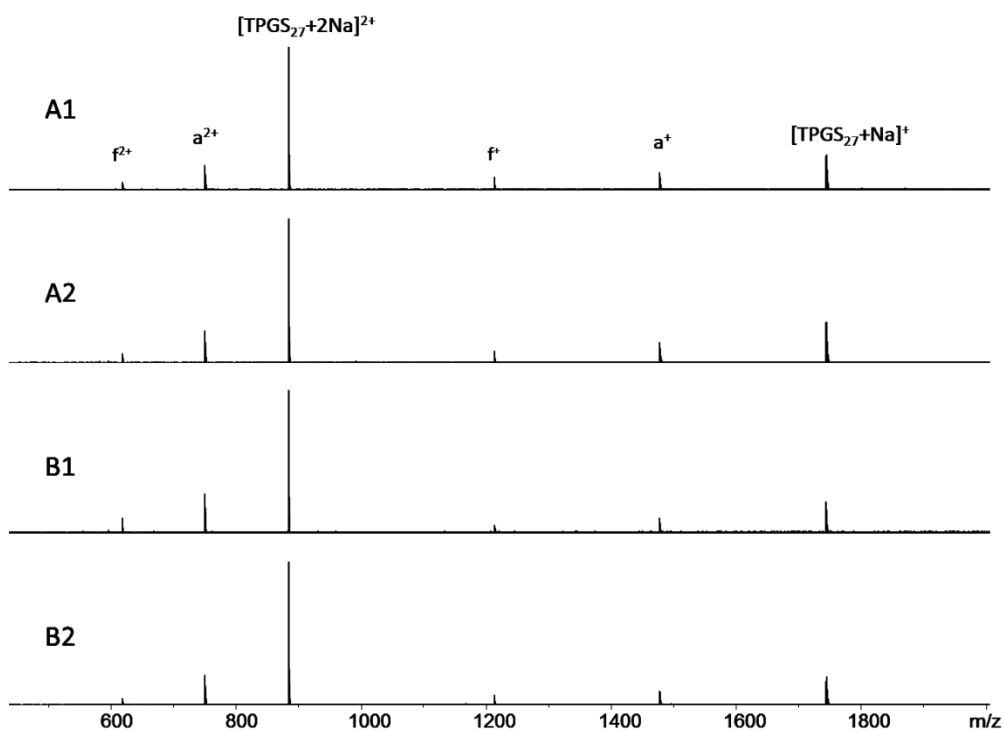


Figure 4.11 CAD spectra of four batches of TPGS samples

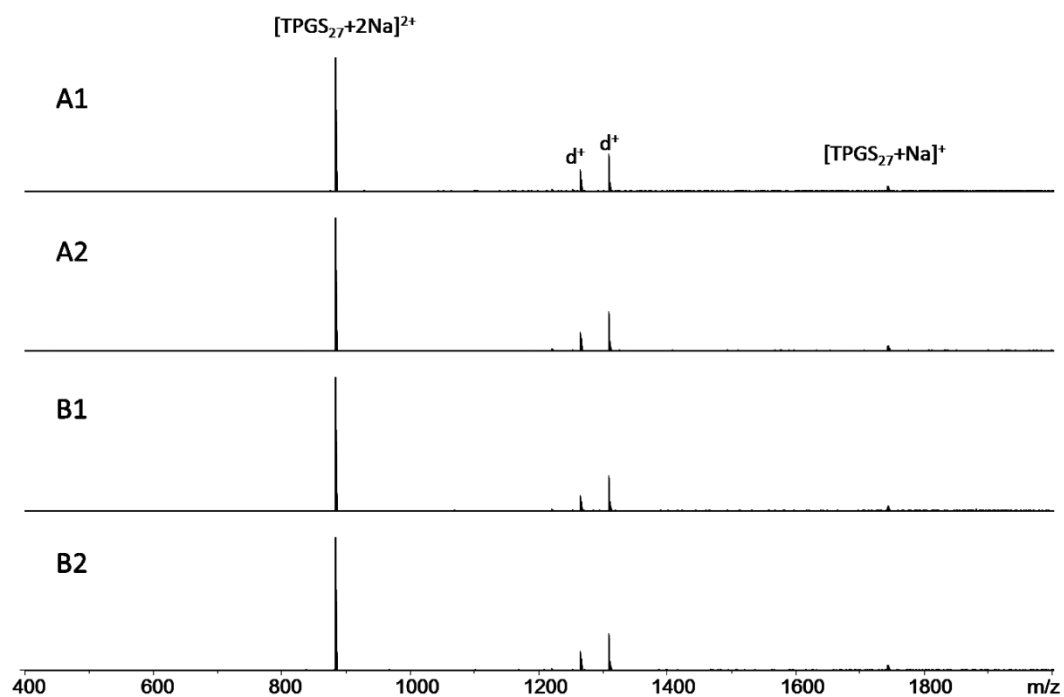


Figure 4.12 ECD spectra of four batches of TPGS samples

Table 4.2 The comparison of four batches of TPGS samples from two manufacturers, first measurement

Batch	TPGS			Di-TPGS			PEG			TPGS %	DiTPGS%	PEG%
	<i>Mn</i>	<i>Mw</i>	<i>n</i>	<i>Mn</i>	<i>Mw</i>	<i>n</i>	<i>Mn</i>	<i>Mw</i>	<i>n</i>			
A1	1461.751	1484.335	21.2	2039.141	2051.342	22.6	905.938	924.673	20.2	90.8	2.7	6.4
A2	1505.268	1529.107	22.1	1951.339	1955.496	20.6	955.860	981.010	21.3	89.4	3.0	7.6
B1	1502.263	1524.667	22.1	2046.761	2057.954	22.8	953.236	977.835	21.2	81.4	4.9	13.7
B2	1520.241	1544.232	22.5	2094.985	2105.985	23.9	957.883	978.756	21.3	84.9	2.8	12.2
A1 heated to 50°C	1452.677	1477.918	20.9	1938.189	1942.591	20.3	926.427	951.560	20.6	90.5	1.6	7.9
A2 heated to 50°C	1492.326	1519.476	21.9	1959.893	1964.136	20.8	956.344	982.313	21.3	89.3	1.6	9.1
A1 melted	1448.261	1473.253	20.8	2037.845	2051.533	22.6	921.633	945.845	20.5	91.0	1.6	7.3
A2 melted	1490.515	1517.504	21.8	2066.633	2079.366	23.3	961.141	989.038	21.4	91.2	2.6	6.2

The batch to batch investigation is repeated using the same experimental condition, and results are summarized in Table 4.3. Compared to the data from the first measurement in Table 4.2, the polymerization extent of each component is slightly different by approximately one monomer unit in the second measurement. For example, the repeat unit of TPGS is 21 ± 1 (n) for all of four batches in the second measurement, where $n = 22 \pm 1$ in the first measurement. On the other hand, although the values of the relative intensity of TPGS, Di-TPGS and PEG in Table 4.3 are not exactly the same with those corresponding numbers in Table 4.2, the trend is the same by showing that batches A1 and A2 contain more TPGS and less PEG than batches B1 and B2, with batch A1 having the most TPGS and batch B1 of the least amount of TPGS. The fluctuation of the experimental values between two measurements could result from the inhomogeneity of the sample, sample preparation, ionization efficiency, and the total ion numbers in the cell during MS detection. Moreover, accurate quantification is always challenging in mass spectrometry, in particular for samples as complex as a polymer mixture. To minimize the fluctuation, all of the measurements should use consistent experimental conditions and instrument settings. Carefully controlling the total ion number in the cell, such as introducing the automatic gain control (AGC) system, and using averaging values from multiple measurements could also be helpful. Because the data analysis was done manually, which is time consuming, using software specially designed to handle with high resolution MS data from complex polymers will not only increase the efficiency, but may also improve the consistency of the data.

Table 4.3 The comparison of four batches of TPGS samples from two manufacturers, second measurement

Batch	TPGS			Di-TPGS			PEG			TPGS %	DiTPGS%	PEG%
	<i>Mn</i>	<i>Mw</i>	<i>n</i>	<i>Mn</i>	<i>Mw</i>	<i>n</i>	<i>Mn</i>	<i>Mw</i>	<i>n</i>			
A1	1424.495	1447.824	20.3	2059.541	2070.365	23.1	878.480	904.019	19.5	91.3	2.6	6.1
A2	1465.787	1490.478	21.2	2110.296	2057.954	24.2	925.456	950.705	20.6	86.8	2.6	10.7
B1	1488.978	1510.992	21.8	2068.166	2074.722	23.3	914.35	937.792	20.4	77.1	4.3	18.6
B2	1489.684	1508.906	21.8	2117.571	2128.128	24.4	934.170	954.180	20.8	79.4	2.6	17.9
A1 heated to 50°C	1428.393	1451.726	20.4	2069.459	2086.451	23.3	905.574	927.426	20.2	88.2	2.3	9.5
A2 heated to 50°C	1467.92	1492.91	21.3	2078.627	2093.237	23.5	938.076	960.881	20.9	85.7	2.0	12.4
A1 melted	1427.071	1449.809	20.4	2026.927	2042.473	22.4	914.256	938.992	20.4	83.5	1.7	14.8
A2 melted	1462.848	1487.792	21.2	2082.895	2097.447	23.6	937.932	960.594	20.9	88.2	2.6	9.2

In the drug industry, the stability of drug excipients is a crucial issue directly relevant to the stability of a drug product and the shelf time. To investigate the stability of TPGS, samples A1 and A2 are processed under circumstances which mimic biology processed by melting the samples in a warm water bath (37°C) and which mimic the extreme ambient environment by exposing the samples to 50°C/ambient humidity for four weeks. The MS data of the processed samples are summarized in Table 4.2, Table 4.3, and Figure C.3. All of the samples listed in the same table are measured on the same day. According to the results, it looks like some subtle changes have occurred to those samples heated to 50°C because the relative ratio of free PEG increases by 1.5%-3.5%, and this trend is consistent between two measurements in Table 4.2 and Table 4.3. In theory, if TPGS or Di-TPGS is decomposed, in addition to free PEG, tocopheryl succinate and/or free tocopherol should be generated at the same time. Peaks indicating tocopheryl succinate or free tocopherol, however, are not observed in the MS spectra, which could due to the low abundance and low ionization efficiency of the two compounds.

In contrast, for samples melted in water bath, results are not consistent between the two batches. 'A1 melted' shows an increase in the amount of free PEG but the observation from 'A2 melted' is opposite. The two measurements of 'A1 melted' differ a lot in values. One possibility is that the sample is not very homogeneous, because solid-like TPGS samples are not likely to flow evenly during the mimic experiments. Moreover, as discussed above, the experimental uncertainty is relatively big due to several factors, so other complementary quantification analysis is necessary to accurately

determine the changes between standard samples and the processed samples.

4.4 Conclusions

FTICR MS and MS/MS were demonstrated as a valuable tool in the compositional study and structural characterization of TPGS samples, which can be used as a complementary tool for traditional spectroscopic techniques in TPGS research. The results show that high mass accuracy and high resolution are of great benefit in elemental formulae assignment and in obtaining detail structural information. Some diagnostic fragments from CAD and ECD MS/MS of $[\text{TPGS}+3\text{Na}]^{3+}$ and $[\text{TPGS}+2\text{Na}]^{2+}$ can be used for the identification of the TPGS structure in the future. Interestingly, no fragment ions were detected from the $[\text{TPGS}+\text{Na}]^+$ precursor under both CAD and EID. By utilizing ECD/ECD MS^3 , more confident supplementary structural information can be achieved. Varying solution conditions were shown to affect the compositional study of TPGS samples, indicating that the solvent selection could be particularly important for the mass spectrometry study of some polymers. Different metallic-cation adducts can strongly influence the fragmentation pattern of TPGS, with the silver adduct providing particularly interesting results. In addition to the methodology study, the MS and MS/MS results from four batches of TPGS samples from two manufacturers were compared. This method can be applied for the rapid compositional and structural investigation of many other polymeric compounds.

Chapter 5 The competitive influence of Li^+ , Na^+ , K^+ , Ag^+ , and H^+ on the fragmentation of TPGS²

5.1 Introduction

5.1.1 Investigation of the influence of metallic adduction on the fragmentation of polymers

Interest in using MS and MS/MS for the study of synthetic polymers has grown sharply in the past decade due to development of raw polymeric products and advances in mass spectrometers. In practice, it can be difficult to ionize or fragment many industrial polymers, and salt doping is becoming one of the most effective solutions, which has been widely investigated.²⁵⁹⁻²⁶⁶ Additionally, inducing metallic adducts to improve the fragmentation efficiency in MS/MS has been frequently applied for many types of molecules, such as oligosaccharides,^{165,267-269} and peptides/proteins.²⁷⁰⁻²⁷⁴

The choice of adducts, and metallic ions in particular, can have a great impact on the ionization²⁵⁹⁻²⁶¹ and fragmentation.²⁷⁵⁻²⁷⁷ By facilitating the ionization, silver ions are frequently used as a cationizing agent for polymers like polystyrene because of a possible binding with the phenyl ring.^{258,259,276} Ag^+ cationization is also very effective for generating MS spectra of polyglycols and can improve fragmentation in CAD.²⁵⁸ The most important class of adducts in polymer research is the alkali metal because of the

²This chapter has been partially adapted from Wei, J.; Bristow, A.W.T.; O'Connor, P. The competitive influence of Li^+ , Na^+ , K^+ , Ag^+ and H^+ on the fragmentation of a PEGylated polymeric excipient, accepted. Copyright 2014 Springer. Bristow, A.W.T. provided the TPGS samples. Wei, J. did all of the experiments and drafted the manuscript under the supervision of O'Connor P. B..

ubiquitous usage of sodium/potassium salt in polymer synthesis^{278,279} and the evidence of improving the ionization and fragmentation efficiency of some polymers.^{258,280} In the presence of binary mixtures of NaCl and another salt (LiCl, KCl, CsCl, or NH₄Cl), the selectivity between poly(propylene glycol) and the cations were found in the order of $\text{NH}_4^+ \approx \text{K}^+ > \text{Na}^+ \approx \text{Cs}^+ > \text{Li}^+$, though the solvent, counter ions, and the conformation are also significant.²⁶¹ In terms of the fragmentation, most literature studies were conducted by CAD, and some trends were monitored. The binding strength of polyethylene glycol (PEG) with alkali metals has been investigated experimentally and theoretically.^{253,260,281} Using a quadrupole ion trap mass spectrometer, the relative affinity of Na⁺, K⁺, and Cs⁺ to PEG was characterized by CAD experiments, and it was found that the larger adduct was lost more easily,²⁵³ which was complemented by other studies carried out on different instruments and polymers.^{143,145,260} Furthermore, the binding energy between alkali cations and PEG was determined to be decreasing in the order of $\text{Li}^+ > \text{Na}^+ > \text{K}^+ > \text{Cs}^+$ using the electronic structure calculation based on density functional theory, and this order is in agreement with experimental results.^{253,281} The calculation also indicates that the binding energy of the cation is not significantly affected by the polymerization degree (n) when $n > 10$. Additionally, it is believed that smaller alkali ions with stronger interaction with the oligomer provide more structural information in CAD.^{145,258,282}

Comparatively, there are fewer studies focused on the influence of the adduct on the fragmentation of polymers using electron-based fragmentation methods. Because electron-based fragmentation methods are not as widely available as CAD, rules for fragmentation of synthetic polymers in electron-

based fragmentation methods are not as well understood as they are for biopolymers. In the past decade, it was demonstrated that ECD or ETD can provide complementary structural information of different polymers,^{81,149,283} though there are also some exceptional cases.^{145,284} Understanding of the influence of different adducts on electron-based fragmentation process can be, therefore, useful in extraction structural information from ECD spectra and valuable in selecting adducts in practice. In Smith and Mosely's recent work,¹⁴³ they studied the CAD, ECD, and hot-ECD behaviours of doubly-charged PEG with the presence of two different charge carriers among Na⁺, K⁺, and Li⁺. A dissociation order, Na⁺ > K⁺ > Li⁺ (loss of Na is preferred), different from the binding strength deduced from CAD experiments, was observed in ECD and hot-ECD experiments and suggests that the reduction potential (also known as the redox potential, the standard reduction potential of a cation is measured in solution using a hydrogen electrode as a reference and reflects the tendency of a species to capture an electron) of the ion may play an important role in the electron-based dissociation process, such that the ions with higher reduction potential are lost more easily.¹⁴³ In addition to reduction potential, second ionization energy,²⁷⁰ charge density,²⁷¹ recombination energy^{165,274} and the electronic configuration²⁸⁵ of the cationizing metal ion were also suggested as factors that might be relevant to the ECD process. In general, for most of the molecules investigated by electron-based fragmentation techniques, introducing the smaller alkali metal ion usually produces more abundant fragments.^{78,143,163,165} The role of the metal ion in electron-based fragmentation process, however, is still far from clear.

5.1.2 Content of the chapter

In Chapter 4, the fragmentation of TPGS was investigated by both CAD and ECD, and TPGS with three silver cations showed different ECD behaviour in contrast to the precursors with 3Li^+ or 3Na^+ ions. The principal thrust of the research in this chapter was to discuss the influence of metal ion adducts in CAD and, particularly, in ECD processes according to the observations from the fragmentation of TPGS. Several widely used metallic ions (Li^+ , Na^+ , K^+ , Ag^+) were selected and also compared with proton adduction. To estimate the impact of each adduct, doubly-charged TPGS_{27} (27 is the degree of polymerization, structure shown in Figure 5.1) ions in the presence of two different charge carriers (Li^+ , Na^+ , K^+ , Ag^+ , H^+) are used in most of the experiments.

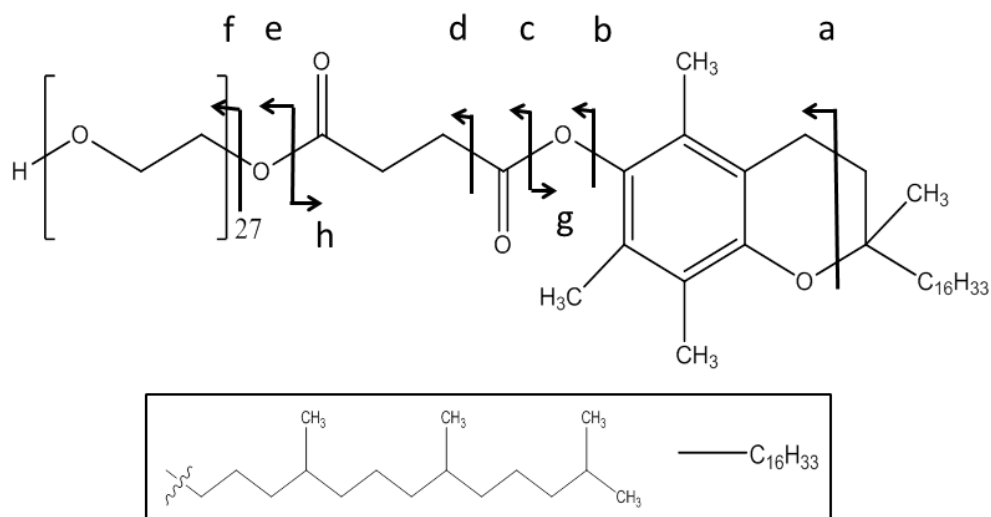


Figure 5.1 Structure of TPGS_{27} (27 is the degree of polymerization)

5.2 Experimental section

5.2.1 Chemicals

TPGS samples (ISOCHEM, Vert-Le-Petit, France) were dissolved in 50:50 methanol:water to a concentration of $\sim 1 \mu\text{M}$ before use. For different experiments, sodium nitrate, lithium nitrate, potassium nitrate, and silver nitrate, (Fisher Scientific UK limited, UK) were added to a final concentration of 1 mM or 0.1 mM depending on the experiment. 0.2% of formic acid (Sigma-Aldrich Co., St. Louis, MO, USA) was used for the protonation. Water was purified by a Millipore Direct-Q purification system.

5.2.2 Mass spectrometry experiments.

All mass spectrometry experiments were carried out on a Bruker 12 T solariX FTICR mass spectrometer (Bruker Daltonik, GmbH, Bremen, Germany) with a homemade nano-electrospray ion source. For CAD, the parent ions were isolated in the quadrupole and then transferred to the collision cell for fragmentation using a collision energy from 9 to 46 V (in general, 11 ± 2 V for precursors with one/two protons, and 42 ± 4 V for all of the other precursors) which was optimized for each sample to provide an even spread of fragments, and fragments were finally detected in the ICR infinity cell.¹¹⁰ In the ECD experiment, the isolated ions were accumulated externally in the collision cell and then transferred to the ICR cell. Trapped ions were then irradiated with electrons from a 1.5 A heated hollow cathode; the bias voltage used for ECD experiments was ~ 2 V and the pulse length was around 0.1 s. To achieve a desirable S/N, up to 20 scans were averaged.

5.3 Results and discussions

5.3.1 The influence of the metallic adduct on the fragmentation of TPGS in CAD

The CAD results of $[M+2Li]^{2+}$, $[M+2Na]^{2+}$, $[M+2K]^{2+}$, and $[M+2Ag]^{2+}$ displayed in Figure 5.2 and summarized in Scheme 5.1, show that diagnostic fragments cleaved at positions 'a', 'f', 'd' and 'c' are detected for TPGS with $2Li^+$, $2Na^+$, or $2Ag^+$, but not for $[M+2K]^{2+}$. The cross-ring cleavage in position 'a' is the most favourable fragmentation channel as it gives the most intense fragment in the CAD spectra of $[M+2Li]^{2+}$, $[M+2Na]^{2+}$, and $[M+2Ag]^{2+}$ (Figure 5.2). The high intensity of this peak is likely driven by the thermodynamic stability of a larger conjugated structure as suggested in Scheme 4.1. The ready cleavage at position 'f' indicates that the connection between the long PEG chain and the tocopheryl succinate is relatively labile, producing another abundant fragment. With regard to the intensities of peaks from cleavages at 'd' and 'c', higher abundance is found in the $[M+2Ag]^{2+}$ spectrum and very low fragmentation abundance is observed in the $[M+2Na]^{2+}$ spectrum. Additionally, losing one charge carrier is an important channel for $[M+2Na]^{2+}$, and in particular for $[M+2K]^{2+}$, but not for $[M+2Li]^{2+}$ and $[M+2Ag]^{2+}$.

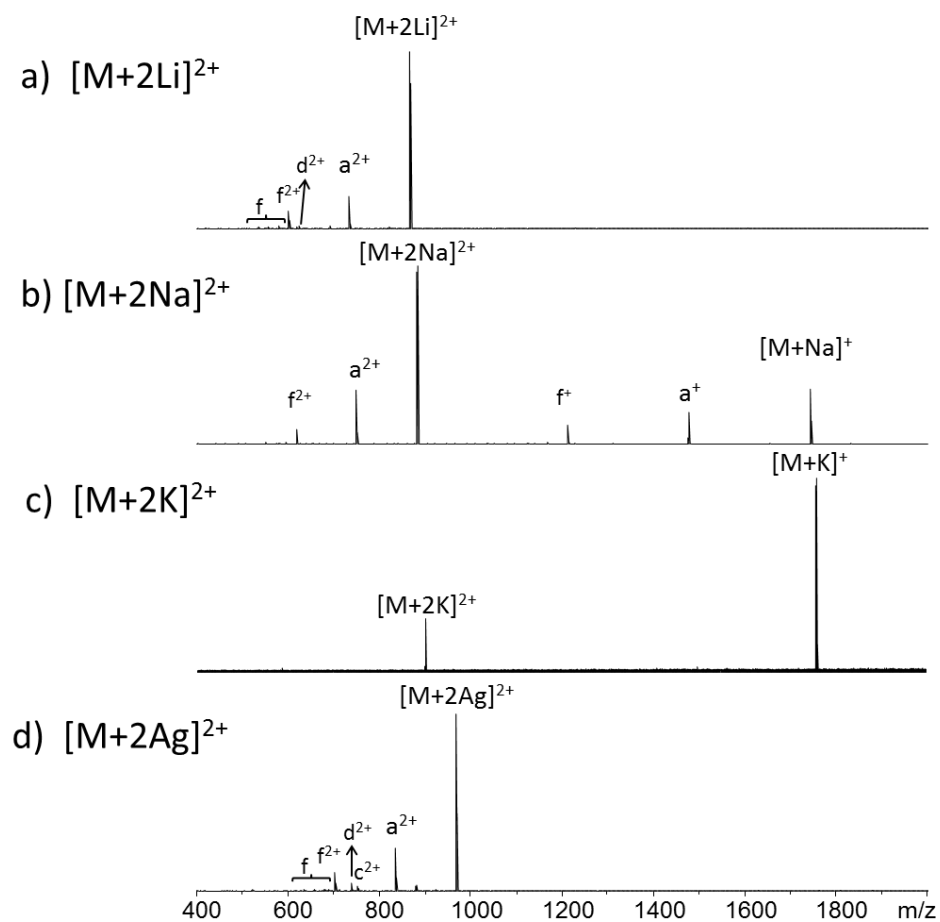
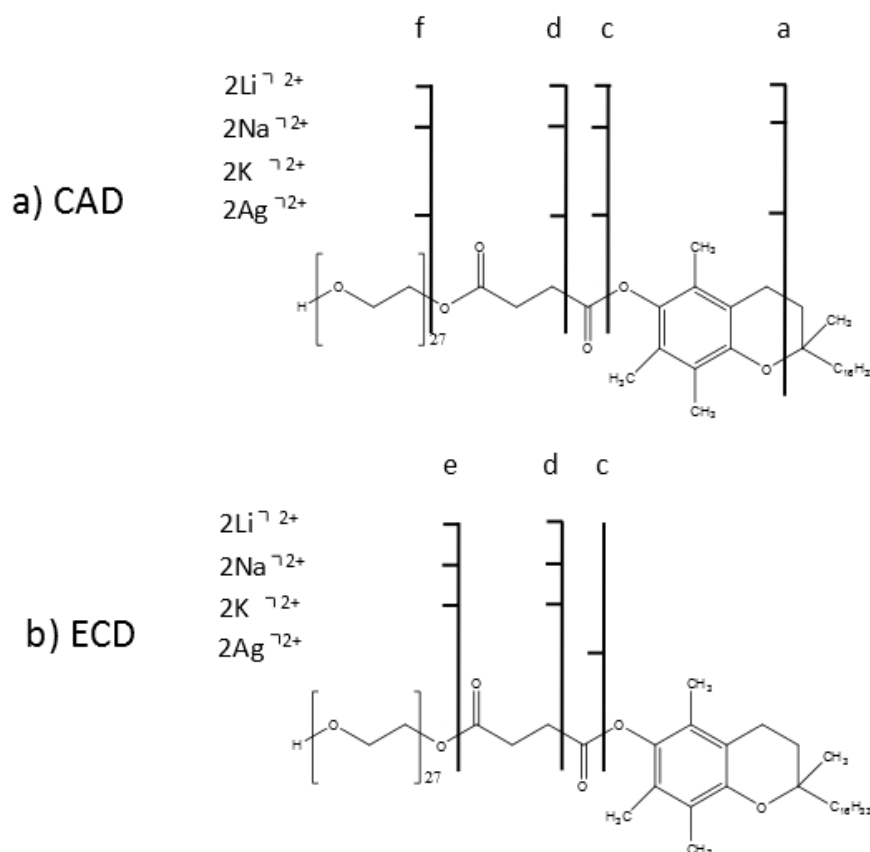


Figure 5.2 CAD spectra of a): $[TPGS+2Li]^{2+}$, b): $[TPGS+2Na]^{2+}$, c): $[TPGS+2K]^{2+}$, and d): $[TPGS+2Ag]^{2+}$.



Scheme 5.1 CAD and ECD results of $[\text{TPGS}+2\text{Li}]^{2+}$, $[\text{TPGS}+2\text{Na}]^{2+}$, $[\text{TPGS}+2\text{K}]^{2+}$, and $[\text{TPGS}+2\text{Ag}]^{2+}$

When combining two different metallic cations, some relative influence information for the various adducts can be determined, and this information is summarized according to the CAD spectra of $[\text{M}+\text{X}_1+\text{X}_2]^{2+}$ (where X_1 and X_2 refer to Li^+ , Na^+ , K^+ , or Ag^+ , and $\text{X}_1 \neq \text{X}_2$) (Figure 5.3). First, precursors having a silver cation, such as $[\text{M}+\text{Ag}+\text{Li}]^{2+}$ and $[\text{M}+\text{Ag}+\text{Na}]^{2+}$, produce abundant fragments from cleavages at 'a', 'f', 'd' and 'c'; however, none of the fragments is detected for $[\text{M}+\text{K}+\text{Ag}]^{2+}$. Moreover, there is also a scarcity of fragments from cleavages at either 'a', 'f', 'd' or 'c' in the $[\text{M}+\text{K}+\text{Na}]^{2+}$ and $[\text{M}+\text{K}+\text{Li}]^{2+}$ CAD spectra (Figure 5.3b and f). Though one doubly-charged

peak at m/z 822.5389 is detected in the $[M+K+Li]^{2+}$ spectrum, it might be preceded by a rearrangement and is assigned to $C_{84}H_{158}O_{27}KLi$ (Table D.2). The result indicates that the silver cation adduct could improve the fragmentation of TPGS in CAD, while, on the contrary, the presence of K^+ inhibits the fragmentation significantly even when accompanying with a Ag^+ cation.

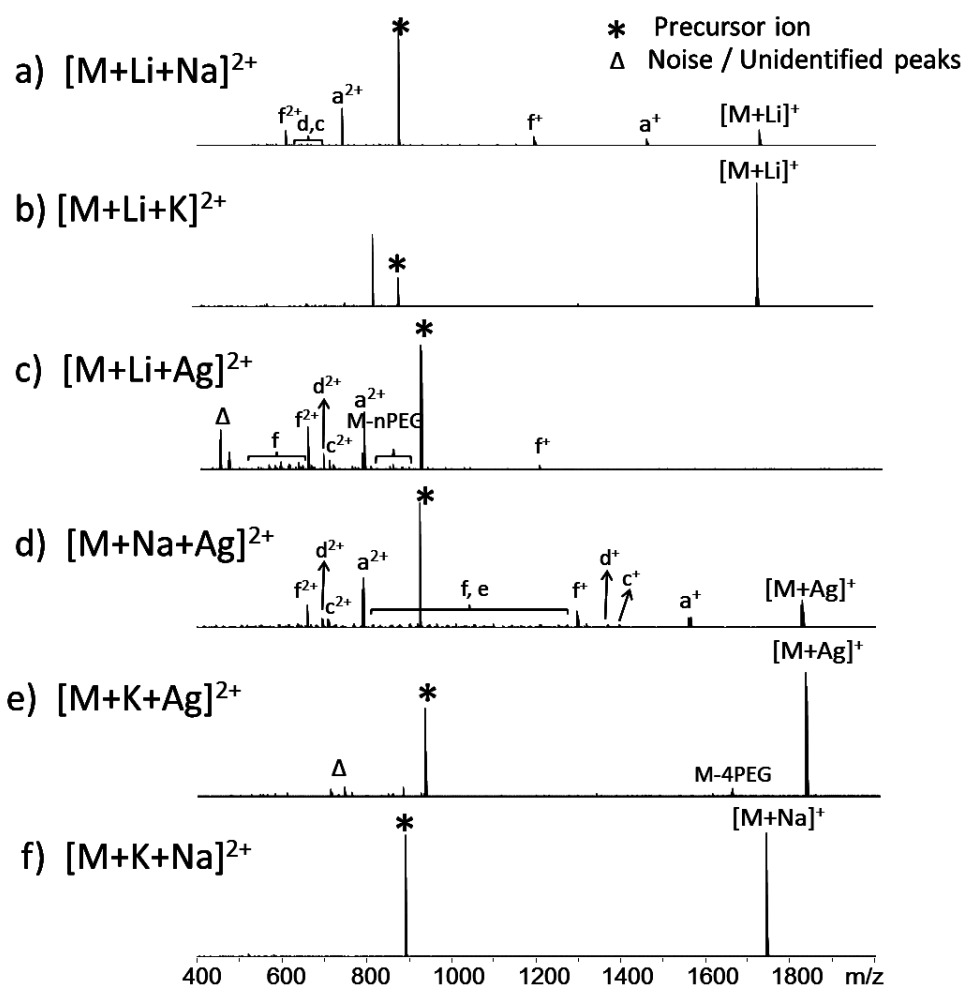


Figure 5.3 CAD spectra of a): $[TPGS+Li+Na]^{2+}$, b): $[TPGS+K+Li]^{2+}$, c): $[TPGS+Li+Ag]^{2+}$, d): $[TPGS+Na+Ag]^{2+}$, e): $[TPGS+K+Ag]^{2+}$, and f): $[TPGS+K+Na]^{2+}$. 'nPEG' in the figure refers to loss of nC_2H_4O units

The ready loss of K^+ from all of the precursors suggests that K^+ has a very weak binding with the TPGS. On the other hand, a very strong binding between TPGS and Li^+ / Ag^+ is also demonstrated by the CAD results, since detachment from the precursors was not found for either Li^+ or Ag^+ . Without losing of any charge carrier from $[M+Ag+Li]^{2+}$ (Figure 5.3c), it is hard to judge the competitive binding strength between the Li^+ and Ag^+ adducts. According to the CAD results of $[M+Na+Li]^{2+}$, $[M+Na+K]^{2+}$, and $[M+Na+Ag]^{2+}$, the affinity of Na^+ is determined to be weaker than Li^+ and Ag^+ but stronger than K^+ . Hence, the binding strength of the metallic cations to the TPGS is in the order of $Ag^+ \approx Li^+ > Na^+ > K^+$. The result is in agreement with the investigations carried out between PEG/PEG methyl ether and Li^+ , Na^+ , or K^+ .^{143,253} The improvement of fragmentation by the Ag^+ cation shown in Figure 5.3c-d is likely because of a strong ion-dipole binding to the oxygen in the PEG region as well as a strong interaction with the ester group (d- π interaction) next to the big π bond region, whereas the lack of fragmentation whenever K^+ is involved might be because that loss of K^+ is the energy release channel and the remained internal energy gained in the collision process is not enough for proceeding any backbone cleavages. In some spectra, a few low intensity peaks cannot be identified which might be from rearrangements.

5.3.2 The influence of the metallic adduct on the fragmentation of TPGS in ECD

For TPGS attached with alkali metal ions, $[M+2Li]^{2+}$, $[M+2Na]^{2+}$, and $[M+2K]^{2+}$, ECD shows different cleavages from the CAD results, and ECD spectra are in Figure 5.4 and the cleavages are summarized in Scheme 5.1b. Cleavages at positions 'e' and 'd' are detected, with the cleavage at 'd' as the

dominating channel (Figure 5.4a-c). For $[M+2Ag]^{2+}$, the only fragment detected indicates a cleavage at position 'c', otherwise, loss of the Ag^+ cation is the only other peak observed (Figure 5.4d).

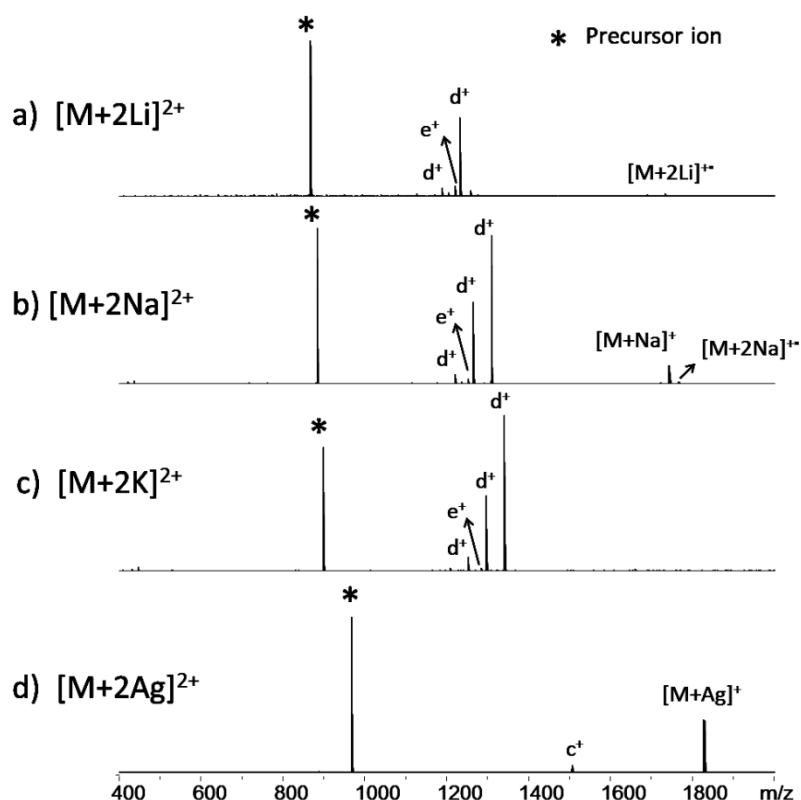


Figure 5.4 ECD spectra of a) $[TPGS+2Li]^{2+}$, b) $[TPGS+2Na]^{2+}$, c) $[TPGS+2K]^{2+}$, and d) $[TPGS+2Ag]^{2+}$

The ECD results of TPGS with two different charge carriers also give some trends. When both of the adducts are alkali metal ions among Na^+ , K^+ , and Li^+ , fragments cleaving at positions 'd' and 'e' are produced (Figure 5.5a-b, f). In contrast, whenever Ag^+ is present (Figure 5.5c-e), the fragment pattern closely resembles the ECD of $[M + 2Ag]^{2+}$ from Figure 4d with only an observed cleavage at position c. In addition to the different fragmentation patterns compared with the CAD results, the charge carrier is lost in a very

different order, $\text{Ag}^+ > \text{Na}^+ > \text{K}^+ \geq \text{Li}^+$ (Ag^+ is lost most easily), which can be seen in Figure 5.5. Loss of the Ag^+ cation always gives the most intense peak if exists. The sodium cation is lost more easily than K^+ and Li^+ ; this was also observed in Smith's ECD and hot-ECD experiments on the PEG methyl ether,¹⁴³ and this order does not follow the binding strength found from the CAD experiments.²⁸¹ In comparison, the lithium adduct and potassium adduct are the most difficult to detach; however, since a tiny peak indicating $[\text{M} + \text{Li}]^+$ is detected on the ECD spectrum of $[\text{M} + \text{Li} + \text{K}]^{2+}$, it suggests that K^+ might be relatively more labile than Li^+ in the ECD process. This trend, $\text{Ag}^+ > \text{Na}^+ > \text{K}^+ \geq \text{Li}^+$ (Ag^+ is lost most easily), follows the decreasing reduction potential of each ion ($0.8 \text{ V} (\text{Ag}^+) > -2.71 \text{ V} (\text{Na}^+) > -2.93 \text{ V} (\text{K}^+) > -3.05 \text{ V} (\text{Li}^+)$).²⁸⁶ Thus, the ion having a higher reduction potential has a higher tendency to be reduced and lost in ECD. The very similar low standard reduction potential values of K^+ and Li^+ explains the ECD spectrum of $[\text{M} + \text{Li} + \text{K}]^{2+}$ in Figure 5.5b where only a tiny peak indicating loss of K^+ is observed.

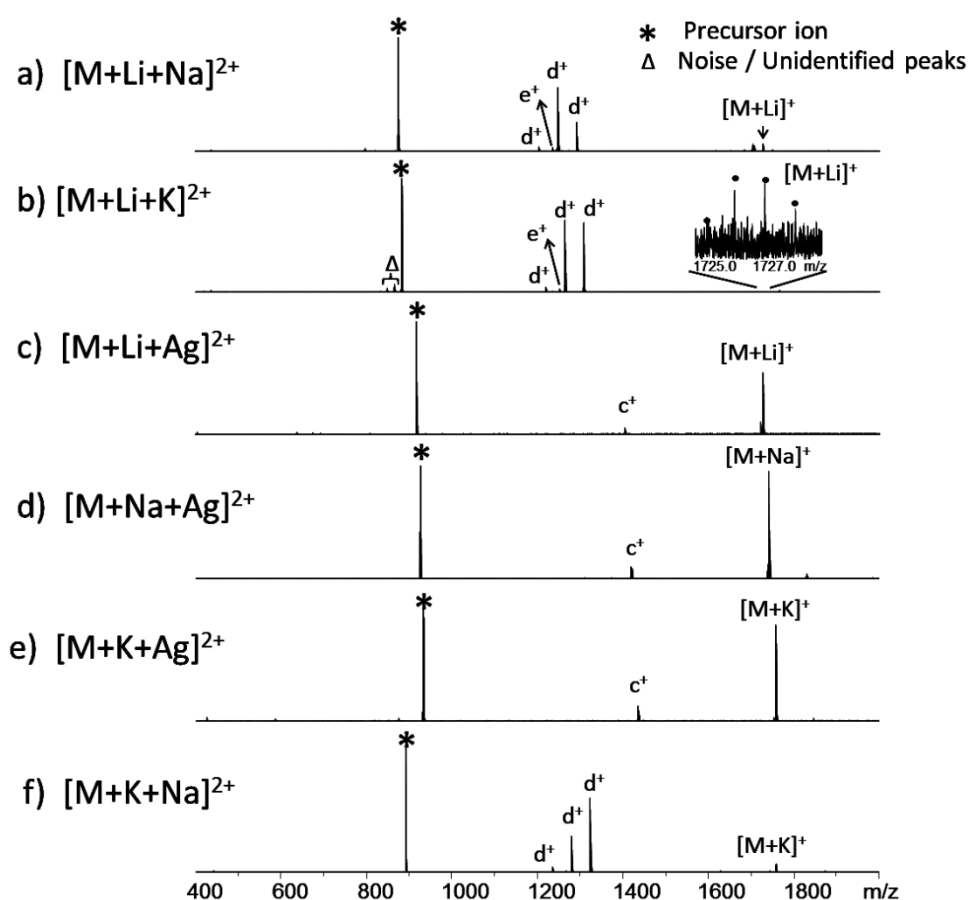


Figure 5.5 ECD spectra of a) $[\text{TPGS}+\text{Li}+\text{Na}]^{2+}$, b) $[\text{TPGS}+\text{K}+\text{Li}]^{2+}$, c) $[\text{TPGS}+\text{Li}+\text{Ag}]^{2+}$, d) $[\text{TPGS}+\text{Na}+\text{Ag}]^{2+}$, e) $[\text{TPGS}+\text{K}+\text{Ag}]^{2+}$, and f) $[\text{TPGS}+\text{K}+\text{Na}]^{2+}$

According to the ECD results, for all of the precursors, there are two possible pathways after the electron is captured by the cation. Take $[\text{M}+\text{Ag}+\text{X}]^{2+}$ as an example, one channel is the neutralization and loss of the Ag^+ cation; the resulting Ag^\bullet adduct is readily lost before leading to any fragmentation. The other pathway is that the Ag^+ attached to the ester group next to the chromanol ring captures one electron competitively and the resulting radical induced a direct α -cleavage at position 'c'. For the Ag^+

adduct, the first pathway of losing the Ag^+ cation seems much more prevalent than the second one, so the fragment from cleavage at 'c' has a very low intensity. On the contrary, for alkali metal ions, the second pathway is much favourable, inducing cleavage at position 'd'. Moreover, whenever the Ag^+ cation is a charge carrier, fragments detected are solely from cleavage at 'c' and loss of Ag^+ , which argues that the Ag^+ cation is dominant in generating fragments in ECD compared to Na^+ , K^+ , or Li^+ , and also demonstrates that the reduction potential of the metallic ion might be a crucial factor in influencing fragmentation during the ECD process. Therefore, when selecting the metallic adduct in an ECD experiment, the ion with a high reduction potential may be more effective in capturing electrons, but may also be readily lost before leading to any fragmentation.

In the ECD spectra of TPGS with alkali metal adducts (Figure 5.4a-c), though cleavage at position 'd' always generates abundant fragments, some subtle differences are observed. For $[\text{M}+2\text{Na}]^{2+}$, and $[\text{M}+2\text{K}]^{2+}$, a direct cleavage at position 'd' without loss of PEG units is the most intense peak; while, for $[\text{M}+2\text{Li}]^{2+}$, a cleavage at 'd' with loss of one PEG unit produces the most abundant fragment (Table D.3). A similar result was observed for TPGS with 3 or 2 sodium adducts as described in section 4.3.3, where the loss of one PEG unit is detected for $[\text{TPGS}+3\text{Na}]^{3+}$, but not for $[\text{TPGS}+2\text{Na}]^{2+}$, which is likely due to different conformations of the two precursors.¹⁴⁶ In the ECD spectra of the precursors with Li^+ as a charge carrier, $[\text{M}+\text{Li}+\text{Na}]^{2+}$ and $[\text{M}+\text{Li}+\text{K}]^{2+}$ (Figure 5a-b), the peak with 26 PEG units (losing one PEG unit) has higher or equivalent intensity in comparison with the other peak with 27 PEG units, while for $[\text{M}+\text{Na}+\text{K}]^{2+}$ (Figure 5.5f), the peak with 27 PEG units from the

direct cleavage at 'd' is more intense. In contrast to the silver cation, all three alkali metal ions, Li^+ , Na^+ , and K^+ , have very similar physical and chemical properties, so the fragmentation patterns are similar; however, precursors with different alkali metal ions may show some subtle differences in inducing fragmentation, such as the relative intensity of each fragment in this case.

5.3.3 In comparison with protonation

Even though, for synthetic polymers, protonation is quite often not as effective as the metal cationization, protons are still one of the most important adducts. It is worth noting that though formic acid is added to improve the protonation of TPGS, the intensity of the $[\text{M}+2\text{H}]^{2+}$ peak is very low, because Na^+ and NH_4^+ are still the main adducts. Herein, the influence of protonation on the fragmentation of TPGS is investigated by CAD and ECD experiments carried on $[\text{M}+\text{H}+\text{X}]^{2+}$ (X is one of the ions from H^+ , Li^+ , Na^+ , K^+ , Ag^+), and some distinct results are observed.

Comparing the CAD results in Figure 5.2 and Figure 5.3 to Figure 5.6I, Figure 5.6I shows that more abundant product ions and different diagnostic fragments are produced by precursors with one or two protons, such as $[\text{M}+2\text{H}]^{2+}$, $[\text{M}+\text{H}+\text{Li}]^{2+}$, $[\text{M}+\text{H}+\text{Na}]^{2+}$, $[\text{M}+\text{H}+\text{K}]^{2+}$, and $[\text{M}+\text{H}+\text{Ag}]^{2+}$. Cleavages at 'e', 'h', and 'c' generate some high intensity peaks, and extensively loss of PEG units is common. The cross-ring cleavage at position 'a' is not observed at all. In Figure 5.6I, almost all of the singly-charged ions are due to the loss of one proton, so based on the CAD experiments, the binding strength for all of the five charge carriers investigated follows the order $\text{Ag}^+ \approx \text{Li}^+ > \text{Na}^+ > \text{K}^+ > \text{H}^+$. This order suggests that the affinity of the adduct ion for the precursor is

not only linked to its size. Instead, except for the proton, for the several metal ions (Figure 5.2 and Figure 5.3), it looks like the one binding stronger with the precursor ion has the potential to generate more structural information. One hypothesis that may explain these results²⁵⁸ is that the internal energy acquired during CAD is partially lost with the loss of the adduct ion, and thus insufficient surplus energy remains for additional fragmentation. Two rational explanations of the abundant CAD spectra of protonated precursors are that: first, the collision voltage used for extensively fragments the precursors with one/two protons is around 11 V, compared to ~42 V used to fragment the precursors without protons, suggesting that protonated species have much more labile structures; second, proton migration could induce fragmentation as it does in proteins.^{87,287}

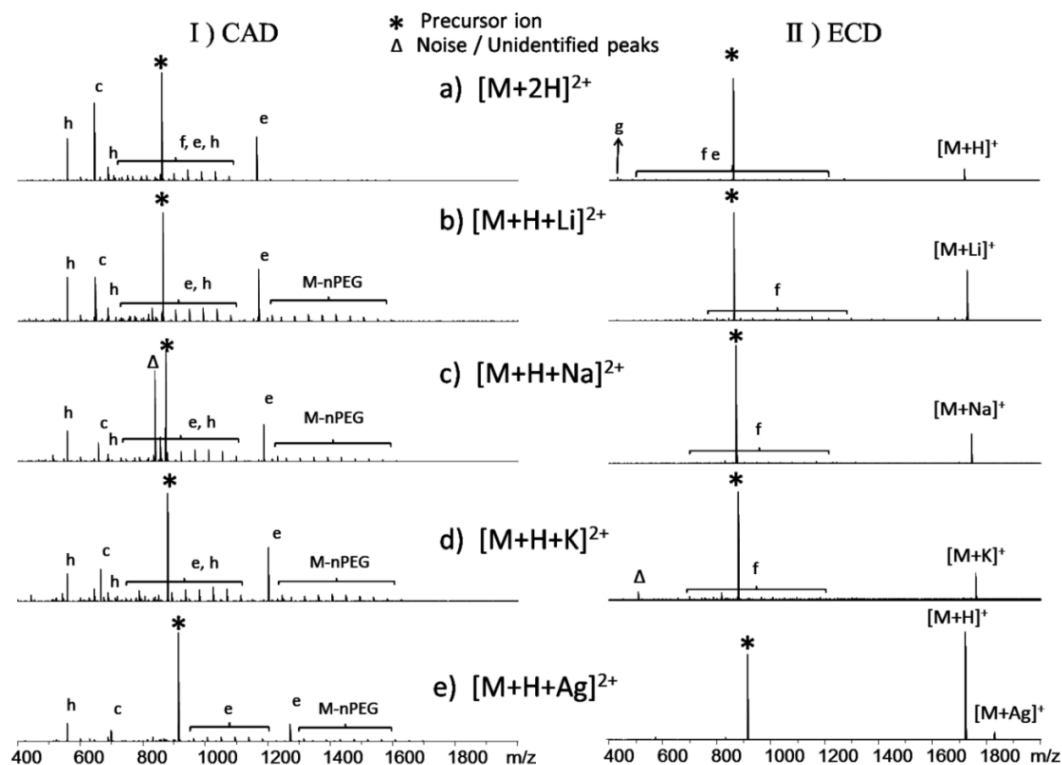


Figure 5.6 CAD and ECD spectra of $[M+2H]^{2+}$, $[M+H+Li]^{2+}$, $[M+H+Na]^{2+}$, $[M+H+K]^{2+}$, and $[M+H+Ag]^{2+}$. 'nPEG' in the figure refers to loss of nC_2H_4O units.

The ECD results of the precursors binding with one proton/two protons in Figure 5.6II also show differences, where no fragments of high abundance are detected. In the ECD spectrum of $[M+2H]^{2+}$ (Figure 5.6II a), a small fragment at m/z 430.3805 ($[C_{29}H_{50}O_2]^+$), is assigned to the protonated tocopheryl labelled as cleavage 'g', which is not detected for any of the other precursors. Extensive loss of PEG units (C_2H_4O) with the cleavage at 'e' or 'f' is observed. The other precursors with two different charge carriers yield some product ions of low intensity from cleavage at 'f' with different numbers of PEG units. One important observation is that the detachment of the proton

in the ECD experiments follows the order, $\text{Ag}^+ > \text{H}^+ > \text{Na}^+ > \text{K}^+ \geq \text{Li}^+$, where the ion with the higher standard reduction potential is lost more easily. The results in Figure 5.6II b-d seem also in agreement with the proposal that the ion with a high reduction potential plays a dominant role in generating fragments, but could be lost easily. The fragment cleavage at position 'c' from $[\text{M}+\text{H}+\text{Ag}]^{2+}$ is not observed in Figure 5.6IIe, which might be due to the high reduction potential of Ag^+ and H^+ , therefore, both of the two charge carriers could be detached easily without yielding any fragmentation.

5.4 Conclusions

The influence of several adducts, H^+ , Li^+ , Na^+ , K^+ , and Ag^+ , on the fragmentation of a PEGylated polymer, TPGS_{27} , in CAD and ECD was investigated. The binding strength of those charge carriers was determined in the order of $\text{Ag}^+ \approx \text{Li}^+ > \text{Na}^+ > \text{K}^+ > \text{H}^+$. Different adducts influence the fragmentation patterns of TPGS , with protonated species producing very different fragments in particular. In ECD, a different order of losing the charge carrier was observed, which follows $\text{Ag}^+ > \text{H}^+ > \text{Na}^+ > \text{K}^+ \geq \text{Li}^+$ (Ag^+ is detached most easily), and this order is in agreement with the decreasing reduction potential of each ion ($0.8 \text{ V} (\text{Ag}^+) > 0 \text{ V} (\text{H}^+) > -2.71 \text{ V} (\text{Na}^+) > -2.93 \text{ V} (\text{K}^+) > -3.05 \text{ V} (\text{Li}^+)$).²⁸⁶ In addition, Ag^+ shows dominant role in producing the fragmentation in cases where two different charge carriers are present, suggesting that the reduction potential of the charge carrier could significantly affect the ECD fragmentation. Distinct fragmentation behaviours of protonated precursors in CAD are likely due to the high mobility of protons.

Chapter 6 Structural characterization of chlorophyll-a³

6.1 Introduction

6.1.1 General characters of chlorophylls

Chlorophylls are omnipresent from algae to higher plants. They serve as crucial electron and energy transfer intermediates in photosynthesis. Particularly, most of these functions depend on its special structure, a large asymmetric 'π-electron box'.²⁸⁸ Chemically, chlorophylls are unstable in both acid and base, easily oxidize under light,²⁸⁹ and have a tendency for aggregation and interaction with molecules in their environment,²⁹⁰ all of which increase the difficulty of study. Improved analytical methods for structural determination are needed to understand the challenges of chlorophyll aggregation,²⁹¹ the structural modification of chlorophylls and catabolites, as well as its applications in energy research.²⁹² In the last 20 years, one of the tough challenges drawing attention is chlorophyll degradation, which has remained an enigma.²⁹³

6.1.2 MS analysis of chlorophylls and porphyrin derivatives

During the last several decades, MS has been used to obtain fragmentation information of many molecules, where MS/MS techniques are

³This chapter has been partially adapted with permission from Wei, J.; Li, H.; Barrow, M.; O'Connor, P. Structural Characterization of Chlorophyll-a by High Resolution Tandem Mass Spectrometry, *J. Am. Soc. Mass. Spectrom.* **2013**, *24*, 753-760. Copyright 2014 Springer. Wei, J. performed all of the experiments with the help of Li, H. and Barrow, M.. Wei, J. drafted the manuscript with the help of O'Connor P. B.. All of the work was done under the supervision of O'Connor P. B..

especially useful for structural breakdown elucidation.^{78,79,294,295} Various MS techniques, e.g. LC-fast atom bombardment (FAB)²⁹⁶/ESI MS,²⁹⁷ LC-atmospheric pressure chemical ionization (APCI) MS,^{298,299} and MALDI MS,³⁰⁰ have proven to be very useful for the identification of chlorophylls and their derivatives. However, to our knowledge there are only a few publications focusing on the MS/MS behaviour of chlorophylls. Several significant publications from the early 1990s reported interesting cascade fragmentations of chlorophyll-a (structure is shown in Figure 6.1), which were attributed to the consistent loss of aliphatic side groups or cleavages from ring IV and V, using ²⁵²Cf plasma desorption,^{301,302} FAB,³⁰³ and laser photoionization mass spectrometry.³⁰⁴ However, due to limited resolution and mass accuracy, most of the product ions cannot be separated and identified unambiguously. In the published research, either hard ionization conditions or high-energy CAD^{300,301,303} were used and generated extensive fragmentation. Motivated by these factors and the numerous MS/MS techniques available with FTICR mass spectrometers, an improved fragmentation characterization method can be established for chlorophyll research.

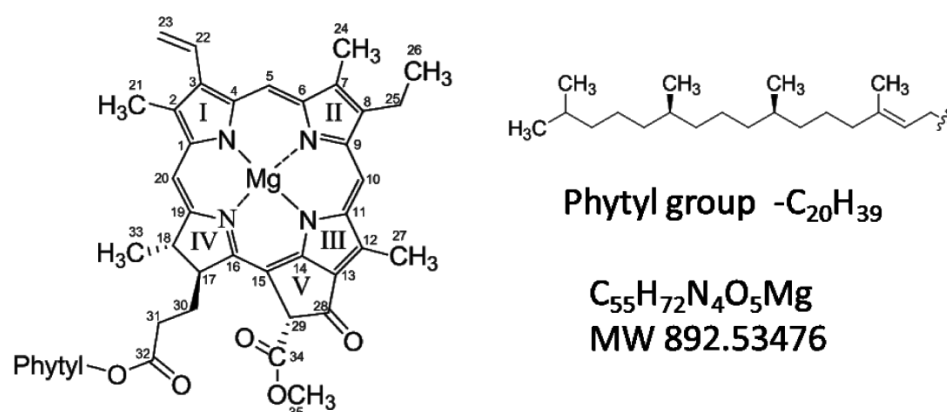


Figure 6.1 Structure of chlorophyll-a

CAD has been used to elucidate the structures of porphyrin pyrrole,³⁰⁵ octaethylporphyrin and its complexes.³⁰⁶ On the other hand, based on the conjugated structure of porphyrin like compounds, electron-based MS/MS can likely lead to fragmentation in a well-regulated way, which may aid understanding of the degradation mechanism. Kaczorowska and Cooper⁷⁶ described the EID behaviour of octaethylporphyrin (OEP) and its iron (III) complex, and found that the α - and β - cleavages generate the most abundant fragments. Even though having a similar porphyrin structure to chlorophylls, different central metal ion and side groups of these two compounds may act differently during MS/MS. Electron capture induced dissociation has been applied to protoporphyrin IX ions by Nielsen and his colleagues.³⁰⁷ Though few fragments were observed, protoporphyrin ions showed high efficiency in electron capture, where $[M + H]^+$ is formed by capture of two electrons.

6.1.3 Content of the chapter

Using chlorophyll-*a* as a representative type of chlorophylls, this study has not only provided new fragmentation information by EID, CAD, and IRMPD using a high resolution FTICR mass spectrometer but also demonstrated the favourable cleavage sites of chlorophyll-*a* and differences between three MS/MS techniques. The formulae and likely structures of the characteristic fragment ions are proposed as well.

6.2 Experimental section

6.2.1 Chemicals

Chlorophyll-*a* from spinach was purchased from Sigma-Aldrich, Gillingham, U.K.. Acetone was obtained from Acros organics (New Jersey,

USA). For mass spectrometric analysis, chlorophyll-*a* was dissolved in acetone/water (7:3) to a final concentration of ~1 μ M. ESI tuning mix (Product No: A182611, Agilent Technologies, USA) was diluted 200 times in 50:50 methanol/water with 1% formic acid before use.

6.2.2 Mass spectrometry experiments

All mass spectrometry experiments were carried on a Bruker 12 T solariX FTICR mass spectrometer (Bruker Daltonik, GmbH, Bremen, Germany) with a homemade nano-electrospray ion source; an infrared laser was used for IRMPD experiments. A 4 M data point time-domain transient was acquired using a broadband sweep excitation providing a m/z range from 200 to 2500 and a theoretical resolving power of 530,000 at m/z 400. To achieve a desirable S/N and spectral quality, up to 200 scans were averaged on all MS/MS experiments. For CAD, using argon as the collision gas, the parent ions were isolated (with a 3-5 Da window) in the first quadrupole (Q_1) and then fragmented in a collision cell; fragments were finally detected in the ICR infinity cell.¹¹⁰ The collision energy was optimized from 15 to 65 V, and 22 V was selected for the final analysis. In the EID experiment, the isolated ions were accumulated externally in the collision cell for 3 s and then transferred to the ICR cell. Trapped ions were irradiated with electrons from a 1.7 A heated hollow cathode under optimized bias voltage and pulse length (12.2 eV, 0.096 s). IRMPD experiments were carried out in the ICR cell by exposing ions to a CO₂ laser beam (75 W, ~10.6 μ m) with varying laser power (15%-30%) and duration (0.5-1 s). ESI tuning mix was run before every experiment to calibrate the instrument externally. All spectra were processed by Data Analysis software manually. By external calibration, the elemental

composition of most peaks can be identified within a mass error of 3 ppm using the Smartformula function in DataAnalysis.

6.3 Results and discussions

The protonated molecular ion $[M + H]^+$ ($C_{55}H_{73}O_5N_4Mg$ m/z 893.5425) was isolated and fragmented by CAD, IRMPD, and EID respectively. The spectra induced by all three MS/MS techniques are shown in Figure 6.2. Under CAD conditions, few fragments were generated, and their identification will be discussed later. More peaks would appear if the collision energy of CAD were increased, but the intensity of fragments in higher m/z ranges, e.g. 614.2, diminishes sharply as well (Figure E.1). Since some secondary fragmentation may be induced during this process, 22 V was chosen as the collision energy in the final experiment where the molecular ion still can be observed. In comparison, the EID and IRMPD spectra are much more abundant with extensive fragmentations in the lower m/z range.

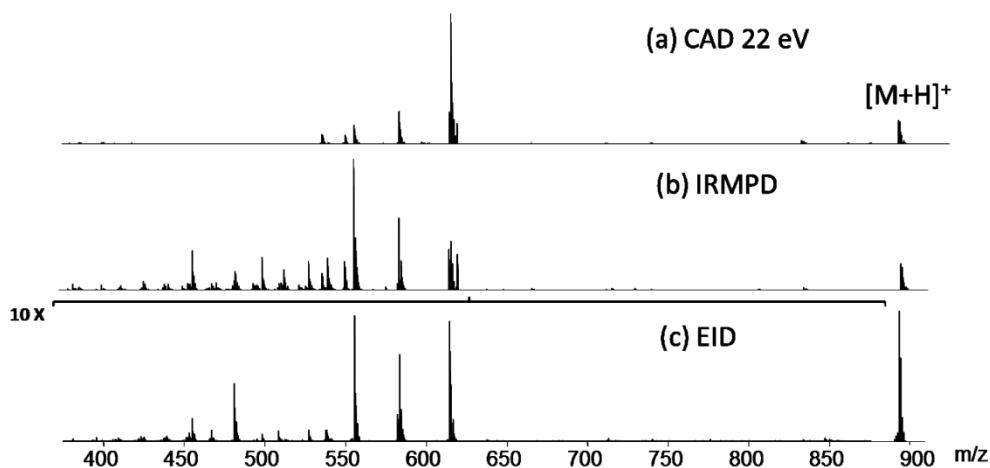


Figure 6.2 Fragmentation of singly-charged chlorophyll-a under conditions of (a) optimized CAD 22 V; (b) IRMPD with pulse length of 0.9 s and 30% pulse power; (c) EID 12.2 V for 0.096 s

6.3.1 Loss of the phytol group

The peak around m/z 614/615, which is the loss of the phytol group from the molecular ion, was named chlorophyllide-*a* ($C_{35}H_{34}O_5N_4Mg$) and can be used as the diagnostic peak of chlorophyll-*a*.^{300,308} Interestingly, with the help of FTICR MS, two peaks, one at m/z 614.2374 ($C_{35}H_{34}O_5N_4Mg$) and another peak at m/z 615.2452 corresponding to $C_{35}H_{35}O_5N_4Mg$, adjacent to the ^{13}C isotopic peak of m/z 614.2374, were both detected unambiguously by all three MS/MS methods when the peaks near m/z 614.2 were examined closely (see Figure 6.3, inset spectra were phased¹⁰⁴). The peak at m/z 614.2374 ($[M - \text{phytyl} + H]^+$) is most likely formed by cleavage between the phytol and ester oxygen. At the same time, one hydrogen migrates from the phytol chain to the main structure, leading to the peak at m/z 615.2452 ($[M - \text{phytyl} + 2H]^+$). With a resolution of $\sim 200,000$, the peak at m/z 615.2452 ($C_{35}H_{35}O_5N_4Mg$) can be separated from m/z 615.2408 ($^{13}CC_{34}H_{34}O_5N_4Mg$), which agrees with the speculation in Chait and Field's original work.³⁰² Overall, the esterifying phytol linkage is quite weak and easily broken. Normally, generating even-electron fragments from an even-electron molecular ion is highly preferred and thus recognized as the major case.³⁰⁹ Comparing the results in Figure 6.3, the relative intensity of $[M - \text{phytyl} + 2H]^+$ is always higher than $[M - \text{phytyl} + H]^+$ in CAD and IRMPD spectra which agrees with this prediction. However, a contrary result is presented in the EID spectrum below due to a different mechanism.

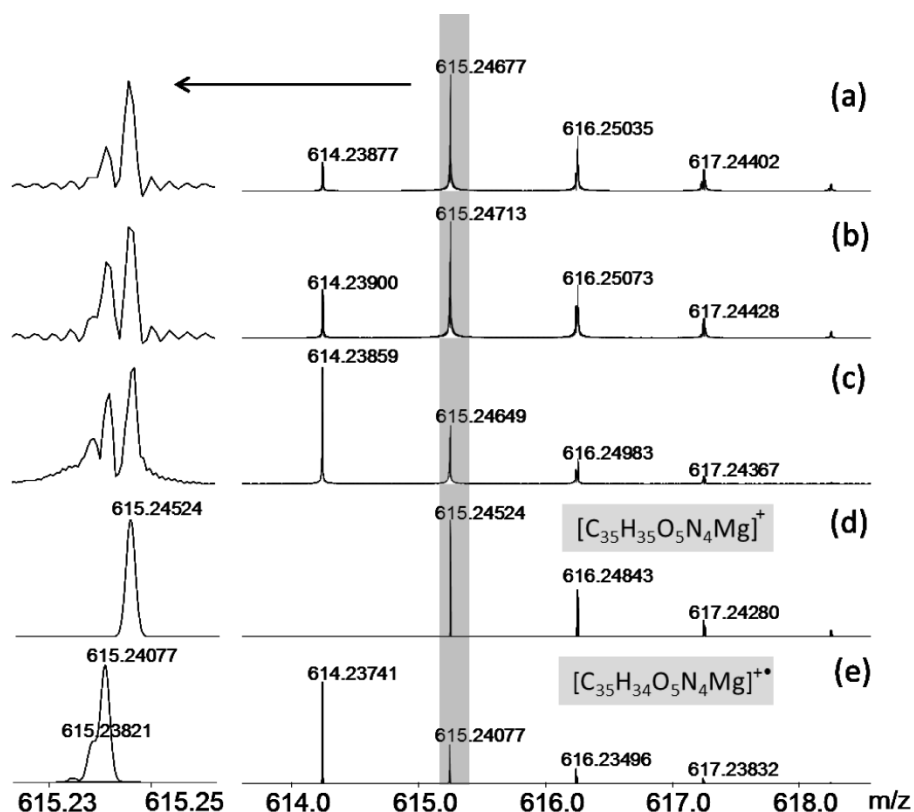
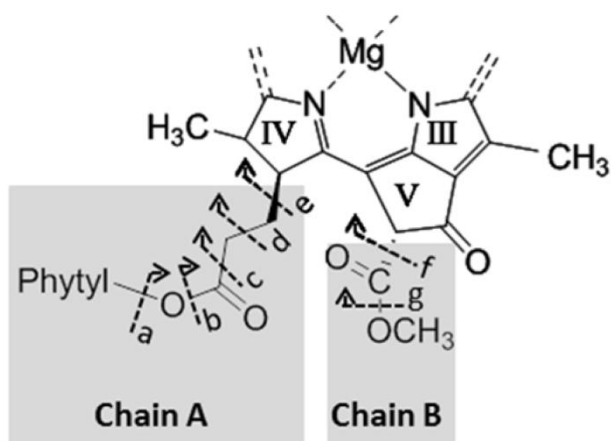


Figure 6.3 Expanded m/z region of 614-619 in Figure 6.2 (a) CAD; (b) IRMPD; (c) EID; (d) and (e) are simulations of $C_{35}H_{34}O_5N_4Mg$ and $C_{35}H_{35}O_5N_4Mg$, respectively. Inset on the left is the further zooming of m/z region of 615.2-615.3

6.3.2 Cleavages from long aliphatic chains

According to the molecular composition predicted from the exact mass value, a series of fragments are proposed from cleavages of the two aliphatic side chains (side chains in sites C-17 and C-29 are named chain A and chain B hereafter, which are highlighted in Scheme 6.1), and summarized in Table 6.1.



Scheme 6.1 Labelling the proposed cleavages sites of chain A and B in ring IV&V

Apart from the cluster around m/z 614.2, the other two high intensity peaks at m/z 583.2190 and m/z 555.2241 generated by all three methods are assigned to the loss of the phytol group and CH₃O/CH₃COO of the B chain respectively. Moreover, a range of peaks, which are also proposed from the cleavages from chain A and B, are identified. These peaks have a relatively higher intensity as well in EID and IRMPD spectra (Relative intensity can be found in Table E.1). The presence of this series suggests that the spatial positions of chain A and chain B may allow interaction, where cyclization could occur between the two cleavages sites due to their proximity.

Table 6.1 Summary of fragments proposed cleavages from Chain A & B

Proposed formula	Theoretical mass	EID ion (<i>m/z</i>) Internally calibrated	Error (ppm)	CAD ion (<i>m/z</i>) Internally calibrated	Error (ppm)	IRMPD ion (<i>m/z</i>) Internally calibrated	Error (ppm)	Proposed cleavage
C ₃₅ H ₃₅ O ₅ N ₄ Mg	615.2452	615.2453	0.16	615.2454	0.32	615.2456	0.65	a
C ₃₅ H ₃₄ O ₅ N ₄ Mg*	614.2374	614.2374	---	614.2374	---	614.2374	---	a- H•
C ₃₄ H ₃₁ O ₄ N ₄ Mg*	583.2190	583.2190	---	583.2193	---	583.2191	---	ag
C ₃₄ H ₃₀ O ₄ N ₄ Mg	582.2112	582.2112	0	582.2114	0.34	582.2113	0.17	ag - H•
C ₃₃ H ₃₁ O ₃ N ₄ Mg	555.2241	555.2240	-0.18	555.2242	0.18	555.2243	0.36	af
C ₃₃ H ₃₁ O ₂ N ₄ Mg	539.2292	539.2292	0	539.2290	-0.37	539.2294	0.37	bf/cg
C ₃₃ H ₃₀ O ₂ N ₄ Mg	538.2214	538.2213	-0.19			538.2216	0.37	bf/cg - H•
C ₃₂ H ₂₉ ON ₄ Mg	509.2186	509.2184	-0.39			509.2189	0.59	cf - H ₂
C ₃₁ H ₂₅ O ₂ N ₄ Mg	509.1822	509.1823	0.20					eg - H ₂
C ₃₂ H ₂₈ ON ₄ Mg	508.2108	508.2108	0			508.2110	0.39	cf - H ₂ - H•
C ₃₁ H ₂₇ ON ₄ Mg	495.2030	495.2030	0			495.2035	1.01	df - H ₂
C ₃₀ H ₂₅ ON ₄ Mg*	481.1873	481.1873	---	481.1873	---	481.1878	---	ef - H ₂
Average			0.03		0.12		0.33	
SD (σ)			0.17		0.29		0.47	

* Peaks used as internal calibrants

Cleavage preference among the different bonds of side chain A and B are summarized on the basis of the fragments detected and their relative intensity (Table 6.1 and Table E.1). Comparatively, cleavages from sites 'a', 'f', 'e', are preferred (Scheme 6.1). As described, site 'a' between the ester group and phytol chain is most fragile. Sites 'e' and 'f' which are adjacent to the conjugated macrocyclic ring also contribute to several intense peaks. This order generally follows the bond strength information provided by crystal x-ray experiments of chlorophyllide-a dihydrate.³¹⁰ Additionally, loss of H₂ was detected almost universally. This loss is most likely from C-17 and C-18 of ring IV (Figure 6.1), leading to a larger conjugated structure which is thermodynamically favourable.

Though similar peaks were formed with EID, IRMPD, and CAD, more radical ions were generated by EID after detailed assignment of the fragments described above (Figure 6.3 and Figure 6.4). As expected, cleavages leading to radical ions are more common during EID than CAD and IRMPD, due to the combination of vibrational excitation and electronic excitation.⁷⁰ However, odd-electron fragments are also observed in IRMPD, and at very low abundance in CAD as well. Figure 6.5 shows the abundance change of several odd-electron species with increasing the laser power in IRMPD. Although the relative abundance of these species is still quite low compared to their abundance in EID, it increases with increase in laser influence. The observation of these unusual odd-electron species in CAD and IRMPD spectra of chlorophyll-a may be related to a structural property of the macrocyclic ring, as a similar phenomenon was observed in octaethylporphyrin using low energy CAD in Rosario's work.³⁰⁶ Additionally,

considering the discovery of ECD was because of an UV photodissociation experiment, where secondary electrons were emitted by UV photons and lead to fragmentation.⁶⁰ In the IRMPD experiment, it is unlikely that secondary electrons are formed by IR photons, but the intensity of EID-like odd-electron fragments suggests otherwise, and the overall intensity of all fragments is 10 times higher in the IRMPD spectrum than in the EID spectrum. Further experimental and computational investigations are necessary to understand the results.

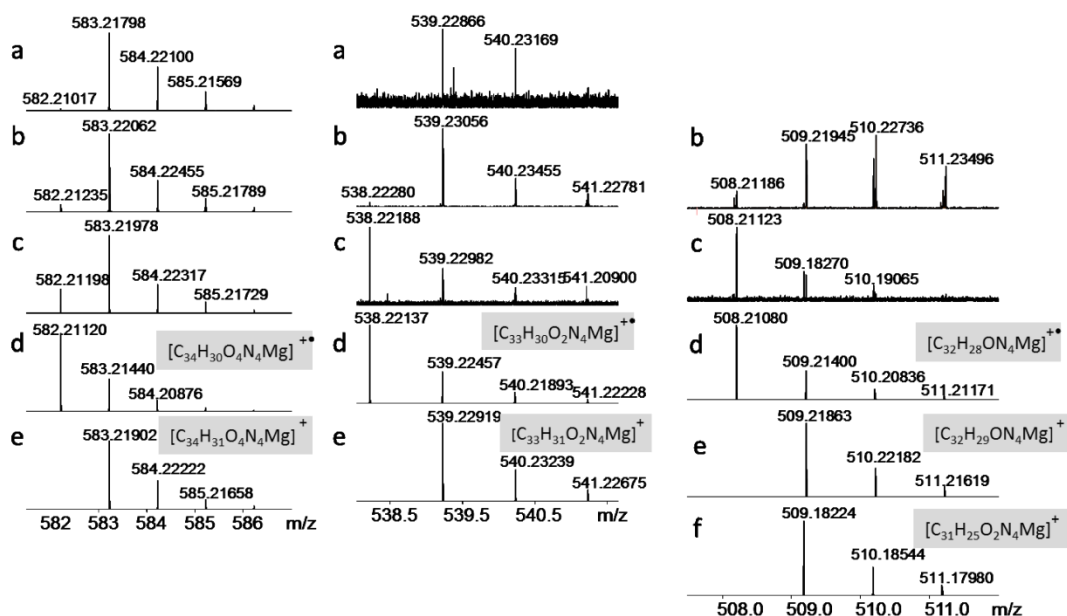


Figure 6.4 From left to right are expansions of m/z regions 582-586, 538-541 and 508-511 (a) CAD; (b) IRMPD; (c) EID; d-f are the corresponding simulations of the elemental compositions in the highlight regions respectively

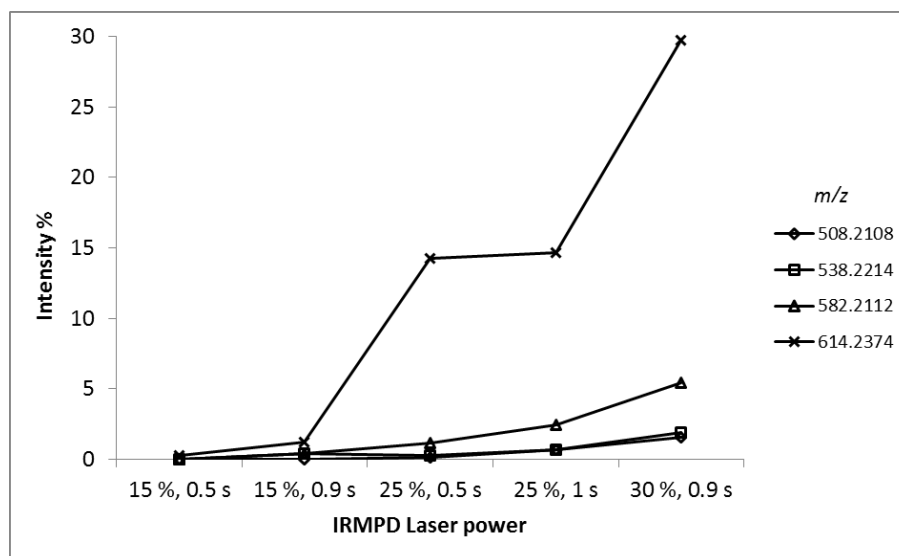


Figure 6.5 Plotting of intensity changes of several radical ions according to the laser power in IRMPD

Two low intensity peaks at m/z 833.5215 ($C_{53}H_{69}O_3N_4Mg$) and m/z 541.2085 ($C_{32}H_{29}O_3N_4Mg$) (Table E.2), repeated in the EID and IRMPD spectra, are interesting. The peak at m/z 833.5215 seems to be the only product ion detected between m/z 614 and m/z 893 from chlorophyll-*a*. As proposed, this peak can be assigned to the facile losses of side chain B and one H atom from C-29 from the protonated molecular ion.³¹¹ In addition, losses of chain A and the H atom from C-18, resulting in a double bond between C-17 and C-18, is speculated to generate the peak at m/z 541.2085. Otherwise, no extensive cleavage within the phytol chain was detected in these experiments. As an unidentified doubly-charged impurity, which has a similar m/z (893.7459) with chlorophyll-*a*, was isolated together with our target ion; several fragments were induced from it as well. However, based

on the charge state and accurate mass value, most of the peaks from the impurity can be distinguished.

In addition to fragments from the cleavages of two long side chains, several peaks that are probably from cleavages of ring V or rearrangements are present (Table E.2). In particular, the high intensity peak at m/z 455.2081 ($C_{29}H_{27}N_4Mg$) (Figure E.2), whose formula suggests all five oxygen atoms are lost from the molecular ion, along with its elemental composition further implying that ring V is probably cleaved.

6.3.3 Extensive cleavages

As extensive fragmentation from chlorophyll-*a* was induced by EID and IRMPD (Figure 6.6), losses of small side groups successively, such as $-CH_3$, $-C_2H_5$ etc., are most likely the reason for regular patterns in the lower mass range. Detailed analysis of these patterns showed that two different groups of peaks were detected in every pattern. One series retains an oxygen atom in the structure which is proposed to be the one from the keto group in ring V, while the other series has no oxygen. The mass difference between the two groups is the difference between CH_4 and O, which is about 36.4 mDa. Additionally, according to the relative abundance of these two group peaks, it seems the oxygen atom (or the whole keto group) in ring V is more easily lost in the IRMPD experiment than during EID. Interestingly, the peak at m/z 455.2081 ($C_{29}H_{27}N_4Mg$) with a very high intensity in the IRMPD spectrum is also consistent with this phenomenon. As a light harvesting pigment, chlorophyll-*a* absorbs strongly in the IR region³¹² which is important for photosynthesis.²⁸⁸ The infrared absorption spectra of chlorophyll-*a*^{313,314}

show a strong series of absorption bands from 5-12 μm which overlaps with the wavelength range of CO_2 laser (around 10.6 μm). This may be the reason why more extensive fragmentation was generated by IRMPD than by CAD, as well as why it showed different preference for cleavage from ring V compared to EID. It is worth mention that EID was reported to produce far more fragments of glycosaminoglycans than IRMPD in Wolff's work.⁷⁹ To contrast, the abundant IRMPD spectrum of chlorophyll-*a* is clearly a different situation. Thus, it is safe to propose that, in addition to the dominating influence of different mechanisms between MS/MS methods, the efficiency of fragmentation also depends a lot on the character of parent ions.

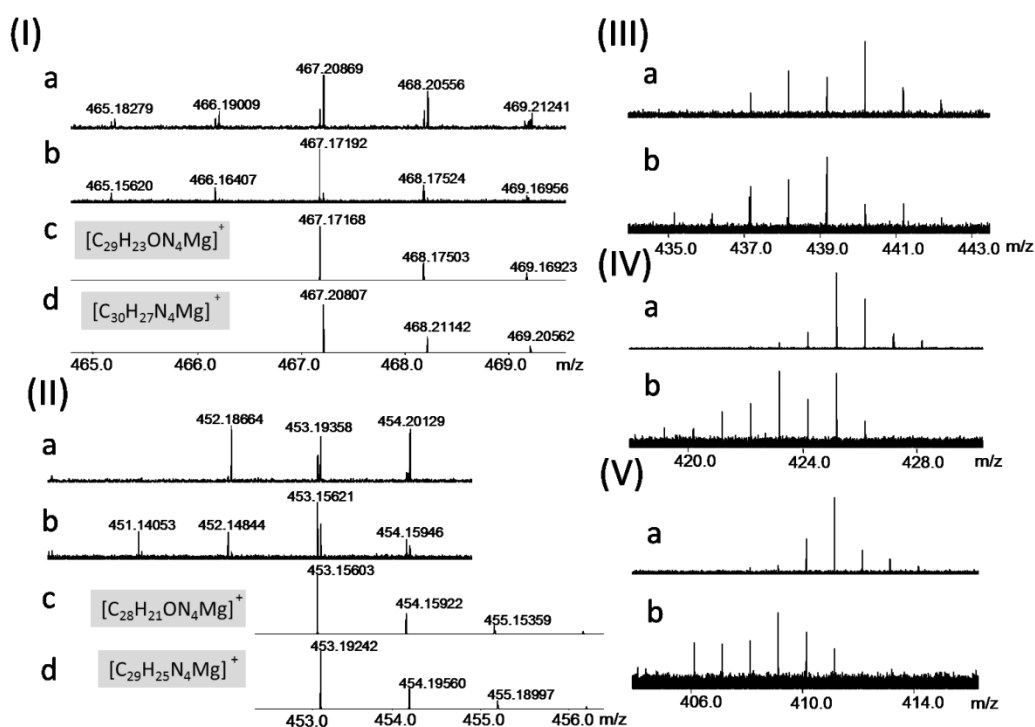


Figure 6.6 (I–V) Representative expanded spectra of several lower m/z regions (a) IRMPD; (b) EID; (c) and (d) are the corresponding simulations of the elemental compositions in the highlight regions respectively

Finally, looking into the spectra III–V in Figure 6.6, the whole pattern in EID is clearly shifting to lower mass regions by several Daltons compared to the same ranges in IRMPD. These whole number differences can be accounted for by a series of H[•] losses from the porphyrin ring. As this phenomenon only appears obviously in the lower *m/z* range, the H[•] loss from the main ring seems less favourable than aliphatic chain cleavages.

6.4 Conclusions

To explore the structural stability of chlorophyll-*a* and provide bond cleavage information for its degradation research, high resolution MS/MS was used. Apart from traditional MS/MS techniques, CAD and IRMPD, the recently developed EID method, is also employed in this study. Generally, similar patterns of peaks are obtained in the higher *m/z* range in all three spectra, and extensive fragmentation of chlorophyll-*a* is produced by EID and IRMPD. Under low collision voltages, CAD can only provide limited information. EID generates many more cleavages including many radical ions, and loss of H[•] from the macrocyclic ring. The extensive cleavage of EID is likely due to a different fragmentation mechanism and the strong absorption in IR region of chlorophyll-*a* can likely explain the abundant IRMPD fragments.

Utilizing the high resolution and mass accuracy provided by the FTICR mass spectrometer, most of the fragments can be identified. Some of them, such as two groups close to each other in the lower *m/z* range, are reported unambiguously for the first time. The high mass accuracy allows calculation of exact elemental compositions for these fragments which also allows bond cleavage preference to be proposed. The ester linkage is the weakest link

leading to abundant fragment ions, followed by loss of the two aliphatic side chains, especially at sites 'f' and 'e' in Scheme 6.1. Extensive cleavages of small side groups of chlorophyll-*a* are generated by EID and IRMPD. Particularly, ring V seems more unstable in IRMPD. Loss of H₂ from ring IV suggests that cleavage leading to increased conjugation is energetically favourable in MS/MS processes.

Overall, the MS/MS experiments using the FTICR mass spectrometer, in particular EID and IRMPD, provided abundant structural information of chlorophyll-*a*. This experiment can be easily applied for other porphyrin-like compounds and their metal complexes. More techniques, particularly computational, are required to provide a complete understanding of the cleavage site and mechanism channels.

Chapter 7 Structural characterization of pheophytin-a

7.1 Background

Porphyrins are recognized as the pigments of life. Due to the big conjugated structures and biological significance, porphyrins and metalloporphyrins have many applications in research and industry.^{315,316}

The MS/MS behaviour of chlorophyll-a was studied in the last chapter, and some interesting results were obtained. A recent study reported that the first step of the degradation of chlorophyll-a is loss of the central Mg^{2+} ion, generating pheophytin-a (structure in Figure 7.1),³¹⁷ which compound also serves as an important intermediate in the photosystems. In order to fully understand the chlorophyll degradation, an effective strategy to identify the relevant metabolites is of significant importance.

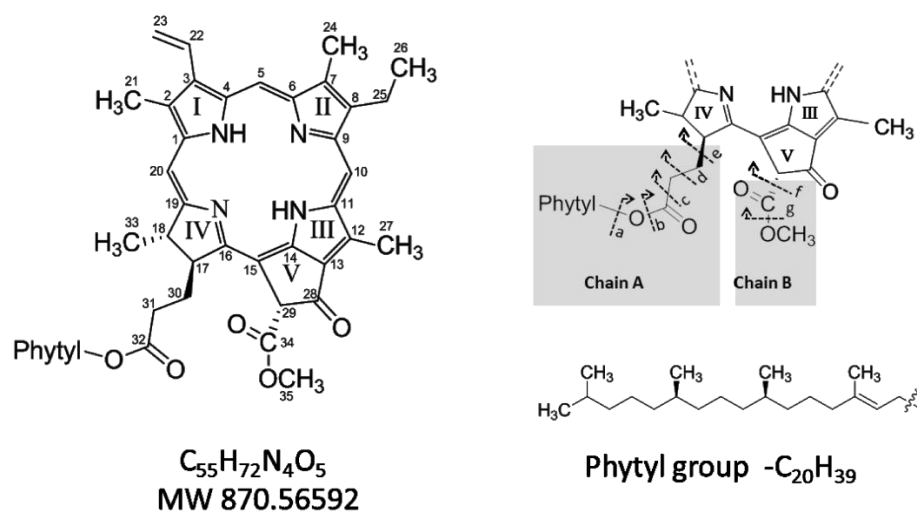


Figure 7.1 Structure of pheophytin-a. Chain A, Chain B, and phytol group are illustrated.

One of the crucial features of chlorophylls is the functional versatility that a single compound can be involved in several diverse photosynthesis processes and performs different functions.³⁰⁸ Moreover, the structural versatility is another character of porphyrins and chlorophylls, where, based on the macrocycle ring, derivatives may have different central metal ions or/and side chains. Some derivatives of chlorophylls are listed in Figure 7.2. To further investigate the fragmentation pattern of pheophytin-a using MS/MS is of benefit for the study of porphyrin related molecules. By comparing the MS/MS results of chlorophyll-a and pheophytin-a, the influence of subtraction of the Mg^{2+} ion on fragmentation will be determined, and some structural information may show the stability of the pigment macrocycle without a central metal ion.

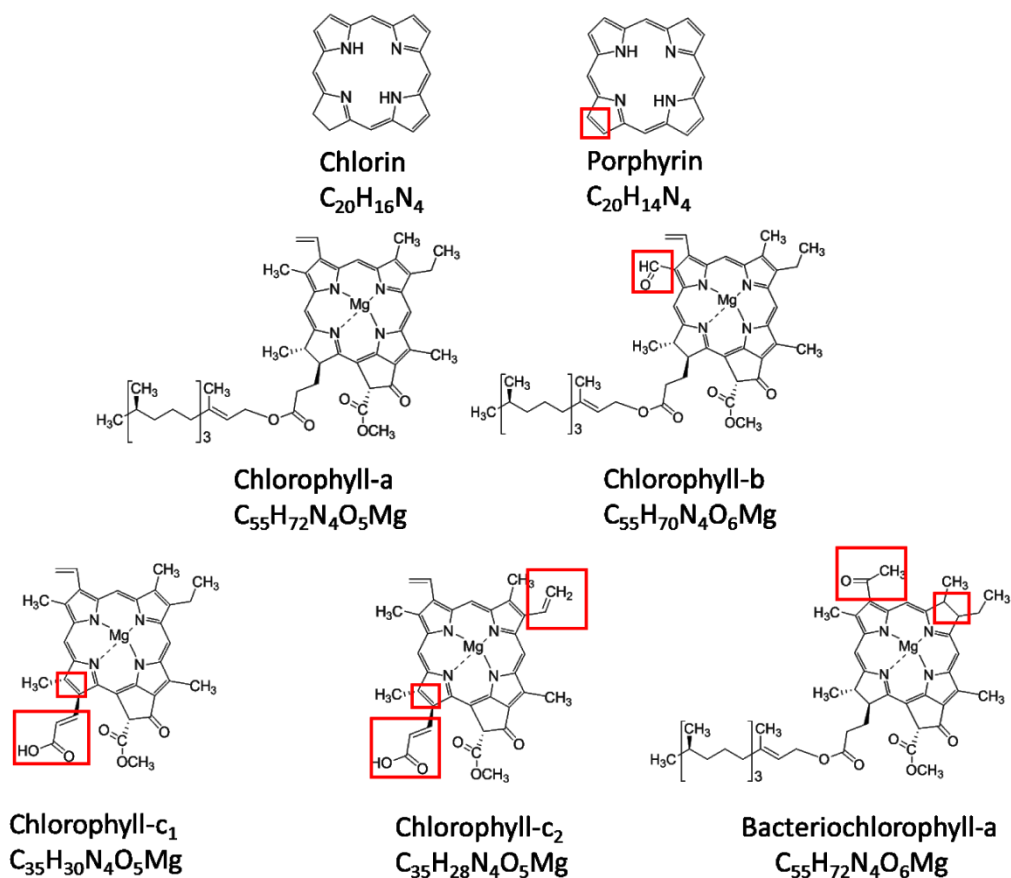


Figure 7.2 List of the structural formulae of several derivatives of porphyrin and chlorophylls. Red boxes highlight the regions of difference among each structure.

7.2 Experimental section

Pheophytin-a is produced by dissolving chlorophyll-a in 50:50 methanol/water with 1% formic acid.

The collision energy was optimized from 0-70 V for the CAD experiments, and 32 V was used. In the EID experiment, trapped ions were irradiated with electrons from a 1.5 A heated hollow cathode under optimized

bias voltage and pulse length (19.5 eV, 0.2 s). IRMPD experiments were carried out in the ICR cell by exposing ions to a CO₂ laser beam (75 W, ~10.6 μm) with varying laser power (20%-80%) and duration (0.1-0.7 s).

7.3 Results and discussions

In solution, the central Mg²⁺ ion in chlorophyll-*a* is labile and could dissociate easily in acid environment, replaced by two H⁺ and generating pheophytin-*a*. Figure 7.3 shows the spectra of chlorophyll-*a* in methanol/water without (top) and with formic acid (bottom) respectively. Almost all of the chlorophyll-*a* molecules turn into pheophytin-*a* when 1% formic acid is added in the solution (Figure 7.3b), and it greatly facilitates applying following MS/MS experiments. Having an elemental composition of C₅₅H₇₂O₅N₄Mg, chlorophyll-*a* is of a molecular weight of 892.53531 Da, and pheophytin-*a* has a formula of C₅₅H₇₄O₅N₄ and a mass of 870.56592 Da.

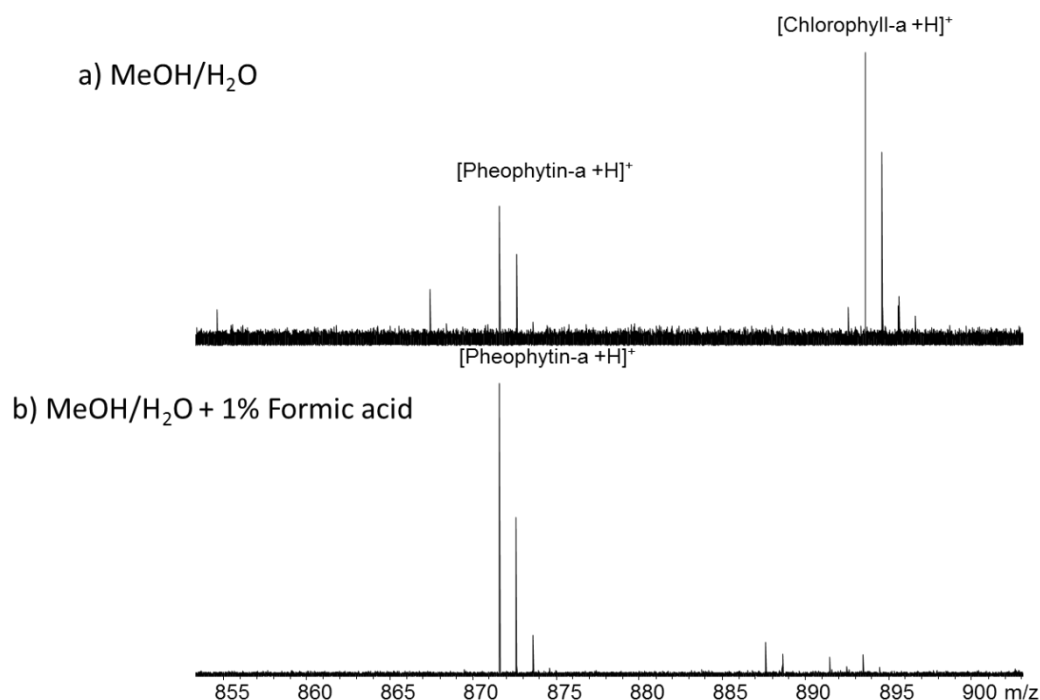


Figure 7.3 MS spectra of chlorophyll-a in a) 50/50 (V/V) methanol/water and b) 50/50 (V/V) methanol/water with 1% Formic acid

For chlorophyll-a, three MS/MS methods produced some similar fragments, but extensive fragmentation was only observed in the EID and IRMPD experiments. In terms of fragmentation efficiency or abundance of fragments, IRMPD yielded fragments of ~10 times intensity compared to fragments in EID spectrum, and which was proposed to be due to the red absorption of chlorophyll-a. In comparison, the MS/MS experiments of pheophytin-a show some similar results, but differences also exist. Singly protonated pheophytin-a, at m/z 871.57320, is used for the MS/MS study, and the CAD, EID and IRMPD spectra of pheophytin-a are shown in Figure 7.4.

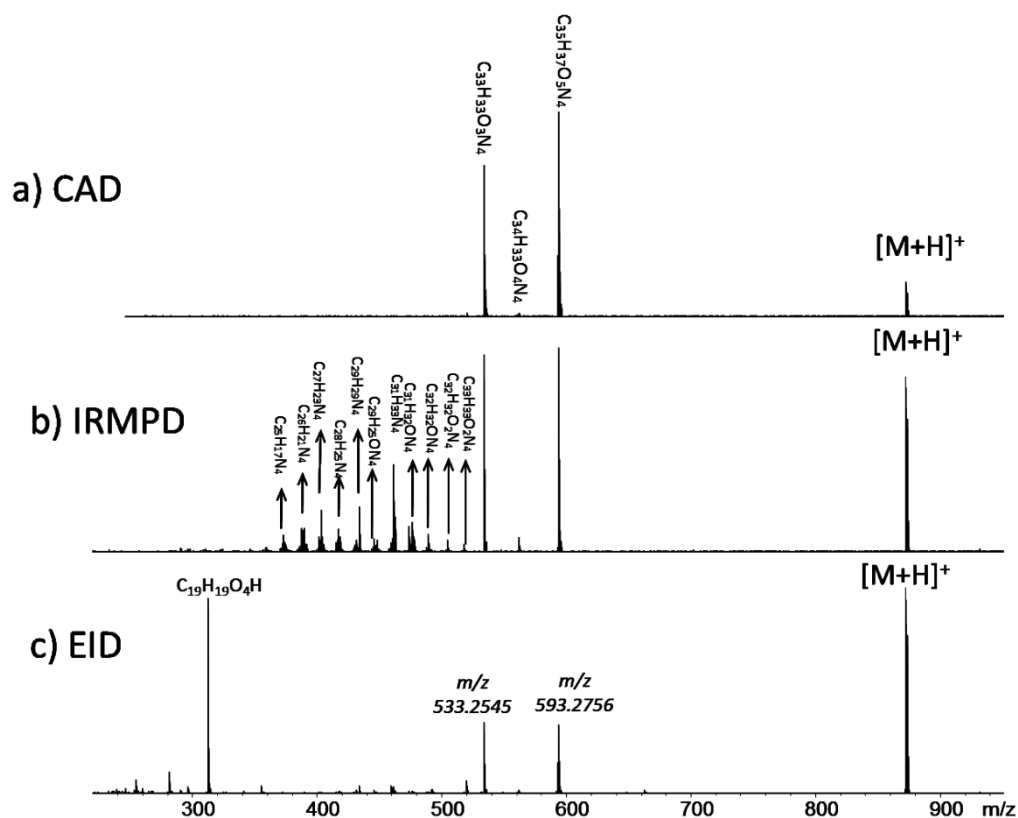
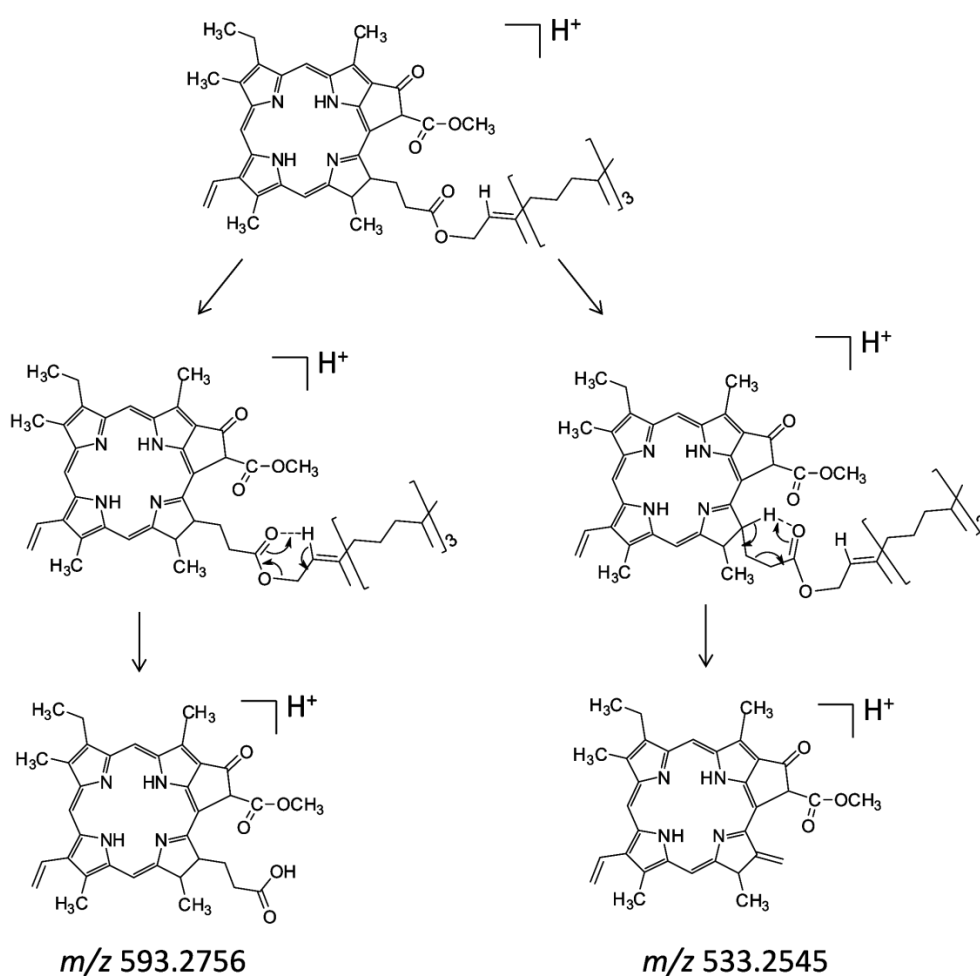


Figure 7.4 a) CAD, b) IRMPD, c) EID MS/MS spectra of singly-charged pheophytin-*a*

7.3.1 CAD spectra of pheophytin-*a*

In the CAD spectrum of pheophytin-*a* in Figure 7.4a, in addition to the precursor, two more peaks of high intensity are detected at m/z 593.2756 and m/z 533.2545, which are also two of the most abundant fragments in the EID and IRMPD spectra. The fragment at m/z 593.2756 is assigned from a cleavage between the phytol and ester oxygen along with one hydrogen atom migrating from the phytol chain to the main structure, which is likely realized through a six member ring rearrangement as illustrated in Scheme 7.1. The peak at m/z 533.2545 could be induced by a similar rearrangement but from

the γ -hydrogen at C-17 (Scheme 7.1); however this m/z can also arise from loss of the phytol chain and the side chain in ring V, so both mechanisms may exist in practice. The high abundance of these two fragments in all three MS/MS spectra in Figure 7.4 shows that the even-electron γ -hydrogen rearrangement is a prevalent channel in this case.



Scheme 7.1 Proposed mechanisms for the formation of peaks at m/z 593.2756 and m/z 533.2545

Meanwhile, a peak from the direct cleavage between the phytol and the ester oxygen is detected, which differs from the peak at m/z 593.2756 by one hydrogen atom. With a resolving power of $\sim 500,000$ at m/z 593 in the experiment, the ^{13}C -substituted peak of $\text{C}_{35}\text{H}_{36}\text{O}_5\text{N}_4$ is distinguished from the $\text{C}_{35}\text{H}_{37}\text{O}_5\text{N}_4$ peak by a mass difference of 4.5 mDa (Figure 7.5). The coexistence of the odd-electron species at m/z 592.2680 and the even-electron species at m/z 593.2756 from loss of the phytol group was also observed for chlorophyll-*a* in Figure 6.3, but the relative intensity of the two species is different between chlorophyll-*a* and pheophytin-*a*. For pheophytin-*a*, ratios of the intensity of the peak at m/z 592.2680 and the peak at m/z 593.2756 in EID, IRMPD, and CAD are 45%, 2%, and 33%, respectively, while for chlorophyll-*a*, the corresponding values are 200%, 42%, and 25%. The odd-electron species seems more abundant in the MS/MS spectra of chlorophyll-*a*, which suggests the structure is more tolerant to free radicals in the presence of the Mg^{2+} ion.

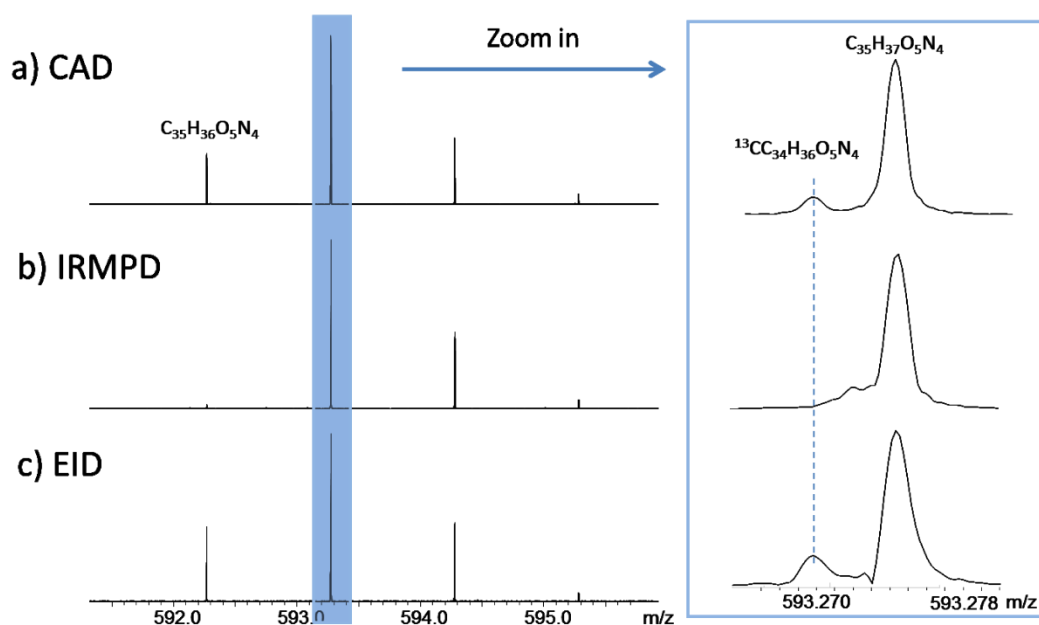


Figure 7.5 The expanded regions from m/z 591-596 in Figure 7.4 a) CAD, b) IRMPD, c) EID MS/MS spectra of singly-charged pheophytin-a

In addition, another abundant fragment ($C_{34}H_{31}O_4N_4M_g$, m/z 583.2190) in the m/z region above 500 detected for chlorophyll-*a* in Figure 6.2 from loss of phytol group and a $-CH_3O$ is almost absent in the MS/MS spectra of pheophytin-*a*. Though a peak at m/z 561.2496 ($C_{34}H_{33}O_4N_4$) corresponding to the cleavage of phytol group and a $-CH_3O$ is observed in Figure 7.4, the intensity is lower than most of the other peaks (Table F.1). Moreover, the only other fragment detected under current CAD condition is a small peak at m/z 533.2545.

7.3.2 IRMPD spectra of pheophytin-a

Figure 7.4b is the IRMPD result of pheophytin-*a*, where much more peaks are present in the region of m/z 280-520 compared to the CAD and EID

spectra in Figure 7.4a and c. The abundant IRMPD spectrum of pheophytin-*a* resembles the IRMPD spectrum of chlorophyll-*a* in Figure 6.2b with extensive cleavages from side groups and ring V observed. According to some fragments detected in *m/z* lower than 350 shown in Figure 7.6c, it seems that even more extensive cleavages possibly from pyrrole groups are produced by pheophytin-*a*, because there are only three nitrogen atoms left in these fragments. The smallest mass assigned in Figure 7.6 has a formula of $C_{19}H_{12}N_3$, and even smaller fragments can be produced by increasing laser power and/or pulse length (Figure 7.7b). As shown in Figure 7.2, the chlorin ring, the basic macrocycle ring without any side chains/groups, has an elemental composition of $C_{20}H_{16}N_4$ (*MW*: 312.1375 Da). Therefore, the fragments in low *m/z* in the IRMPD spectrum are likely from cross-ring cleavages from the chlorin ring. In contrast to pheophytin-*a*, no fragments from cleavages of the chlorin ring were observed from the MS/MS, including EID, IRMPD, and CAD, spectra of chlorophyll-*a*. A comparison of the IRMPD spectra of chlorophyll-*a* and pheophytin-*a* exposed to the same laser power and pulse length in Figure 7.7 shows that much more fragments smaller than *m/z* 300 are produced by pheophytin-*a*, but no fragments are detected for chlorophyll-*a*. An investigation on the influence of the central Mg^{2+} ion on the structures of chlorophylls reveals that removal of the metal ion increases the flexibility of the macrocycle.³⁰⁸ The IRMPD results in Figure 7.7 also suggest that the macrocycle of pheophytin-*a* in the absence of the central Mg^{2+} ion is more fragile compared to chlorophyll-*a*.

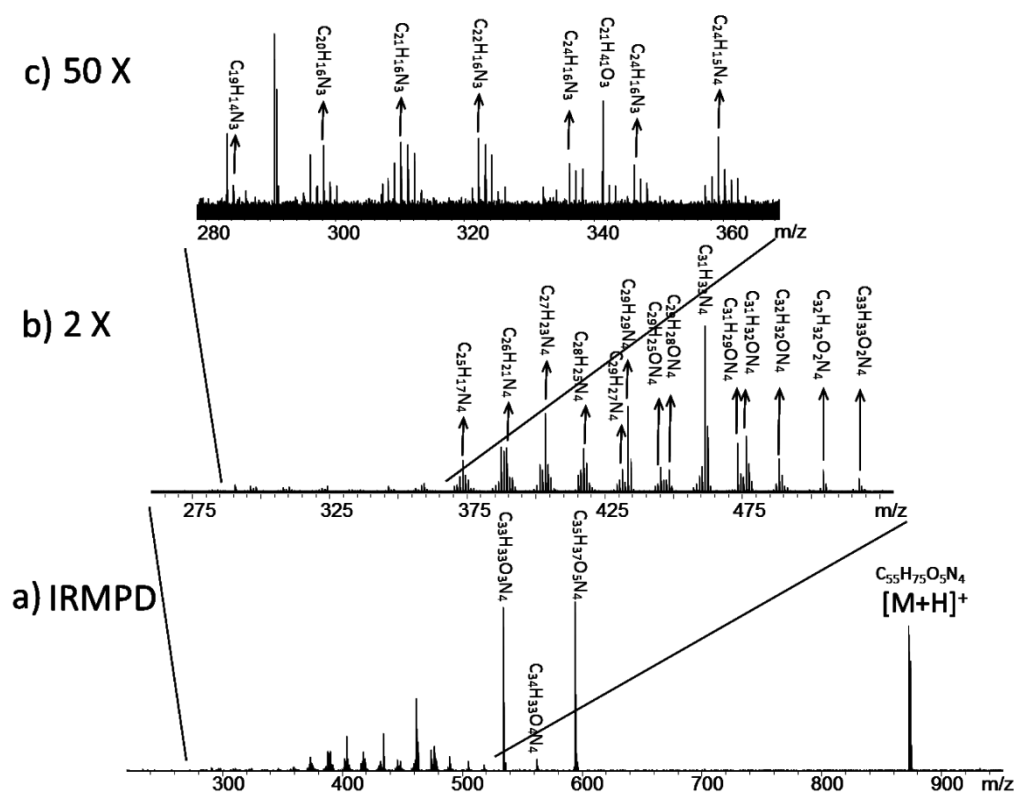


Figure 7.6 Extensive fragmentation of pheophytin-a in IRMPD spectrum (70% laser power and 0.2 s pulse length). Peaks assignment is in Table F.1

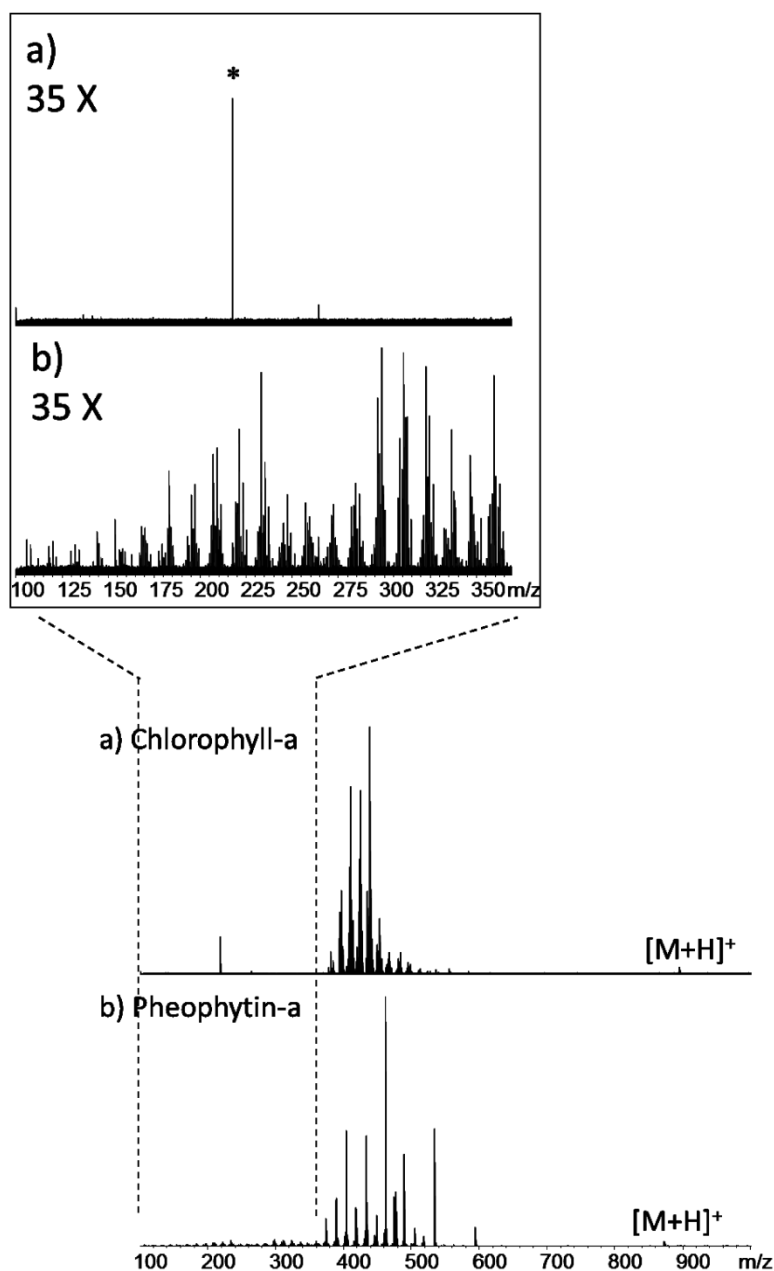


Figure 7.7 IRMPD spectra of a): chlorophyll-a and b): pheophytin-a with 70% laser power and 0.5 s pulse length. Insets in the square are expanded regions from m/z 100-350. Peaks with asterisk are harmonics or noise

Based on the MS/MS results in Chapter 6 and this chapter, IRMPD is demonstrated to be the most effective method in fragmenting both

chlorophyll-*a* and pheophytin-*a* by producing most abundant and extensive fragments. Even though, due to extensive side chain cleavages and the symmetrical structure of the chlorin ring, it is still difficult to assign all of the fragments in the low m/z region to the exact side group loss, IRMPD displays the potential to be a useful technique in studying the structures of porphyrin like components. Additionally, inducing isotopic labelling, such as ^2H , ^{13}C , or ^{18}O , would be a useful strategy to nail down the detail assignment of the fragments in the MS/MS spectrum, assisting the interpretation of the fragmentation channels. Comparing the fragmentation of chlorophyll-*a* or pheophytin-*a* to the fragmentation of some derivatives such as chlorophyll-*b* (Figure 7.2) or pheophytin-*b*, where only one or two substitutes are different, could also help understanding the fragmentation mechanisms.

One of the most likely reasons that IRMPD is effective in fragmenting chlorophyll-*a* and pheopytin-*a* is that both of the two molecules have strong absorptions in the region around 10.1 μm due to the vinyl C-H (at C-3) bending vibration,³¹³ where the CO_2 laser used in the IRMPD experiments has a wavelength band centred at $\sim 10.6 \mu\text{m}$, so that strong infrared absorption during the laser irradiation could happen. Additionally, because the experimental pulse length of the IRMPD process is in the range of several hundred milliseconds, it is possible that this time scale allows fragments having a strong absorption of the CO_2 laser to absorb IR photons successively and yield secondary fragmentation. In contrast, for CAD experiments, the internal energy of molecules accumulated during the collision process is released after fragmentation and the fragments can hardly gain sufficient energy for further fragmentation. This hypothesis could explain

the CAD and IRMPD spectra in Figure 7.4a and Figure 7.4b that much fewer fragments are detected in the CAD spectrum in low m/z . Moreover, increasing the collision energy in CAD (from 32 V to 62 V shown in Figure F.1) causes more peaks in the low m/z to appear, but the intensity of the fragments in the high m/z ranges drops significantly. The changes of peak intensity in high m/z and low m/z when ramping up the collision energy also indicate secondary fragmentation may be induced in CAD under higher collision energy and during IRMPD.

Another hypothesis to explain the abundant IRMPD spectrum is based on the observation of ubiquitous odd-electron fragments produced from both chlorophyll-*a* and pheophytin-*a*, where the unique macrocyclic structure displays a good tolerance to radicals particularly in the presence of the central Mg^{2+} . Therefore, followed by the formation of those radical ions, secondary fragmentation induced by free radical rearrangements is also possible.^{59,318} In addition, radical-driven dissociation has been extensively investigated in recent years.³¹⁸ However, the fact that odd-electron species were generated by protonated chlorophyll-*a* and pheophytin-*a* ions in IRMPD and CAD in the first place is interesting. Though the formation of odd-electron fragments from even-electron precursors does not follow the ‘even electron rule’,³¹⁹ exceptions have been observed in low energy CAD experiments.³²⁰⁻³²⁴ In particular, almost all of the molecules that have been reported to violate this rule contain an aromatic ring or a big conjugated structure, and computational studies showed that the stabilization of the radical can facilitate the formation the odd-electron fragments.^{321,324} In this case, the macrocycle of a large

conjugated structure is very likely the most important reason for the formation of the odd-electron species.

7.3.3 EID spectra of pheophytin-a

In the EID spectrum of pheophytin-a (Figure 7.4c), the most abundant fragment is an odd-electron species at m/z 312.1356 with an elemental composition of $C_{19}H_{19}O_4H$. The formula suggests that there is no nitrogen atoms left in the structure, but it still has four oxygen atoms and 10 DBE, which indicates multiply bonds cleavages from ring III and ring IV (Figure 7.1) and also a cleavage in the phytol chain. The cross-ring cleavage from the macrocycle along with eliminating two nitrogen atoms from pyrrole groups, which was not observed from CAD and IRMPD, is also unexpected in EID because more than four bonds have to be cleaved to form this fragment. Rearrangement is likely involved for the formation of $C_{19}H_{19}O_4H$, but the exact mechanism is not clear. Further EID/SORI-CAD MS³ did not provide any more information on this fragment.

Some small fragments are also produced and detected in the EID spectrum. The one at m/z 519.2385 having an elemental formula of $C_{32}H_{31}O_3N_4$ is proposed from loss of the chain A and a hydrogen atom at C-18, yielding a double bond between C-17 and C-18, which leads a larger conjugated structure. Some other small ions are likely from the extensive cleavages from Chain A and B, and ring V (Table F.1).

7.4 Conclusions

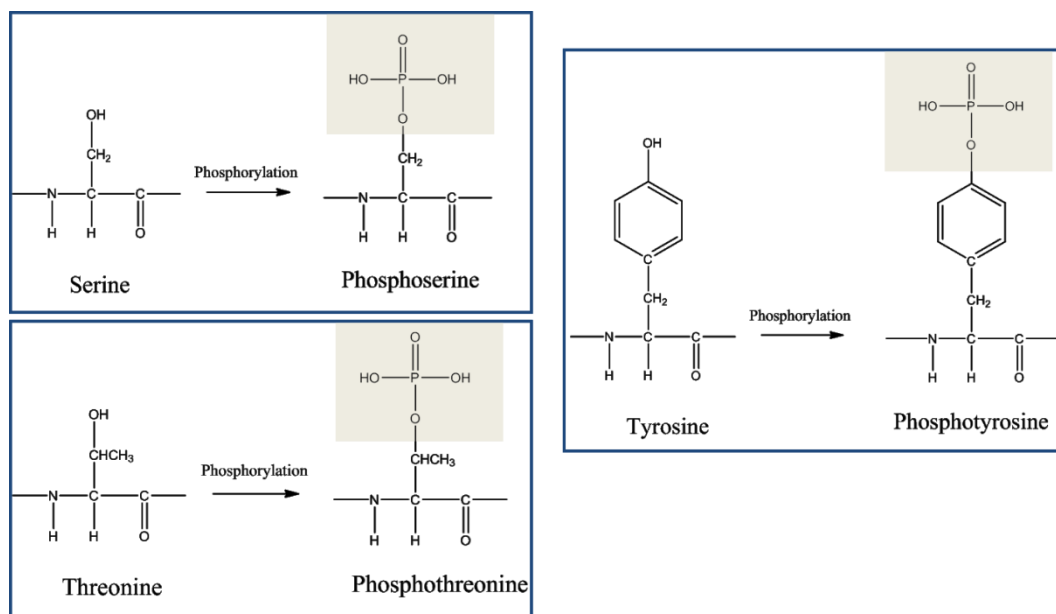
For pheophytin-*a*, some similar fragments of high abundance from the cleavage of the phytol group were detected from all three MS/MS methods, CAD, EID, and IRMPD. Most abundant and extensive fragments were observed in the IRMPD spectrum, which is also the case for chlorophyll-*a*. EID of pheophytin-*a* shows differences from that of chlorophyll-*a*, where the most intense peak detected for pheophytin-*a* has no nitrogen atoms left indicating multiply bonds cleavages from the macrocycle. On the other hand, the EID spectrum of chlorophyll-*a* resembles its IRMPD spectrum. The difference could only because of the central Mg^{2+} ion. CAD is not as effective as IRMPD in generating extensive fragmentation for both molecules. Odd-electron species are observed from both chlorophyll-*a* and pheophytin-*a* in CAD, IRMPD, and EID, so the unique macrocycle structure has the capability to stabilize radicals. In some extent, the abundant IRMPD spectra could be explained by the strong absorption of the two molecules in the CO_2 laser wavelength range. Fragments from cleavages of the pyrrole groups suggest that the chlorin ring of pheophytin-*a* is much more labile than the macrocycle with the central Mg^{2+} ion in chlorophyll-*a*. Nevertheless, IRMPD shows great potential in studying the structures of porphyrin like molecules.

Chapter 8 Top-down analysis of p65 proteins

8.1 Introduction

8.1.1 Protein phosphorylation

Protein phosphorylation in eukaryotic cells, mostly occurring on serine, threonine, and tyrosine residues (Scheme 8.1), is recognized as a crucial character of signal transduction and is one of the most biological relevant post-translational modifications (PTMs) in proteins.^{325,326} It is very effective at integrating information from various incoming signals by modifying amino acid residues of the target protein to influence the corresponding aspect of transcription functions.^{327,328} At any given point, over 30% of proteins in a eukaryotic cell are undergoing phosphorylation, which can either modulate their structures or activities.³²⁵ Until now only less than 2% of protein phosphorylation has been identified among an approximate 100,000 potential phosphorylation sites in the human proteome due to the lack of reliable and sensitive high throughput technologies.³²⁹ Moreover, the biased distribution of phosphorylation ratio makes it even harder to locate the phosphorylation site comprehensively.



Scheme 8.1 Diagram shows the phosphorylation of serine, threonine, and tyrosine

Several most popular analytical strategies used for phosphorylation analysis are ³²P-labelling and phosphopeptide mapping, edman sequencing, and mass spectrometry.³²⁵ Although ³²P-labelling is the most sensitive method, it requires large amount of radioactivity and has difficulties in locating the phosphorylated sites, which makes this method less advantageous than MS. In contrast, the MS/MS strategies improve the possibility of fully sequence coverage of the protein interested. Based on the sensitivity and sophisticated fragmentation techniques, MS shows great potential in PTMs characterization, in particular, the top-down MS becomes an important complementary method to bottom-up MS with higher efficiency. In practice, the biased distribution of phosphorylation ratio and the low stoichiometry of protein phosphorylation, however, make it challenging to locate the

phosphorylation site comprehensively. Therefore, enrichment is often necessary in phosphorylation analysis, and a variety of techniques is available and has been summarized elsewhere.³²⁹⁻³³¹

8.1.2 Significance of p65/RelA

Nuclear factor- κ B (NF- κ B) is a protein complex that is vital for the regulation of inflammation, immune responses, and cell proliferation, apoptosis.³³²⁻³³⁵ NF- κ B has also been shown to play a crucial role in many diseases like cancer, asthma, sepsis.^{336,337} In mammals, NF- κ B comprises by five family members, NF- κ B1 (p105/p50), NF- κ B2 (p100/p52), RelA (p65), RelB and c-Rel, and these proteins can form various homo-/hetero-dimers according to their different functions in respond to specific biological activities.³³³ Among all of the dimeric complexes, the p65:p50 heterodimer was the first form of NF- κ B members identified and is also the most abundant one in lots of cell types.^{338,332} Even though each NF- κ B protein has specific roles in cell regulation, only p65 was found to be essential for survival,^{339,340} and the phosphorylation of the p65 subunit caused by various stimulations has also been assigned to change the activity of NF- κ B transcription.³³⁴ In addition, it seems that p65 phosphorylation varies a lot depending on the stimulus, however which has not yet been fully characterized.³²⁷ Until now, more than 10 possible phosphorylation sites have been reported on the p65 subunit alone including Ser205, Ser238, Thr 254, Ser276, Ser281, Ser311, Ser337, Ser435, Ser 468, Thr505, Ser529, and Ser536, many of which can be stimulated by different enzymes.^{341,342} These modifications can then stimulate NF- κ B translocation to the nucleus and are related to transcriptional activities.³⁴¹ In respond to lipopolysaccharide (LPS) and tumour necrosis

factor (TNF)- α , likely other inducers as well, p65 is phosphorylated at the highly conserved Ser-276 residue by the catalytic subunit of protein kinase A (PKAc) leading to a positively regulation of the transactivation potential of p65.^{327,343} Ser-311 is another residue that is targeted for phosphorylation in TNF- α stimulated cells.³⁴⁴ P65 can also be inducibly phosphorylated at Thr-254 which will interrupt its recognition with NF- κ B inhibitor α (I κ B α) and leaves NF- κ B localization to the nucleus,³⁴⁵ at Ser-529 by casein kinase II (CKII); at Ser-468, Ser-536 by I κ B kinase β (IKK β) and glycogen synthase kinase 3 (GSK3).³⁴¹ Phosphorylation at Ser-536 in macrophages can stimulate p65 degradation and promotes resolution of inflammation.³⁴⁶ Due to the complexity and variety, to fully characterize p65 phosphorylation still has a long way to go, while establishing a reliable and effective strategy to locate the phosphorylation sites would be a big step.

8.1.3 Top-down mass spectrometry in studying protein phosphorylation

Top-down mass spectrometry has become a powerful technology for analyzing proteomics and characterizing PTMs. For the phosphorylation modification specifically, a molecular mass will show an apparent 80 Da (HPO₃ 79.97 Da or multiplies) shift due to the covalent connection with phosphoric acids.

Zubarev and McLafferty have firstly reported the characterization of phosphorylated peptide and phosphoprotein using top-down ECD MS,^{53,347} where the modification is remained in ECD process and can be located. Cardiac troponin I (cTnI) is an important regulatory protein in cardiac muscle, and its phosphorylation plays a key role in modulating cardiac function, which

has been studied systematically by Ge and her coworkers.^{181,348-351} Five sites of cTnI, Ser22/Ser23, Ser42/Ser44, and Thr143, are liable to be phosphorylated under the regulation of protein kinase A (PKA) and protein kinase C (PKC).³⁴⁸ With the help of high resolution top-down MS, Ge and her colleagues have unambiguously identified that Ser22/23 as the only two sites phosphorylated in wild-type mouse,³⁴⁸ swine,³⁵⁰ and human,^{83,351} which is significant for the clinical biomarker discovery.

8.1.4 Aims of the project

Generally, the main challenges of analyzing PTMs of intact proteins are to separate and identify the isoforms and isotopes with high resolution and mass accuracy, and to obtain a high sequence coverage by MS/MS. The target of the project is to study the phosphorylation state of p65 stimulated by enzymes using FTICR MS and MS/MS, correlating the results with physiological importance.

8.2 Experimental section

8.2.1 Sample preparation

The p65 protein was expressed in *E. coli* system and then separated by SDS PAGE. IKK β was induced in cell culture to stimulate phosphorylation. The protein stock solution contains 500 mM NaCl, 1 mM EDTA, and 2 mM dithiothreitol (DTT). All protein samples were washed with 100 mM ammonium acetate solution using centrifugal filters (10-30 kDa molecular weight cut off, Millipore, Ireland) to remove salts before MS experiments and were dissolved in acetonitrile/water/formic acid (50:50:1%) to a concentration of ~1-5 μ M.

8.2.2 Mass spectrometry experiments

All mass spectrometry experiments were carried on a Bruker 12 T solariX FTICR mass spectrometer (Bruker Daltonik, GmbH, Bremen, Germany) with a homemade nano-electrospray ion source. A 5-10 V in source dissociation was employed to improve the S/N and ions were cooled in the collision cell for 0.5-3 s before transferred to the ICR cell. For MS/MS experiments, ions of interest were isolated with a 15-30 Da window. The collisional energy in CAD was ~22 V. In the ECD experiment, ions were irradiated with electrons from a 1.5 A heated hollow cathode, and the bias voltages and pulse length were tuned to produce most electron captures. Up to 200 scans were averaged.

8.3 Results and discussions

8.3.1 MS analysis

The protein sample is a segment of p65 proteins from amino acid 12 to 317, which has more than 30 potential phosphorylation sites including 19 Serine, 9 Tyrosine, and 16 Threonine. First, non-phosphorylated p65 is analyzed by MS to determine its molecular weight and purity. The charge distribution of p65 is displayed in Figure 8.1a, and a measured molecular mass, 35073.03973 Da is obtained (Figure 8.1b). The theoretical molecular weight of p65 from aa 12-317, is 34930.25133 Da ($C_{1526}H_{2418}N_{456}O_{460}S_{13}$), which is 142.78840 Da less than the experimental value. According to the mass difference, modifications/decorations or mutations are likely occurred to the p65 sample. In order to check the sequence and particularly to map the PTMs sites using the top-down approach in the future, a fully understanding

of the amino acid sequence is necessary, so MS/MS methods are applied to fragment p65.

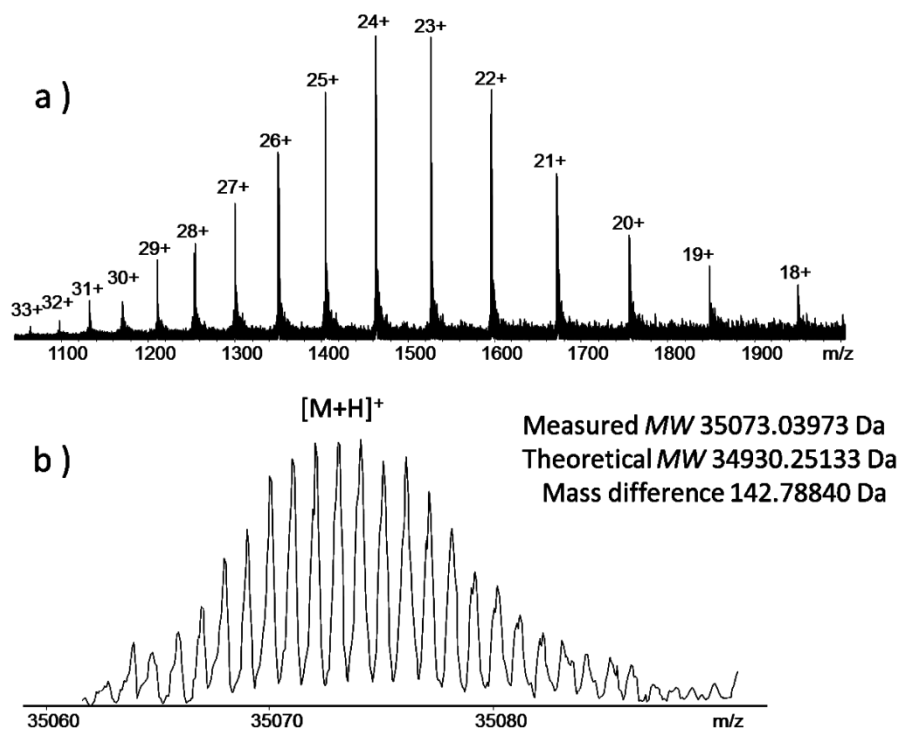


Figure 8.1 a): a nano-ESI spectrum of p65 sample showing its charge distribution; b): deconvolution spectrum of a)

8.3.2 MS/MS sequencing

Figure 8.2 is the CAD spectrum of $[M+30H]^{30+}$. Many peaks are observed, but only a few peaks of low abundance could be assigned to *b/y* fragments as labelled in the figure, which are summarized in Table G.1. If those unassigned peaks in Figure 8.2 are due to modifications/mutations of p65 or side chain losses, some regular patterns or consistent mass differences would be digged out by comparing the experimental masses to the theoretical masses of *b/y* fragments. No useful clues, however, have been found to

identify those intense peaks in CAD spectrum. Eight peaks likely from the N-terminal, b_3 - b_6 , are observed, but each of the 'b' ion is either ~144.04 Da or ~126.03 Da heavier than the corresponding theoretical mass value. Based on the accurate mass difference of the several b ions in the CAD spectrum, it is clear that 144.04 differs from 126.03 by a mass of H_2O . The rest several peaks assigned are y ions from the C-terminal of low abundance. Otherwise, no other ions could be assigned.



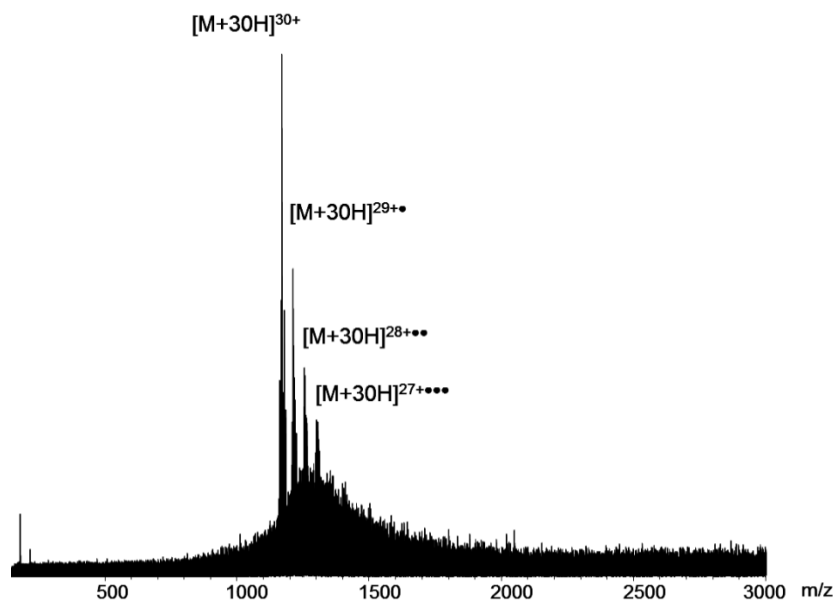


Figure 8.3 ECD results of p65 ions, $[M+30H]^{30+}$. Charge-reduced species, $[M+30H]^{29+•}$, $[M+30H]^{28+••}$, and $[M+30H]^{27+•••}$ etc., are detected showing electron capture

The fragmentation information extracted from the CAD result so far suggested there is a modification/mutation having a mass of ~144.04 Da in the N-terminal from aa 12-14 of the p65 protein. According to the MS measurement, the observed *MW* of the protein is about 142.79 Da heavier than the theoretical mass. It is possible that the molecular mass difference is because of a 144.04 Da modification in the N-terminal in the protein, but more sequence information has to be obtained. In addition, those unknown high intensity peaks in the CAD spectrum are confusing and holding back the conclusion.

8.3.3 Phosphorylation investigation by MS

Even though to locate the PTMs sites by top-down analysis seems not possible at this stage, the mass spectrum of phosphorylated p65 is generated to check the status of phosphorylation stimulated by IKK β . In comparison with the MS result of non-phosphorylated p65, phosphorylated peaks that are about 80 Da heavier than the corresponding non-phosphorylated ones are present in Figure 8.4a. Though the abundance of the phosphorylated p65 is low, it shows that the IKK β does have influence on the phosphorylation of p65; however, further MS/MS investigation will be required to locate the phosphorylation site.

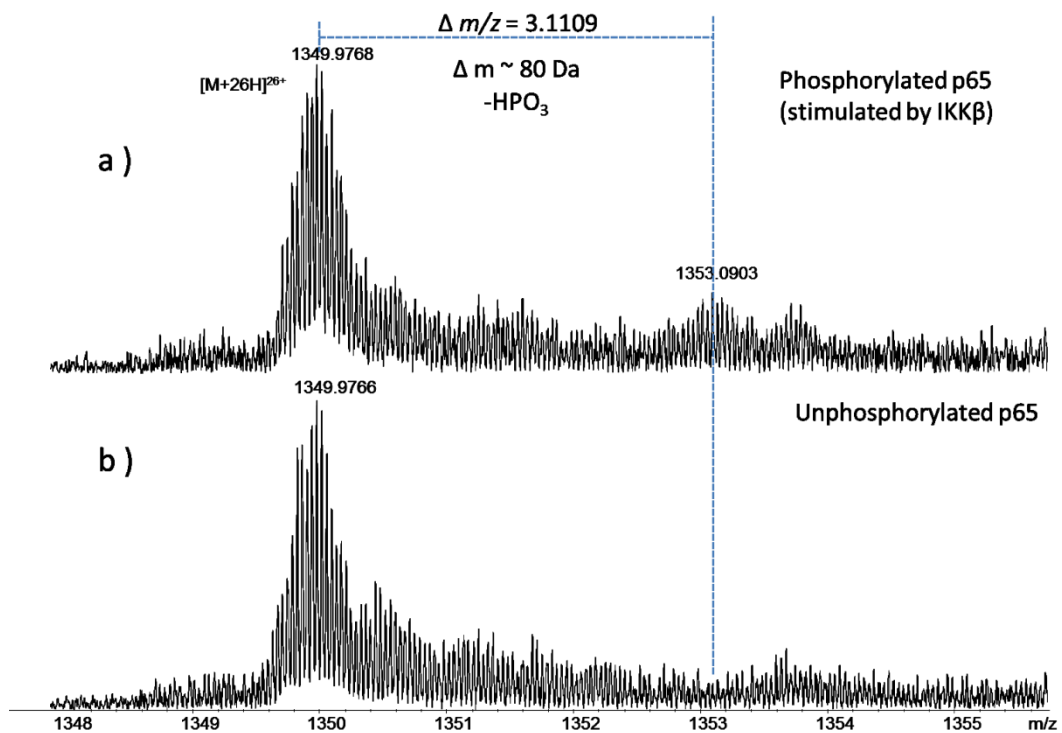


Figure 8.4 MS spectra of a): phosphorylated p65 stimulated by Ikk β and b): non-phosphorylated p65

8.4 Conclusions

A standard experimental protocol to study intact proteins using FTICR MS was built up. The molecular weight of a segment of p65 proteins from aa12-317 was measured, and the phosphorylation of p65 stimulated by IKK β was studied by MS. The difference between theoretical *MW* and the experimental *MW* is about 142.79 Da. A modification/mutation having a mass of ~144.04 Da, suggesting a formula of C₆H₈O₄ (*MW*: 144.04223 Da), in the N-terminal from aa 12-14 was detected by the MS/MS results. Because limited fragments were obtained from the CAD and ECD experiments, the sequence of the protein cannot be fully understood, and it is not valid to study the phosphorylation position of modified p65 at this moment.

To improve the understanding of the protein sequence, introducing a middle down strategy could be one choice by digesting the protein to several smaller segments, which will reduce the molecular weight of the analyte and should greatly facilitate the MS and MS/MS investigation. On the other hand, by carefully tuning, IRMPD and IR-ECD MS/MS might provide more fragmentation information.

Chapter 9 Conclusions and future work

9.1 Conclusions

The advanced performance of FTICR MS, in particular high resolution, high mass accuracy, and flexible tandem mass spectrometry capability, has been demonstrated by a number of applications in the thesis, including the isotopic fine structure measurement of A β peptides (Chapters 2 and 3), the compositional and structural investigation of a polymeric mixture (Chapter 4), the characterization of the fragmentation of chlorophyll-a and pheophytin-a (Chapter 6 and 7), and a little bit of top-down proteomics (Chapter 8).

In Chapter 2 and 3, to estimate the ^{17}O labelling ratio in several A β peptides, their isotopic fine structures were obtained. High resolving power is vital for the measurement because the mass difference between ^{13}C - and ^{17}O -substituted species is about 0.86 mDa. Three peptides, A β_{16-22} (*MW*: 894.498124 Da), A β_{11-25} (*MW*: 1757.885869 Da), and A β_{37-42} (*MW*: 515.30855 Da), were analyzed with ultra-high resolving power, 5.0 M, 6.0 M, and 3.5 M, respectively. Without adding any standard control, the uncertainty of the ^{17}O labelling ratio measurement in each peptide could be calculated according to the difference between the theoretical and experimental ratio of ^{13}C in the same peptide, which is ~2.0% for small peptides, A β_{16-22} and A β_{37-42} , and ~5.2% for A β_{11-25} . The results will be helpful in interpreting the NMR signal to estimate the distance between atoms. In addition to ^{17}O labelling, all of the three peptides are also labelled with ^{15}N or/and ^{13}C , so it is crucial to assign each isotopic peak correctly using high mass accuracy. Dual nano-electrospray experiments were introduced to internally calibrate the spectra

by a standard (HPmix or PEG400 depending on the mass range), and less than 0.1 ppm errors were obtained. MS/MS methods are particularly valuable to determine the isotopic labelling position. Isotope labelled counterparts have similar chemical and physical properties, which are very difficult to be separated using traditional techniques, however, could be qualitatively and quantitatively distinguished by FTICR MS without any extra separation/chemistry.

In chapter 4, the composition of TPGS samples, a PEGylated drug excipient, was studied, because differing compositions of TPGS between batches could result in variable performance of the formulated product. In addition to TPGS, Di-TPGS and free PEG were also detected. The coexistent of different polymeric components and different adducts such as H^+ , NH_4^+ , and Na^+ , arises the complexity of the spectra, so that a high resolving power (450,000 at m/z 500) and high mass accuracy (< 1 ppm) are important to assign peaks with high confidence. For TPGS samples, the ionization solution condition was shown to be a very crucial factor influencing the peaks observed in the MS spectrum, indicating that the solvent selection can be particularly important for the compositional study of some polymers by MS. On the other hand, the fragmentation pattern of TPGS was investigated using different MS/MS methods and with different adducts. Diagnostic fragments from CAD and ECD MS/MS can be used for the identification of the TPGS structure in the future, where ECD and CAD show different preferences in bond cleavages. In addition to the methodology study, based on the MS and MS/MS results of TPGS samples from different suppliers, it was found that the composition of each TPGS sample and the structure of TPGS in each

sample were the same; however, the relative intensity of free PEG and TPGS shows differences between samples from two suppliers. FTICR MS demonstrated the promising role in studying complex mixtures, and FTICR MS/MS is a valuable structural characterization tool for polymers complementary to traditional spectroscopy techniques.

Cationization is a hot-topic in MS/MS field, as introducing different cations usually gives different fragments, and there are also cases that fragmentation patterns were fully changed by simply using different adducts.²⁸⁵ To understand the role of adducts in MS/MS processes is always of great interest. In Chapter 4, silver adducted TPGS showed different ECD behaviour in contrast to the precursors with Li⁺ or Na⁺ ions, so the influence of several adduct ions on the fragmentation processes of CAD and ECD was further studied in Chapter 5. Li⁺, Na⁺, K⁺, Ag⁺, and H⁺ were chosen for this study, and the competitive influence of each ion was investigated by fragmenting TPGS attached with two different cations, $[M+X_1+X_2]^{2+}$ (X_1 and X_2 refer to Li⁺, Na⁺, K⁺, Ag⁺, H⁺). The observation in CAD experiments agrees with previous research carried on other molecules that the dissociation of ionic adducts from the precursor is most likely depending on the binding strength, and, to some extent, ions binding stronger increase fragmentation. While during ECD, the charge carriers are lost in an order which appears to correlate with the relative reduction potential of the ions, which suggests that the reduction potential of the charge carrier is an important factor influencing the fragmentation pattern. The ion with a high reduction potential seems to be more effective in capturing electrons; however, it may also be lost easily before leading to any fragmentation. The trends observed from TPGS are of

benefit for selecting adducts in MS/MS investigations and may facilitate the understanding of the ECD results when cationization is involved.

Porphyrins include a large category of compounds that play important roles in life, where chlorophylls are the ones significant in plants. In contrast to the biosynthesis of chlorophylls, the biodegradation process is less well understood. One of the key steps on the way to unveil the enigma is to identify the metabolites in degradation; therefore, an efficient structural characterization strategy accessible to species of low concentration would be significant. In Chapter 6 and 7, chlorophyll-*a* and the corresponding Mg-depleted species, pheophytin-*a*, were exposed to three different MS/MS methods, CAD, EID, and IRMPD, respectively to investigate the fragmentation efficiency of the two analogues. Again, the importance of high mass accuracy and high resolution were demonstrated in peak assignment. For both molecules, most abundant and extensive fragments were observed from IRMPD, which technique shows great potential in studying the structures of porphyrin like molecules. On the other hand, the EID spectrum of chlorophyll-*a* resembles its IRMPD spectrum, but EID results of pheophytin-*a* show differences. In comparison, the macrocycle of pheophytin-*a* having no central Mg^{2+} ion is more fragile compared to chlorophyll-*a* because fragments from cleavages of the pyrrole groups were only observed from pheophytin-*a*. Moreover, the unique macrocyclic structure shows tolerance to radicals, and odd-electron species were detected from all three MS/MS methods.

In an on-going project, a segment of protein p65 having a mass of *ca* 35 kDa was explored using the top-down approach. FTICR MS displayed capabilities in dealing with big molecules; along with MS/MS, the molecular

weight and some information of the sequence were obtained. Even though it is not feasible to locate the phosphorylation site of phosphorylated p65 so far since only a few sequential fragments were assigned from CAD and ECD, MS/MS definitely has the potential to be used in studying PTMs. A modification of ~144.04 Da, suggesting a formula of $C_6H_8O_4$ (MW : 144.04223 Da), in the N-terminal from aa 12-14 was detected by MS/MS. Sample preparation was found particularly crucial to the success of the MS detection of big proteins. For FTICR MS, the ion capacity and detection sensitivity of an ICR cell is limited, which means good signal could only be approached with right amount of ions in the cell. As proteins tend to present with different charge states and attach with different adducts, all of these could dilute the signal of target ions disturbing the detection. Moreover, the present of modifications and wide isotopic distribution will further exacerbate the signal.

9.2 Future work

Using isotopic fine structure to measure the isotope ratio of an element in a molecule has distinct advantages and shows as a promising complementary strategy. In our experiments, the uncertainty of the measurement is approximately 0.5% for molecules smaller than 300 Da, and the error is bigger for large molecules. Because the ion population in the cell was minimized in practice, a small change of ion number during detection may have big influence on the isotope ratio measurement. In theory, the precision could be improved by signal average, but the peak shift between scans can kill the resolution or lead to split peaks. To avoid frequency shift and obtain a better S/N, one solution has been used in Marshall's group is to align spectra before frequency-domain coaddition,¹²¹ hence, the experimental S/N and

precision could be further improved. Enhancement of the S/N may also assist the detection of low abundance isotopes.

One limitation of the current method is the mass of the analyte, where the isotopic fine structure measurement becomes very challenging for molecules bigger than 1500 Da. In FTICR, resolution is inversely proportional to m/z (section 1.2.1), so the difficulty of isotopic fine structure measurement increases with mass. Moreover, peak coalescence effect is more severe for big molecules.^{240,241} So far, the best resolving power achieved by our 12 T solariX FTICR MS instrument is ~ 6.0 M at m/z 880 to detect the fine structure of doubly-charged $A\beta_{11-25}$. For example, to resolve the ^{13}C - and ^{17}O -substituted peaks of $A\beta_{1-42}$ (MW : 4514 Da) in the baseline will require a resolving power of ~15.0 M, which is currently unapproachable by our instrument. However, a resolving power of ~12.0 M at m/z 675 has been reported on a 4.7 T magnet using a dynamically harmonized ICR cell recently.¹³² Therefore, new cell designs provide a promising future for fine separation in MS. Additionally, on the contrary to peak coalescence effect, the resolving power is proportional to the magnetic field; thus the detection of isotopic fine structure would be more feasible and practical by using higher magnetic field.

Compositional analysis of complex mixtures is a big advantage of high performance MS. Coupling with MS/MS techniques could provide information in another dimension. Though it is difficult to accurately quantify each component in a polymeric mixture solely by MS results, the changes of relative intensity of each component can be monitored. To compare the batch to batch data obtained by FTICR MS with results from other traditional

methods, such as HPLC or size exclusion chromatography (SEC), will be useful. Introducing techniques to control the number of ions in the ICR cell such as automatic gain control (AGC) may also improve the consistence between experiments. Additionally, coupling nano-HPLC with FTICR MS would be a choice for the further analysis of TPGS samples of interest.

In Chapter 5, the reduction potential of the adduct ion was demonstrated as a crucial factor influencing ECD MS/MS behaviours. In order to check the applicability of the rules observed from TPGS, more molecules should be studied systematically. In the meantime, introducing more singly-charged ions will be of benefit for drawing a final conclusion. On the other hand, computational calculation may also be helpful in understanding the fragmentation channels when using different metal ions.

Precursors of a higher charge state are always beneficial for ECD experiments, so using divalent or trivalent metal ions is one of the strategies to increase the charges of analytes. Alkaline earth metals and lanthanides are two series most frequently used. Thus, it may be of interest to explore the fragmentation pattern of TPGS binding with different divalent/trivalent metal ions.

According to the MS/MS results of chlorophyll-*a* and pheophytin-*a*, compared to CAD and EID, IRMPD yielded the most abundant and extensive fragments for both molecules, but it is still difficult to assign all of the fragments in the low m/z region to the exact side group loss due to extended side chain cleavages and the symmetric structure of the macrocycle. One of the experiments may be helpful to nail down the detail assignment is to

induce isotopic labelling, such as ^2H , ^{13}C , or ^{18}O , in specific positions, which should be useful to trace the fragments. Comparing the fragmentation of chlorophyll-*a*/pheophytin-*a* to the fragmentation of some derivatives such as chlorophyll-*b*/pheophytin-*b*, where only one or two substitutes are different, could be another valuable experiment to implement to understand the fragmentation channels. Moreover, by investigating the MS/MS behaviour of molecules with different central metal ions should show the influence of the central metal ion on fragmentation.

In the on-going project in Chapter 8, the most important task is to improve the sequence coverage of the protein by tandem MS/MS. First, by carefully tuning, IRMPD MS/MS is worth trying. Second, though DTT was added in the protein stock solution, to make sure disulfide bonds were not formed, capping cysteine residues by alkylation will be necessary in the future experiments. Last but not least, introducing middle down strategy might be helpful in sequencing the protein by easing the MS and MS/MS investigation.

BIBLIOGRAPHY

- (1) Marshall, A.G.; Hendrickson, C.L.; Jackson, G.S. Fourier transform ion cyclotron resonance mass spectrometry: A primer, *Mass Spectrom. Rev.* **1998**, *17*, 1-35.
- (2) Fenn, J.B.; Mann, M.; Meng, C.K.; Wong, S.F.; Whitehouse, C.M. Electrospray ionization for mass spectrometry of large biomolecules, *Science (New York, N.Y.)* **1989**, *246*, 64-71.
- (3) Tanaka, K.; Waki, H.; Ido, Y.; Akita, S.; Yoshida, Y.; Yoshida, T.; Matsuo, T. Protein and polymer analyses up to m/z 100,000 by laser ionization time-of-flight mass spectrometry, *Rapid Commun. Mass Spectrom.* **1988**, *2*, 151-153.
- (4) Karas, M.; Hillenkamp, F. Laser desorption ionization of proteins with molecular masses exceeding 10,000 daltons, *Anal. Chem.* **1988**, *60*, 2299-2301.
- (5) Cech, N.B.; Enke, C.G. Practical implications of some recent studies in electrospray ionization fundamentals, *Mass Spectrom. Rev.* **2001**, *20*, 362-387.
- (6) Kebarle, P.; Tang, L. From ions in solution to ions in the gas phase-the mechanism of electrospray mass spectrometry, *Anal. Chem.* **1993**, *65*, 972A-986A.
- (7) Konermann, L.; Ahadi, E.; Rodriguez, A.D.; Vahidi, S. Unraveling the mechanism of electrospray ionization, *Anal. Chem.* **2012**, *85*, 2-9.
- (8) Yue, X.; Vahidi, S.; Konermann, L. Insights into the Mechanism of Protein Electrospray Ionization From Salt Adduction Measurements, *J. Am. Soc. Mass. Spectrom.* **2014**, *25*, 1322-1331.
- (9) Iribarne, J.V.; Thomson, B.A. On the evaporation of small ions from charged droplets, *The Journal of Chemical Physics* **1976**, *64*, 2287-2294.
- (10) Taflin, D.C.; Ward, T.L.; Davis, E.J. Electrified droplet fission and the Rayleigh limit, *Langmuir* **1989**, *5*, 376-384.
- (11) Dole, M.; Hines, R.L.; Mack, L.L.; Mobley, R.C.; Ferguson, L.D.; Alice, M.B. Gas phase macroions, *Macromolecules* **1968**, *1*, 96-97.
- (12) Wilm, M.; Mann, M. Analytical properties of the nanoelectrospray ion source, *Anal. Chem.* **1996**, *68*, 1-8.
- (13) Karas, M.; Bachmann, D.; Hillenkamp, F. Influence of the wavelength in high-irradiance ultraviolet laser desorption mass spectrometry of organic molecules, *Anal. Chem.* **1985**, *57*, 2935-2939.
- (14) Jaskolla, T.W.; Karas, M. Compelling evidence for lucky survivor and gas phase protonation: the unified MALDI analyte protonation mechanism, *J. Am. Soc. Mass. Spectrom.* **2011**, *22*, 976-988.
- (15) McLafferty, F.W.; Bente, P.F.; Kornfeld, R.; Tsai, S.-C.; Howe, I. Metastable ion characteristics. XXII. Collisional activation spectra of organic ions, *J. Am. Chem. Soc.* **1973**, *95*, 2120-2129.
- (16) Jennings, K.R. Collision-induced decompositions of aromatic molecular ions, *Int. J. Mass Spectrom. Ion Phys.* **1968**, *1*, 227-235.
- (17) Mitchell Wells, J.; McLuckey, S.A. Collision-induced dissociation (CID) of peptides and proteins, *Methods Enzymol.* **2005**, *402*, 148-185.

- (18) Crecelius, A.C.; Baumgaertel, A.; Schubert, U.S. Tandem mass spectrometry of synthetic polymers, *J. Mass Spectrom.* **2009**, *44*, 1277-1286.
- (19) Zhao, C.; Xie, B.; Chan, S.-Y.; Costello, C.E.; O'Connor, P.B. Collisionally activated dissociation and electron capture dissociation provide complementary structural information for branched permethylated oligosaccharides, *J. Am. Soc. Mass. Spectrom.* **2008**, *19*, 138-150.
- (20) Sleno, L.; Volmer, D.A. Ion activation methods for tandem mass spectrometry, *J. Mass Spectrom.* **2004**, *39*, 1091-1112.
- (21) Carr, S.A.; Huddleston, M.J.; Annan, R.S. Selective detection and sequencing of phosphopeptides at the femtomole level by mass spectrometry, *Anal. Biochem.* **1996**, *239*, 180-192.
- (22) Little, D.P.; Speir, J.P.; Senko, M.W.; O'Connor, P.B.; McLafferty, F.W. Infrared multiphoton dissociation of large multiply charged ions for biomolecule sequencing, *Anal. Chem.* **1994**, *66*, 2809-2815.
- (23) Loo, J.A.; Udseth, H.R.; Smith, R.D.; Futrell, J.H. Collisional effects on the charge distribution of ions from large molecules, formed by electrospray-ionization mass spectrometry, *Rapid Commun. Mass Spectrom.* **1988**, *2*, 207-210.
- (24) Zhai, H.; Han, X.; Breuker, K.; McLafferty, F.W. Consecutive ion activation for top down mass spectrometry: improved protein sequencing by nozzle-skimmer dissociation, *Anal. Chem.* **2005**, *77*, 5777-5784.
- (25) Horn, D.M.; Ge, Y.; McLafferty, F.W. Activated ion electron capture dissociation for mass spectral sequencing of larger (42 kDa) proteins, *Anal. Chem.* **2000**, *72*, 4778-4784.
- (26) Han, X.; Jin, M.; Breuker, K.; McLafferty, F.W. Extending Top-Down Mass Spectrometry to Proteins with Masses Greater Than 200 Kilodaltons, *Science* **2006**, *314*, 109-112.
- (27) Carlin, T.; Freiser, B. Pulsed valve addition of collision and reagent gases in Fourier transform mass spectrometry, *Anal. Chem.* **1983**, *55*, 571-574.
- (28) Gauthier, J.W.; Trautman, T.R.; Jacobson, D.B. Sustained off-resonance irradiation for collision-activated dissociation involving Fourier transform mass spectrometry. Collision-activated dissociation technique that emulates infrared multiphoton dissociation, *Anal. Chim. Acta* **1991**, *246*, 211-225.
- (29) Lee, S.A.; Jiao, C.Q.; Huang, Y.; Freiser, B.S. Multiple excitation collisional activation in Fourier-transform mass spectrometry, *Rapid Commun. Mass Spectrom.* **1993**, *7*, 819-821.
- (30) Williams, E.R.; McLafferty, F.W. High resolution and tandem Fourier-transform mass spectrometry with californium-252 plasma desorption, *J. Am. Soc. Mass. Spectrom.* **1990**, *1*, 427-430.
- (31) Boering, K.A.; Rolfe, J.; Brauman, J.I. Low energy collision induced dissociation: phase-shifting excitation control of ion kinetic energy in ion cyclotron resonance spectrometry, *Int. J. Mass Spectrom. Ion Processes* **1992**, *117*, 357-386.
- (32) Senko, M.W.; Speir, J.P.; McLafferty, F.W. Collisional activation of large multiply charged ions using Fourier transform mass spectrometry, *Anal. Chem.* **1994**, *66*, 2801-2808.

- (33) Jones, C.M.; Beardsley, R.L.; Galhena, A.S.; Dagan, S.; Cheng, G.; Wysocki, V.H. Symmetrical gas-phase dissociation of noncovalent protein complexes via surface collisions, *J. Am. Chem. Soc.* **2006**, *128*, 15044-15045.
- (34) Mabud, M.A.; Dekrey, M.J.; Graham Cooks, R. Surface-induced dissociation of molecular ions, *Int. J. Mass Spectrom. Ion Processes* **1985**, *67*, 285-294.
- (35) Chorush, R.A.; Little, D.P.; Beu, S.C.; Wood, T.D.; McLafferty, F.W. Surface-induced dissociation of multiply-protonated proteins, *Anal. Chem.* **1995**, *67*, 1042-1046.
- (36) Meroueh, O.; Hase, W.L. Dynamics of energy transfer in peptide-surface collisions, *J. Am. Chem. Soc.* **2002**, *124*, 1524-1531.
- (37) Woodin, R.L.; Bomse, D.S.; Beauchamp, J.L. Multiphoton dissociation of molecules with low power continuous wave infrared laser radiation, *J. Am. Chem. Soc.* **1978**, *100*, 3248-3250.
- (38) McLuckey, S.A.; Goeringer, D.E. SPECIAL FEATURE:TUTORIAL Slow heating methods in tandem mass spectrometry, *J. Mass Spectrom.* **1997**, *32*, 461-474.
- (39) Crowe, M.C.; Brodbelt, J.S. Infrared multiphoton dissociation (IRMPD) and collisionally activated dissociation of peptides in a quadrupole ion trap with selective IRMPD of phosphopeptides, *J. Am. Soc. Mass. Spectrom.* **2004**, *15*, 1581-1592.
- (40) Vasicek, L.; Ledvina, A.; Shaw, J.; Griep-Raming, J.; Westphall, M.; Coon, J.; Brodbelt, J. Implementing photodissociation in an orbitrap mass spectrometer, *J. Am. Soc. Mass. Spectrom.* **2011**, *22*, 1105-1108.
- (41) Dass, C., (Ed.), *Fundamentals of Contemporary Mass Spectrometry*, John Wiley & Sons, Inc., New Jersey, 2007.
- (42) Song, H.; Hakansson, K. Electron detachment dissociation and negative ion infrared multiphoton dissociation of electrosprayed intact proteins, *Anal. Chem.* **2012**, *84*, 871-876.
- (43) Lancaster, K.S.; An, H.J.; Li, B.; Lebrilla, C.B. Interrogation of N-Linked oligosaccharides using infrared multiphoton dissociation in FT-ICR mass spectrometry, *Anal. Chem.* **2006**, *78*, 4990-4997.
- (44) Xie, Y.; Lebrilla, C.B. Infrared multiphoton dissociation of alkali metal-coordinated oligosaccharides, *Anal. Chem.* **2003**, *75*, 1590-1598.
- (45) Fukui, K.; Takada, Y.; Sumiyoshi, T.; Imai, T.; Takahashi, K. Infrared multiphoton dissociation spectroscopic analysis of peptides and oligosaccharides by using Fourier transform ion cyclotron resonance mass spectrometry with a midinfrared free-electron laser, *J. Phys. Chem. B* **2006**, *110*, 16111-16116.
- (46) Yoo, H.J.; Håkansson, K. Determination of phospholipid regiochemistry by Ag(I) adduction and tandem mass spectrometry, *Anal. Chem.* **2011**, *83*, 1275-1283.
- (47) Yoo, H.J.; Liu, H.; Håkansson, K. Infrared multiphoton dissociation and electron-induced dissociation as alternative MS/MS strategies for metabolite identification, *Anal. Chem.* **2007**, *79*, 7858-7866.
- (48) Wei, J.; Li, H.; Barrow, M.; O'Connor, P. Structural characterization of chlorophyll-a by high resolution tandem mass spectrometry, *J. Am. Soc. Mass. Spectrom.* **2013**, *24*, 753-760.

- (49) Hofstadler, S.A.; Sannes-Lowery, K.A.; Griffey, R.H. Infrared multiphoton dissociation in an external ion reservoir, *Anal. Chem.* **1999**, *71*, 2067-2070.
- (50) Jose J. Valle, J.R.E., Jos Oomens, David T. Moore, A. F. G. van der Meer, Gert von Helden, Gerard Meijer, Christopher L. Hendrickson, Alan G. Marshall, Gregory T. Blakney Free electron laser-Fourier transform ion cyclotron resonance mass spectrometry facility for obtaining infrared multiphoton dissociation spectra of gaseous ions, *Rev. Sci. Instrum.* **2005**, *76*, 1-8.
- (51) Martens, S.M.; Marta, R.A.; Martens, J.K.; McMahon, T.B. Consecutive fragmentation mechanisms of protonated ferulic acid probed by infrared multiple photon dissociation spectroscopy and electronic structure calculations, *J. Am. Soc. Mass. Spectrom.* **2012**, *23*, 1697-1706.
- (52) Guan, Z.; Kelleher, N.L.; O'Connor, P.B.; Aaserud, D.J.; Little, D.P.; McLafferty, F.W. 193 nm photodissociation of larger multiply-charged biomolecules, *Int. J. Mass Spectrom. Ion Processes* **1996**, *157*, 357-364.
- (53) Shi, S.D.H.; Hemling, M.E.; Carr, S.A.; Horn, D.M.; Lindh, I.; McLafferty, F.W. Phosphopeptide/Phosphoprotein mapping by electron capture dissociation mass spectrometry, *Anal. Chem.* **2000**, *73*, 19-22.
- (54) Zubarev, R.A.; Kruger, N.A.; Fridriksson, E.K.; Lewis, M.A.; Horn, D.M.; Carpenter, B.K.; McLafferty, F.W. Electron capture dissociation of gaseous multiply-charged proteins is favored at disulfide bonds and other sites of high hydrogen atom affinity, *J. Am. Chem. Soc.* **1999**, *121*, 2857-2862.
- (55) Cerda, B.; Horn, D.; Breuker, K.; Carpenter, B.; McLafferty, F. Electron capture dissociation of multiply-charged oxygenated cations. A nonergodic process, *Eur. J. Mass Spectrom.* **1999**, *5*, 335-338.
- (56) Zubarev, R.A.; Kelleher, N.L.; McLafferty, F.W. Electron capture dissociation of multiply charged protein cations. A nonergodic process, *J. Am. Chem. Soc.* **1998**, *120*, 3265-3266.
- (57) Bardsley, J.; Biondi, M. Dissociative recombination, *Adv. Appl. Mol. Phys.* **1970**, *6*, 1-57.
- (58) Zubarev, R.A. Reactions of polypeptide ions with electrons in the gas phase, *Mass Spectrom. Rev.* **2003**, *22*, 57-77.
- (59) Leymarie, N.; Costello, C.E.; O'Connor, P.B. Electron capture dissociation initiates a free radical reaction cascade, *J. Am. Chem. Soc.* **2003**, *125*, 8949-8958.
- (60) Zubarev, R.A.; Haselmann, K.F.; Budnik, B.; Kjeldsen, F.; Jensen, F. Towards an understanding of the mechanism of electron-capture dissociation: A historical perspective and modern ideas, *Eur. J. Mass Spectrom.* **2002**, *8*, 337-350.
- (61) Syrstad, E.A.; Tureček, F. Toward a general mechanism of electron capture dissociation, *J. Am. Soc. Mass. Spectrom.* **2005**, *16*, 208-224.
- (62) Tureček, F. NC α bond dissociation energies and kinetics in amide and peptide radicals. Is the dissociation a non-ergodic process?, *J. Am. Chem. Soc.* **2003**, *125*, 5954-5963.
- (63) Świercz, I.; Skurski, P.; Simons, J. Dipole and Coulomb forces in electron capture dissociation and electron transfer dissociation mass spectroscopy, *J. Phys. Chem. A* **2012**, *116*, 1828-1837.

- (64) Chamot-Rooke, J.; Malosse, C.; Frison, G.; Tureček, F. Electron capture in charge-tagged peptides. Evidence for the role of excited electronic states, *J. Am. Soc. Mass. Spectrom.* **2007**, *18*, 2146-2161.
- (65) Lin, C.; Cournoyer, J.J.; O'Connor, P.B. Probing the gas-phase folding kinetics of peptide ions by IR activated DR-ECD, *J. Am. Soc. Mass. Spectrom.* **2008**, *19*, 780-789.
- (66) Oh, H.; McLafferty, F.W. A variety of activation methods employed in "activated-ion" electron capture dissociation mass spectrometry: A test against bovine ubiquitin 7+ ions, *B. Kor. Chem. Soc.* **2006**, *27*, 389.
- (67) Kjeldsen, F.; Haselmann, K.F.; Budnik, B.A.; Jensen, F.; Zubarev, R.A. Dissociative capture of hot (3–13 eV) electrons by polypeptide polycations: an efficient process accompanied by secondary fragmentation, *Chem. Phys. Lett.* **2002**, *356*, 201-206.
- (68) Nielsen, M.L.; Budnik, B.A.; Haselmann, K.F.; Olsen, J.V.; Zubarev, R.A. Intramolecular hydrogen atom transfer in hydrogen-deficient polypeptide radical cations, *Chem. Phys. Lett.* **2000**, *330*, 558-562.
- (69) Gord, J.R.; Horning, S.R.; Wood, J.M.; Cooks, R.G.; Freiser, B.S. Energy deposition during electron-induced dissociation, *J. Am. Soc. Mass. Spectrom.* **1993**, *4*, 145-151.
- (70) Lioe, H.; O'Hair, R. Comparison of collision-induced dissociation and electron-induced dissociation of singly protonated aromatic amino acids, cystine and related simple peptides using a hybrid linear ion trap–FT-ICR mass spectrometer, *Anal. Bioanal. Chem.* **2007**, *389*, 1429-1437.
- (71) Fung, Y.M.E.; Adams, C.M.; Zubarev, R.A. Electron ionization dissociation of singly and multiply charged peptides, *J. Am. Chem. Soc.* **2009**, *131*, 9977-9985.
- (72) Cody, R.B.; Freiser, B.S. Electron impact excitation of ions in Fourier transform mass spectrometry, *Anal. Chem.* **1987**, *59*, 1054-1056.
- (73) Cody, R.B.; Freiser, B.S. Electron impact excitation of ions from organics: an alternative to collision induced dissociation, *Anal. Chem.* **1979**, *51*, 547-551.
- (74) Budnik, B.A.; Zubarev, R.A. MH²⁺ ion production from protonated polypeptides by electron impact: observation and determination of ionization energies and a cross-section, *Chem. Phys. Lett.* **2000**, *316*, 19-23.
- (75) Prakash, A.; Smith, M.P.; Kaabia, Z.; Hurst, G.; Yan, C.; Sims, M.; Bristow, A.T.; Stokes, P.; Parker, D.; Mosely, J. Using Electron Induced Dissociation (EID) on an LC time-scale to characterize a mixture of analogous small organic molecules, *J. Am. Soc. Mass. Spectrom.* **2012**, *23*, 850-857.
- (76) Kaczorowska, M.A.; Cooper, H.J. Electron induced dissociation (EID) tandem mass spectrometry of octaethylporphyrin and its iron(iii) complex, *Chem. Commun.* **2011**, *47*, 418-420.
- (77) Kalli, A.; Grigorean, G.; Håkansson, K. Electron induced dissociation of singly deprotonated peptides, *J. Am. Soc. Mass. Spectrom.* **2011**, *22*, 2209-2221.
- (78) Mosely, J.A.; Smith, M.J.P.; Prakash, A.S.; Sims, M.; Bristow, A.W.T. Electron-induced dissociation of singly charged organic cations as a tool for structural characterization of pharmaceutical type molecules, *Anal. Chem.* **2011**, *83*, 4068-4075.

- (79) Wolff, J.J.; Laremore, T.N.; Aslam, H.; Linhardt, R.J.; Amster, I.J. Electron-induced dissociation of glycosaminoglycan tetrasaccharides, *J. Am. Soc. Mass. Spectrom.* **2008**, *19*, 1449-1458.
- (80) Syka, J.E.P.; Coon, J.J.; Schroeder, M.J.; Shabanowitz, J.; Hunt, D.F. Peptide and protein sequence analysis by electron transfer dissociation mass spectrometry, *Proc. Natl. Acad. Sci. U. S. A.* **2004**, *101*, 9528-9533.
- (81) Scionti, V.; Wesdemiotis, C. Electron transfer dissociation versus collisionally activated dissociation of cationized biodegradable polyesters, *J. Mass Spectrom.* **2012**, *47*, 1442-1449.
- (82) Tsybin, Y.O.; Fornelli, L.; Stoermer, C.; Luebeck, M.; Parra, J.; Nallet, S.; Wurm, F.M.; Hartmer, R. Structural analysis of intact monoclonal antibodies by electron transfer dissociation mass spectrometry, *Anal. Chem.* **2011**, *83*, 8919-8927.
- (83) Zabrouskov, V.; Ge, Y.; Schwartz, J.; Walker, J.W. Unraveling molecular complexity of phosphorylated human Cardiac Troponin I by top down electron capture dissociation/electron transfer dissociation mass spectrometry, *Mol. Cell. Proteomics* **2008**, *7*, 1838-1849.
- (84) Simons, J.; Ledvina, A.R. Spatial extent of fragment-ion abundances in electron transfer dissociation and electron capture dissociation mass spectrometry of peptides, *Int. J. Mass spectrom.* **2012**, *330–332*, 85-94.
- (85) Shukla, A.K.; Futrell, J.H., Fundamental studies of collision-induced dissociation of ions, *Experimental Mass Spectrometry*, Springer, 1994, pp. 71-112.
- (86) Dongré, A.R.; Jones, J.L.; Somogyi, Á.; Wysocki, V.H. Influence of peptide composition, gas-phase basicity, and chemical modification on fragmentation efficiency: Evidence for the mobile proton model, *J. Am. Chem. Soc.* **1996**, *118*, 8365-8374.
- (87) Wysocki, V.H.; Tsaprailis, G.; Smith, L.L.; Brei, L.A. Mobile and localized protons: a framework for understanding peptide dissociation, *J. Mass Spectrom.* **2000**, *35*, 1399-1406.
- (88) Polfer, N.C.; Oomens, J.; Suhai, S.; Paizs, B. Infrared spectroscopy and theoretical studies on gas-phase protonated Leu-enkephalin and its fragments: Direct experimental evidence for the mobile proton, *J. Am. Chem. Soc.* **2007**, *129*, 5887-5897.
- (89) Anusiewicz, I.; Skurski, P.; Simons, J. Refinements to the Utah–Washington mechanism of electron capture dissociation, *J. Phys. Chem. B* **2014**, *118*, 10.
- (90) Gross, J.H., Mass Spectrometry, *digital Encyclopedia of Applied Physics*, Wiley-VCH Verlag GmbH & Co. KGaA, 2003.
- (91) Comisarow, M.B.; Marshall, A.G. Fourier transform ion cyclotron resonance spectroscopy, *Chem. Phys. Lett.* **1974**, *25*, 282-283.
- (92) Kolhinen, V.S.; Bussmann, M.; Gartzke, E.; Habs, D.; Neumayr, J.B.; Schürmann, C.; Szerypo, J.; Thierolf, P.G. Commissioning of the double Penning trap system MLLTRAP, *Nucl. Instrum. Meth. A* **2009**, *600*, 391-397.
- (93) Amster, I.J. Fourier transform mass spectrometry, *J. Mass Spectrom.* **1996**, *31*, 1325-1337.

- (94) Shockley, W. Currents to conductors induced by a moving point charge, *J. Appl. Phys.* **1938**, 9, 635.
- (95) Comisarow, M.B.; Marshall, A.G. Frequency-sweep fourier transform ion cyclotron resonance spectroscopy, *Chem. Phys. Lett.* **1974**, 26, 489-490.
- (96) Marshall, A.G.; Wang, T.C.L.; Ricca, T.L. Tailored excitation for Fourier transform ion cyclotron mass spectrometry, *J. Am. Chem. Soc.* **1985**, 107, 7893-7897.
- (97) Zhang, L.K.; Rempel, D.; Pramanik, B.N.; Gross, M.L. Accurate mass measurements by Fourier transform mass spectrometry, *Mass Spectrom. Rev.* **2005**, 24, 286-309.
- (98) Marshall, A.G.; Verdun, F.R. Fourier transforms in NMR, optical, and mass spectrometry, **1990**.
- (99) Qi, Y.; O'Connor, P.B. Data processing in Fourier transform ion cyclotron resonance mass spectrometry, *Mass Spectrom. Rev.* **2014**, 33, 333-352.
- (100) Cho, Y.; Qi, Y.; O'Connor, P.B.; Barrow, M.P.; Kim, S. Application of phase correction to improve the interpretation of crude oil spectra obtained using 7 T Fourier transform ion cyclotron resonance mass spectrometry, *J. Am. Soc. Mass. Spectrom.* **2014**, 25, 154-157.
- (101) Kilgour, D.P.A.; Wills, R.; Qi, Y.; O'Connor, P.B. Autophaser: An algorithm for automated generation of absorption mode spectra for FT-ICR MS, *Anal. Chem.* **2013**, 85, 3903-3911.
- (102) Qi, Y.; Barrow, M.P.; Li, H.; Meier, J.E.; Van Orden, S.L.; Thompson, C.J.; O'Connor, P.B. Absorption-mode: The next generation of Fourier transform mass spectra, *Anal. Chem.* **2012**, 84, 2923-2929.
- (103) Qi, Y.; Witt, M.; Jertz, R.; Baykut, G.; Barrow, M.P.; Nikolaev, E.N.; O'Connor, P.B. Absorption-mode spectra on the dynamically harmonized Fourier transform ion cyclotron resonance cell, *Rapid Commun. Mass Spectrom.* **2012**, 26, 2021-2026.
- (104) Qi, Y.; Thompson, C.; Van Orden, S.; O'Connor, P. Phase correction of Fourier transform ion cyclotron resonance mass spectra using MatLab, *J. Am. Soc. Mass. Spectrom.* **2011**, 22, 138-147.
- (105) Aarstol, M.; Comisarow, M.B. Apodization of FT-ICR spectra, *Int. J. Mass Spectrom. Ion Processes* **1987**, 76, 287-297.
- (106) Nikolaev, E.N.; Rakov, V.S.; Futrell, J.H. Analysis of harmonics for an elongated FTMS cell with multiple electrode detection, *Int. J. Mass Spectrom. Ion Processes* **1996**, 157-158, 215-232.
- (107) Comisarow, M.B. Cubic trapped-ion cell for ion cyclotron resonance, *Int. J. Mass Spectrom. Ion Phys.* **1981**, 37, 251-257.
- (108) Guan, S.; Marshall, A.G. Ion traps for Fourier transform ion cyclotron resonance mass spectrometry: principles and design of geometric and electric configurations, *Int. J. Mass Spectrom. Ion Processes* **1995**, 146, 261-296.
- (109) Nikolaev, E.; Boldin, I.; Jertz, R.; Baykut, G. Initial experimental characterization of a new ultra-high resolution FTICR cell with dynamic harmonization, *J. Am. Soc. Mass. Spectrom.* **2011**, 22, 1125-1133.

- (110) Caravatti, P.; Allemann, M. The 'infinity cell': A new trapped-ion cell with radiofrequency covered trapping electrodes for Fourier transform ion cyclotron resonance mass spectrometry, *Org. Mass Spectrom.* **1991**, 26, 514-518.
- (111) Brustkern, A.M.; Rempel, D.L.; Gross, M.L. An electrically compensated trap designed to eighth order for FT-ICR mass spectrometry, *J. Am. Soc. Mass. Spectrom.* **2008**, 19, 1281-1285.
- (112) Ledford, E.B.; Rempel, D.L.; Gross, M.L. Space charge effects in Fourier transform mass spectrometry. II. Mass calibration, *Anal. Chem.* **1984**, 56, 2744-2748.
- (113) Easterling, M.L.; Mize, T.H.; Amster, I.J. Routine part-per-million mass accuracy for high- mass ions: space-charge effects in MALDI FT-ICR, *Anal. Chem.* **1998**, 71, 624-632.
- (114) Aizikov, K.; O'Connor, P.B. Use of the filter diagonalization method in the study of space charge related frequency modulation in Fourier transform ion cyclotron resonance mass spectrometry, *J. Am. Soc. Mass. Spectrom.* **2006**, 17, 836-843.
- (115) Uechi, G.T.; Dunbar, R.C. Space charge effects on relative peak heights in fourier transform-ion cyclotron resonance spectra, *J. Am. Soc. Mass. Spectrom.* **1992**, 3, 734-741.
- (116) Jeffries, J.; Barlow, S.; Dunn, G. Theory of space-charge shift of ion cyclotron resonance frequencies, *Int. J. Mass Spectrom. Ion Processes* **1983**, 54, 169-187.
- (117) Aizikov, K.; Mathur, R.; O'Connor, P. The spontaneous loss of coherence catastrophe in fourier transform ion cyclotron resonance mass spectrometry, *J. Am. Soc. Mass. Spectrom.* **2009**, 20, 247-256.
- (118) Naito, Y.; Inoue, M. Peak confluence phenomenon in Fourier transform ion cyclotron resonance mass spectrometry, *Journal of the Mass Spectrometry Society of Japan* **1994**, 42, 1-9.
- (119) Mitchell, D.W.; Smith, R.D. Cyclotron motion of two Coulombically interacting ion clouds with implications to Fourier-transform ion cyclotron resonance mass spectrometry, *Physical Review E* **1995**, 52, 4366-4386.
- (120) Brenton, A.G.; Godfrey, A.R. Accurate mass measurement: terminology and treatment of data, *J. Am. Soc. Mass. Spectrom.* **2010**, 21, 1821-1835.
- (121) Shi, S.D.-H.; Hendrickson, C.L.; Marshall, A.G. Counting individual sulfur atoms in a protein by ultrahighresolution Fourier transform ion cyclotron resonance mass spectrometry: Experimental resolution of isotopic fine structure in proteins, *Proc. Natl. Acad. Sci.* **1998**, 95, 11532-11537.
- (122) He, F.; Hendrickson, C.L.; Marshall, A.G. Baseline mass resolution of peptide isobars: a record for molecular mass resolution, *Anal. Chem.* **2000**, 73, 647-650.
- (123) Nikolaev, E.N.; Jertz, R.; Grigoryev, A.; Baykut, G. Fine structure in isotopic peak distributions measured using a dynamically harmonized Fourier transform ion cyclotron resonance cell at 7 T, *Anal. Chem.* **2012**, 84, 2275-2283.
- (124) Blake, S.; Walker, S.H.; Muddiman, D.; Hinks, D.; Beck, K. Spectral accuracy and sulfur counting capabilities of the LTQ-FT-ICR and the LTQ-

Orbitrap XL for small molecule analysis, *J. Am. Soc. Mass. Spectrom.* **2011**, *22*, 2269-2275.

(125) Miladinović, S.M.; Kozhinov, A.N.; Gorshkov, M.V.; Tsybin, Y.O. On the utility of isotopic fine structure mass spectrometry in protein identification, *Anal. Chem.* **2012**, *84*, 4042-4051.

(126) Blank, L.M.; Desphande, R.R.; Schmid, A.; Hayen, H. Analysis of carbon and nitrogen co-metabolism in yeast by ultrahigh-resolution mass spectrometry applying ¹³C- and ¹⁵N-labeled substrates simultaneously, *Anal. Bioanal. Chem.* **2012**, *403*, 2291-2305.

(127) Smith, D.; Kiss, A.; Leach, F., III; Robinson, E.; Paša-Tolić, L.; Heeren, R.A. High mass accuracy and high mass resolving power FT-ICR secondary ion mass spectrometry for biological tissue imaging, *Anal. Bioanal. Chem.* **2013**, *405*, 6069-6076.

(128) Liu, Q.; Easterling, M.L.; Agar, J.N. Resolving isotopic fine structure to detect and quantify natural abundance- and Hydrogen/Deuterium exchange-derived isotopomers, *Anal. Chem.* **2013**, *86*, 820-825.

(129) Miura, D.; Tsuji, Y.; Takahashi, K.; Wariishi, H.; Saito, K. A strategy for the determination of the elemental composition by Fourier transform ion cyclotron resonance mass spectrometry based on isotopic peak ratios, *Anal. Chem.* **2010**, *82*, 5887-5891.

(130) Nakabayashi, R.; Sawada, Y.; Yamada, Y.; Suzuki, M.; Hirai, M.Y.; Sakurai, T.; Saito, K. Combination of liquid chromatography–Fourier transform ion cyclotron resonance-mass spectrometry with ¹³C-labeling for chemical assignment of sulfur-containing metabolites in onion bulbs, *Anal. Chem.* **2013**, *85*, 1310-1315.

(131) Paša-Tolić, L.; Huang, Y.; Guan, S.; Kim, H.S.; Marshall, A.G. Ultrahigh-resolution matrix-assisted laser desorption/ionization Fourier transform ion cyclotron resonance mass spectra of peptides, *J. Mass Spectrom.* **1995**, *30*, 825-833.

(132) Popov, I.; Nagornov, K.; N.Vladimirov, G.; Kostyukevich, Y.; Nikolaev, E. Twelve million resolving power on 4.7 T Fourier transform ion cyclotron resonance instrument with Dynamically Harmonized Cell—observation of fine structure in peptide mass spectra, *J. Am. Soc. Mass. Spectrom.* **2014**, 1-10.

(133) Mann, M.; Kelleher, N.L. Precision proteomics: The case for high resolution and high mass accuracy, *Proc. Natl. Acad. Sci.* **2008**, *105*, 18132-18138.

(134) Perez Hurtado, P.; O'Connor, P.B. Deamidation of collagen, *Anal. Chem.* **2012**, *84*, 3017-3025.

(135) Chamot-Rooke, J.; Rousseau, B.; Lanternier, F.; Mikaty, G.; Mairey, E.; Malosse, C.; Bouchoux, G.; Pelicic, V.; Camoin, L.; Nassif, X. Alternative *Neisseria* spp. type IV pilin glycosylation with a glyceramido acetamido trideoxyhexose residue, *Proc. Natl. Acad. Sci.* **2007**, *104*, 14783-14788.

(136) Gault, J.; Malosse, C.; Duménil, G.; Chamot-Rooke, J. A combined mass spectrometry strategy for complete posttranslational modification mapping of *Neisseria meningitidis* major pilin, *J. Mass Spectrom.* **2013**, *48*, 1199-1206.

- (137) Marshall, A.G.; Blakney, G.T.; Beu, S.C.; Hendrickson, C.L.; McKenna, A.M.; Purcell, J.M.; Rodgers, R.P.; Xian, F. Petroleomics: a test bed for ultra-high-resolution Fourier transform ion cyclotron resonance mass spectrometry, *Eur. J. Mass Spectrom.* **2010**, *16*, 367-371.
- (138) Bae, E.J.; Na, J.G.; Chung, S.H.; Kim, H.S.; Kim, S. Identification of about 30 000 chemical components in shale oils by electrospray ionization (ESI) and atmospheric pressure photoionization (APPI) coupled with 15 T Fourier transform ion cyclotron resonance mass spectrometry (FT-ICR MS) and a comparison to conventional oil, *Energy & Fuels* **2010**, *24*, 2563-2569.
- (139) Schaub, T.M.; Hendrickson, C.L.; Horning, S.; Quinn, J.P.; Senko, M.W.; Marshall, A.G. High-performance mass spectrometry: Fourier transform ion cyclotron resonance at 14.5 Tesla, *Anal. Chem.* **2008**, *80*, 3985-3990.
- (140) Hsu, C.S.; Hendrickson, C.L.; Rodgers, R.P.; McKenna, A.M.; Marshall, A.G. Petroleomics: advanced molecular probe for petroleum heavy ends, *J. Mass Spectrom.* **2011**, *46*, 337-343.
- (141) Oro, N.E.; Lucy, C.A. Analysis of the nitrogen content of distillate cut gas oils and treated heavy gas oils using normal phase HPLC, fraction collection and petroleomic FT-ICR MS data, *Energy & Fuels* **2012**, *27*, 35-45.
- (142) Cho, Y.; Na, J.-G.; Nho, N.-S.; Kim, S.; Kim, S. Application of saturates, aromatics, resins, and asphaltenes crude oil fractionation for detailed chemical characterization of heavy crude oils by Fourier transform ion cyclotron resonance mass spectrometry equipped with atmospheric pressure photoionization, *Energy & Fuels* **2012**, *26*, 2558-2565.
- (143) Smith, M., Jonathan, Paul, Applications of new mass spectrometric technologies for the structural characterisation of synthetic polymers, Doctor of Philosophy, Durham University, Durham, 2013.
- (144) Perez Hurtado, P.; Lam, P.Y.; Kilgour, D.; Bristow, A.; McBride, E.; O'Connor, P.B. Use of high resolution mass spectrometry for analysis of polymeric excipients in drug delivery formulations, *Anal. Chem.* **2012**, *84*, 8579-8586.
- (145) Miladinović, S.M.; Kaeser, C.J.; Knust, M.M.; Wilkins, C.L. Tandem Fourier transform mass spectrometry of block and random copolymers, *Int. J. Mass spectrom.* **2011**, *301*, 184-194.
- (146) Wei, J.; Bristow, A.; McBride, E.; Kilgour, D.; O'Connor, P.B. D- α -tocopheryl polyethylene glycol 1000 succinate: a view from FTICR MS and tandem MS, *Anal. Chem.* **2014**, *86*, 1567-1574.
- (147) O'Connor, P.B.; McLafferty, F.W. Oligomer Characterization of 4-23 kDa polymers by electrospray Fourier transform mass spectrometry, *J. Am. Chem. Soc.* **1995**, *117*, 12826-12831.
- (148) Song, J.; van Velde, J.W.; Vertommen, L.L.T.; Smith, D.F.; Heeren, R.M.A.; van den Brink, O.F. End-group analysis of methacrylic (Co)polymers by LC-ESI-MS², *Macromolecules* **2011**, *44*, 1319-1326.
- (149) Kaczorowska, M.A.; Cooper, H.J. Characterization of polyphosphoesters by fourier transform ion cyclotron resonance mass spectrometry, *J. Am. Soc. Mass. Spectrom.* **2009**, *20*, 2238-2247.

- (150) McDonnell, L.A.; Heeren, R.; Andr  n, P.E.; Stoeckli, M.; Corthals, G.C. Going forward: Increasing the accessibility of imaging mass spectrometry, *J. Proteomics* **2012**, *75*, 5113-5121.
- (151) Heeren, R.M.A.; Smith, D.F.; Stauber, J.; K  krer-Kaletas, B.; MacAleese, L. Imaging mass spectrometry: Hype or Hope?, *J. Am. Soc. Mass. Spectrom.* **2009**, *20*, 1006-1014.
- (152) Cornett, D.S.; Frappier, S.L.; Caprioli, R.M. MALDI-FTICR imaging mass spectrometry of drugs and metabolites in tissue, *Anal. Chem.* **2008**, *80*, 5648-5653.
- (153) Taban, I.M.; Altelaar, A.; van der Burgt, Y.E.M.; McDonnell, L.A.; Heeren, R.; Fuchser, J.; Baykut, G. Imaging of peptides in the rat brain using MALDI-FTICR mass spectrometry, *J. Am. Soc. Mass. Spectrom.* **2007**, *18*, 145-151.
- (154) Andersson, M.; Groseclose, M.R.; Deutch, A.Y.; Caprioli, R.M. Imaging mass spectrometry of proteins and peptides: 3D volume reconstruction, *Nat. Methods* **2008**, *5*, 101-108.
- (155) Witting, M.; Lucio, M.; Tziotis, D.; Schmitt-Kopplin, P., Ultrahigh resolution mass spectrometry based non-targeted microbial metabolomics. in: Suhre, K., (Ed.), *Genetics Meets Metabolomics*, Springer New York, 2012, pp. 57-71.
- (156) Lei, Z.; Huhman, D.V.; Sumner, L.W. Mass spectrometry strategies in metabolomics, *J. Biol. Chem.* **2011**, *286*, 25435-25442.
- (157) Ohta, D.; Kanaya, S.; Suzuki, H. Application of Fourier-transform ion cyclotron resonance mass spectrometry to metabolic profiling and metabolite identification, *Curr. Opin. Biotechnol.* **2010**, *21*, 35-44.
- (158) Guo, K.; Bamforth, F.; Li, L. Qualitative metabolome analysis of human cerebrospinal fluid by ¹³C-/¹²C-isotope dansylation labeling combined with liquid chromatography Fourier transform ion cyclotron resonance mass spectrometry, *J. Am. Soc. Mass. Spectrom.* **2011**, *22*, 339-347.
- (159) Han, J.; Danell, R.M.; Patel, J.R.; Gumerov, D.R.; Scarlett, C.O.; Speir, J.P.; Parker, C.E.; Rusyn, I.; Zeisel, S.; Borchers, C.H. Towards high-throughput metabolomics using ultrahigh-field Fourier transform ion cyclotron resonance mass spectrometry, *Metabolomics* **2008**, *4*, 128-140.
- (160) Cho, K.; Mahieu, N.G.; Ivanisevic, J.; Uritboonthai, W.; Chen, Y.-J.; Siuzdak, G.; Patti, G.J. isoMETLIN: A database for isotope-based metabolomics, *Anal. Chem.* **2014**, *86*, 9358-9361.
- (161) Wishart, D.S.; Jewison, T.; Guo, A.C.; Wilson, M.; Knox, C.; Liu, Y.; Djoumbou, Y.; Mandal, R.; Aziat, F.; Dong, E. HMDB 3.0—the human metabolome database in 2013, *Nucleic Acids Res.* **2012**, *40*, 801-807.
- (162) Zubarev, R.A.; Horn, D.M.; Fridriksson, E.K.; Kelleher, N.L.; Kruger, N.A.; Lewis, M.A.; Carpenter, B.K.; McLafferty, F.W. Electron capture dissociation for structural characterization of multiply charged protein cations, *Anal. Chem.* **2000**, *72*, 563-573.
- (163) Wills, R.H.; Tosin, M.; O'Connor, P.B. Structural characterization of polyketides using high mass accuracy tandem mass spectrometry, *Anal. Chem.* **2012**, *84*, 8863-8870.
- (164) Leach, F., III; Ly, M.; Laremore, T.; Wolff, J.; Perlow, J.; Linhardt, R.; Amster, I.J. Hexuronic acid stereochemistry determination in chondroitin sulfate

glycosaminoglycan oligosaccharides by electron detachment dissociation, *J. Am. Soc. Mass. Spectrom.* **2012**, *23*, 1488-1497.

(165) Yu, X.; Huang, Y.; Lin, C.; Costello, C.E. Energy-dependent electron activated dissociation of metal-adducted permethylated oligosaccharides, *Anal. Chem.* **2012**, *84*, 7487-7494.

(166) Jin, Z.; Daiya, S.; Kenttämä, H.I. Characterization of nonpolar lipids and selected steroids by using laser-induced acoustic desorption/chemical ionization, atmospheric pressure chemical ionization, and electrospray ionization mass spectrometry, *Int. J. Mass spectrom.* **2011**, *301*, 234-239.

(167) Taucher, M.; Breuker, K. Characterization of modified RNA by top-down mass spectrometry, *Angew. Chem.* **2012**, *124*, 11451-11454.

(168) Xian, F.; Hendrickson, C.L.; Marshall, A.G. High resolution mass spectrometry, *Anal. Chem.* **2012**, *84*, 708-719.

(169) Harkewicz, R.; Dennis, E.A. Applications of mass spectrometry to lipids and membranes, *Annu. Rev. Biochem.* **2011**, *80*, 301.

(170) Park, Y.; Lebrilla, C.B. Application of Fourier transform ion cyclotron resonance mass spectrometry to oligosaccharides, *Mass Spectrom. Rev.* **2005**, *24*, 232-264.

(171) Hofstadler, S.A.; Sannes-Lowery, K.A.; Hannis, J.C. Analysis of nucleic acids by FTICR MS, *Mass Spectrom. Rev.* **2004**, *24*, 265-285.

(172) Kelleher, N.L.; Lin, H.Y.; Valaskovic, G.A.; Aaserud, D.J.; Fridriksson, E.K.; McLafferty, F.W. Top down versus bottom up protein characterization by tandem high-resolution mass spectrometry, *J. Am. Chem. Soc.* **1999**, *121*, 806-812.

(173) Chait, B.T. Mass Spectrometry: Bottom-Up or Top-Down?, *Science* **2006**, *314*, 65-66.

(174) Bogdanov, B.; Smith, R.D. Proteomics by FTICR mass spectrometry: Top down and bottom up, *Mass Spectrom. Rev.* **2005**, *24*, 168-200.

(175) Siuti, N.; Kelleher, N.L. Decoding protein modifications using top-down mass spectrometry, *Nat Meth* **2007**, *4*, 817-821.

(176) McLafferty, F.W.; Breuker, K.; Jin, M.; Han, X.; Infusini, G.; Jiang, H.; Kong, X.; Begley, T.P. Top-down MS, a powerful complement to the high capabilities of proteolysis proteomics, *FEBS J.* **2007**, *274*, 6256-6268.

(177) Pan, J.; Borchers, C.H. Top-down structural analysis of posttranslationally modified proteins by Fourier transform ion cyclotron resonance-MS with hydrogen/deuterium exchange and electron capture dissociation, *Proteomics* **2013**, 974-981.

(178) Li, H.; Lin, T.-Y.; Van Orden, S.L.; Zhao, Y.; Barrow, M.P.; Pizarro, A.M.; Qi, Y.; Sadler, P.J.; O'Connor, P.B. Use of Top-Down and Bottom-Up Fourier transform ion cyclotron resonance mass spectrometry for mapping calmodulin sites modified by platinum anticancer drugs, *Anal. Chem.* **2011**, *83*, 9507-9515.

(179) Zhao, C.; Sethuraman, M.; Clavreul, N.; Kaur, P.; Cohen, R.A.; O'Connor, P.B. Detailed map of oxidative post-translational modifications of human P21Ras using Fourier transform mass spectrometry, *Anal. Chem.* **2006**, *78*, 5134-5142.

(180) Sweet, S.M.M.; Bailey, C.M.; Cunningham, D.L.; Heath, J.K.; Cooper, H.J. Large scale localization of protein phosphorylation by use of electron capture dissociation mass spectrometry, *Mol. Cell. Proteomics* **2009**, *8*, 904-912.

- (181) Zhang, H.; Ge, Y. Comprehensive analysis of protein modifications by top-down mass spectrometry, *Circ.: Cardiovasc. Genet.* **2011**, *4*, 711.
- (182) Gault, J.; Malosse, C.; Machata, S.; Millien, C.; Podglajen, I.; Ploy, M.-C.; Costello, C.E.; Duménil, G.; Chamot-Rooke, J. Complete posttranslational modification mapping of pathogenic *Neisseria meningitidis* pilins requires top-down mass spectrometry, *Proteomics* **2014**, *14*, 1141-1151.
- (183) Sze, S.K.; Ge, Y.; Oh, H.; McLafferty, F.W. Top-down mass spectrometry of a 29-kDa protein for characterization of any posttranslational modification to within one residue, *Proc. Natl. Acad. Sci.* **2002**, *99*, 1774-1779.
- (184) Yin, S.; Loo, J.A. Top-down mass spectrometry of supercharged native protein–ligand complexes, *Int. J. Mass spectrom.* **2011**, *300*, 118-122.
- (185) Siuti, N.; Kelleher, N.L. Decoding protein modifications using top-down mass spectrometry, *Nat. Methods* **2007**, *4*, 817-821.
- (186) Sargaeva, N.P.; Lin, C.; O'Connor, P.B. Identification of aspartic and isoaspartic acid residues in amyloid β peptides, including A β 1-42, using electron–ion reactions, *Anal. Chem.* **2009**, *81*, 9778-9786.
- (187) Tran, J.C.; Zamdborg, L.; Ahlf, D.R.; Lee, J.E.; Catherman, A.D.; Durbin, K.R.; Tipton, J.D.; Vellaichamy, A.; Kellie, J.F.; Li, M.; Wu, C.; Sweet, S.M.M.; Early, B.P.; Siuti, N.; LeDuc, R.D.; Compton, P.D.; Thomas, P.M.; Kelleher, N.L. Mapping intact protein isoforms in discovery mode using top-down proteomics, *Nature* **2011**, *480*, 254-258.
- (188) Halgand, F.; Zabrouskov, V.; Bassilian, S.; Souda, P.; Loo, J.A.; Faull, K.F.; Wong, D.T.; Whitelegge, J.P. Defining intact protein primary structures from saliva: A step toward the human proteome project, *Anal. Chem.* **2012**, *84*, 4383-4395.
- (189) Wu, S.; Brown, J.N.; Tolić, N.; Meng, D.; Liu, X.; Zhang, H.; Zhao, R.; Moore, R.J.; Pevzner, P.; Smith, R.D.; Paša-Tolić, L. Quantitative analysis of human salivary gland-derived intact proteome using top-down mass spectrometry, *Proteomics* **2014**, *14*, 1211-1222.
- (190) Tipton, J.D.; Tran, J.C.; Catherman, A.D.; Ahlf, D.R.; Durbin, K.R.; Kelleher, N.L. Analysis of intact protein isoforms by mass spectrometry, *J. Biol. Chem.* **2011**, *286*, 25451-25458.
- (191) Peng, Y.; Chen, X.; Sato, T.; Rankin, S.A.; Tsuji, R.F.; Ge, Y. Purification and high-resolution top-down mass spectrometric characterization of human salivary α -amylase, *Anal. Chem.* **2012**, *84*, 3339-3346.
- (192) Lee, S.-W.; Berger, S.J.; Martinović, S.; Paša-Tolić, L.; Anderson, G.A.; Shen, Y.; Zhao, R.; Smith, R.D. Direct mass spectrometric analysis of intact proteins of the yeast large ribosomal subunit using capillary LC/FTICR, *Proc. Natl. Acad. Sci.* **2002**, *99*, 5942-5947.
- (193) Aebersold, R.; Mann, M. Mass spectrometry-based proteomics, *Nature* **2003**, *421*, 198-207.
- (194) Ryan, C.M.; Souda, P.; Halgand, F.; Wong, D.T.; Loo, J.A.; Faull, K.F.; Whitelegge, J.P. Confident assignment of intact mass tags to human salivary cystatins using top-down Fourier-transform ion cyclotron resonance mass spectrometry, *J. Am. Soc. Mass. Spectrom.* **2010**, *21*, 908-917.

- (195) Laitaoja, M.; Sankhala, R.S.; Swamy, M.J.; Jänis, J. Top-down mass spectrometry reveals new sequence variants of the major bovine seminal plasma protein PDC-109, *J. Mass Spectrom.* **2012**, *47*, 853-859.
- (196) Xie, Y.; Zhang, J.; Yin, S.; Loo, J.A. Top-Down ESI-ECD-FT-ICR mass spectrometry localizes noncovalent protein-ligand binding sites, *J. Am. Chem. Soc.* **2006**, *128*, 14432-14433.
- (197) Haselmann, K.F.; Jørgensen, T.J.D.; Budnik, B.A.; Jensen, F.; Zubarev, R.A. Electron capture dissociation of weakly bound polypeptide polycationic complexes, *Rapid Commun. Mass Spectrom.* **2002**, *16*, 2260-2265.
- (198) Clarke, D.; Murray, E.; Hupp, T.; Mackay, C.; Langridge-Smith, P. Mapping a Noncovalent Protein-Peptide Interface by Top-Down FTICR Mass Spectrometry Using Electron Capture Dissociation, *J. Am. Soc. Mass. Spectrom.* **2011**, *22*, 1432-1440.
- (199) Yin, S.; Loo, J.A. Elucidating the site of protein-ATP binding by top-down mass spectrometry, *J. Am. Soc. Mass. Spectrom.* **2010**, *21*, 899-907.
- (200) Zheng, Y.; John, S.; Pesavento, J.J.; Schultz-Norton, J.R.; Schiltz, R.L.; Baek, S.; Nardulli, A.M.; Hager, G.L.; Kelleher, N.L.; Mizzen, C.A. Histone H1 phosphorylation is associated with transcription by RNA polymerases I and II, *The Journal of Cell Biology* **2010**, *189*, 407-415.
- (201) Parks, B.A.; Jiang, L.; Thomas, P.M.; Wenger, C.D.; Roth, M.J.; Boyne, M.T.; Burke, P.V.; Kwast, K.E.; Kelleher, N.L. Top-Down proteomics on a chromatographic time scale using linear ion trap Fourier transform hybrid mass spectrometers, *Anal. Chem.* **2007**, *79*, 7984-7991.
- (202) Thomas, C.E.; Kelleher, N.L.; Mizzen, C.A. Mass spectrometric characterization of human histone H3: a bird's eye view, *J. Proteome Res.* **2006**, *5*, 240-247.
- (203) Yang, H.; Pesavento, J.J.; Starnes, T.W.; Cryderman, D.E.; Wallrath, L.L.; Kelleher, N.L.; Mizzen, C.A. Preferential dimethylation of histone H4 lysine 20 by Suv4-20, *J. Biol. Chem.* **2008**, *283*, 12085-12092.
- (204) Valeja, S.G.; Kaiser, N.K.; Xian, F.; Hendrickson, C.L.; Rouse, J.C.; Marshall, A.G. Unit mass baseline resolution for an intact 148 kDa therapeutic monoclonal antibody by Fourier transform ion cyclotron resonance mass spectrometry, *Anal. Chem.* **2011**, *83*, 8391-8395.
- (205) Zhang, H.; Cui, W.; Wen, J.; Blankenship, R.E.; Gross, M.L. Native Electrospray and Electron-Capture Dissociation FTICR Mass Spectrometry for Top-Down Studies of Protein Assemblies, *Anal. Chem.* **2011**, *83*, 5598-5606.
- (206) Zhang, H.; Cui, W.; Wen, J.; Blankenship, R.E.; Gross, M.L. Native electrospray and electron-capture dissociation in FTICR mass spectrometry provide top-down sequencing of a protein component in an intact protein assembly, *J. Am. Soc. Mass. Spectrom.* **2010**, *21*, 1966-1968.
- (207) Wen, J.; Zhang, H.; Gross, M.L.; Blankenship, R.E. Native electrospray mass spectrometry reveals the nature and stoichiometry of pigments in the FMO photosynthetic antenna protein, *Biochemistry* **2011**, *50*, 3502-3511.
- (208) Li, H.; Wolff, J.J.; Van Orden, S.L.; Loo, J.A. Native top-down electrospray ionization-mass spectrometry of 158 kDa protein complex by high-resolution

Fourier transform ion cyclotron resonance mass spectrometry, *Anal. Chem.* **2013**, *86*, 317-320.

(209) Van Agthoven, M.A.; Delsuc, M.-A.; Bodenhausen, G.; Rolando, C. Towards analytically useful two-dimensional Fourier transform ion cyclotron resonance mass spectrometry, *Anal. Bioanal. Chem.* **2013**, *405*, 51-61.

(210) Pfaendler, P.; Bodenhausen, G.; Rapin, J.; Walser, M.E.; Gaeumann, T. Broad-band two-dimensional Fourier transform ion cyclotron resonance, *J. Am. Chem. Soc.* **1988**, *110*, 5625-5628.

(211) van der Rest, G.; Marshall, A.G. Noise analysis for 2D tandem Fourier transform ion cyclotron resonance mass spectrometry, *Int. J. Mass spectrom.* **2001**, *210*, 101-111.

(212) Ross, C.W.; Simonsick, W.J.; Aaserud, D.J. Application of stored waveform ion modulation 2D-FTICR MS/MS to the analysis of complex mixtures, *Anal. Chem.* **2002**, *74*, 4625-4633.

(213) van Agthoven, M.A.; Chiron, L.; Coutouly, M.-A.; Sehgal, A.A.; Pelupessy, P.; Delsuc, M.-A.; Rolando, C. Optimization of the discrete pulse sequence for two-dimensional FT-ICR mass spectrometry using infrared multiphoton dissociation, *Int. J. Mass spectrom.* **2014**, *370*, 114-124.

(214) van Agthoven, M.A.; Chiron, L.; Coutouly, M.-A.; Delsuc, M.-A.; Rolando, C. Two-dimensional ECD FT-ICR mass spectrometry of peptides and glycopeptides, *Anal. Chem.* **2012**, *84*, 5589-5595.

(215) Thomson, J.; Aston, F.; Soddy, F.; Merton, T.; Lindemann, F. Discussion on isotopes, *P. Roy. Soc. Lond. A* **1921**, *99*, 87-104.

(216) Becker, J.S. State-of-the-art and progress in precise and accurate isotope ratio measurements by ICP-MS and LA-ICP-MS Plenary Lecture, *J. Anal. At. Spectrom.* **2002**, *17*, 1172-1185.

(217) Heumann, K.; Schmidt, T. Isotope ratio measurements: new developments and applications, *Anal. Bioanal. Chem.* **2013**, *405*, 2747-2748.

(218) Meier-Augenstein, W. Applied gas chromatography coupled to isotope ratio mass spectrometry, *J. Chromatogr. A* **1999**, *842*, 351-371.

(219) G. Heumann, K.; M. Gallus, S.; Radlinger, G.; Vogl, J. Precision and accuracy in isotope ratio measurements by plasma source mass spectrometry, *J. Anal. At. Spectrom.* **1998**, *13*, 1001-1008.

(220) Berman, E.S.; Levin, N.E.; Landais, A.; Li, S.; Owano, T. Measurement of $\delta^{18}\text{O}$, $\delta^{17}\text{O}$, and ^{17}O -excess in water by off-axis integrated cavity output spectroscopy and isotope ratio mass spectrometry, *Anal. Chem.* **2013**, *85*, 10392-10398.

(221) Brand, W.A.; Geilmann, H.; Crosson, E.R.; Rella, C.W. Cavity ring-down spectroscopy versus high-temperature conversion isotope ratio mass spectrometry; a case study on $\delta^2\text{H}$ and $\delta^{18}\text{O}$ of pure water samples and alcohol/water mixtures, *Rapid Commun. Mass Spectrom.* **2009**, *23*, 1879-1884.

(222) Zare, R.N.; Kuramoto, D.S.; Haase, C.; Tan, S.M.; Crosson, E.R.; Saad, N.M.R.; Thieme, M.H. High-precision optical measurements of $^{13}\text{C}/^{12}\text{C}$ isotope ratios in organic compounds at natural abundance, *Proc. Natl. Acad. Sci. U. S. A.* **2009**, *106*, 10928-10932.

- (223) Selkoe, D.J. Alzheimer's disease, *Cold Spring Harbor Perspectives in Biology* **2011**, 3, 42-58.
- (224) Chimon, S.; Shaibat, M.A.; Jones, C.R.; Calero, D.C.; Aizezi, B.; Ishii, Y. Evidence of fibril-like [beta]-sheet structures in a neurotoxic amyloid intermediate of Alzheimer's [beta]-amyloid, *Nat Struct Mol Biol* **2007**, 14, 1157-1164.
- (225) Petkova, A.T.; Leapman, R.D.; Guo, Z.; Yau, W.-M.; Mattson, M.P.; Tycko, R. Self-propagating, molecular-level polymorphism in Alzheimer's β -amyloid fibrils, *Science* **2005**, 307, 262-265.
- (226) Selkoe, D.J. Folding proteins in fatal ways, *Nature* **2003**, 426, 900-904.
- (227) Lührs, T.; Ritter, C.; Adrian, M.; Riek-Loher, D.; Bohrmann, B.; Döbeli, H.; Schubert, D.; Riek, R. 3D structure of Alzheimer's amyloid- β (1-42) fibrils, *Proc. Natl. Acad. Sci. U. S. A.* **2005**, 102, 17342-17347.
- (228) Gu, L.; Liu, C.; Guo, Z. Structural insights into A β 42 oligomers using site-directed spin labeling, *J. Biol. Chem.* **2013**, 288, 18673-18683.
- (229) Hung, I.; Uldry, A.-C.; Becker-Baldus, J.; Webber, A.L.; Wong, A.; Smith, M.E.; Joyce, S.n.N.A.; Yates, J.R.; Pickard, C.J.; Dupree, R.; Brown, S.P. Probing heteronuclear ^{15}N - ^{17}O and ^{13}C - ^{17}O connectivities and proximities by Solid-state NMR spectroscopy, *J. Am. Chem. Soc.* **2009**, 131, 1820-1834.
- (230) Antzutkin, O.N.; Iuga, D.; Filippov, A.V.; Kelly, R.T.; Becker-Baldus, J.; Brown, S.P.; Dupree, R. Hydrogen bonding in Alzheimer's amyloid- β fibrils probed by $^{15}\text{N}\{^{17}\text{O}\}$ REAPDOR solid-state NMR spectroscopy, *Angew. Chem. Int. Ed.* **2012**, 51, 10289-10292.
- (231) Balbach, J.J.; Ishii, Y.; Antzutkin, O.N.; Leapman, R.D.; Rizzo, N.W.; Dyda, F.; Reed, J.; Tycko, R. Amyloid fibril formation by A β 16-22, a seven-residue fragment of the Alzheimer's β -amyloid peptide, and structural characterization by solid state NMR, *Biochemistry* **2000**, 39, 13748-13759.
- (232) Petkova, A.T.; Buntkowsky, G.; Dyda, F.; Leapman, R.D.; Yau, W.M.; Tycko, R. Solid state NMR reveals a pH-dependent antiparallel β -sheet registry in fibrils formed by a β -amyloid peptide, *J. Mol. Biol.* **2004**, 335, 247-260.
- (233) West, A.G.; Goldsmith, G.R.; Brooks, P.D.; Dawson, T.E. Discrepancies between isotope ratio infrared spectroscopy and isotope ratio mass spectrometry for the stable isotope analysis of plant and soil waters, *Rapid Commun. Mass Spectrom.* **2010**, 24, 1948-1954.
- (234) Audi, G.; Wapstra, A. The 1995 update to the atomic mass evaluation, *Nucl. Phys. A* **1995**, 595, 409-480.
- (235) Rosman, K.; Taylor, P. Table of isotopic masses and natural abundances, *Pure Appl. Chem* **1999**, 71, 1593-1607.
- (236) Drader, J.J.; Shi, S.D.H.; Blakney, G.T.; Hendrickson, C.L.; Laude, D.A.; Marshall, A.G. Digital quadrature heterodyne detection for high-resolution Fourier transform ion cyclotron resonance mass spectrometry, *Anal. Chem.* **1999**, 71, 4758-4763.
- (237) Senko, M. Isopro 3.0, **2003**.
- (238) Stults, J.T. Minimizing peak coalescence: high-resolution separation of isotope peaks in partially deamidated peptides by Matrix-Assisted Laser Desorption/Ionization Fourier transform Ion cyclotron resonance mass spectrometry, *Anal. Chem.* **1997**, 69, 1815-1819.

- (239) Chen, S.-P.; Comisarow, M.B. Simple physical models for coulomb-induced frequency shifts and coulomb-induced inhomogeneous broadening for like and unlike ions in fourier transform ion cyclotron resonance mass spectrometry, *Rapid Commun. Mass Spectrom.* **1991**, *5*, 450-455.
- (240) Naito, Y.; Inoue, M. Collective motion of ions in an ion trap for Fourier transform ion cyclotron resonance mass spectrometry, *Int. J. Mass Spectrom. Ion Processes* **1996**, *157*, 85-96.
- (241) Boldin, I.A.; Nikolaev, E.N. Theory of peak coalescence in Fourier transform ion cyclotron resonance mass spectrometry, *Rapid Commun. Mass Spectrom.* **2009**, *23*, 3213-3219.
- (242) Taylor, P.K.; Amster, I.J. Space charge effects on mass accuracy for multiply charged ions in ESI-FTICR, *Int. J. Mass spectrom.* **2003**, *222*, 351-361.
- (243) Pasch, H.; Schrepp, W., MALDI-TOF mass spectrometry of synthetic polymers, Springer, 2003.
- (244) Yan, A.; Von Dem Bussche, A.; Kane, A.B.; Hurt, R.H. Tocopheryl polyethylene glycol succinate as a safe, antioxidant surfactant for processing carbon nanotubes and fullerenes, *Carbon* **2007**, *45*, 2463-2470.
- (245) Mu, L.; Seow, P.H. Application of TPGS in polymeric nanoparticulate drug delivery system, *Colloids Surf. B. Biointerfaces* **2006**, *47*, 90-97.
- (246) Guo, Y.; Luo, J.; Tan, S.; Otieno, B.O.; Zhang, Z. The applications of Vitamin E TPGS in drug delivery, *Eur. J. Pharm. Sci.* **2013**, *49*, 175-186.
- (247) Dintaman, J.; Silverman, J. Inhibition of P-glycoprotein by D- α -tocopheryl polyethylene glycol 1000 succinate (TPGS), *Pharm. Res.* **1999**, *16*, 1550-1556.
- (248) Zhang, Z.; Tan, S.; Feng, S.-S. Vitamin E TPGS as a molecular biomaterial for drug delivery, *Biomaterials* **2012**, *33*, 4889-4906.
- (249) Kong, L.Y.; Su, B.G.; Bao, Z.B.; Xing, H.B.; Yang, Y.W.; Ren, Q.L. Direct quantification of mono- and di-d- α -tocopherol polyethylene glycol 1000 succinate by high performance liquid chromatography, *J. Chromatogr. A* **2011**, *1218*, 8664-8671.
- (250) Wang, J.; Su, B.; Xing, H.; Yang, Y.; Ren, Q. Preparation and characterization of mono- and di-d- α -tocopheryl polyethylene glycol 1000 succinate, *J. Appl. Polym. Sci.* **2011**, *119*, 3026-3033.
- (251) Christiansen, A.; Backensfeld, T.; Kühn, S.; Weitschies, W. Investigating the stability of the nonionic surfactants tocopheryl polyethylene glycol succinate and sucrose laurate by HPLC-MS, DAD, and CAD, *J. Pharm. Sci.* **2011**, *100*, 1773-1782.
- (252) Cao, N.; Feng, S.-S. Doxorubicin conjugated to d- α -tocopheryl polyethylene glycol 1000 succinate (TPGS): Conjugation chemistry, characterization, in vitro and in vivo evaluation, *Biomaterials* **2008**, *29*, 3856-3865.
- (253) Bogan, M.J.; Agnes, G.R. Poly(ethylene glycol) doubly and singly cationized by different alkali metal ions: Relative cation affinities and cation-dependent resolution in a quadrupole ion trap mass spectrometer, *J. Am. Soc. Mass. Spectrom.* **2002**, *13*, 177-186.
- (254) Kilgour, D.P.; Wills, R.; Qi, Y.; O'Connor, P.B. Autophaser: an algorithm for automated generation of absorption mode spectra for FT-ICR MS, *Anal Chem* **2013**, *85*, 3903-3911.

- (255) Mautjana, N.A.; Pasch, H. Matrix-assisted laser desorption ionization mass spectrometry of synthetic polymers, *Macromol. Symp.* **2012**, 313-314, 157-161.
- (256) Jackson, A.T.; Williams, J.P.; Scrivens, J.H. Desorption electrospray ionisation mass spectrometry and tandem mass spectrometry of low molecular weight synthetic polymers, *Rapid Commun. Mass Spectrom.* **2006**, 20, 2717-2727.
- (257) Deery, M.J.; Jennings, K.R.; Jasieczek, C.B.; Haddleton, D.M.; Jackson, A.T.; Yates, H.T.; Scrivens, J.H. A study of cation attachment to polystyrene by means of matrix-assisted laser desorption/ionization and electrospray ionization-mass spectrometry, *Rapid Commun. Mass Spectrom.* **1997**, 11, 57-62.
- (258) Chen, R.; Li, L. Lithium and transition metal ions enable low energy collision-induced dissociation of polyglycols in electrospray ionization mass spectrometry, *J. Am. Soc. Mass. Spectrom.* **2001**, 12, 832-839.
- (259) Rashidezadeh, H.; Guo, B. Investigation of metal attachment to polystyrenes in matrix-assisted laser desorption ionization, *J. Am. Soc. Mass. Spectrom.* **1998**, 9, 724-730.
- (260) Kuki, Á.; Nagy, L.; Shemirani, G.; Memboeuf, A.; Drahos, L.; Vékey, K.; Zsuga, M.; Kéki, S. A simple method to estimate relative stabilities of polyethers cationized by alkali metal ions, *Rapid Commun. Mass Spectrom.* **2012**, 26, 304-308.
- (261) Kéki, S.; Nagy, L.; Deák, G.; Zsuga, M. Multiple charging of poly (propylene glycol) by binary mixtures of cations in electrospray, *J. Am. Soc. Mass. Spectrom.* **2005**, 16, 152-157.
- (262) Li, X.; Guo, L.; Casiano-Maldonado, M.; Zhang, D.; Wesdemiotis, C. Top-down multidimensional mass spectrometry methods for synthetic polymer analysis, *Macromolecules* **2011**, 44, 4555-4564.
- (263) Nielen, M.W. MALDI time-of-flight mass spectrometry of synthetic polymers, *Mass Spectrom. Rev.* **1999**, 18, 309-344.
- (264) Kéki, S.; Deák, G.; Zsuga, M. Copper(I) chloride: a simple salt for enhancement of polystyrene cationization in matrix-assisted laser desorption/ionization mass spectrometry, *Rapid Commun. Mass Spectrom.* **2001**, 15, 675-678.
- (265) Gidden, J.; Wyttenbach, T.; Jackson, A.T.; Scrivens, J.H.; Bowers, M.T. Gas-phase conformations of synthetic polymers: Poly (ethylene glycol), poly (propylene glycol), and poly (tetramethylene glycol), *J. Am. Chem. Soc.* **2000**, 122, 4692-4699.
- (266) Nasioudis, A.; Joyce, W.F.; Velde, J.W.v.; Heeren, R.M.A.; Brink, O.F.v.d. Formation of low charge state ions of synthetic polymers using quaternary ammonium compounds, *Anal. Chem.* **2010**, 82, 5735-5742.
- (267) Adamson, J.T.; Håkansson, K. Electron capture dissociation of oligosaccharides ionized with alkali, alkaline earth, and transition metals, *Anal. Chem.* **2007**, 79, 2901-2910.
- (268) Cancilla, M.T.; Penn, S.G.; Carroll, J.A.; Lebrilla, C.B. Coordination of alkali metals to oligosaccharides dictates fragmentation behavior in matrix

assisted laser desorption ionization/Fourier transform mass spectrometry, *J. Am. Chem. Soc.* **1996**, *118*, 6736-6745.

(269) Ropartz, D.; Bodet, P.-E.; Przybylski, C.; Gonnet, F.; Daniel, R.; Fer, M.; Helbert, W.; Bertrand, D.; Rogniaux, H. Performance evaluation on a wide set of matrix-assisted laser desorption ionization matrices for the detection of oligosaccharides in a high-throughput mass spectrometric screening of carbohydrate depolymerizing enzymes, *Rapid Commun. Mass Spectrom.* **2011**, *25*, 2059-2070.

(270) Liu, H.; Håkansson, K. Divalent metal ion-peptide interactions probed by electron capture dissociation of trications, *J. Am. Soc. Mass. Spectrom.* **2006**, *17*, 1731-1741.

(271) Mosely, J.; Murray, B.; Parker, D. Electron-capture dissociation and collision-induced dissociation of lanthanide metal–ligand complexes and lanthanide metal–ligand complexes bound to phosphopeptides, *Eur. J. Mass Spectrom.* **2009**, *15*, 145-155.

(272) Fung, Y.M.E.; Liu, H.; Chan, T.W.D. Electron capture dissociation of peptides metalated with alkaline-earth metal ions, *J. Am. Soc. Mass. Spectrom.* **2006**, *17*, 757-771.

(273) Flick, T.; Donald, W.; Williams, E. Electron capture dissociation of trivalent metal ion-peptide complexes, *J. Am. Soc. Mass. Spectrom.* **2013**, *24*, 193-201.

(274) Iavarone, A.T.; Paech, K.; Williams, E.R. Effects of charge state and cationizing agent on the electron capture dissociation of a peptide, *Anal. Chem.* **2004**, *76*, 2231-2238.

(275) Lattimer, R.P. Tandem mass spectrometry of lithium-attachment ions from polyglycols, *J. Am. Soc. Mass. Spectrom.* **1992**, *3*, 225-234.

(276) Gidden, J.; Bowers, M.T.; Jackson, A.T.; Scrivens, J.H. Gas-phase conformations of cationized poly(styrene) oligomers, *J. Am. Soc. Mass. Spectrom.* **2002**, *13*, 499-505.

(277) Selby, T.L.; Wesdemiotis, C.; Lattimer, R.P. Dissociation characteristics of $[M+X]^+$ ions ($X=H, Li, Na, K$) from linear and cyclic polyglycols, *J. Am. Soc. Mass. Spectrom.* **1994**, *5*, 1081-1092.

(278) Wallow, T.I.; Novak, B.M. In aqua synthesis of water-soluble poly (p-phenylene) derivatives, *J. Am. Chem. Soc.* **1991**, *113*, 7411-7412.

(279) McNeill, I.C.; Zulficar, M. Preparation and degradation of salts of poly(methacrylic acid). I. Lithium, sodium, potassium, and caesium salts, *J. Polym. Sci. A Polym. Chem.* **1978**, *16*, 3201-3212.

(280) Gao, S.; Zhang, Z.-P.; Karnes, H.T. Sensitivity enhancement in liquid chromatography/atmospheric pressure ionization mass spectrometry using derivatization and mobile phase additives, *J. Chromatogr. B* **2005**, *825*, 98-110.

(281) Vékey, K.; Memboeuf, A.; Lendvay, G. Structure and energetics of poly(ethylene glycol) cationized by Li^+ , Na^+ , K^+ and Cs^+ : a first-principles study, *Eur. J. Mass Spectrom.* **2011**, *17*, 33-46.

(282) Girod, M.; Carissan, Y.; Humbel, S.; Charles, L. Tandem mass spectrometry of doubly charged poly (ethylene oxide) oligomers produced by electrospray ionization, *Int. J. Mass spectrom.* **2008**, *272*, 1-11.

- (283) Cerda, B.A.; Horn, D.M.; Breuker, K.; McLafferty, F.W. Sequencing of specific copolymer oligomers by electron-capture-dissociation mass spectrometry, *J. Am. Chem. Soc.* **2002**, *124*, 9287-9291.
- (284) Koster, S.; Duursma, M.; Boon, J.; Heeren, R.A.; Ingemann, S.; Benthem, R.T.M.; Koster, C. Electron capture and collisionally activated dissociation mass spectrometry of doubly charged hyperbranched polyesteramides, *J. Am. Soc. Mass. Spectrom.* **2003**, *14*, 332-341.
- (285) Chen, X.; Fung, Y.; Chan, W.; Wong, P.; Yeung, H.; Chan, T.W.D. Transition metal ions: Charge carriers that mediate the electron capture dissociation pathways of peptides, *J. Am. Soc. Mass. Spectrom.* **2011**, *22*, 2232-2245.
- (286) Atkins, P.; De Paula, J., Elements of physical chemistry, Macmillan, 2009, pp. 216-220.
- (287) Paizs, B.; Suhai, S. Fragmentation pathways of protonated peptides, *Mass Spectrom. Rev.* **2005**, *24*, 508-548.
- (288) Björn, L.; Papageorgiou, G.; Blankenship, R.; Govindjee, G. A viewpoint: Why chlorophyll a?, *Photosynth. Res.* **2009**, *99*, 85-98.
- (289) Aronoff, S.; Mackinney, G. The photo-oxidation of chlorophyll, *J. Am. Chem. Soc.* **1943**, *65*, 956-958.
- (290) Scheer, H., An Overview of Chlorophylls and Bacteriochlorophylls: Biochemistry, Biophysics, Functions and Applications. in: Grimm, B.; Porra, R.J.; Rüdiger, W.; Scheer, H., (Eds.), *Chlorophylls and Bacteriochlorophylls*, Springer Netherlands, 2006, pp. 1-26.
- (291) De Paula, J.C.; Robblee, J.H.; Pasternack, R.F. Aggregation of chlorophyll a probed by resonance light scattering spectroscopy, *Biophys. J.* **1995**, *68*, 335-341.
- (292) Wang, X.-F.; Xiang, J.; Wang, P.; Koyama, Y.; Yanagida, S.; Wada, Y.; Hamada, K.; Sasaki, S.-i.; Tamiaki, H. Dye-sensitized solar cells using a chlorophyll a derivative as the sensitizer and carotenoids having different conjugation lengths as redox spacers, *Chem. Phys. Lett.* **2005**, *408*, 409-414.
- (293) Hörtensteiner, S.; Kräutler, B. Chlorophyll breakdown in higher plants, *Biochim. Biophys. Acta, Bioenerg.* **2011**, *1807*, 977-988.
- (294) Sleno, L.; Windust, A.; Volmer, D. Structural study of spirolide marine toxins by mass spectrometry, *Anal. Bioanal. Chem.* **2004**, *378*, 969-976.
- (295) Hanson, C.W.; Thaler, E.R. Electronic nose prediction of a clinical pneumonia score: Biosensors and microbes, *Anesthesiology* **2005**, *102*, 63-68.
- (296) Van Breemen, R.B.; Canjura, F.L.; Schwartz, S.J. Identification of chlorophyll derivatives by mass spectrometry, *J. Agric. Food. Chem.* **1991**, *39*, 1452-1456.
- (297) Suman, M.; De Maria, R.; Catellani, D. Chromatographic evaluation of chlorophyll derivatives in pasta-based food products: effects of pasteurization treatments and correlation with sensory profiles, *J. Sci. Food Agric.* **2008**, *88*, 471-478.
- (298) Kao, T.H.; Chen, C.J.; Chen, B.H. An improved high performance liquid chromatography-photodiode array detection-atmospheric pressure chemical ionization-mass spectrometry method for determination of chlorophylls and their

derivatives in freeze-dried and hot-air-dried *Rhinacanthus nasutus* (L.) Kurz, *Talanta* **2011**, *86*, 349-355.

(299) Bale, N.J.; Llewellyn, C.A.; Airs, R.L. Atmospheric pressure chemical ionisation liquid chromatography/mass spectrometry of type II chlorophyll-a transformation products: Diagnostic fragmentation patterns, *Org. Geochem.* **2010**, *41*, 473-481.

(300) Suzuki, T.; Midonoya, H.; Shioi, Y. Analysis of chlorophylls and their derivatives by matrix-assisted laser desorption/ionization–time-of-flight mass spectrometry, *Anal. Biochem.* **2009**, *390*, 57-62.

(301) Hunt, J.E.; Macfarlane, R.D.; Katz, J.J.; Dougherty, R.C. High-energy fragmentation of chlorophyll a and its fully deuterated analog by californium-252 plasma desorption mass spectrometry, *J. Am. Chem. Soc.* **1981**, *103*, 6775-6778.

(302) Chait, B.T.; Field, F.H. Californium-252 fission fragment ionization mass spectrometry of chlorophyll a, *J. Am. Chem. Soc.* **1984**, *106*, 1931-1938.

(303) Grese, R.P.; Cerny, R.L.; Gross, M.L.; Senge, M. Determination of structure and properties of modified chlorophylls by using fast atom bombardment combined with tandem mass spectrometry, *J. Am. Soc. Mass. Spectrom.* **1990**, *1*, 72-84.

(304) Dale, M.J.; Costello, K.F.; Jones, A.C.; Langridge-Smith, P.R.R. Investigation of porphyrins and metalloporphyrins using two-step laser mass spectrometry, *J. Mass Spectrom.* **1996**, *31*, 590-601.

(305) Van Berkel, G.J.; Glish, G.L.; McLuckey, S.A.; Tuinman, A.A. Porphyrin pyrrole sequencing: low-energy collision-induced dissociation of $(M + 7H)^+$ generated in-situ during ammonia chemical ionization, *Anal. Chem.* **1990**, *62*, 786-793.

(306) Rosario, M.; Domingues, M.; Nemirovskiy, O.; Graço, M.; Marques, O.; Neves, M.; Cavaleiro, J.; Ferrer-Correia, A.; Gross, M. High- and low-energy collisionally activated decompositions of octaethylporphyrin and its metal complexes, *J. Am. Soc. Mass. Spectrom.* **1998**, *9*, 767-774.

(307) Bernigaud, V.; Drenck, K.; Huber, B.A.; Hvelplund, P.; Jabot, T.; Kadhane, U.; Kirketerp, M.-B.S.; Liu, B.; Lykkegaard, M.K.; Manil, B.; Nielsen, S.B. Electron capture induced dissociation of protoporphyrin IX ions, *J. Am. Soc. Mass. Spectrom.* **2008**, *19*, 809-813.

(308) Fiedor, L.; Kania, A.; Myśliwa-Kurdziel, B.; Orzeł, Ł.; Stochel, G. Understanding chlorophylls: Central magnesium ion and phytol as structural determinants, *Biochim. Biophys. Acta, Bioenerg.* **2008**, *1777*, 1491-1500.

(309) Hoffmann, d.E.; Stroobant, V., *Mass Spectrometry: Principles and Applications*, John Wiley & Son Ltd, England, 2007.

(310) Chow, H.-C.; Serlin, R.; Strouse, C.E. Crystal and molecular structure and absolute configuration of ethyl chlorophyllide a-dihydrate. Model for the different spectral forms of chlorophyll a, *J. Am. Chem. Soc.* **1975**, *97*, 7230-7237.

(311) Grese, R.P.; Cerny, R.L.; Gross, M.L.; Senge, M. Determination of structure and properties of modified chlorophylls by using fast atom bombardment combined with tandem mass spectrometry, *J. Am. Soc. Mass. Spectrom.* **1999**, *1*, 72-84.

- (312) Mauzerall, D. Multiple excitations in photosynthetic systems, *Biophys. J.* **1976**, *16*, 87-91.
- (313) Weigl, J.W.; Livingston, R. Infrared spectra of chlorophyll and related compounds, *J. Am. Chem. Soc.* **1953**, *75*, 2173-2176.
- (314) Holt, A.S.; Jacobs, E.E. Infra-red absorption spectra of chlorophylls and derivatives, *Plant Physiol.* **1955**, *30*, 553-559.
- (315) Kadish, K.M.; Smith, K.M.; Guillard, R., The porphyrin handbook: phthalocyanines: synthesis, Academic Press, 2003.
- (316) Biesaga, M.; Pyrzyńska, K.; Trojanowicz, M. Porphyrins in analytical chemistry. A review, *Talanta* **2000**, *51*, 209-224.
- (317) Eckardt, N.A. A new chlorophyll degradation pathway, *Plant Cell* **2009**, *21*, 700.
- (318) Oh, H.B.; Moon, B. Radical-driven peptide backbone dissociation tandem mass spectrometry, *Mass Spectrom. Rev.* **2014**, DOI: 10.1002/mas.21426.
- (319) Karni, M.; Mandelbaum, A. The 'even-electron rule', *Org. Mass Spectrom.* **1980**, *15*, 53-64.
- (320) Fornal, E. Formation of odd-electron product ions in collision-induced fragmentation of electrospray-generated protonated cathinone derivatives: aryl α -primary amino ketones, *Rapid Commun. Mass Spectrom.* **2013**, *27*, 1858-1866.
- (321) Chai, Y.; Sun, H.; Pan, Y.; Sun, C. N-centered odd-electron ions formation from collision-induced dissociation of electrospray ionization generated even-electron ions: single electron transfer via ion/neutral complex in the fragmentation of protonated N, N'-dibenzylpiperazines and protonated N-benzylpiperazines, *J. Am. Soc. Mass. Spectrom.* **2011**, *22*, 1526-1533.
- (322) Chen, K.; Rannulu, N.S.; Cai, Y.; Lane, P.; Liebl, A.L.; Rees, B.B.; Corre, C.; Challis, G.L.; Cole, R.B. Unusual odd-electron fragments from even-electron protonated prodigine precursors using positive-ion electrospray tandem mass spectrometry, *J. Am. Soc. Mass. Spectrom.* **2008**, *19*, 1856-1866.
- (323) Williams, J.P.; Nibbering, N.M.; Green, B.N.; Patel, V.J.; Scrivens, J.H. Collision-induced fragmentation pathways including odd-electron ion formation from desorption electrospray ionisation generated protonated and deprotonated drugs derived from tandem accurate mass spectrometry, *J. Mass Spectrom.* **2006**, *41*, 1277-1286.
- (324) Cai, Y.; Mo, Z.; Rannulu, N.S.; Guan, B.; Kannupal, S.; Gibb, B.C.; Cole, R.B. Characterization of an exception to the 'even-electron rule' upon low-energy collision induced decomposition in negative ion electrospray tandem mass spectrometry, *J. Mass Spectrom.* **2010**, *45*, 235-240.
- (325) Mann, M.; Ong, S.-E.; Grønborg, M.; Steen, H.; Jensen, O.N.; Pandey, A. Analysis of protein phosphorylation using mass spectrometry: deciphering the phosphoproteome, *Trends Biotechnol.* **2002**, *20*, 261-268.
- (326) Paradela, A.; Albar, J.P. Advances in the analysis of protein phosphorylation, *J. Proteome Res.* **2008**, *7*, 1809-1818.
- (327) Vermeulen, L.; De Wilde, G.; Van Damme, P.; Vanden Berghe, W.; Haegeman, G. Transcriptional activation of the NF-[kappa]B p65 subunit by mitogen- and stress-activated protein kinase-1 (MSK1), *EMBO J* **2003**, *22*, 1313-1324.

- (328) Jackson, S.P. Regulating transcription factor activity by phosphorylation, *Trends Cell Biol.* **1992**, *2*, 104-108.
- (329) Kalume, D.E.; Molina, H.; Pandey, A. Tackling the phosphoproteome: tools and strategies, *Curr. Opin. Chem. Biol.* **2003**, *7*, 64-69.
- (330) Nilsson, C.L. Advances in quantitative phosphoproteomics, *Anal. Chem.* **2011**, *84*, 735-746.
- (331) Goshe, M.B. Characterizing phosphoproteins and phosphoproteomes using mass spectrometry, *Brief. Funct. Genomic. Proteomic.* **2006**, *4*, 363-376.
- (332) Karin, M.; Ben-Neriah, Y. Phosphorylation meets ubiquitination: The control of NF- κ B activity, *Annu. Rev. Immunol.* **2000**, *18*, 621-663.
- (333) Bonizzi, G.; Karin, M. The two NF- κ B activation pathways and their role in innate and adaptive immunity, *Trends Immunol.* **2004**, *25*, 280-288.
- (334) Vermeulen, L.; De Wilde, G.; Notebaert, S.; Vanden Berghe, W.; Haegeman, G. Regulation of the transcriptional activity of the nuclear factor- κ B p65 subunit, *Biochem. Pharmacol.* **2002**, *64*, 963-970.
- (335) Karin, M.; Delhase, M. The I κ B kinase (IKK) and NF- κ B: key elements of proinflammatory signalling, *Semin. Immunol.* **2000**, *12*, 85-98.
- (336) Escárcega, R.O.; Fuentes-Alexandro, S.; García-Carrasco, M.; Gatica, A.; Zamora, A. The transcription factor nuclear factor-kappa B and cancer, *Clinical Oncology* **2007**, *19*, 154-161.
- (337) Monaco, C.; Andreacos, E.; Kiriakidis, S.; Mauri, C.; Bicknell, C.; Foxwell, B.; Cheshire, N.; Paleolog, E.; Feldmann, M. Canonical pathway of nuclear factor κ B activation selectively regulates proinflammatory and prothrombotic responses in human atherosclerosis, *Proc. Natl. Acad. Sci. U. S. A.* **2004**, *101*, 5634-5639.
- (338) Attar, R.M.; Caamaño, J.; Carrasco, D.; Iotsova, V.; Ishikawa, H.; Ryseck, R.-P.; Weih, F.; Bravo, R. Genetic approaches to study Rel/NF- κ B/I κ B function in mice, *Semin. Cancer Biol.* **1997**, *8*, 93-101.
- (339) Sha, W.C.; Liou, H.C.; Tuomanen, E.I.; Baltimore, D. Targeted disruption of the p50 subunit of NF-kappa B leads to multifocal defects in immune responses, *Cell* **1995**, *80*, 321-30.
- (340) Snapper, C.M.; Zelazowski, P.; Rosas, F.R.; Kehry, M.R.; Tian, M.; Baltimore, D.; Sha, W.C. B cells from p50/NF-kappa B knockout mice have selective defects in proliferation, differentiation, germ-line CH transcription, and Ig class switching, *J. Immunol.* **1996**, *156*, 183-91.
- (341) Perkins, N.D. Post-translational modifications regulating the activity and function of the nuclear factor kappa B pathway, *Oncogene* **2006**, *25*, 6717-6730.
- (342) Viatour, P.; Merville, M.-P.; Bours, V.; Chariot, A. Phosphorylation of NF- κ B and I κ B proteins: implications in cancer and inflammation, *Trends Biochem. Sci* **2005**, *30*, 43-52.
- (343) Zhong, H.; SuYang, H.; Erdjument-Bromage, H.; Tempst, P.; Ghosh, S. The transcriptional activity of NF- κ B is regulated by the I κ B-associated PKAc subunit through a cyclic AMP-Independent mechanism, *Cell* **1997**, *89*, 413-424.
- (344) Duran, A.; Diaz-Meco, M.T.; Moscat, J. Essential role of RelA Ser311 phosphorylation by [zeta]PKC in NF-[kappa]B transcriptional activation, *EMBO J* **2003**, *22*, 3910-3918.

- (345) Ryo, A.; Suizu, F.; Yoshida, Y.; Perrem, K.; Liou, Y.-C.; Wulf, G.; Rottapel, R.; Yamaoka, S.; Lu, K.P. Regulation of NF- κ B signaling by Pin1-Dependent prolyl isomerization and ubiquitin-mediated proteolysis of p65/RelA, *Mol. Cell* **2003**, *12*, 1413-1426.
- (346) Perkins, N.D. Integrating cell-signalling pathways with NF-[kappa]B and IKK function, *Nat Rev Mol Cell Biol* **2007**, *8*, 49-62.
- (347) Stensballe, A.; Jensen, O.N.; Olsen, J.V.; Haselmann, K.F.; Zubarev, R.A. Electron capture dissociation of singly and multiply phosphorylated peptides, *Rapid Commun. Mass Spectrom.* **2000**, *14*, 1793-1800.
- (348) Ayaz-Guner, S.; Zhang, J.; Li, L.; Walker, J.W.; Ge, Y. In vivo phosphorylation site mapping in mouse Cardiac Troponin I by high resolution top-down electron capture dissociation mass spectrometry: Ser22/23 Are the only sites basally phosphorylated, *Biochemistry* **2009**, *48*, 8161-8170.
- (349) Ge, Y.; Lawhorn, B.G.; ElNaggar, M.; Strauss, E.; Park, J.-H.; Begley, T.P.; McLafferty, F.W. Top down characterization of larger proteins (45 kDa) by electron capture dissociation mass spectrometry, *J. Am. Chem. Soc.* **2002**, *124*, 672-678.
- (350) Zhang, J.; Dong, X.; Hacker, T.; Ge, Y. Deciphering modifications in swine cardiac troponin I by top-down high-resolution tandem mass spectrometry, *J. Am. Soc. Mass. Spectrom.* **2010**, *21*, 940-948.
- (351) Zhang, J.; Guy, M.J.; Norman, H.S.; Chen, Y.-C.; Xu, Q.; Dong, X.; Guner, H.; Wang, S.; Kohmoto, T.; Young, K.H.; Moss, R.L.; Ge, Y. Top-down quantitative proteomics identified phosphorylation of Cardiac Troponin I as a candidate biomarker for chronic heart failure, *J. Proteome Res.* **2011**, *10*, 4054-4065.

Appendix A. (Supporting information for Chapter 2)

Figure A.1 The dual nano-electrospray setup

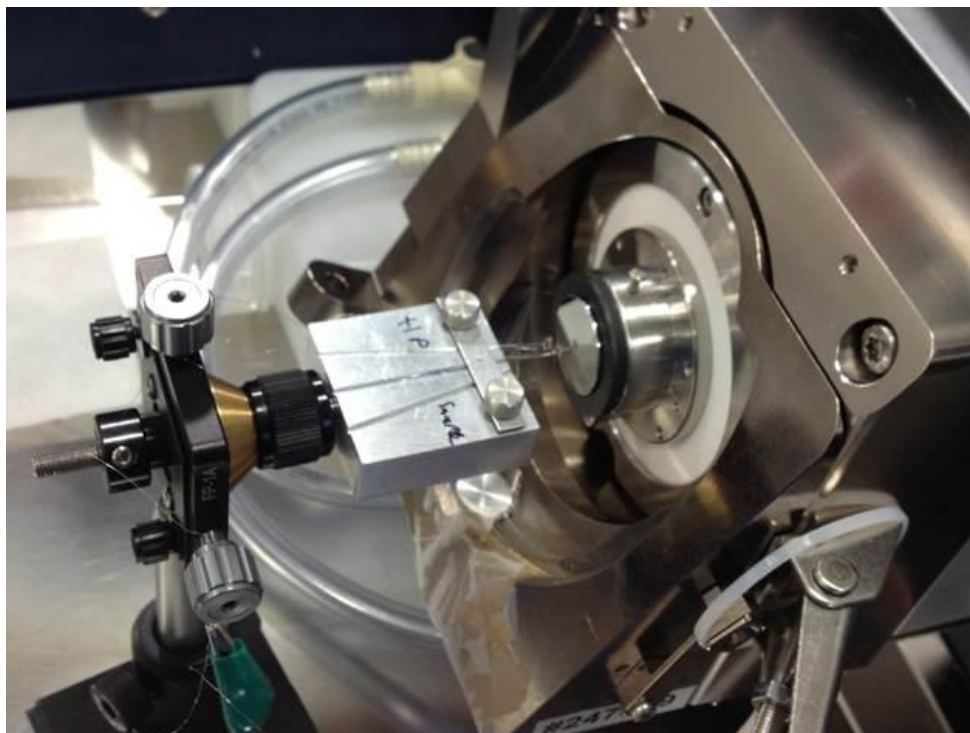


Figure A.2 The intensity change of ions at m/z 896.6 with different excitation power in percentage (top) or V_{pp} (bottom)

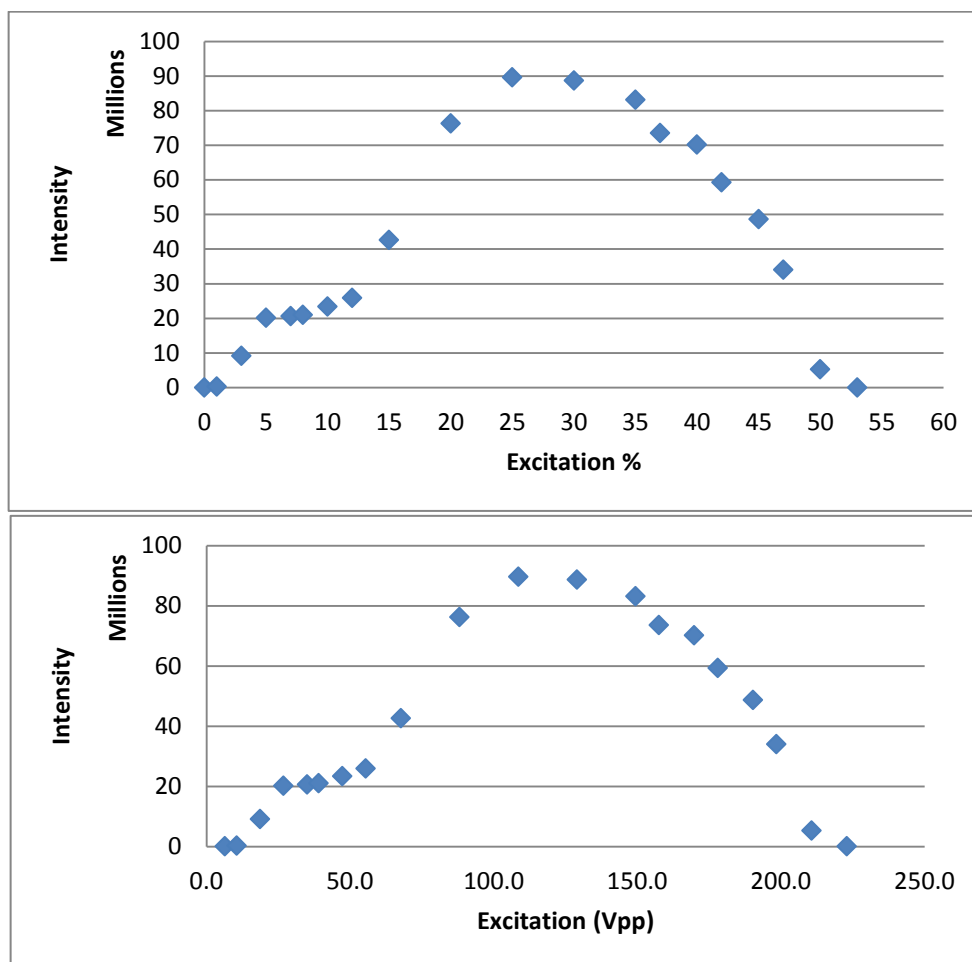


Table A.1 The calculation of the abundance of the ^{13}C , ^{16}O , ^{17}O , and ^{18}O in $\text{A}\beta_{16-22}$

	A			A+1 (^{13}C ^{16}O)			A+1 (^{17}O ^{12}C)			A+2 (^{18}O ^{12}C)			A+2 (^{13}C ^{17}O)			A+3 (^{13}C ^{18}O)			^{13}C -substitute		^{12}C ^{17}O -substitute		^{12}C ^{18}O -substitute		^{12}C ^{16}O -substitute	
run	Area	Intensity	R.P	Area	Intensity	R.P	Area	Intensity	R.P	Area	Intensity	R.P	Area	Intensity	R.P	Area	Intensity	R.P	$R(A^{13}\text{C})$	$R(I^{13}\text{C})$	$R(A^{17}\text{O})$	$R(I^{17}\text{O})$	$R(A^{18}\text{O})$	$R(I^{18}\text{O})$	$R(A^{16}\text{O})$	$R(I^{16}\text{O})$
1	0.726	0.578	4.0	0.284	0.310	5.5	1.000	1.000	4.9	0.219	0.207	4.8	0.579	0.410	4.1	0.096	0.083	4.0	0.281	0.349	0.514	0.560	0.113	0.116	0.373	0.324
2	0.825	0.579	3.9	0.442	0.379	4.9	1.000	1.000	5.4	0.160	0.161	3.8	0.472	0.391	3.3	0.087	0.069	3.9	0.349	0.380	0.504	0.575	0.081	0.093	0.416	0.333
3	0.537	0.569	5.7	0.329	0.283	3.9	1.000	1.000	5.7	0.207	0.152	2.6	0.426	0.391	4.0	0.065	0.097	5.9	0.380	0.332	0.573	0.581	0.119	0.088	0.308	0.330
4	0.783	0.703	5.7	0.383	0.247	2.5	1.000	1.000	5.2	0.187	0.164	4.5	0.484	0.381	4.8	0.077	0.090	6.6	0.328	0.260	0.507	0.536	0.095	0.088	0.397	0.377
5	0.760	0.700	4.7	0.295	0.265	3.6	1.000	1.000	4.8	0.259	0.204	4.9	0.538	0.454	5.2	0.056	0.101	6.4	0.280	0.274	0.495	0.525	0.128	0.107	0.376	0.368
6	0.787	0.595	4.2	0.235	0.277	4.3	1.000	1.000	4.2	0.245	0.206	3.9	0.484	0.381	3.6	0.095	0.104	4.3	0.230	0.317	0.492	0.555	0.121	0.115	0.387	0.330
average																			0.308	0.319	0.514	0.555	0.109	0.101	0.376	0.344
SD																			0.055	0.045	0.030	0.022	0.018	0.013	0.037	0.023

*Area: Normalized peak area; Intensity: Normalized peak intensity; R.P: Resolving power;

* $R(I^{17}\text{O})$, $R(I^{13}\text{C})$, $R(I^{18}\text{O})$ and $R(I^{16}\text{O})$: The ratio of ^{17}O ^{13}C , ^{18}O and ^{16}O abundance calculated by the peak intensity using Equations 1, A-1, A-2 and A-3 in Table A-2

* $R(A^{17}\text{O})$, $R(A^{13}\text{C})$, $R(A^{18}\text{O})$ and $R(A^{16}\text{O})$: The ratio of ^{17}O ^{13}C , ^{18}O and ^{16}O abundance calculated by the peak area using Equations A-4, A-5, A-6 and A-7 in Table A-2

Table A.2 The statistics of the abundance of ^{17}O , ^{18}O , and ^{13}C

	Equation
$R(I^{13}\text{C})$	the ratio of $^{13}\text{C} = \frac{I(^{13}\text{C}^{16}\text{O})}{I(^{12}\text{C}^{16}\text{O}) + I(^{13}\text{C}^{16}\text{O})}$ Equation (A-1)
$R(I^{18}\text{O})$	^{18}O abundance $= \frac{I(^{12}\text{C}^{18}\text{O})}{I(^{12}\text{C}^{16}\text{O}) + I(^{12}\text{C}^{17}\text{O}) + I(^{12}\text{C}^{18}\text{O})}$ Equation (A-2)
$R(I^{16}\text{O})$	^{16}O abundance $= \frac{I(^{12}\text{C}^{16}\text{O})}{I(^{12}\text{C}^{16}\text{O}) + I(^{12}\text{C}^{17}\text{O}) + I(^{12}\text{C}^{18}\text{O})}$ Equation (A-3)
$R(A^{17}\text{O})$	^{17}O abundance $= \frac{A(^{12}\text{C}^{17}\text{O})}{A(^{12}\text{C}^{16}\text{O}) + A(^{12}\text{C}^{17}\text{O}) + A(^{12}\text{C}^{18}\text{O})}$ Equation (A-4)
$R(A^{13}\text{C})$	the ratio of $^{13}\text{C} = \frac{A(^{13}\text{C}^{16}\text{O})}{A(^{12}\text{C}^{16}\text{O}) + A(^{13}\text{C}^{16}\text{O})}$ Equation (A-5)
$R(A^{18}\text{O})$	^{18}O abundance $= \frac{A(^{12}\text{C}^{18}\text{O})}{A(^{12}\text{C}^{16}\text{O}) + A(^{12}\text{C}^{17}\text{O}) + A(^{12}\text{C}^{18}\text{O})}$ Equation (A-6)
$R(A^{16}\text{O})$	^{16}O abundance $= \frac{A(^{12}\text{C}^{17}\text{O})}{A(^{12}\text{C}^{16}\text{O}) + A(^{12}\text{C}^{17}\text{O}) + A(^{12}\text{C}^{18}\text{O})}$ Equation (A-7)
$R(I^{17}\text{O}^{13}\text{C})$	^{17}O abundance $= \frac{I(^{13}\text{C}^{17}\text{O})}{I(^{13}\text{C}^{16}\text{O}) + I(^{13}\text{C}^{17}\text{O}) + I(^{13}\text{C}^{18}\text{O})}$ Equation (A-8)

* $I(^{12}\text{C}^{16}\text{O})$, $I(^{12}\text{C}^{17}\text{O})$, $I(^{12}\text{C}^{18}\text{O})$, and $I(^{13}\text{C}^{16}\text{O})$ are the peak intensity of $^{12}\text{C}^{16}\text{O}$ -, $^{12}\text{C}^{17}\text{O}$ -, $^{12}\text{C}^{18}\text{O}$ -, and $^{13}\text{C}^{16}\text{O}$ - substituted peaks

* $A(^{12}\text{C}^{16}\text{O})$, $A(^{12}\text{C}^{17}\text{O})$, $A(^{12}\text{C}^{18}\text{O})$, and $A(^{13}\text{C}^{16}\text{O})$ are the peak area of $^{12}\text{C}^{16}\text{O}$ -, $^{12}\text{C}^{17}\text{O}$ -, $^{12}\text{C}^{18}\text{O}$ -, and $^{13}\text{C}^{16}\text{O}$ - substituted peaks

Table A.3 The mass list of proposed peaks in Figure 2.4

Formula	Theoretical m/z	Experimental m/z	Error/ppm
$C_{45}H_{68}N_8^{15}NO_{10}$	895.50540	895.50539	-0.01
$C_{45}H_{68}N_8^{15}N^{17}OO_9$	896.50962	896.50944	-0.20
$C_{45}H_{68}N_8^{15}N^{18}OO_9$	897.50965	897.50920	-0.49
$C_{44}H_{68}N_8^{15}NO_9^{17}O^{13}C$	897.51297	897.51029	-2.98
* $C_{12}H_{19}F_{12}N_3O_6P_3$	622.02896	622.02896	---
* $C_{18}H_{19}F_{24}N_3O_6P_3$	922.0098	922.00981	---
* $C_{24}H_{19}F_{36}N_3O_6P_3$	1221.99064	1221.99060	---
* $C_{30}H_{19}F_{48}N_3O_6P_3$	1521.97149	1521.97150	---

* Peaks from Tuning mix and used as calibrants

Table A.4 The mass list of peaks on the CAD spectrum of the A β_{16-22} in Figure 2.5

ions	Theoretical <i>m/z</i>	Experimental <i>m/z</i>	ppm
M-NH ₃	878.47890	878.47855	-0.40
M-NH ₃ -H ₂ O	860.46834	860.46828	-0.07
M-CONH ₃	850.48394	850.48403	0.11
M-NH ₃ -2H ₂ O	842.45772	842.45787	0.18
M-CO-NH ₃ -H ₂ O	832.47337	832.47348	0.13
M-CO-2NH ₃	833.45694	833.45742	0.58
M-C ₃ H ₈ N ₂ O	807.44174	807.44205	0.38
M-C ₃ H ₁₀ N ₂ O ₂	789.43117	789.43114	-0.04
M-C ₅ H ₁₂ N ₂ O	779.41044	779.41073	0.37
M-C ₆ H ₁₄ N ₂ O	765.39479	765.39509	0.39
M-C ₅ H ₁₄ N ₂ O ₂	761.39987	761.40019	0.42
b6	749.43626	749.43662	0.48
y5	678.39913	678.39963	0.74
b4	530.33370	530.33426	1.06
b3	383.26528	383.26572	1.15
b2	284.19686	284.19710	0.84
b6-H ₂ O	731.42569	731.42609	0.55
b5-H ₂ O	660.38858	660.38905	0.71
b4-H ₂ O	512.32313	512.32365	1.01
b3-H ₂ O	365.25471	365.25513	1.15
b2-H ₂ O	266.18630	266.18657	1.01
a6	721.44134	721.44177	0.60
a5	650.40423	650.40470	0.72
a3	355.27037	355.27079	1.18
a6-NH ₃	704.41479	704.41515	0.51
a5-NH ₃	633.37768	633.37822	0.85
a4-NH ₃	485.31223	485.31278	1.13
a3-NH ₃	338.24382	338.24420	1.12
y6	725.39985	725.40034	0.68
y5	612.31579	612.31636	0.93
y4	513.24738	513.24794	1.09
y3	366.17897	366.17942	1.23
y6-NH ₃	708.37335	708.37376	0.58
y5-NH ₃	595.28929	595.28978	0.82
y4-NH ₃	496.22088	496.22137	0.99
y3-NH ₃	349.15247	349.15284	1.06
y6-NH ₃ -H ₂ O	690.36366	690.36322	-0.64
y5-NH ₃ -H ₂ O	577.27870	577.27924	0.94
C ₃₈ H ₅₁ N ₅ O ₈ ¹⁵ N	720.37332	720.37374	0.58
C ₃₄ H ₄₃ N ₅ O ₇ ¹⁵ N	648.31581	648.31627	0.71
C ₃₃ H ₄₉ N ₆ O ₇	641.36572	641.36621	0.76
C ₃₂ H ₄₂ N ₄ O ₇ ¹⁵ N	609.30491	609.30543	0.85
C ₃₀ H ₄₆ N ₅ O ₅	556.34935	556.34987	0.93
C ₃₁ H ₄₄ N ₄ O ₄ ¹⁵ N	551.33582	551.33633	0.93
C ₂₉ H ₃₉ N ₃ O ₄ ¹⁵ N	508.29359	508.29415	1.10
C ₂₄ H ₄₀ N ₅ O ₆	494.29731	494.29785	1.09
C ₂₈ H ₃₉ N ₃ O ₃ ¹⁵ N	480.29962	480.29923	-0.81

$C_{27}H_{35}N_3O_3^{15}N$	480.26232	480.26285	1.10
$C_{26}H_{33}N_3O_4^{15}N$	466.24667	466.24718	1.09
$C_{23}H_{40}N_5O_5$	466.30240	466.30291	1.09
$C_{25}H_{39}N_4O_3$	443.30167	443.30218	1.15
$C_{25}H_{35}N_3O_3^{15}N$	438.25175	438.25225	1.14
$C_{25}H_{30}N_2O_3^{15}N$	421.22510	421.22567	1.35
$C_{19}H_{31}N_4O_5$	395.22890	395.22935	1.14

Table A.5 The calculation of the abundance of the ^{13}C , ^{16}O , ^{17}O , and ^{18}O in $\text{A}\beta_{11-25}$

	A	A+1 (^{13}C ^{16}O)	A+1 (^{17}O ^{12}C)	A+2 (^{13}C ^{17}O)	A+2 ($^{18}\text{O}^{12}\text{C}$)	^{13}C - substitute	$^{12}\text{C}^{17}\text{O}$ - substitute	$^{12}\text{C}^{18}\text{O}$ - substitute	$^{12}\text{C}^{16}\text{O}$ - substitute
run	Intensity	Intensity	Intensity	Intensity	Intensity	$\text{R}(\text{I}^{13}\text{C})$	$\text{R}(\text{I}^{17}\text{O})$	$\text{R}(\text{I}^{18}\text{O})$	$\text{R}(\text{I}^{16}\text{O})$
1	0.449	0.470	1.000	0.761	0.246	0.511	0.590	0.145	0.265
2	0.549	0.510	1.000	0.857	0.282	0.481	0.546	0.154	0.300
3	0.481	0.397	1.000	0.709	0.282	0.452	0.567	0.160	0.273
average						0.482	0.568	0.153	0.279
SD						0.029	0.022	0.007	0.018

* $\text{R}(\text{I}^{17}\text{O})$, $\text{R}(\text{I}^{13}\text{C})$, $\text{R}(\text{I}^{18}\text{O})$ and $\text{R}(\text{I}^{16}\text{O})$: The ratio of ^{17}O ^{13}C , ^{18}O and ^{16}O abundance calculated by the peak intensity using Equations 1, A-1, A-2 and A-3 in Table A-2

Table A.6 The mass list of peaks on the CAD spectrum of the A β_{11-25} in Figure 2.8

Charge state	ions	Theoretical m/z	Experimental m/z	ppm
2	M	879.95021		
2	M-H ₂ O	870.94493	870.94494	0.01
2	M-2H ₂ O	861.93965	861.93976	0.13
2	b14	842.43418	842.43422	0.05
2	b13	792.89997	792.90007	0.13
2	b12	735.38650	735.38664	0.18
2	b11	670.86521	670.86541	0.30
1	b11	1340.72314	1340.72238	-0.57
1	b10	1265.67893	1265.67848	-0.36
1	b9	1118.61052	1118.61024	-0.25
1	b8	971.54211	971.54201	-0.10
1	b7	872.47370	872.47371	0.01
1	b6	759.38964	759.38975	0.15
1	b5	631.29468	631.29485	0.27
1	b4	503.23610	503.23632	0.44
1	b3	366.17719	366.17741	0.60
2	b14-H ₂ O	833.42890	833.42895	0.06
2	b13-H ₂ O	783.89469	783.89478	0.11
2	b12-H ₂ O	726.38122	726.38135	0.18
2	b11-H ₂ O	661.85993	661.86013	0.31
1	b11-H ₂ O	1322.71258	1322.71206	-0.39
1	b10-H ₂ O	1247.66836	1247.66779	-0.46
1	b9-H ₂ O	1100.59995	1100.59967	-0.26
1	b8-H ₂ O	953.53154	953.53147	-0.08
1	b7-H ₂ O	854.46313	854.46316	0.03
1	b6-H ₂ O	741.37907	741.37918	0.15
1	b5-H ₂ O	613.28411	613.2843	0.30
1	b4-H ₂ O	485.22553	485.22578	0.51
1	b3-H ₂ O	348.16662	348.16689	0.76
2	y14	815.42890	815.42896	0.08
2	y13	765.89469	765.89473	0.05
2	y12	697.36524	697.36531	0.11
1	y12	1393.72319	1393.7226	-0.43
1	y11	1256.66428	1256.66398	-0.24
1	y10	1128.60570	1128.60553	-0.15
1	y9	1000.51074	1000.51154	0.80
1	y8	887.42668	887.42675	0.07
1	y7	788.35827	788.35838	0.13
1	y6	641.28986	641.29004	0.27
1	y5	494.22145	494.22169	0.48
1	y4	419.17724	419.17751	0.64
1	y11-H ₂ O	1238.65372	1238.65332	-0.32
1	y4-H ₂ O	401.16668	401.16696	0.71

Table A.7 The mass list of proposed peaks in Figure 2.9

Formula	R. P /M	Theoretical m/z	Experimental m/z	Error/ppm
$C_{79}^{13}C_2H_{121}O_{23}N_{20}^{15}N$	12.49	879.448533	879.448541	0.009
* $C_{78}^{13}C_3H_{121}O_{23}N_{20}^{15}N$	10.40	879.950211	879.950211	-----
$C_{77}^{13}C_4H_{121}O_{23}N_{20}^{15}N$	9.70	880.451888	880.451933	0.051
$C_{78}^{13}C_3H_{121}O_{22}N_{20}^{15}N^{17}O$	8.18	880.452319	880.452284	-0.040
$C_{78}^{13}C_3H_{121}O_{22}N_{19}^{15}N^{17}_2O$	11.07	880.950837	880.950842	0.006
$C_{78}^{13}C_3H_{121}O_{22}N_{20}^{15}N^{18}O$	9.85	880.952334	880.952337	0.003
$C_{76}^{13}C_5H_{121}O_{23}N_{20}^{15}N$	8.37	880.953566	880.953565	-0.001
$C_{77}^{13}C_4H_{121}O_{22}N_{20}^{15}N^{17}O$	7.31	880.953997	880.953952	-0.051
$C_{78}^{13}CH_{120}^2HO_{22}N_{20}^{15}N^{17}O$	6.47	880.955458	880.95544	-0.020
$C_{76}^{13}C_5H_{121}O_{22}N_{20}^{15}N^{17}O$	9.74	881.455674	881.455621	-0.060
Average of the absolute value	9.36			0.027
SD				0.024

* The peak used as lock mass

R.P.: resolving power

Table A.8 The calculation of the abundance of the ^{13}C , ^{16}O , ^{17}O , and ^{18}O in Fmoc-valine

	A (^{16}O)	A+1 (^{17}O)	A+2 ($^{13}\text{C}^{17}\text{O}$)	A+2 (^{18}O)	A+2 ($^{17}\text{O}_2$)	A+3 ($^{18}\text{O}^{17}\text{O}$)	^{13}C - substitute	^{17}O - substitute	^{18}O - substitute	^{16}O - substitute
run	Intensity	Intensity	Intensity	Intensity	Intensity	Intensity	R($I^{13}\text{C}$)	R($I^{17}\text{O}$)	R($I^{18}\text{O}$)	R($I^{16}\text{O}$)
1	0.176	1.000	0.164	0.182	0.903	0.585	0.141	0.596	0.135	0.270
2	0.185	1.000	0.187	0.226	0.948	0.495	0.158	0.594	0.126	0.280
3	0.232	1.000	0.285	0.246	1.081	0.634	0.222	0.594	0.138	0.268
4	0.205	1.000	0.193	0.233	0.995	0.479	0.162	0.596	0.122	0.282
5	0.179	1.000	0.241	0.263	1.064	0.636	0.194	0.599	0.143	0.258
6	0.185	1.000	0.193	0.223	0.910	0.549	0.162	0.588	0.135	0.278
average							0.173	0.594	0.133	0.272
SD							0.030	0.004	0.008	0.009

*Intensity: Normalized peak intensity;

* The ratio of ^{13}C abundance: $R(I^{13}\text{C}) = \frac{I(^{13}\text{C}^{16}\text{O})}{I(^{12}\text{C}^{16}\text{O}) + I(^{13}\text{C}^{16}\text{O})}$;

* The ratio of ^{17}O abundance: $R(I^{17}\text{O}) = \frac{I(^{16}\text{O}^{17}\text{O})/2 + I(^{17}\text{O}^{17}\text{O}) + I(^{17}\text{O}^{18}\text{O})/2}{I(^{16}\text{O}^{16}\text{O}) + I(^{16}\text{O}^{17}\text{O}) + I(^{16}\text{O}^{18}\text{O}) + I(^{17}\text{O}^{17}\text{O}) + I(^{17}\text{O}^{18}\text{O})}$;

* The ratio of ^{18}O abundance: $R(I^{18}\text{O}) = \frac{I(^{16}\text{O}^{18}\text{O})/2 + I(^{17}\text{O}^{18}\text{O})/2}{I(^{16}\text{O}^{16}\text{O}) + I(^{16}\text{O}^{17}\text{O}) + I(^{16}\text{O}^{18}\text{O}) + I(^{17}\text{O}^{17}\text{O}) + I(^{17}\text{O}^{18}\text{O})}$;

* The ratio of ^{16}O abundance: $R(I^{16}\text{O}) = \frac{I(^{16}\text{O}^{16}\text{O}) + I(^{16}\text{O}^{17}\text{O})/2 + I(^{16}\text{O}^{18}\text{O})/2}{I(^{16}\text{O}^{16}\text{O}) + I(^{16}\text{O}^{17}\text{O}) + I(^{16}\text{O}^{18}\text{O}) + I(^{17}\text{O}^{17}\text{O}) + I(^{17}\text{O}^{18}\text{O})}$;

Appendix B. (Supporting information for Chapter 3)

Table B.1 The calculation of the abundance of the ^{13}C , ^{16}O , and ^{17}O in $\text{A}\beta_{37-42}$

run	A			A+1 (^{13}C ^{16}O)			A+1 (^{17}O ^{12}C)			^{13}C -substitute		^{12}C ^{17}O -substitute		^{12}C ^{16}O -substitute	
	Area	Intensity	R.P. /M	Area	Intensity	R.P. /M	Area	Intensity	R.P. /M	R(A ^{13}C)	R(I ^{13}C)	R(A ^{17}O)	R(I ^{17}O)	R(A ^{16}O)	R(I ^{16}O)
1	1.000	1.000	3.4	0.177	0.289	4.6	1.643	1.567	2.9	0.150	0.224	0.622	0.610	0.378	0.390
2	1.000	1.000	2.7	0.301	0.288	2.8	1.466	1.382	2.9	0.231	0.224	0.594	0.580	0.406	0.420
3	1.000	1.000	3.2	0.364	0.267	2.3	1.745	1.632	3.3	0.267	0.211	0.636	0.620	0.364	0.380
4	1.000	1.000	3.2	0.154	0.212	3.2	1.331	1.471	2.8	0.134	0.175	0.571	0.595	0.429	0.405
5	1.000	1.000	2.9	0.183	0.220	2.6	1.583	1.632	2.7	0.155	0.180	0.613	0.620	0.387	0.380
average										0.187	0.203	0.607	0.605	0.393	0.395
SD										0.058	0.024	0.025	0.017	0.025	0.017

*Area: Normalized peak area; Intensity: Normalized peak intensity; R.P: Resolving power;

*R(I ^{17}O), R(I ^{13}C), and R(I ^{16}O): The ratio of ^{17}O ^{13}C , and ^{16}O abundance calculated by the peak intensity using Equations 1, B-1, B-2 in Table B-2

*R(A ^{17}O), R(A ^{13}C), and R(A ^{16}O): The ratio of ^{17}O ^{13}C , and ^{16}O abundance calculated by the peak area using Equations B-3, B-4, B-5 in Table B-2

Table B.2 The statistics of the abundance of ^{17}O , ^{13}C , and the mass accuracy

	Equation	
$R(I^{13}\text{C})$	the ratio of $^{13}\text{C} = \frac{I(^{13}\text{C}^{16}\text{O})}{I(^{12}\text{C}^{16}\text{O}) + I(^{13}\text{C}^{16}\text{O})}$	Equation (B-1)
$R(I^{16}\text{O})$	^{16}O abundance $= \frac{I(^{12}\text{C}^{16}\text{O})}{I(^{12}\text{C}^{16}\text{O}) + I(^{12}\text{C}^{17}\text{O})}$	Equation (B-2)
$R(A^{17}\text{O})$	^{17}O abundance $= \frac{A(^{12}\text{C}^{17}\text{O})}{A(^{12}\text{C}^{16}\text{O}) + A(^{12}\text{C}^{17}\text{O})}$	Equation (B-3)
$R(A^{13}\text{C})$	the ratio of $^{13}\text{C} = \frac{A(^{13}\text{C}^{16}\text{O})}{A(^{12}\text{C}^{16}\text{O}) + A(^{13}\text{C}^{16}\text{O})}$	Equation (B-4)
$R(A^{16}\text{O})$	^{16}O abundance $= \frac{A(^{12}\text{C}^{17}\text{O})}{A(^{12}\text{C}^{16}\text{O}) + A(^{12}\text{C}^{17}\text{O})}$	Equation (B-5)

* $I(^{12}\text{C}^{16}\text{O})$, $I(^{12}\text{C}^{17}\text{O})$, and $I(^{13}\text{C}^{16}\text{O})$ are the peak intensity of $^{12}\text{C}^{16}\text{O}$ -, $^{12}\text{C}^{17}\text{O}$ -, and $^{13}\text{C}^{16}\text{O}$ - substituted peaks

* $A(^{12}\text{C}^{16}\text{O})$, $A(^{12}\text{C}^{17}\text{O})$, and $A(^{13}\text{C}^{16}\text{O})$ are the peak area of $^{12}\text{C}^{16}\text{O}$ -, $^{12}\text{C}^{17}\text{O}$ -, and $^{13}\text{C}^{16}\text{O}$ - substituted peaks

Table B.3 The mass list of proposed peaks in Figure 3.2

Formula	Resolving power/million	Theoretical m/z	Experimental m/z	Error/ppm
$C_{23}H_{43}N_6O_7$	0.86	515.318774	515.31876	-0.03
$C_{23}H_{43}N_5^{15}NO_7$	0.88	516.315809	516.315804	-0.01
$C_{22}^{13}CH_{43}N_6O_7$	1.07	516.322129	516.321907	-0.43
$C_{23}H_{43}N_6O_6^{17}O$	0.85	516.322991	516.322987	-0.01
$C_{22}^{13}CH_{43}N_5^{15}NO_7$	0.84	517.319164	517.319165	0.00
$C_{22}^{13}CH_{43}N_6^{17}OO_6$	0.86	517.326346	517.326349	0.01
* $C_{18}H_{38}O_{10}Na$	0.93	437.235719	437.235718	---
* $C_{20}H_{42}O_{11}Na$	0.89	481.261933	481.261934	---
* $C_{22}H_{46}O_{12}Na$	0.87	525.288148	525.288132	---
* $C_{24}H_{50}O_{13}Na$	0.69	569.314363	569.314368	---
Average of the absolute value	0.87			0.08
STDEV				0.02

* The peaks used as calibrants

Table B.4 The calculation of the abundance of the ^{13}C , ^{16}O , and ^{17}O in Fmoc-glycine

	A	A+1 (^{13}C ^{16}O)	A+1 (^{17}O ^{12}C)	A+2 (^{17}O ^{17}O)	^{13}C - substitute	^{12}C ^{17}O - substitute
Run	Intensity	Intensity	Intensity	Intensity	R($I^{13}\text{C}$)	R($I^{17}\text{O}$)
1	1.000	0.187	2.976	1.971	0.157	0.582
2	1.000	0.175	2.913	2.046	0.149	0.588
3	1.000	0.168	2.873	1.994	0.144	0.585
4	1.000	0.201	3.095	2.170	0.167	0.593
5	1.000	0.197	3.124	2.120	0.164	0.590
average					0.156	0.587
SD					0.010	0.005

*R($I^{17}\text{O}$), R($I^{13}\text{C}$): The ratio of ^{17}O and ^{13}C abundance calculated by the peak intensity using Equations 1 and B-1 in Table B-2

Figure B.1 The structure of the ^{17}O labelled Fmoc-glycine

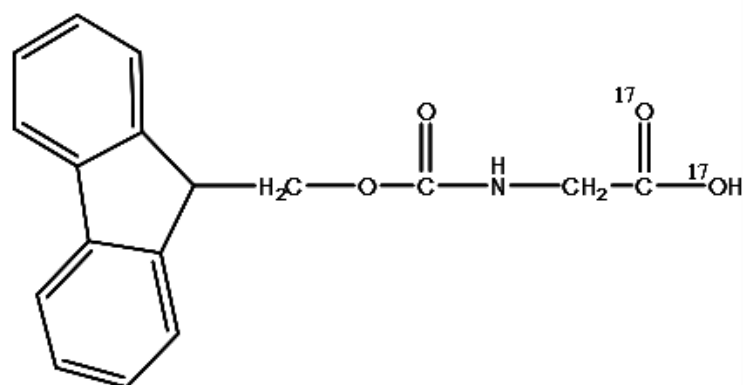


Table B.5 The mass list of proposed peaks in Figure 3.3

Formula	Resolving power/million	Theoretical m/z	Experimental m/z	Error/ppm
* C ₁₇ H ₁₆ NO ₄	2.7	298.107384	298.107380	----
C ₁₆ ¹³ CH ₁₆ NO ₄	2.1	299.110739	299.110733	-0.02
C ₁₇ H ₁₆ NO ₃ ¹⁷ O	2.6	299.111601	299.111598	-0.01
C ₁₆ ¹³ CH ₁₆ NO ₃ ¹⁷ O	2.7	300.114956	300.114954	-0.01
C ₁₇ H ₁₆ NO ₂ ¹⁷ O ₂	2.6	300.115818	300.115818	0.00
C ₁₅ ¹³ C ₂ H ₁₆ NO ₃ ¹⁷ O	3.1	301.118311	301.118319	0.03
C ₁₆ ¹³ CH ₁₆ NO ₂ ¹⁷ O ₂	2.8	301.119173	301.119179	0.02
Average of the absolute value	2.6			0.01
STDEV				0.02

Appendix C. (Supporting information for Chapter 4)

Figure C.1 Zooming in peaks losing one PEG unit from the precursor on the ECD spectrum of $[\text{TPGS}+3\text{Na}]^{3+}$

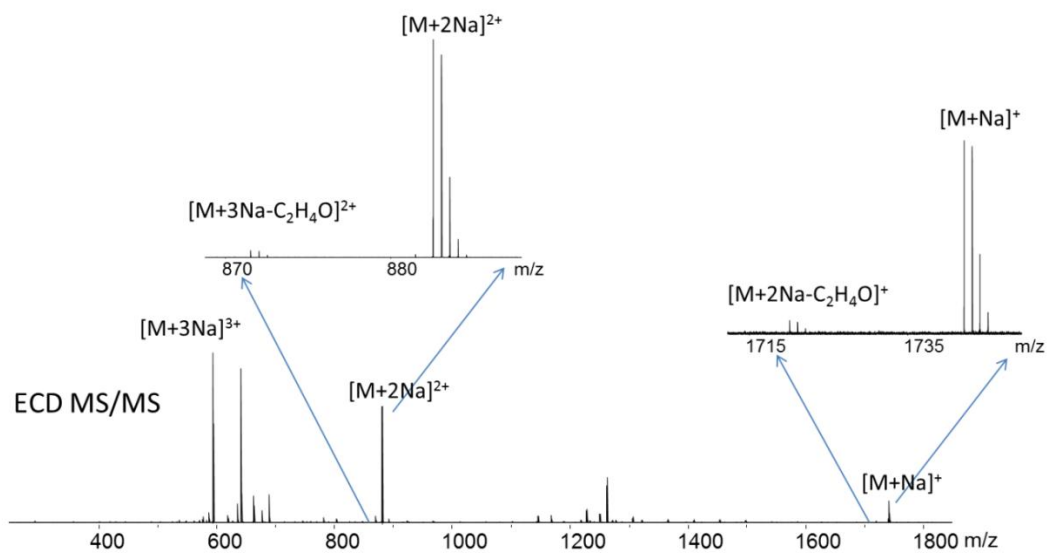


Figure C.2 A ECD spectrum of $[\text{TPGS}_{27}+3\text{Ag}]^{3+}$

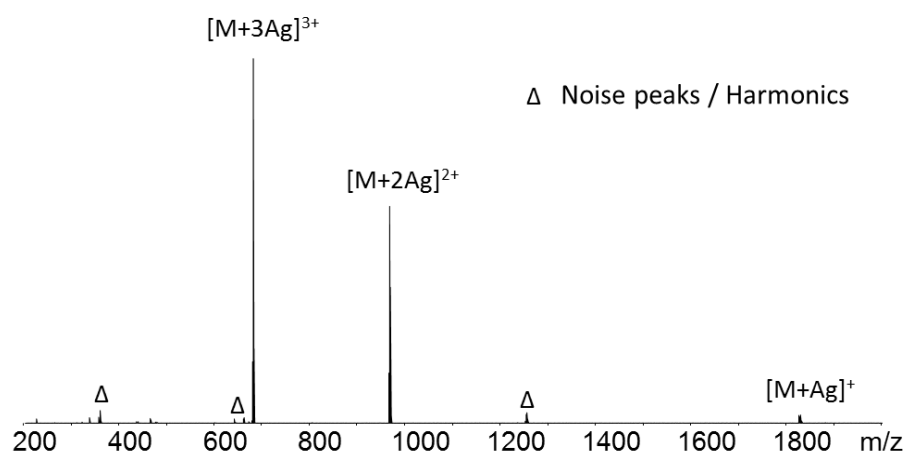


Figure C.3 Mass spectra of four batches of processed TPGS samples: A1 heated and A2 heated are A1 and A2 exposed to 50°C for 1 month; A1 melted and A2 melted are A1 and A2 melted in warm water bath (37°C)

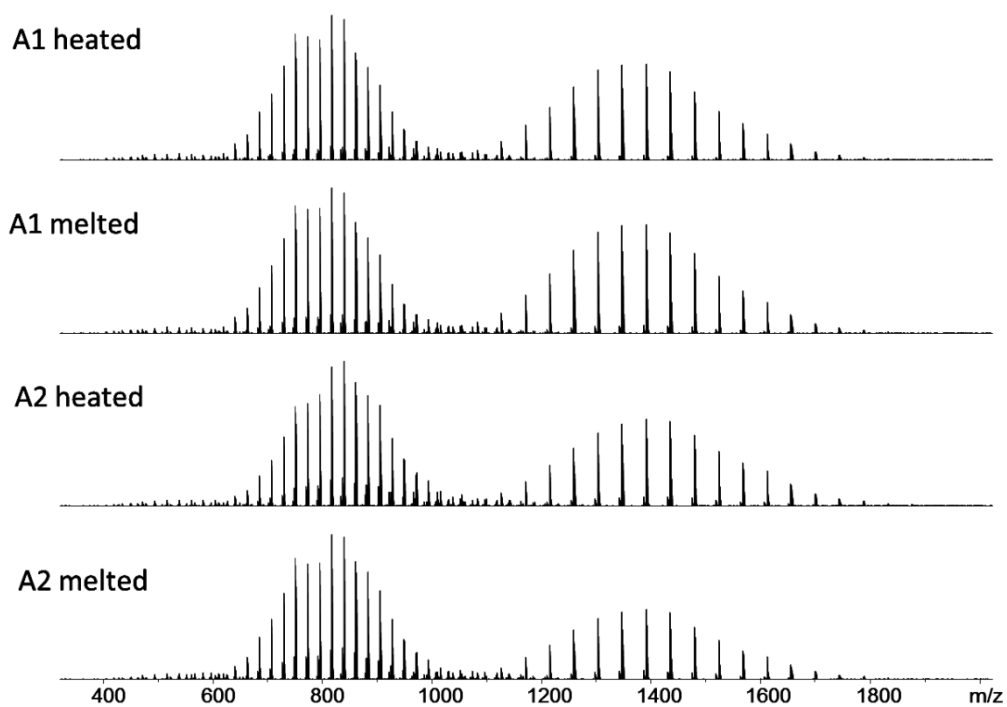


Table C.1 Mass list of proposed peaks in Figure 4.2

Mass list of free PEG (H (C ₂ H ₄ O) _n Na _m) m=1, 2, 3									
PEG repeat unit, n	Theoretical m/z (1+)	Experimental m/z (1+)	Error (ppm)	Theoretical m/z (2+)	Experimental m/z (2+)	Error (ppm)	Theoretical m/z (3+)	Experimental m/z (3+)	Error (ppm)
13	613.34058	613.34059	-0.02						
14	657.36679	657.36657	0.34						
15	701.39301	701.3928	0.30						
16	745.41922	745.41949	-0.36						
17	789.44544	789.44498	0.58	406.21733	406.21716	0.42			
18	833.47165	833.47151	0.17	428.23043	428.23029	0.35			
19	877.49787	877.4981	-0.26	450.24354	450.24352	0.06			
20	921.52408	921.52412	-0.04	472.25665	472.25658	0.15			
21				494.26976	494.26982	-0.12			
22				516.28286	516.28292	-0.10			
23				538.29597	538.29601	-0.06			
24				560.30908	560.30909	-0.01			
25				582.32219	582.321944	0.42			
26				604.33529	604.33528	0.03	410.55345	410.55315	0.74
27				626.34840	626.34815	0.41	425.22886	425.22854	0.75
28				648.36151	648.36161	-0.15	439.90425	439.90401	0.58
29				670.37462	670.37467	-0.07			
Average of absolute value			0.26			0.14			0.69
SD			0.18			0.17			0.1
Mass list of [TPGS+mNa] ^{m+} (H (C ₂ H ₄ O) _n C ₃₃ H ₅₃ O ₅ Na _m) m=1, 2, 3									
PEG repeat unit, n	Theoretical m/z (1+)	Experimental m/z (1+)	Error (ppm)	Theoretical m/z (2+)	Experimental m/z (2+)	Error (ppm)	Theoretical m/z (3+)	Experimental m/z (3+)	Error (ppm)
15	1213.77957	1213.7795	0.06						
16	1257.80578	1257.80661	-0.66	640.39750	640.39726	0.38			
17	1301.83200	1301.83328	-0.98	*662.41061	-----	-----			

18	1345.85821	1345.8584	-0.14	684.42371	684.42367	0.07			
19	*1389.8844	-----	-----	706.43682	706.43696	-0.19			
20	1433.91064	1433.91407	-2.39	728.44993	728.45005	-0.16			
21	1477.93686	1477.93823	0.93	750.46304	750.46302	0.03	507.97177	507.97184	-0.15
22				772.47615	772.47629	-0.18	*522.64717	-----	-----
23				794.48925	794.48941	-0.19	537.32258	537.32264	-0.12
24				816.50236	816.50222	0.17	551.99798	551.99804	-0.1
25				838.51547	838.51549	-0.02	566.67339	566.67336	0.05
26				860.52857	860.52853	0.06	581.34879	581.34880	-0.02
27				882.54168	882.54173	-0.05	596.02420	596.02429	-0.15
28				904.55479	904.55477	0.03	610.69960	610.69949	0.18
29				926.56790	926.56757	0.36	625.37501	625.37496	0.07
30				*948.58101	-----	-----	640.05041	640.05037	0.06
31				970.59412	970.59367	0.46	654.72582	654.72587	-0.07
32							669.40122	669.40108	0.22
33							684.07663	684.07672	-0.14
34							698.75203	698.75222	-0.27
35							713.42744	713.42764	-0.29
Average of absolute value			0.44			0.17			0.13
Standard deviation			0.85			0.13			0.08
Mass list of [TPGS+2Na+H]³⁺(H (C₂H₄O)_n C₃₃H₅₃O₅Na₂H) and [TPGS+Na+H]²⁺(H (C₂H₄O)_n C₃₃H₅₃O₅NaH)									
PEG repeat unit, n	Theoretical m/z (1+)	Experimental m/z (1+)	Error (ppm)	Theoretical m/z (2+)	Experimental m/z (2+)	Error (ppm)	Theoretical m/z (3+)	Experimental m/z (3+)	Error (ppm)
18				673.43275	673.43305	-0.17			
19				695.44585	695.44606	-0.05			
20				717.45896	717.45939	-0.28			
21				739.47207	739.47232	-0.03			
22				761.48518	761.48562	-0.20	515.31986	515.31990	-0.18
23				783.49828	783.49843	0.11	529.99526	529.99523	-0.02

24				805.51139	805.51122	0.21	544.67067	544.67066	0.01
25				827.52450	827.52498	-0.23	559.34607	559.34612	0.00
26				849.53761	849.53790	-0.05	574.02148	574.02130	0.34
27				871.55071	871.55079	0.18	588.69688	588.69675	0.23
28				893.56382	893.56401	0.02	603.37229	603.37266	0.01
29							618.04769	618.04746	0.38
30							632.72310	632.72317	0.01
31							647.39850	647.39832	0.28
32							662.07391	662.07366	0.37
33							676.74931	676.74956	-0.09
Average of absolute value						0.14			0.16
SD						0.17			0.19
Mass list of [TPGS+2Na+NH₄]³⁺ (H (C₂H₄O)_n C₃₃H₅₃O₅Na₂NH₄)									
PEG repeat unit, n	Theoretical m/z (1+)	Experimental m/z (1+)	Error (ppm)	Theoretical m/z (2+)	Experimental m/z (2+)	Error (ppm)	Theoretical m/z (3+)	Experimental m/z (3+)	Error (ppm)
24							550.34618	550.34629	-0.14
25							565.02159	565.02157	0.10
26							579.69699	579.69703	0.02
27							594.37240	594.37215	0.45
28							609.04780	609.04765	0.26
29							623.72321	623.72315	0.10
30							638.39861	638.39875	-0.01
31							653.07402	653.07393	0.26
32							667.74942	667.74941	0.15
33							550.34618	550.34629	-0.14
Average of absolute value									0.17
SD									0.16
Mass list of [TPGS+3H]³⁺ (H (C₂H₄O)_n C₃₃H₅₃O₅H₃)									
PEG repeat unit,							Theoretical	Experimental	Error

n							m/z (3+)	m/z (3+)	(ppm)
23							515.34063	515.34061	-0.58
24							530.01604	530.01582	-0.20
25							544.69144	544.69155	-0.81
26							559.36685	559.36688	-0.65
27							574.04225	574.04207	-0.28
28							588.71766	588.71740	-0.16
29							603.39306	603.39278	-0.11
30							618.06847	618.06815	-0.06
31							632.74387	632.74391	-0.63
32							647.41928	647.41923	-0.50
Average of absolute value									0.20
SD									0.21

* Peaks used as internal calibrants

Table C.2 Mass list of proposed peaks in Figure 4.5

Mass list of free PEG (H (C₂H₄O)_nNa_m) m=1, 2, 3									
PEG repeat unit, n	Theoretical m/z (1+)	Experimental m/z (1+)	Error (ppm)	Theoretical m/z (2+)	Experimental m/z (2+)	Error (ppm)	Theoretical m/z (3+)	Experimental m/z (3+)	Error (ppm)
15	701.39301	701.39286	-0.21						
16	745.41922	745.41905	-0.23						
17	789.44544	789.44527	-0.22	406.21733	384.20428	0.15			
18	833.47165	833.4714	-0.31	428.23043	406.21734	-0.03			
19	877.49787	877.49762	-0.28	450.24354	428.2304	0.09			
20	921.52408	921.52376	-0.35	472.25665	450.24351	0.08			
21	965.550300	965.54997	-0.34	494.26976	472.25662	0.07			
22	1009.57652	1009.57618	-0.33	516.28286	494.26969	0.14			
23	1053.60273	1053.60236	-0.35	538.29597	516.28278	0.17			
24	1097.62895	1097.62857	-0.34	560.30908	538.2959	0.14			
25	1141.65516	1141.65481	-0.31	582.32219	560.30898	0.18			
26				604.33529	582.32212	0.12			
27				626.34840	604.33519	0.18			
28				648.36151					
29				670.37462					
Average of absolute value			0.27			0.17			
SD			0.05			0.03			
Mass list of [TPGS+mNa]^{m+} (H (C₂H₄O)_n C₃₃H₅₃O₅Na_m) m=1, 2, 3									
PEG repeat unit, n	Theoretical m/z (1+)	Experimental m/z (1+)	Error (ppm)	Theoretical m/z (2+)	Experimental m/z (2+)	Error (ppm)	Theoretical m/z (3+)	Experimental m/z (3+)	Error (ppm)
8	905.59606	905.59579	0.30						
9	949.62228	949.62207	0.22						
10	993.64849	993.64808	0.42						
11	1037.67471	1037.67427	0.42						
12	1081.70092	1081.70057	0.33						
13	1125.72714	1125.72665	0.43	574.35818	574.35803	0.26			
14	1169.75335	1169.75296	0.34	596.37129	596.37113	0.26			
15	1213.77957	1213.77906	0.42	618.38439	618.38427	0.20			
16	1257.80578	1257.80532	0.37	640.39750	640.39736	0.22			
17	1301.83200	1301.83147	0.41	662.41061	662.41046	0.23			

18	1345.85821	1345.85772	0.37	684.42371	684.42357	0.21			
19	1389.8844	1389.88384	0.43	706.43682	706.43667	0.22			
20	1433.91064	1433.90999	0.46	728.44993	728.44978	0.21			
21	1477.93686	1477.93610	0.51	750.46304	750.46287	0.23	507.97177	507.97171	0.11
22	1521.96308	1521.96216	0.60	772.47615	772.47597	0.23	522.64717	522.6471	0.14
23	1565.98929	1565.98839	0.58	794.48925	794.48906	0.24	537.32258	537.32254	0.07
24	1610.01551	1610.01451	0.62	816.50236	816.50216	0.25	551.99798	551.99789	0.16
25	1654.04172	1654.04057	0.70	838.51547	838.51523	0.29	566.67339	566.67333	0.10
26	1698.06794	1698.06731	0.37	860.52857	860.52832	0.30	581.34879	581.34862	0.29
27	1742.09415	1742.09365	0.29	882.54168	882.54141	0.31	596.02420	596.02407	0.21
28	1786.12037	1786.11893	0.80	904.55479	904.55448	0.34	610.69960	610.69949	0.18
29	1830.14658	1830.14638	0.11	926.56790	926.56757	0.36	625.37501	625.37487	0.22
30				948.58101	948.58067	0.36	640.05041	640.05033	0.13
31				970.59412	970.59376	0.37	654.72582	654.7256	0.33
32				992.60722	992.60688	0.34	669.40122	669.40107	0.23
33				1014.62033	1014.61995	0.37			
34				1036.63344	1036.633	0.42			
Average of absolute value			0.40			0.27			0.18
SD			0.16			0.09			0.08
Mass list of [TPGS+Na+NH₄]²⁺ (H (C₂H₄O)_n C₃₃H₅₃O₅Na NH₄) and [TPGS+NH₄]⁺ (H (C₂H₄O)_n C₃₃H₅₃O₅NH₄)									
PEG repeat unit, n	Theoretical m/z (1+)	Experimental m/z (1+)	Error (ppm)	Theoretical m/z (2+)	Experimental m/z (2+)	Error (ppm)	Theoretical m/z (3+)	Experimental m/z (3+)	Error (ppm)
12	1120.77174	1120.7714	0.31						
13	1164.79796	1164.79755	0.35						
14	1208.82417	1208.82371	0.38						
15	1252.85039	1252.85004	0.28	615.90670	615.90652	-0.29			
16	1296.87660	1296.87616	0.34	637.91981	637.9196	-0.32			
17	1340.90282	1340.90232	0.37	659.93291	659.93274	-0.26			
18	1384.92903	1384.92852	0.37	681.94602	681.94585	-0.25			
19	1428.95525	1428.95448	0.54	703.95913	703.95898	-0.21			
20	1472.98146	1472.98063	0.57	725.97224	725.97207	-0.23			
21	1517.00768	1517.00658	0.72	747.98534	747.98517	-0.23			
22	1561.03389	1561.03303	0.55	769.99845	769.99824	-0.27			
23	1605.06011	1605.05937	0.46	792.01156	792.01139	-0.21			
24				814.02467	814.02446	-0.25			

25				836.03777	836.03751	-0.31			
26				858.05088	858.05059	-0.34			
27				880.06399	880.06374	-0.28			
28				902.07710	902.07676	-0.37			
29				924.09020	924.08988	-0.35			
30				946.10331	946.10285	-0.49			
31				968.11642	968.1161	-0.33			
32				990.12953	990.12916	-0.37			
33				1012.14263	1012.1426	-0.08			
Average of absolute value			0.43			0.29			
SD			0.13			0.08			
Mass list of [TPGS+Na+H]²⁺ (H (C₂H₄O)_n C₃₃H₅₃O₅NaH)									
PEG repeat unit, n	Theoretical m/z (1+)	Experimental m/z (1+)	Error (ppm)	Theoretical m/z (2+)	Experimental m/z (2+)	Error (ppm)	Theoretical m/z (3+)	Experimental m/z (3+)	Error (ppm)
18				673.43275	673.43253	0.32			
19				695.44585	695.44567	0.26			
20				717.45896	717.45886	0.14			
21				739.47207	739.47182	0.34			
22				761.48518	761.48503	0.19			
23				783.49828	783.49805	0.30			
24				805.51139	805.51112	0.34			
25				827.52450	827.52426	0.29			
26				849.53761	849.53736	0.29			
27				871.55071	871.55041	0.35			
28				893.56382	893.56341	0.46			
29				915.57693	915.57675	0.19			
Average of absolute value						0.29			
SD						0.08			
Mass list of [Di-TPGS+2Na]²⁺ (H (C₂H₄O)_n C₆₆H₁₀₆O₉Na₂) and [Di-TPGS+Na+NH₄]²⁺ (H (C₂H₄O)_n C₆₆H₁₀₆O₉NaNH₄)									
				[Di-TPGS+2Na]²⁺			[Di-TPGS+Na+NH₄]²⁺		
PEG repeat unit, n				Theoretical m/z (2+)	Experimental m/z (2+)	Error (ppm)	Theoretical m/z (2+)	Experimental m/z (2+)	Error (ppm)
17				918.60418	918.60337	0.88			
18				940.61729	940.61685	0.47			

19				962.63040	962.62971	0.71	982.16551	982.16510	0.42
20				984.64350	984.64288	0.63	1004.17862	1004.17810	0.52
21				1006.65661	1006.65596	0.65	1026.19173	1026.19124	0.48
22				1028.66972	1028.66903	0.67	1048.20484	1048.20446	0.36
23				1050.68283	1050.68216	0.63	1070.21794	1070.21757	0.35
24				1072.69593	1072.69524	0.65	1092.23105	1092.23068	0.34
25				1094.70904	1094.70836	0.62	1114.24416	1114.24378	0.34
26				1116.72215	1116.72138	0.69	1136.25727	1136.25689	0.33
27				1138.73526	1138.73456	0.61			
28				1160.74836	1160.74767	0.60			
29				1182.76147	1182.76072	0.63			
30				1204.77458	1204.77386	0.60			
31				1226.78769	1226.7873	0.31			
Average of absolute value						0.62			0.39
SD						0.12			0.07

Table C.3 Proposed formulae of peaks on CAD spectra of [TPGS+3Na]³⁺ and [TPGS+2Na]²⁺ in Figure 4.6

Proposed formulae of peaks on CAD spectrum of [TPGS+3Na] ³⁺ (C ₈₇ H ₁₆₂ O ₃₂ Na ₃) in Figure 4.6c					
Proposed cleavage site	Proposed Formula	Theoretical <i>m/z</i>	Experimental <i>m/z</i>	Error (ppm)	Charge state
	C ₈₇ H ₁₆₂ O ₃₂ Na	1742.09414	1742.09469	0.31	1+
	*C ₈₇ H ₁₆₂ O ₃₂ Na ₂	882.54168			2+
	C ₈₇ H ₁₆₂ O ₃₂ Na ₃	596.02420			3+
a	C ₆₈ H ₁₂₄ O ₃₂ Na	1475.79679	1475.79739	0.41	1+
a	C ₆₄ H ₁₁₆ O ₃₀ Na	1387.74436	1387.74489	0.38	1+
a	C ₆₂ H ₁₁₂ O ₂₉ Na	1343.71815	1343.71758	-0.42	1+
a	C ₆₀ H ₁₀₈ O ₂₈ Na	1299.69193	1299.69165	-0.22	1+
a	C ₅₈ H ₁₀₄ O ₂₇ Na	1255.66572	1255.66503	-0.55	1+
a	C ₆₈ H ₁₂₄ O ₃₂ Na ₂	749.39301	749.39286	-0.20	2+
a	C ₆₄ H ₁₁₆ O ₃₀ Na ₂	705.36679	705.36648	-0.44	2+
C ₂₀ H ₃₈	C ₆₇ H ₁₂₄ O ₃₂ Na	1463.79679	1463.79680	0.00	1+
C ₂₀ H ₃₈	C ₆₇ H ₁₂₄ O ₃₂ Na ₂	743.39301	743.39265	-0.48	2+
b	C ₅₈ H ₁₁₄ O ₃₁ Na	1329.72363	1329.72380	0.13	1+
b	C ₅₈ H ₁₁₄ O ₃₁ Na ₂	676.35642	676.35599	-0.63	2+
b	C ₅₈ H ₁₁₂ O ₃₁ Na	1327.70798	1327.70728	-0.53	1+
b	C ₅₈ H ₁₁₂ O ₃₁ Na ₂	675.34860	675.34860	0.00	2+
c	C ₅₈ H ₁₁₂ O ₃₀ Na	1311.71306	1311.71376	0.53	1+
c	C ₅₈ H ₁₁₂ O ₃₀ Na ₂	667.35114	667.35083	-0.47	2+
d	C ₅₇ H ₁₁₂ O ₂₉ Na	1283.71815	1283.71890	0.58	1+
d	C ₅₇ H ₁₁₂ O ₂₉ Na ₂	653.35369	653.35362	-0.10	2+
e	C ₅₄ H ₁₁₀ O ₂₈ Na	1229.70758	1229.70750	-0.07	1+
e	C ₅₂ H ₁₀₆ O ₂₇ Na	1185.68137	1185.68118	-0.16	1+
e	C ₅₀ H ₁₀₂ O ₂₆ Na	1141.65515	1141.65540	0.22	1+
e	C ₄₈ H ₉₈ O ₂₅ Na	1097.62894	1097.62913	0.18	1+
e	C ₄₆ H ₉₄ O ₂₄ Na	1053.60272	1053.60298	0.25	1+
e	C ₄₄ H ₉₀ O ₂₃ Na	1009.57651	1009.57686	0.35	1+
e	C ₄₂ H ₈₆ O ₂₂ Na	965.55029	965.55050	0.22	1+
e	C ₄₀ H ₈₂ O ₂₁ Na	921.52408	921.52455	0.52	1+
e	C ₃₈ H ₇₈ O ₂₀ Na	877.49786	877.49839	0.60	1+
e	C ₃₆ H ₇₄ O ₁₉ Na	833.47165	833.47163	-0.02	1+
e	C ₃₄ H ₇₀ O ₁₈ Na	789.44543	789.44513	-0.38	1+

e	C ₃₂ H ₆₆ O ₁₇ Na	745.41922	745.41919	-0.03	1+
e	C ₃₀ H ₆₂ O ₁₆ Na	701.39300	701.39271	-0.41	1+
e	C ₂₈ H ₅₈ O ₁₅ Na	657.36679	657.36634	-0.68	1+
e	C ₂₆ H ₅₄ O ₁₅ Na	613.34057	613.34020	-0.60	1+
e	C ₂₄ H ₅₀ O ₁₃ Na	569.31436	569.31444	0.15	1+
e	C ₂₂ H ₄₆ O ₁₂ Na	525.28814	525.28795	-0.36	1+
e	C ₂₀ H ₄₂ O ₁₁ Na	481.26193	481.26177	-0.32	1+
e	C ₅₄ H ₁₁₀ O ₂₈ Na ₂	626.34840	626.34812	-0.45	2+
e	C ₅₂ H ₁₀₆ O ₂₇ Na ₂	604.33523	604.33502	-0.34	2+
e	C ₄₈ H ₉₈ O ₂₅ Na ₂	560.30888	560.30877	-0.19	2+
e	C ₄₆ H ₉₄ O ₂₄ Na ₂	538.29570	538.29560	-0.19	2+
e	C ₅₄ H ₁₀₈ O ₂₈ Na	1227.69193	1227.69236	0.35	1+
e	C ₅₂ H ₁₀₄ O ₂₇ Na	1183.66572	1183.66572	0.00	1+
e	C ₅₀ H ₁₀₀ O ₂₆ Na	1139.63950	1139.63961	0.10	1+
e	C ₄₈ H ₉₆ O ₂₅ Na	1095.61329	1095.61355	0.24	1+
e	C ₄₆ H ₉₂ O ₂₄ Na	1051.58707	1051.58725	0.17	1+
e	C ₄₄ H ₈₈ O ₂₃ Na	1007.56086	1007.56077	-0.08	1+
e	C ₄₂ H ₈₄ O ₂₂ Na	963.53464	963.53473	0.09	1+
e	C ₄₀ H ₈₀ O ₂₁ Na	919.50843	919.50861	0.20	1+
e	C ₃₈ H ₇₆ O ₂₀ Na	875.48221	875.48211	-0.11	1+
e	C ₃₆ H ₇₂ O ₁₉ Na	831.45600	831.45593	-0.08	1+
e	C ₃₄ H ₆₈ O ₁₈ Na	787.42978	787.42971	-0.09	1+
e	C ₃₂ H ₆₄ O ₁₇ Na	743.40357	743.40317	-0.53	1+
e	C ₃₀ H ₆₀ O ₁₆ Na	699.37735	699.37693	-0.60	1+
e	C ₂₈ H ₅₆ O ₁₅ Na	655.35114	655.35078	-0.54	1+
e	C ₂₆ H ₅₂ O ₁₅ Na	611.32492	611.32454	-0.62	1+
e	C ₂₄ H ₄₈ O ₁₃ Na	567.29871	567.29840	-0.54	1+
e	C ₂₂ H ₄₄ O ₁₂ Na	523.27249	523.27214	-0.67	1+
e	C ₂₀ H ₄₀ O ₁₁ Na	479.24628	479.24611	-0.34	1+
e	C ₁₈ H ₃₆ O ₁₀ Na	435.22006	435.22001	-0.11	1+
e	C ₅₄ H ₁₀₈ O ₂₈ Na ₂	625.34058	625.34032	-0.41	2+
e	C ₅₂ H ₁₀₄ O ₂₇ Na ₂	603.32740	603.32707	-0.55	2+
e	C ₅₀ H ₁₀₀ O ₂₆ Na ₂	581.31423	581.31416	-0.12	2+
e	C ₄₈ H ₉₆ O ₂₅ Na ₂	559.30105	559.30100	-0.09	2+
e	C ₄₆ H ₉₂ O ₂₄ Na ₂	537.28788	537.28791	0.06	2+
e	C ₄₄ H ₈₈ O ₂₃ Na ₂	515.27470	515.27478	0.15	2+

e	C ₄₂ H ₈₄ O ₂₂ Na ₂	493.26153	493.26170	0.35	2+
e	C ₄₀ H ₈₀ O ₂₁ Na ₂	471.24835	471.24859	0.50	2+
f	C ₅₄ H ₁₀₈ O ₂₇ Na	1211.69702	1211.69740	0.31	1+
f	C ₅₂ H ₁₀₄ O ₂₆ Na	1167.67081	1167.67100	0.17	1+
f	C ₅₀ H ₁₀₀ O ₂₅ Na	1123.64459	1123.64471	0.11	1+
f	C ₄₈ H ₉₆ O ₂₄ Na	1079.61838	1079.61856	0.17	1+
f	C ₄₆ H ₉₂ O ₂₃ Na	1035.59216	1035.59241	0.24	1+
f	C ₄₄ H ₈₈ O ₂₂ Na	991.56595	991.56589	-0.06	1+
f	C ₄₂ H ₈₄ O ₂₁ Na	947.53973	947.53983	0.11	1+
f	C ₄₀ H ₈₀ O ₂₀ Na	903.51352	903.51380	0.32	1+
f	C ₃₈ H ₇₆ O ₁₉ Na	859.48730	859.48701	-0.34	1+
f	C ₃₆ H ₇₂ O ₁₈ Na	815.46109	815.46095	-0.17	1+
f	C ₃₄ H ₆₈ O ₁₇ Na	771.43487	771.43484	-0.04	1+
f	C ₃₂ H ₆₄ O ₁₆ Na	727.40866	727.40846	-0.27	1+
f	C ₃₀ H ₆₀ O ₁₅ Na	683.38244	683.38217	-0.40	1+
f	C ₂₈ H ₅₆ O ₁₄ Na	639.35623	639.35598	-0.38	1+
f	C ₅₄ H ₁₀₈ O ₂₇ Na ₂	617.34312	617.34281	-0.50	2+
f	C ₅₂ H ₁₀₄ O ₂₆ Na ₂	595.33001	595.33044	0.72	2+
f	C ₅₀ H ₁₀₀ O ₂₅ Na ₂	573.31691	573.31699	0.15	2+
f	C ₄₈ H ₉₆ O ₂₄ Na ₂	551.30380	551.30349	-0.56	2+
f	C ₄₆ H ₉₂ O ₂₃ Na ₂	529.29069	529.29050	-0.36	2+
f	C ₄₄ H ₈₈ O ₂₂ Na ₂	507.27758	507.27732	-0.52	2+
f	C ₄₂ H ₈₄ O ₂₁ Na ₂	485.26448	485.26431	-0.34	2+
f	C ₄₀ H ₈₀ O ₂₀ Na ₂	463.25137	463.25128	-0.19	2+
f	C ₃₈ H ₇₆ O ₁₉ Na ₂	441.23826	441.23816	-0.23	2+
f	C ₃₆ H ₇₂ O ₁₈ Na ₂	419.22515	419.22509	-0.15	2+
g	C ₂₈ H ₅₆ O ₁₃ Na	623.36129	623.36099	-0.47	1+
g	C ₂₆ H ₅₂ O ₁₂ Na	579.33507	579.33489	-0.31	1+
g	C ₂₄ H ₄₈ O ₁₁ Na	535.30886	535.30853	-0.61	1+
g	C ₂₂ H ₄₄ O ₁₀ Na	491.28264	491.28238	-0.53	1+
g	C ₂₀ H ₄₀ O ₉ Na	447.25643	447.25633	-0.21	1+
g	C ₁₈ H ₃₆ O ₈ Na	403.23021	403.23036	0.37	1+
h	C ₈₃ H ₁₅₄ O ₃₀ Na	1654.04171	1654.04120	-0.31	1+
h	C ₈₂ H ₁₅₀ O ₂₉ Na	1610.01550	1610.01661	0.69	1+
h	C ₆₁ H ₁₁₀ O ₁₉ Na	1169.75335	1169.75369	0.29	1+
h	C ₅₇ H ₁₀₆ O ₁₈ Na	1125.72714	1125.72759	0.40	1+

h	C ₅₅ H ₁₀₂ O ₁₇ Na	1081.70092	1081.70156	0.59	1+
h	C ₅₄ H ₉₈ O ₁₆ Na	1037.67471	1037.67490	0.19	1+
h	C ₅₂ H ₉₄ O ₁₅ Na	993.64849	993.64878	0.29	1+
Average of absolute value				0.32	
SD				0.19	
Proposed formulae of peaks on CAD spectrum of [TPGS+2Na]²⁺ (C₈₇H₁₆₂O₃₂Na₂) in Figure 4.6b					
Proposed cleavage site	Proposed Formula	Theoretical <i>m/z</i>	Experimental <i>m/z</i>	Error (ppm)	Charge state
	*C ₈₇ H ₁₆₂ O ₃₂ Na ₂	882.54168			
	C ₈₇ H ₁₆₂ O ₃₂ Na	1742.09414	1742.09512	-0.56	
a	C ₆₈ H ₁₂₄ O ₃₂ Na	1475.79679	1475.79760	-0.55	1+
a	C ₆₈ H ₁₂₄ O ₃₂ Na ₂	749.39301	749.39263	0.50	2+
b	C ₅₈ H ₁₁₄ O ₃₁ Na ₂	676.35642	676.35588	0.79	2+
b	C ₅₈ H ₁₁₂ O ₃₁ Na ₂	675.34860	675.34875	-0.22	2+
c	C ₅₈ H ₁₁₂ O ₃₀ Na	1311.71306	1311.71516	-1.60	1+
c	C ₅₈ H ₁₁₂ O ₃₀ Na ₂	667.35114	667.35032	1.23	2+
d	C ₅₇ H ₁₁₂ O ₂₉ Na ₂	653.35369	653.35257	1.6	2+
e	C ₅₄ H ₁₀₈ O ₂₈ Na	1227.69193	1227.69334	-1.15	1+
e	C ₅₂ H ₁₀₄ O ₂₇ Na	1183.66572	1183.66691	-1.01	1+
e	C ₅₀ H ₁₀₀ O ₂₆ Na	1139.63950	1139.64038	-0.77	1+
e	C ₄₈ H ₉₆ O ₂₅ Na	1095.61329	1095.61272	0.52	1+
e	C ₄₆ H ₉₂ O ₂₄ Na	1051.58707	1051.58652	0.52	1+
e	C ₄₄ H ₈₈ O ₂₃ Na	1007.56086	1007.56064	0.21	1+
e	C ₄₂ H ₈₄ O ₂₂ Na	963.53464	963.53495	-0.32	1+
e	C ₄₀ H ₈₀ O ₂₁ Na	919.50843	919.50819	0.26	1+
e	C ₃₈ H ₇₆ O ₂₀ Na	875.48221	875.48225	-0.05	1+
e	C ₃₆ H ₇₂ O ₁₉ Na	831.45600	831.45607	-0.09	1+
e	C ₃₄ H ₆₈ O ₁₈ Na	787.42978	787.42945	0.42	1+
e	C ₃₀ H ₆₀ O ₁₆ Na	699.37735	699.37714	0.30	1+
e	C ₂₆ H ₅₂ O ₁₅ Na	611.32492	611.32462	0.49	1+
e	C ₂₄ H ₄₈ O ₁₃ Na	567.29871	567.29833	0.66	1+
e	C ₂₂ H ₄₄ O ₁₂ Na	523.27249	523.27217	0.61	1+
e	C ₅₄ H ₁₀₈ O ₂₈ Na ₂	625.34058	625.34011	0.75	2+
f	C ₅₄ H ₁₀₈ O ₂₇ Na	1211.69702	1211.69737	-0.29	1+
f	C ₅₂ H ₁₀₄ O ₂₆ Na	1167.67081	1167.67148	-0.58	1+

f	C ₅₀ H ₁₀₀ O ₂₅ Na	1123.64459	1123.64465	-0.05	1+
f	C ₄₈ H ₉₆ O ₂₄ Na	1079.61838	1079.61856	-0.17	1+
f	C ₄₆ H ₉₂ O ₂₃ Na	1035.59216	1035.59218	-0.02	1+
f	C ₄₄ H ₈₈ O ₂₂ Na	991.56595	991.56618	-0.24	1+
f	C ₄₂ H ₈₄ O ₂₁ Na	947.53973	947.53985	-0.13	1+
f	C ₄₀ H ₈₀ O ₂₀ Na	903.51352	903.51350	0.02	1+
f	C ₃₈ H ₇₆ O ₁₉ Na	859.48730	859.48739	-0.10	1+
f	C ₃₆ H ₇₂ O ₁₈ Na	815.46109	815.46079	0.36	1+
f	C ₃₂ H ₆₄ O ₁₆ Na	727.40866	727.40827	0.53	1+
f	C ₃₀ H ₆₀ O ₁₅ Na	683.38244	683.38185	0.86	1+
f	C ₂₈ H ₅₆ O ₁₄ Na	639.35623	639.35579	0.68	1+
f	C ₅₄ H ₁₀₈ O ₂₇ Na ₂	617.34312	617.34264	0.78	2+
f	C ₅₂ H ₁₀₄ O ₂₆ Na ₂	595.33001	595.32946	0.93	2+
f	C ₅₀ H ₁₀₀ O ₂₅ Na ₂	573.31691	573.31632	1.02	2+
f	C ₄₈ H ₉₆ O ₂₄ Na ₂	551.30380	551.30333	0.85	2+
f	C ₄₆ H ₉₂ O ₂₃ Na ₂	529.29069	529.29016	1.00	2+
f	C ₄₄ H ₈₈ O ₂₂ Na ₂	507.27758	507.27702	1.11	2+
f	C ₄₀ H ₈₀ O ₂₀ Na ₂	463.25137	463.25120	0.36	2+
Average of absolute value				0.55	
SD				0.38	

* Peaks used as internal calibrants

Table C.4 Proposed formulae of peaks on ECD spectra of [TPGS+3Na]³⁺ and [TPGS+2Na]²⁺ in Figure 4.7

Proposed formulae of peaks on ECD spectrum of [TPGS+3Na] ³⁺ (C ₈₇ H ₁₆₂ O ₃₂ Na ₃) in Figure 4.7c					
Proposed cleavage site	Proposed Formula	Theoretical m/z	Experimental m/z	Error (ppm)	Charge state
	*C ₈₇ H ₁₆₂ O ₃₂ Na	1742.09414	1742.09413		1+
	*C ₈₇ H ₁₆₂ O ₃₂ Na ₂	882.54168	882.54148		2+
	*C ₈₇ H ₁₆₂ O ₃₂ Na ₃	596.02420	596.0242		3+
	*C ₈₇ H ₁₆₂ O ₃₂ Na ₃	894.03657	894.03677		2+
d	C ₅₇ H ₁₁₃ O ₂₉ Na ₂	1307.71574	1307.71546	0.22	1+
d	C ₅₇ H ₁₁₃ O ₂₉ Na ₃	665.35248	665.35239	0.14	1+
d	C ₅₅ H ₁₀₉ O ₂₈ Na ₃	643.33938	643.33935	0.04	2+
d	C ₅₅ H ₁₀₉ O ₂₈ Na ₂	1263.68953	1263.68965	-0.10	1+
d	C ₅₃ H ₁₀₅ O ₂₇ Na ₂	1219.66331	1219.66298	0.27	1+
e	C ₅₃ H ₁₀₅ O ₂₇ Na ₃	621.32627	621.3263	-0.05	2+
e	C ₅₄ H ₁₀₉ O ₂₈ Na ₂	1251.68953	1251.68964	-0.09	1+
e	C ₅₄ H ₁₀₉ O ₂₈ Na ₃	637.33937	637.33922	0.24	2+
e	C ₅₂ H ₁₀₄ O ₂₇ Na ₃	1229.64526	1229.64543	-0.14	1+
e	C ₅₀ H ₁₀₀ O ₂₆ Na ₃	1185.61904	1185.61971	-0.56	1+
f	C ₅₄ H ₁₀₈ O ₂₈ Na ₃	1273.67147	1273.67227	-0.63	1+
f	C ₅₄ H ₁₀₉ O ₂₇ Na ₂	1235.69461	1235.69382	0.64	1+
f	C ₅₂ H ₁₀₅ O ₂₆ Na ₂	1191.66840	1191.66785	0.46	1+
f	C ₅₀ H ₁₀₁ O ₂₅ Na ₂	1147.64218	1147.64196	0.20	1+
f	C ₄₈ H ₉₇ O ₂₄ Na ₂	1103.61597	1103.6154	0.52	1+
f	C ₄₆ H ₉₃ O ₂₃ Na ₂	1059.58975	1059.59054	-0.74	1+
f	C ₅₂ H ₁₀₃ O ₂₆ Na ₂	1189.65275	1189.65388	-0.95	1+
f	C ₅₀ H ₉₉ O ₂₅ Na ₂	1145.62653	1145.62507	1.28	1+
f	C ₄₈ H ₉₅ O ₂₄ Na ₂	1101.60032	1101.60035	-0.03	1+
f	C ₄₄ H ₈₇ O ₂₂ Na ₂	1013.54789	1013.54752	0.36	1+
f	C ₄₂ H ₈₃ O ₂₁ Na ₂	969.52167	969.52145	0.23	1+
f	C ₄₀ H ₇₉ O ₂₀ Na ₂	925.49546	925.49509	0.40	1+
f	C ₃₈ H ₇₅ O ₁₉ Na ₂	881.46924	881.46861	0.72	1+
f	C ₃₆ H ₇₁ O ₁₈ Na ₂	837.44303	837.44247	0.67	1+
f	C ₃₄ H ₆₈ O ₁₇ Na	771.43487	771.43447	0.52	1+
f	C ₃₂ H ₆₄ O ₁₆ Na	727.40866	727.40828	0.52	1+
f	C ₃₀ H ₆₀ O ₁₅ Na	683.38244	683.38272	-0.41	1+
f	C ₂₈ H ₅₆ O ₁₄ Na	639.35623	639.35628	-0.09	1+
f	C ₂₆ H ₅₂ O ₁₃ Na	595.33001	595.33018	-0.29	1+

f	C ₂₄ H ₄₈ O ₁₂ Na	551.30380	551.30392	-0.23	1+
f	C ₂₂ H ₄₄ O ₁₁ Na	507.27758	507.27802	-0.87	1+
f	C ₂₀ H ₄₀ O ₁₀ Na	463.25137	463.25199	-1.35	1+
f	C ₁₈ H ₃₆ O ₉ Na	419.22515	419.22575	-1.43	1+
f	C ₁₆ H ₃₂ O ₈ Na	375.19894	375.19909	-0.41	1+
f	C ₁₄ H ₂₈ O ₇ Na	331.17272	331.17292	-0.60	1+
g	C ₃₀ H ₆₀ O ₁₄ Na	667.38753	667.38758	-0.08	1+
g	C ₂₈ H ₅₆ O ₁₃ Na	623.36131	623.36151	-0.32	1+
g	C ₂₆ H ₅₂ O ₁₂ Na	579.33510	579.33561	-0.88	1+
g	C ₂₄ H ₄₈ O ₁₁ Na	535.30888	535.30913	-0.46	1+
g	C ₂₂ H ₄₄ O ₁₀ Na	491.28267	491.28322	-1.12	1+
g	C ₂₀ H ₄₀ O ₉ Na	447.25645	447.257	-1.22	1+
g	C ₁₈ H ₃₆ O ₈ Na	403.23024	403.23079	-1.37	1+
h	C ₈₅ H ₁₅₇ O ₃₁ Na ₃	871.51955	871.51899	0.64	2+
h	C ₈₃ H ₁₅₃ O ₃₀ Na ₃	849.50644	849.50666	-0.26	2+
h	C ₈₁ H ₁₄₉ O ₂₉ Na ₃	827.49333	827.49325	0.10	2+
h	C ₇₉ H ₁₄₅ O ₂₈ Na ₃	805.48023	805.48019	0.05	2+
h	C ₇₇ H ₁₄₁ O ₂₇ Na ₃	783.46712	783.467	0.15	2+
h	C ₇₅ H ₁₃₇ O ₂₆ Na ₂	1499.91880	1499.919	-0.13	1+
h	C ₇₃ H ₁₃₃ O ₂₅ Na ₂	1455.89259	1455.89346	-0.60	1+
h	C ₇₁ H ₁₂₉ O ₂₄ Na ₂	1411.86637	1411.8661	0.19	1+
h	C ₆₉ H ₁₂₅ O ₂₃ Na ₂	1367.84016	1367.84028	-0.09	1+
h	C ₆₇ H ₁₂₁ O ₂₂ Na ₂	1323.81394	1323.8144	-0.35	1+
h	C ₆₅ H ₁₁₇ O ₂₁ Na ₂	1279.78773	1279.78807	-0.27	1+
h	C ₆₃ H ₁₁₃ O ₂₀ Na ₂	1235.76151	1235.762	-0.40	1+
h	C ₆₁ H ₁₀₉ O ₁₉ Na ₂	1191.73530	1191.7353	0.00	1+
Average of absolute value				0.46	
SD				0.38	
Proposed formulae of peaks on ECD spectrum of [TPGS+2Na]²⁺ (C₈₇H₁₆₂O₃₂Na₂) in Figure 4.7b					
Proposed cleavage site	Proposed Formula	Theoretical <i>m/z</i>	Experimental <i>m/z</i>	Error (ppm)	Charge state
	*C ₈₇ H ₁₆₂ O ₃₂ Na ₂	882.54168	882.54168		2+
	C ₈₇ H ₁₆₂ O ₃₂ Na	1742.09414	1742.09467	-0.30	1+
	C ₈₇ H ₁₆₂ O ₃₂ Na ₂	1765.08391	1765.08406	-0.08	1+
d	C ₅₇ H ₁₁₃ O ₂₉ Na ₂	1307.71574	1307.71582	-0.05	1+
d	C ₅₅ H ₁₀₉ O ₂₈ Na ₂	1263.68953	1263.68976	-0.18	1+
d	C ₅₃ H ₁₀₅ O ₂₇ Na ₂	1219.66331	1219.66369	-0.30	1+
e	C ₅₄ H ₁₀₉ O ₂₈ Na ₂	1251.68953	1251.68984	-0.24	1+
f	C ₅₄ H ₁₀₉ O ₂₇ Na ₂	1235.69461	1235.69465	-0.02	1+

Average of absolute value				0.17	
SD				0.12	

* Peaks used as internal calibrants

Table C.5 Proposed formulae of peaks on ECD/ECD MS³ spectrum of peak at m/z 643.3394 in Figure 4.8c

Proposed cleavage site	Proposed Formula	Theoretical m/z	Experimental m/z	Error (ppm)	Charge state
d	C ₅₅ H ₁₀₉ O ₂₈ Na ₂	1263.68953	1263.69066	-0.89	1+
f	C ₅₀ H ₁₀₁ O ₂₅ Na ₂	1147.64218	1147.64253	-0.30	1+
e	C ₅₂ H ₁₀₄ O ₂₇ Na ₃	1229.64526	1229.64615	-0.72	1+

Table C.6 The statistics of TPGS%, Di-TPGS%, and PEG%

TPGS%	Relative intensity of TPGS	$\frac{\text{Total ion intensity of TPGS}}{\text{Total ion intensity of (TPGS + DiTPGS + PEG)}}$
Di-TPGS%	Relative intensity of Di-TPGS	$\frac{\text{Total ion intensity of DiTPGS}}{\text{Total ion intensity of (TPGS + DiTPGS + PEG)}}$
PEG%	Relative intensity of PEG	$\frac{\text{Total ion intensity of PEG}}{\text{Total ion intensity of (TPGS + DiTPGS + PEG)}}$

Appendix D. (Supporting information for Chapter 5)

Table D.1 Mass list of proposed peaks on the CAD spectra of $[\text{TPGS}+2\text{Li}]^{2+}$, $[\text{TPGS}+2\text{Na}]^{2+}$, $[\text{TPGS}+2\text{K}]^{2+}$ and $[\text{TPGS}+2\text{Ag}]^{2+}$ in Figure 5.2

Proposed formulae of peaks on CAD spectra of $[\text{TPGS}+2\text{Li}]^{2+}$ in Figure 5.2a					
Charge state	Proposed Formula	Theoretical m/z	Experimental m/z	Error (ppm)	Proposed cleavage site
2	$\text{C}_{87}\text{H}_{162}\text{O}_{32}\text{Li}_2$	866.56808	866.56792	0.18	M
2	$\text{C}_{68}\text{H}_{124}\text{O}_{32}\text{Li}_2$	733.41924	733.4189	0.46	a
2	$\text{C}_{54}\text{H}_{108}\text{O}_{27}\text{Li}_2$	601.36935	601.36884	0.84	f
2	$\text{C}_{52}\text{H}_{104}\text{O}_{26}\text{Li}_2$	579.35624	579.35582	0.72	f
2	$\text{C}_{50}\text{H}_{100}\text{O}_{25}\text{Li}_2$	557.34313	557.34271	0.76	f
2	$\text{C}_{48}\text{H}_{96}\text{O}_{24}\text{Li}_2$	535.33002	535.32956	0.87	f
2	$\text{C}_{46}\text{H}_{92}\text{O}_{23}\text{Li}_2$	513.31692	513.31619	1.42	f
2	$\text{C}_{58}\text{H}_{112}\text{O}_{30}\text{Li}_2$	651.37749	651.3767	1.21	c
2	$\text{C}_{57}\text{H}_{112}\text{O}_{29}\text{Li}_2$	637.38003	637.37952	0.80	d
2	$\text{C}_{65}\text{H}_{118}\text{O}_{21}\text{Li}_2$	624.42374	624.42323	0.81	??
average				0.81	
SD				0.34	
Proposed formulae of peaks on CAD spectra of $[\text{TPGS}+2\text{Na}]^{2+}$ in Figure 5.2b					
Charge state	Proposed Formula	Theoretical m/z	Experimental m/z	Error (ppm)	Proposed cleavage site
1	$\text{C}_{87}\text{H}_{162}\text{O}_{32}\text{Na}_2$	882.54168	882.54259	1.03	M
1	$\text{C}_{87}\text{H}_{162}\text{O}_{32}\text{Na}$	1742.09414	1742.09904	2.81	M-Na
1	$\text{C}_{68}\text{H}_{124}\text{O}_{32}\text{Na}$	1475.79679	1475.80083	2.73	a
2	$\text{C}_{68}\text{H}_{124}\text{O}_{32}\text{Na}_2$	749.39301	749.3936	0.78	a
1	$\text{C}_{54}\text{H}_{108}\text{O}_{27}\text{Na}$	1211.69702	1211.69935	1.92	f
1	$\text{C}_{52}\text{H}_{104}\text{O}_{26}\text{Na}$	1167.67081	1167.67302	1.89	f
1	$\text{C}_{50}\text{H}_{100}\text{O}_{25}\text{Na}$	1123.64459	1123.64676	1.93	f
1	$\text{C}_{48}\text{H}_{96}\text{O}_{24}\text{Na}$	1079.61838	1079.62027	1.75	f
1	$\text{C}_{46}\text{H}_{92}\text{O}_{23}\text{Na}$	1035.59216	1035.59388	1.66	f
1	$\text{C}_{44}\text{H}_{88}\text{O}_{22}\text{Na}$	991.56595	991.56755	1.61	f
2	$\text{C}_{54}\text{H}_{108}\text{O}_{27}\text{Na}_2$	617.34312	617.34335	0.37	f
2	$\text{C}_{52}\text{H}_{104}\text{O}_{26}\text{Na}_2$	595.33001	595.33042	0.68	f
2	$\text{C}_{58}\text{H}_{112}\text{O}_{30}\text{Na}_2$	667.35114	667.35147	0.493	d

2	C ₅₇ H ₁₁₂ O ₂₉ Na ₂	653.35369	653.35452	1.27	c
average				1.60	
SD				0.76	
Proposed formulae of peaks on CAD spectra of [TPGS+2K] ²⁺ in Figure 5.2c					
Charge state	Proposed Formula	Theoretical <i>m/z</i>	Experimental <i>m/z</i>	Error (ppm)	Proposed cleavage site
2	C ₈₇ H ₁₆₂ O ₃₂ K ₂	898.51562	898.51506	-0.62	M
1	C ₈₇ H ₁₆₂ O ₃₂ K	1758.06808	1758.07041	-1.33	M-K
1	C ₇₉ H ₁₄₆ O ₂₈ K	1493.91079	1493.91163	-0.56	??
1	C ₇₅ H ₁₃₈ O ₂₆ K	1491.77073	1491.77171	-0.66	??
average				-0.79	
SD				0.36	
Proposed formulae of peaks on CAD spectra of [TPGS+2Ag] ²⁺ in Figure 5.2d					
Charge state	Proposed Formula	Theoretical <i>m/z</i>	Experimental <i>m/z</i>	Error (ppm)	Proposed cleavage site
2	C ₈₇ H ₁₆₂ O ₃₂ Ag ₂	966.45701	966.45605	0.99	M
2	C ₆₈ H ₁₂₄ O ₃₂ Ag ₂	833.30833	833.30801	0.38	a
2	C ₅₈ H ₁₁₂ O ₃₀ Ag ₂	751.26647	751.26594	0.71	c
2	C ₅₇ H ₁₁₂ O ₂₉ Ag ₂	737.26901	737.26842	0.80	d
2	C ₅₄ H ₁₀₈ O ₂₇ Ag ₂	701.25844	701.25790	0.77	f
2	C ₅₂ H ₁₀₄ O ₂₆ Ag ₂	679.24533	679.24471	0.92	f
2	C ₅₀ H ₁₀₀ O ₂₅ Ag ₂	657.23223	657.23142	1.22	f
2	C ₄₈ H ₉₆ O ₂₄ Ag ₂	635.21912	635.21838	1.16	f
2	C ₄₆ H ₉₂ O ₂₃ Ag ₂	613.20601	613.20547	0.88	f
2	C ₄₄ H ₈₈ O ₂₂ Ag ₂	591.19290	591.19220	1.19	f
2			879.90406		???
average				0.90	
SD				0.26	

Table D.2 Mass list of proposed peaks on the CAD spectra of [TPGS+Li+Na]²⁺, [TPGS+K+Li]²⁺, [TPGS+Li+Ag]²⁺, [TPGS+Na+Ag]²⁺, [TPGS+K+Ag]²⁺, and [TPGS+K+Na]²⁺ in Figure 5.3

Proposed formulae of peaks on CAD spectra of [TPGS+Li+Na] ²⁺ in Figure 5.3a					
Charge state	Proposed Formula	Theoretical <i>m/z</i>	Experimental <i>m/z</i>	Error (ppm)	Proposed cleavage site
2	C ₈₇ H ₁₆₂ O ₃₂ NaLi	874.55480	874.55576	1.09	M
1	C ₈₇ H ₁₆₂ O ₃₂ Li	1726.12038	1726.12321	1.63	M-Na
1	C ₆₈ H ₁₂₄ O ₃₂ Li	1459.82317	1459.82397	0.54	a
1	C ₅₄ H ₁₀₈ O ₂₇ Li	1195.72337	1195.72464	1.06	f
1	C ₅₂ H ₁₀₄ O ₂₆ Li	1151.69715	1151.69815	0.86	f
1	C ₅₀ H ₁₀₀ O ₂₅ Li	1107.67093	1107.67209	1.04	f
2	C ₆₈ H ₁₂₄ O ₃₂ LiNa	741.40619	741.40675	0.75	a
2	C ₅₈ H ₁₁₂ O ₃₀ LiNa	659.36432	659.36499	1.01	c
2	C ₅₇ H ₁₁₂ O ₂₉ LiNa	654.36686	654.36696	0.15	d
2	C ₅₄ H ₁₀₈ O ₂₇ LiNa	609.35629	609.35635	0.09	f
2	C ₅₂ H ₁₀₄ O ₂₆ LiNa	587.34318	587.34354	0.61	f
2	C ₅₀ H ₁₀₀ O ₂₅ LiNa	565.33008	565.33050	0.74	f
2	C ₄₈ H ₉₆ O ₂₄ LiNa	543.31697	543.31699	0.03	f
2	C ₈₃ H ₁₅₄ O ₃₀ LiNa	830.52867	830.52961	1.13	M-2C ₂ H ₄ O
average				0.77	
SD				0.45	
Proposed formulae of peaks on CAD spectra of [TPGS+Li+K] ²⁺ in Figure 5.3b					
Charge state	Proposed Formula	Theoretical <i>m/z</i>	Experimental <i>m/z</i>	Error (ppm)	Proposed cleavage site
2	C ₈₇ H ₁₆₂ O ₃₂ KLi	882.54177	882.54119	-0.66	M
1	C ₈₇ H ₁₆₂ O ₃₂ Li	1726.12039	1726.11915	-0.72	M-K
2	C ₈₄ H ₁₅₈ O ₂₇ KLi	822.53892	822.54019	1.54	???
average				0.06	
SD				1.28	
Proposed formulae of peaks on CAD spectra of [TPGS+Li+Ag] ²⁺ in Figure 5.3c					
Charge state	Proposed Formula	Theoretical <i>m/z</i>	Experimental <i>m/z</i>	Error (ppm)	Proposed cleavage site
2	C ₈₇ H ₁₆₂ O ₃₂ LiAg	916.51246	916.51199	-0.51	M
2	C ₆₈ H ₁₂₄ O ₃₂ AgLi	783.36386	783.36366	-0.26	a
1	C ₅₄ H ₁₀₈ O ₂₇ Li	1195.72337	1195.72366	0.24	f
2	C ₅₈ H ₁₁₂ O ₃₀ AgLi	701.32192	701.32183	-0.13	c

2	C ₅₇ H ₁₁₂ O ₂₉ AgLi	687.32446	687.32430	-0.23	d
2	C ₅₄ H ₁₀₈ O ₂₇ AgLi	651.31390	651.31371	-0.29	f
2	C ₅₂ H ₁₀₄ O ₂₆ AgLi	629.30079	629.30059	-0.32	f
2	C ₅₀ H ₁₀₀ O ₂₅ AgLi	607.28768	607.28717	-0.84	f
2	C ₄₈ H ₉₆ O ₂₄ AgLi	585.27458	585.27419	-0.66	f
2	C ₄₆ H ₉₂ O ₂₃ AgLi	563.26147	563.26119	-0.49	f
2	C ₄₄ H ₈₈ O ₂₂ AgLi	541.24836	541.24741	-1.76	f
2	C ₈₃ H ₁₅₄ O ₃₀ AgLi	872.48633	872.48605	-0.32	M-2C ₂ H ₄ O
2	C ₈₁ H ₁₅₀ O ₂₉ AgLi	850.47322	850.47311	-0.13	M-3C ₂ H ₄ O
2	C ₇₃ H ₁₃₄ O ₂₅ AgLi	762.42079	762.42064	-0.20	M-7 C ₂ H ₄ O
2	C ₇₈ H ₁₄₉ O ₂₉ Li	778.51668	778.51536	-1.70	??
1	C ₃₄ H ₆₈ O ₁₇ Li	755.46111	755.46110	-0.01	e
1	C ₂₁ H ₄₂ O ₄ Ag	465.21285	465.21263	-0.47	??
1		444.23878			??
average				-0.48	
SD				0.53	
Proposed formulae of peaks on CAD spectra of [TPGS+Na+Ag] ²⁺ in Figure 5.3d					
Charge state	Proposed Formula	Theoretical <i>m/z</i>	Experimental <i>m/z</i>	Error (ppm)	Proposed cleavage site
2	C ₈₇ H ₁₆₂ O ₃₂ NaAg	924.49934	924.50074	1.51	M
1	C ₈₇ H ₁₆₂ O ₃₂ Ag	1826.00947	1826.01225	1.52	M-Na
1	C ₆₈ H ₁₂₄ O ₃₂ Ag	1559.71212	1559.71538	2.09	a
1	C ₅₄ H ₁₀₈ O ₂₇ Ag	1295.61234	1295.61387	1.18	f
1	C ₅₂ H ₁₀₄ O ₂₆ Ag	1251.58613	1251.58828	1.72	f
1	C ₅₀ H ₁₀₀ O ₂₅ Ag	1207.55991	1207.56209	1.81	f
1	C ₄₈ H ₉₆ O ₂₄ Ag	1163.53370	1163.53577	1.78	f
1	C ₄₆ H ₉₂ O ₂₃ Ag	1119.50748	1119.50859	0.99	f
1	C ₄₄ H ₈₈ O ₂₂ Ag	1075.48127	1075.48235	1.01	f
1	C ₄₂ H ₈₄ O ₂₁ Ag	1031.45505	1031.45624	1.15	f
1	C ₄₀ H ₈₀ O ₂₀ Ag	987.42884	987.43040	1.58	f
1	C ₃₈ H ₇₆ O ₁₉ Ag	943.40262	943.40385	1.30	f
1	C ₃₆ H ₇₂ O ₁₈ Ag	899.37641	899.37724	0.93	f
1	C ₃₄ H ₆₈ O ₁₇ Ag	855.35019	855.35108	1.04	f
1	C ₃₂ H ₆₄ O ₁₆ Ag	811.32398	811.32465	0.83	f
2	C ₆₈ H ₁₂₄ O ₃₂ AgNa	791.35067	791.35078	0.14	a
1	C ₅₈ H ₁₁₂ O ₃₀ Ag	1395.62839	1395.63008	1.21	c

1	C ₅₇ H ₁₁₂ O ₂₉ Ag	1367.63347	1367.63691	2.52	d
2	C ₅₄ H ₁₀₈ O ₂₇ AgNa	659.30078	659.30176	1.49	f
2	C ₅₈ H ₁₁₂ O ₃₀ AgNa	709.30880	709.30945	0.92	c
2	C ₅₇ H ₁₁₂ O ₂₉ AgNa	695.31135	695.31191	0.81	d
1	C ₅₂ H ₁₀₆ O ₂₇ Ag	1185.68137	1185.68329	1.62	e
1	C ₅₀ H ₁₀₂ O ₂₆ Ag	1141.65515	1141.65605	0.79	e
1	C ₄₈ H ₉₈ O ₂₅ Ag	1097.62894	1097.63015	1.11	e
1	C ₄₆ H ₉₄ O ₂₄ Ag	1053.60272	1053.60389	1.11	e
1	C ₄₄ H ₉₀ O ₂₃ Ag	1009.57651	1009.57804	1.52	e
1	C ₄₂ H ₈₆ O ₂₂ Ag	965.55029	965.55153	1.28	e
1	C ₄₀ H ₈₂ O ₂₁ Ag	921.52408	921.52513	1.14	e
1	C ₃₈ H ₇₈ O ₂₀ Ag	877.49786	877.49881	1.08	e
1	C ₃₆ H ₇₄ O ₁₉ Ag	833.47165	833.47219	0.65	e
average				1.26	
SD				0.47	
Proposed formulae of peaks on CAD spectra of [TPGS+K+Ag] ²⁺ in Figure 5.3e					
Charge state	Proposed Formula	Theoretical <i>m/z</i>	Experimental <i>m/z</i>	Error (ppm)	Proposed cleavage site
2	C ₈₇ H ₁₆₂ O ₃₂ AgK	932.48631	932.48507	-1.33	M
1	C ₈₇ H ₁₆₂ O ₃₂ Ag	1826.00947	1826.00394	-3.03	M-K
1	C ₇₉ H ₁₄₈ O ₂₈ Ag	1651.92026	1651.91681	-2.09	??
average				-2.15	
SD				0.85	
Proposed formulae of peaks on CAD spectra of [TPGS+K+Na] ²⁺ in Figure 5.3f					
Charge state	Proposed Formula	Theoretical <i>m/z</i>	Experimental <i>m/z</i>	Error (ppm)	Proposed cleavage site
2	C ₈₇ H ₁₆₂ O ₃₂ NaK	890.52865	890.52833	-0.35	M
1	C ₈₇ H ₁₆₂ O ₃₂ Na	1742.09414	1742.09537	0.70	M-K

Table D.3 Mass list of proposed peaks on the ECD spectra of [TPGS+2Li]²⁺, [TPGS+2Na]²⁺, [TPGS+2K]²⁺ and [TPGS+2Ag]²⁺ in Figure 5.4

Proposed formulae of peaks on ECD spectra of [TPGS+2Li] ²⁺ in Figure 5.4a					
Charge state	Proposed Formula	Theoretical <i>m/z</i>	Experimental <i>m/z</i>	Error (ppm)	Proposed cleavage site
2	C ₈₇ H ₁₆₂ O ₃₂ Li ₂	866.56808	866.56772	-0.42	M
1	C ₅₅ H ₁₀₉ O ₂₈ Li ₂	1231.74222	1231.74113	-0.89	d- C ₂ H ₄ O
1	C ₅₃ H ₁₀₅ O ₂₇ Li ₂	1187.71600	1187.71491	-0.91	d-2C ₂ H ₄ O
1	C ₅₄ H ₁₀₉ O ₂₈ Li ₂	1219.74221	1219.74111	-0.90	e
1	C ₅₆ H ₁₀₇ O ₂₉ Li ₂	1257.72126	1257.72043	-0.66	c-C ₂ H ₆ O
average				-0.75	
SD				0.21	
Proposed formulae of peaks on ECD spectra of [TPGS+2Na] ²⁺ in Figure 5.4b					
Charge state	Proposed Formula	Theoretical <i>m/z</i>	Experimental <i>m/z</i>	Error (ppm)	Proposed cleavage site
2+	C ₈₇ H ₁₆₂ O ₃₂ Na ₂	882.54168	882.54158	-0.11	M
1+	C ₈₇ H ₁₆₂ O ₃₂ Na	1742.09414	1742.09456	0.24	M-Ag
1+	C ₈₇ H ₁₆₂ O ₃₂ Na ₂	1765.08391	1765.08422	0.17	M
1+	C ₅₇ H ₁₁₃ O ₂₉ Na ₂	1307.71574	1307.71559	-0.11	d
1+	C ₅₅ H ₁₀₉ O ₂₈ Na ₂	1263.68953	1263.68959	0.04	d- C ₂ H ₄ O
1+	C ₅₃ H ₁₀₅ O ₂₇ Na ₂	1219.66331	1219.66362	0.25	d-2C ₂ H ₄ O
1+	C ₅₄ H ₁₀₉ O ₂₈ Na ₂	1251.68953	1251.68985	0.25	e
average				0.10	
SD				0.16	
Proposed formulae of peaks on ECD spectra of [TPGS+2K] ²⁺ in Figure 5.4c					
Charge state	Proposed Formula	Theoretical <i>m/z</i>	Experimental <i>m/z</i>	Error (ppm)	Proposed cleavage site
2	C ₈₇ H ₁₆₂ O ₃₂ K ₂	898.51562	898.51517	-0.50	M
1	C ₈₇ H ₁₆₂ O ₃₂ K	1758.06808	1758.07027	1.25	M-K
1	C ₅₇ H ₁₁₃ O ₂₉ K ₂	1339.66362	1339.66426	0.48	d
1	C ₅₅ H ₁₀₉ O ₂₈ K ₂	1295.63740	1295.63796	0.43	d- C ₂ H ₄ O
1	C ₅₃ H ₁₀₅ O ₂₇ K ₂	1251.61119	1251.61174	0.44	d-2C ₂ H ₄ O
average				0.42	
SD				0.62	
Proposed formulae of peaks on ECD spectra of [TPGS+2Ag] ²⁺ in Figure 5.4d					
Charge state	Proposed Formula	Theoretical <i>m/z</i>	Experimental <i>m/z</i>	Error (ppm)	Proposed cleavage

					site
2	$C_{87}H_{162}O_{32}Ag_2$	966.45701	966.45671	-0.31	M
1	$C_{87}H_{162}O_{32}Ag$	1826.00947	1826.00803	-0.79	M-Ag
1	$C_{58}H_{113}O_{30}Ag_2$	1503.54131	1503.54123	-0.05	c
average				-0.38	
SD				0.38	

Table D.4 Mass list of proposed peaks on the ECD spectra of [TPGS+Li+Na]²⁺, [TPGS+K+Li]²⁺, [TPGS+Li+Ag]²⁺, [TPGS+Na+Ag]²⁺, [TPGS+K+Ag]²⁺, and [TPGS+K+Na]²⁺ in Figure 5.5

Proposed formulae of peaks on ECD spectra of [TPGS+Li+Na] ²⁺ in Figure 5.5a					
Charge state	Proposed Formula	Theoretical <i>m/z</i>	Experimental <i>m/z</i>	Error (ppm)	Proposed cleavage site
2	C ₈₇ H ₁₆₂ O ₃₂ NaLi	874.55480	874.55462	-0.20	M
1	C ₈₇ H ₁₆₂ O ₃₂ Li	1726.12038	1726.12042	0.02	M-Na
1	C ₅₇ H ₁₁₃ O ₂₉ NaLi	1291.7421	1291.74186	-0.18	d
1	C ₅₅ H ₁₀₉ O ₂₈ NaLi	1247.71588	1247.715620	-0.20	d- C ₂ H ₄ O
1	C ₅₃ H ₁₀₅ O ₂₇ NaLi	1203.68966	1203.68937	-0.24	d-2C ₂ H ₄ O
1	C ₅₄ H ₁₀₉ O ₂₈ LiNa	1235.71588	1235.7157	-0.14	e
average				-0.16	
SD				0.09	
Proposed formulae of peaks on ECD spectra of [TPGS+Li+K] ²⁺ in Figure 5.5b					
Charge state	Proposed Formula	Theoretical <i>m/z</i>	Experimental <i>m/z</i>	Error (ppm)	Proposed cleavage site
2	C ₈₇ H ₁₆₂ O ₃₂ KLi	898.51562	898.51589	0.30	M
1	C ₈₇ H ₁₆₂ O ₃₂ Li	1726.12039	1726.12273	1.36	M-K
1	C ₅₇ H ₁₁₃ O ₂₉ KLi	1307.71604	1307.71636	0.24	d
1	C ₅₅ H ₁₀₉ O ₂₈ KLi	1263.68982	1263.69009	0.21	d- C ₂ H ₄ O
1	C ₅₃ H ₁₀₅ O ₂₇ KLi	1219.66360	1219.66393	0.27	d-2C ₂ H ₄ O
1	C ₅₄ H ₁₀₉ O ₂₈ KLi	1251.68982	1251.69036	0.43	e
average				0.47	
SD				0.44	
Proposed formulae of peaks on ECD spectra of [TPGS+Li+Ag] ²⁺ in Figure 5.5c					
Charge state	Proposed Formula	Theoretical <i>m/z</i>	Experimental <i>m/z</i>	Error (ppm)	Proposed cleavage site
2	C ₈₇ H ₁₆₂ O ₃₂ LiAg	916.51246	916.51309	0.69	M
1	C ₈₇ H ₁₆₂ O ₃₂ Li	1726.12038	1726.11910	0.74	M-Ag
1	C ₅₈ H ₁₁₃ O ₃₀ LiAg	1403.65234	1403.65092	1.01	c
average				0.81	
SD				0.17	
Proposed formulae of peaks on ECD spectra of [TPGS+Na+Ag] ²⁺ in Figure 5.5d					
Charge state	Proposed Formula	Theoretical <i>m/z</i>	Experimental <i>m/z</i>	Error (ppm)	Proposed cleavage site
2	C ₈₇ H ₁₆₂ O ₃₂ NaAg	924.49934	924.49775	-1.72	M

1	C ₈₇ H ₁₆₂ O ₃₂ Na	1742.09414	1742.09136	-1.60	M-Ag
1	C ₅₈ H ₁₁₃ O ₃₀ NaAg	1419.62598	1419.62329	-1.89	c
average				-1.74	
SD				0.15	
Proposed formulae of peaks on ECD spectra of [TPGS+K+Ag] ²⁺ in Figure 5.5e					
Charge state	Proposed Formula	Theoretical <i>m/z</i>	Experimental <i>m/z</i>	Error (ppm)	Proposed cleavage site
2	C ₈₇ H ₁₆₂ O ₃₂ KAg	932.48631	932.48540	0.98	M
1	C ₈₇ H ₁₆₂ O ₃₂ K	1758.06808	1758.06506	1.72	M-Ag
1	C ₅₈ H ₁₁₃ O ₃₀ KAg	932.48631	932.48540	0.98	c
average				1.22	
SD				0.43	
Proposed formulae of peaks on ECD spectra of [TPGS+K+Na] ²⁺ in Figure 5.5f					
Charge state	Proposed Formula	Theoretical <i>m/z</i>	Experimental <i>m/z</i>	Error (ppm)	Proposed cleavage site
2	C ₈₇ H ₁₆₂ O ₃₂ NaK	890.52865	890.52798	-0.75	M
1	C ₈₇ H ₁₆₂ O ₃₂ K	1758.06808	1758.07102	1.67	M-Na
1	C ₅₇ H ₁₁₃ O ₂₉ KNa	1323.68968	1323.69030	0.47	d
1	C ₅₅ H ₁₀₉ O ₂₈ KNa	1279.66347	1279.66382	0.27	d- C ₂ H ₄ O
1	C ₅₃ H ₁₀₅ O ₂₇ KNa	1235.63725	1235.63751	0.21	d-2C ₂ H ₄ O
average				0.37	
SD				0.86	

Table D.5 Mass list of proposed peaks on the CAD spectra of $[M+2H]^{2+}$, $[M+H+Li]^{2+}$, $[M+H+Na]^{2+}$, $[M+H+K]^{2+}$, and $[M+H+Ag]^{2+}$ in Figure 5.6f

Proposed formulae of peaks on CAD spectra of $[TPGS+2H]^{2+}$ in Figure 5.6f							
Charge state	Proposed Formula	Theoretical m/z	Experimental m/z	Error (ppm)	Experimental m/z Internally calibrated	Error (ppm)	Proposed cleavage site
2	*C ₈₇ H ₁₆₂ O ₃₂ H ₂	860.55974	860.55873	-1.17	860.55969	---	M
1	*C ₈₁ H ₁₄₉ O ₂₉ H ₂	1588.03356	1588.03513	0.99	1588.0334	---	M-3 C ₂ H ₄ O
1	C ₇₉ H ₁₄₅ O ₂₈ H ₂	1544.00735	1544.00855	0.78	1544.00708	-0.17	M-4 C ₂ H ₄ O
1	C ₇₇ H ₁₄₁ O ₂₇ H ₂	1499.98113	1499.98181	0.45	1499.98059	-0.36	M-5 C ₂ H ₄ O
1	C ₇₅ H ₁₃₇ O ₂₆ H ₂	1455.95492	1455.95566	0.51	1455.95468	-0.16	M-6 C ₂ H ₄ O
1	C ₇₃ H ₁₃₃ O ₂₅ H ₂	1411.92870	1411.92895	0.18	1411.92819	-0.36	M-7 C ₂ H ₄ O
1	C ₇₁ H ₁₂₉ O ₂₄ H ₂	1367.90249	1367.90304	0.41	1367.9025	0.01	M-8 C ₂ H ₄ O
1	C ₆₉ H ₁₂₅ O ₂₃ H ₂	1323.87627	1323.87683	0.42	1323.87649	0.17	M-9 C ₂ H ₄ O
1	C ₆₇ H ₁₂₁ O ₂₂ H ₂	1279.85006	1279.85087	0.64	1279.85071	0.51	M-10 C ₂ H ₄ O
1	C ₄₉ H ₈₅ O ₁₂	865.60355	865.60259	-1.11	865.60353	-0.02	h + 8C ₂ H ₄ O
1	C ₄₇ H ₈₁ O ₁₁	821.57734	821.57650	-1.02	821.57751	0.21	h + 7C ₂ H ₄ O
1	C ₄₅ H ₇₇ O ₁₀	777.55112	777.55007	-1.35	777.55111	-0.01	h + 6C ₂ H ₄ O
1	C ₄₃ H ₇₃ O ₉	733.52491	733.52390	-1.37	733.52497	0.09	h + 5C ₂ H ₄ O
1	C ₄₁ H ₆₉ O ₈	689.49836	689.49771	-0.94	689.49879	0.62	h + 4C ₂ H ₄ O
1	C ₃₉ H ₆₅ O ₇	645.47215	645.47142	-1.12	645.4725	0.55	h + 3 C ₂ H ₄ O
1	C ₃₇ H ₆₁ O ₆	601.44593	601.44522	-1.18	601.44629	0.60	h + 2C ₂ H ₄ O
1	*C ₃₅ H ₅₇ O ₅	557.42005	557.41901	-1.87	557.42005	---	h + C ₂ H ₄ O
2	C ₅₈ H ₁₁₂ O ₃₀ H ₂	645.36920	645.36867	-0.82	645.36918	-0.03	c
1	*C ₅₄ H ₁₁₁ O ₂₈	1207.72564	1207.72570	0.05	1207.72581	---	e
1	C ₅₂ H ₁₀₆ O ₂₇ H	1163.69942	1163.69921	-0.18	1163.69947	0.04	e
1	C ₅₀ H ₁₀₂ O ₂₆ H	1119.67320	1119.67259	-0.55	1119.67299	-0.19	e
1	C ₄₈ H ₉₈ O ₂₅ H	1075.64699	1075.64655	-0.41	1075.64708	0.08	e

1	C ₄₆ H ₉₄ O ₂₄ H	1031.62077	1031.62027	-0.49	1031.62091	0.13	e
1	C ₄₄ H ₉₀ O ₂₃ H	987.59456	987.59385	-0.72	987.5946	0.04	e
1	C ₄₂ H ₈₆ O ₂₂ H	943.56834	943.56762	-0.77	943.56845	0.11	e
1	C ₄₀ H ₈₂ O ₂₁ H	899.54213	899.54151	-0.69	899.54242	0.32	e
1	C ₃₈ H ₇₈ O ₂₀ H	855.51591	855.51504	-1.02	855.51601	0.11	e
1	C ₃₆ H ₇₄ O ₁₉ H	811.48970	811.48879	-1.12	811.48981	0.14	e
1	C ₃₄ H ₇₀ O ₁₈ H	767.46348	767.46257	-1.19	767.46362	0.18	e
1	C ₃₂ H ₆₆ O ₁₇ H	723.43727	723.43627	-1.38	723.43735	0.11	e
1	C ₄₆ H ₉₃ O ₂₃	1013.61022	1013.60936	-0.85	1013.61004	-0.18	f
1	C ₄₄ H ₈₈ O ₂₂ H	969.58401	969.58339	-0.63	969.58417	0.17	f
1	C ₄₂ H ₈₄ O ₂₁ H	925.55779	925.55707	-0.78	925.55793	0.15	f
1	C ₄₀ H ₈₀ O ₂₀ H	881.53158	881.53100	-0.65	881.53193	0.40	f
1	C ₃₈ H ₇₆ O ₁₉ H	837.50536	837.50436	-1.19	837.50535	-0.01	f
1	C ₃₆ H ₇₂ O ₁₈ H	793.47915	793.47821	-1.18	793.47924	0.12	f
1	C ₃₂ H ₆₄ O ₁₆ H	749.45293	749.45198	-1.27	749.45304	0.15	f
1	C ₃₀ H ₆₀ O ₁₅ H	705.42672	705.42576	-1.35	705.42684	0.18	f
1	C ₂₈ H ₅₆ O ₁₄ H	661.40050	661.39945	-1.59	661.40053	0.05	f
average				-0.6		0.11	
SD				0.83		0.27	
Proposed formulae of peaks on CAD spectra of [TPGS+Li+H] ²⁺ in Figure 5.6lb							
Charge state	Proposed Formula	Theoretical <i>m/z</i>	Experimental <i>m/z</i>	Error (ppm)	Experimental <i>m/z</i> Internally calibrated	Error (ppm)	Proposed cleavage site
2	*C ₈₇ H ₁₆₂ O ₃₂ HLi	863.56383	863.56306	-0.89	863.56384	---	M
1	*C ₈₁ H ₁₄₉ O ₂₉ HLi	1594.04173	1594.04469	1.86	1594.04175	---	M-3 C ₂ H ₄ O
1	C ₇₉ H ₁₄₅ O ₂₈ HLi	1550.01552	1550.01784	1.50	1550.01566	0.09	M-4 C ₂ H ₄ O
1	C ₇₇ H ₁₄₁ O ₂₇ HLi	1505.98930	1505.99185	1.69	1505.98979	0.33	M-5 C ₂ H ₄ O
1	C ₇₅ H ₁₃₇ O ₂₆ HLi	1461.96309	1461.96527	1.49	1461.96319	0.07	M-6 C ₂ H ₄ O
1	C ₇₃ H ₁₃₃ O ₂₅ HLi	1417.93687	1417.93839	1.07	1417.93701	0.10	M-7 C ₂ H ₄ O
1	C ₇₁ H ₁₂₉ O ₂₄ HLi	1373.91066	1373.91194	0.94	1373.91064	-0.01	M-8 C ₂ H ₄ O
1	C ₆₉ H ₁₂₅ O ₂₃ HLi	1329.88444	1329.88532	0.66	1329.88447	0.02	M-9 C ₂ H ₄ O

1	C ₆₇ H ₁₂₁ O ₂₂ HLi	1285.85823	1285.8588 9	0.52	1285.85835	0.10	M-10 C ₂ H ₄ O
1	C ₆₅ H ₁₁₇ O ₂₁ HLi	1241.83201	1241.8323 5	0.27	1241.83198	- 0.02	M-11 C ₂ H ₄ O
1	C ₆₃ H ₁₁₃ O ₂₀ HLi	1197.80580	1197.8061 4	0.29	1197.80585	0.05	M-12 C ₂ H ₄ O
1	*C ₅₂ H ₁₀₅ O ₂₇ LiH	1169.70771	1169.7078 6	0.13	1169.70769	---	e
1	C ₅₀ H ₁₀₁ O ₂₆ LiH	1125.68150	1125.6817 1	0.19	1125.68157	0.07	e
1	C ₄₈ H ₉₇ O ₂₅ LiH	1081.65528	1081.6551 1	-0.16	1081.65532	0.04	e
1	C ₄₆ H ₉₃ O ₂₄ LiH	1037.62907	1037.6286 9	-0.36	1037.62901	- 0.05	e
1	C ₄₄ H ₈₉ O ₂₃ LiH	993.60285	993.60232	-0.53	993.60278	- 0.07	e
1	C ₄₂ H ₈₅ O ₂₂ LiH	949.57664	949.57598	-0.69	949.57659	- 0.05	e
1	C ₄₀ H ₈₁ O ₂₁ LiH	905.55042	905.54967	-0.83	905.55036	- 0.07	e
1	C ₃₈ H ₇₇ O ₂₀ LiH	861.52421	861.52337	-0.97	861.52423	0.03	e
1	C ₃₆ H ₇₃ O ₁₉ LiH	817.49799	817.49701	-1.20	817.4979	- 0.11	e
1	C ₃₄ H ₆₉ O ₁₈ LiH	773.47178	773.47079	-1.27	773.47173	- 0.06	e
1	C ₃₀ H ₆₁ O ₁₆ LiH	729.44556	729.44451	-1.44	729.44549	- 0.10	e
2	C ₅₈ H ₁₁₃ O ₃₀ Li	648.37335	648.37262	-1.13	648.37328	- 0.11	c
1	C ₄₁ H ₆₉ O ₈	689.49836	689.49770	-0.96	689.49876	0.58	h +4 C ₂ H ₄ O
1	C ₃₇ H ₆₁ O ₆	601.44627	601.44516	-1.84	601.44633	0.11	h + 2C ₂ H ₄ O
1	*C ₃₅ H ₅₇ O ₅	557.42005	557.41892	-2.03	557.42005	---	h + C ₂ H ₄ O
average				-0.14		0.04	
SD				1.12		0.15	
Proposed formulae of peaks on CAD spectra of [TPGS+H+Na] ²⁺ in Figure 5.6lc							
Charge state	Proposed Formula	Theoretical m/z	Experimental m/z	Error (ppm)	Experimental m/z Internally calibrated	Error (ppm)	Proposed cleavage site
2	*C ₈₇ H ₁₆₂ O ₃₂ NaH	871.55071	871.55042	-0.33	871.55074	---	M
1	*C ₈₁ H ₁₄₉ O ₂₉ HNa	1610.01550	1610.01927	2.34	1610.01559	---	M-3 C ₂ H ₄ O
1	C ₇₉ H ₁₄₅ O ₂₈ HNa	1565.98929	1565.99264	2.14	1565.98929	0.00	M-4 C ₂ H ₄ O
1	C ₇₇ H ₁₄₁ O ₂₇ HNa	1521.96307	1521.96609	1.98	1521.96308	0.01	M-5 C ₂ H ₄ O
1	C ₇₅ H ₁₃₇ O ₂₆ HNa	1477.93686	1477.93968	1.91	1477.93698	0.08	M-6 C ₂ H ₄ O
1	C ₇₃ H ₁₃₃ O ₂₅ HNa	1433.91064	1433.91307	1.69	1433.91068	0.03	M-7 C ₂ H ₄ O
1	C ₇₁ H ₁₂₉ O ₂₄ HNa	1389.88443	1389.88653	1.51	1389.88444	0.01	M-8 C ₂ H ₄ O
1	C ₆₉ H ₁₂₅ O ₂₃ HNa	1345.85821	1345.86002	1.34	1345.8582	- 0.01	M-9 C ₂ H ₄ O

1	C ₆₇ H ₁₂₁ O ₂₂ HNa	1301.83200	1301.83354	1.19	1301.83199	0.00	M-10 C ₂ H ₄ O
1	C ₆₅ H ₁₁₇ O ₂₁ HNa	1257.80578	1257.80705	1.01	1257.80575	- 0.02	M-11 C ₂ H ₄ O
1	C ₆₃ H ₁₁₃ O ₂₀ HNa	1213.77957	1213.78066	0.90	1213.77959	0.02	M-12 C ₂ H ₄ O
1	C ₆₁ H ₁₀₉ O ₁₉ HNa	1169.75335	1169.75413	0.67	1169.75329	- 0.05	M-13 C ₂ H ₄ O
1	C ₅₉ H ₁₀₅ O ₁₈ HNa	1125.72714	1125.72773	0.53	1125.72709	- 0.04	M-14 C ₂ H ₄ O
1	*C ₅₂ H ₁₀₅ O ₂₇ NaH	1185.68137	1185.68219	0.69	1185.68127	---	e
1	C ₅₀ H ₁₀₁ O ₂₆ NaH	1141.65516	1141.65576	0.53	1141.65505	- 0.09	e
1	C ₄₈ H ₉₇ O ₂₅ NaH	1097.62894	1097.62934	0.36	1097.62883	- 0.10	e
1	C ₄₆ H ₉₃ O ₂₄ NaH	1053.60273	1053.60294	0.20	1053.60263	- 0.09	e
1	C ₄₄ H ₈₉ O ₂₃ NaH	1009.57651	1009.57659	0.08	1009.57651	0.00	e
1	C ₄₂ H ₈₅ O ₂₂ NaH	965.55030	965.55019	-0.11	965.55022	- 0.08	e
1	C ₄₀ H ₈₁ O ₂₁ NaH	921.52408	921.52386	-0.24	921.52403	- 0.05	e
1	C ₃₈ H ₇₇ O ₂₀ NaH	877.49787	877.49749	-0.43	877.4978	- 0.07	e
1	C ₃₆ H ₇₃ O ₁₉ NaH	833.47165	833.47118	-0.56	833.4716	- 0.06	e
1	C ₃₄ H ₆₉ O ₁₈ NaH	789.44544	789.44485	-0.74	789.44538	- 0.07	e
1	C ₃₀ H ₆₁ O ₁₆ NaH	745.41922	745.41853	-0.93	745.41916	- 0.08	e
1	C ₂₈ H ₅₇ O ₁₅ NaH	701.39301	701.39227	-1.05	701.39298	- 0.04	e
2	C ₅₈ H ₁₁₃ O ₃₀ Na	656.36017	656.35961	0.85	656.36014	- 0.05	c
1	C ₄₁ H ₆₉ O ₈	689.49836	689.49795	-0.59	689.49868	0.46	h + 4 C ₂ H ₄ O
1	C ₃₇ H ₆₁ O ₆	601.44627	601.44544	-1.37	601.44628	0.02	h + 2C ₂ H ₄ O
1	*C ₃₅ H ₅₇ O ₅	557.42005	557.41917	-1.58	557.42005	---	h + C ₂ H ₄ O
1	C ₈₅ H ₁₅₃ O ₃₀ Na	838.51667	838.51499	-2.00	838.5154	- 1.51	??
1	C ₅₈ H ₁₁₃ O ₃₀ Na	656.36017	656.35961	0.85	656.36014	- 0.05	??
1			855.51548		855.51585	0.03	???
average				0.35		- 0.06	
SD				1.14		0.30	
Proposed formulae of peaks on CAD spectra of [TPGS+H+K] ²⁺ in Figure 5.6ld							
Charge state	Proposed Formula	Theoretical m/z	Experimental m/z	Error (ppm)	Experimental m/z Internally calibrated	Error (ppm)	Proposed cleavage site
2	*C ₈₇ H ₁₆₂ O ₃₂ HK	879.53768	879.53895	1.44	879.53770	---	M
1	*C ₅₄ H ₁₀₉ O ₂₈ KH	1245.68152	1245.68576	3.40	1245.68145	---	e
1	C ₅₂ H ₁₀₅ O ₂₇ KH	1201.65531	1201.65921	3.25	1201.655343	0.03	e

1	C ₅₀ H ₁₀₁ O ₂₆ KH	1113.60288	1113.60585	2.67	1113.60279	-0.08	e
1	C ₄₈ H ₉₇ O ₂₅ KH	1069.57666	1069.57935	2.51	1069.57669	0.03	e
1	C ₄₆ H ₉₃ O ₂₄ KH	1025.55045	1025.55278	2.27	1025.55042	-0.03	e
1	C ₄₄ H ₈₉ O ₂₃ KH	981.52423	981.52618	1.98	981.52423	0.00	e
1	C ₄₂ H ₈₅ O ₂₂ KH	937.49802	937.49962	1.71	937.49794	-0.08	e
1	C ₄₀ H ₈₁ O ₂₁ KH	893.47180	893.47325	1.62	893.4718	0.00	e
1	C ₃₈ H ₇₇ O ₂₀ KH	849.44559	849.44671	1.32	849.44548	-0.13	e
1	C ₃₆ H ₇₃ O ₁₉ KH	805.41937	805.42015	0.97	805.41932	-0.06	e
2	C ₅₈ H ₁₁₃ O ₃₀ K	664.34714	664.34726	0.18	664.34719	0.08	c
1	C ₄₁ H ₆₉ O ₈	689.49836	689.49895	0.86	689.49877	0.59	h + 4 C ₂ H ₄ O
1	*C ₃₇ H ₆₁ O ₆	601.44627	601.44607	-0.32	601.44627	---	h + 2C ₂ H ₄ O
1	C ₃₅ H ₅₇ O ₅	557.42005	557.41977	-0.50	557.42013	0.14	h + C ₂ H ₄ O
1	C ₈₁ H ₁₄₉ O ₂₉ HK	1625.98944	1625.98844	-0.62	1625.98957	0.08	M-3 C ₂ H ₄ O
1	*C ₇₉ H ₁₄₅ O ₂₈ HK	1581.96323	1581.97155	5.26	1581.96329	---	M-4 C ₂ H ₄ O
1	C ₇₇ H ₁₄₁ O ₂₇ HK	1537.93701	1537.9447	5.00	1537.93701	0.00	M-5 C ₂ H ₄ O
1	C ₇₅ H ₁₃₇ O ₂₆ HK	1493.91080	1493.91788	4.74	1493.91076	-0.02	M-6 C ₂ H ₄ O
1	C ₇₃ H ₁₃₃ O ₂₅ HK	1449.88458	1449.89131	4.64	1449.88473	0.10	M-7 C ₂ H ₄ O
1	C ₇₁ H ₁₂₉ O ₂₄ HK	1405.85837	1405.86455	4.40	1405.85849	0.09	M-8 C ₂ H ₄ O
1	C ₆₉ H ₁₂₅ O ₂₃ HK	1361.83215	1361.83762	4.02	1361.83207	-0.06	M-9 C ₂ H ₄ O
1	C ₆₇ H ₁₂₁ O ₂₂ HK	1317.80594	1317.81133	4.09	1317.80626	0.25	M-10 C ₂ H ₄ O
1	C ₆₅ H ₁₁₇ O ₂₁ HK	1273.77972	1273.78451	3.76	1273.77949	-0.18	M-11 C ₂ H ₄ O
average				2.44		0.04	
SD				1.82		0.16	
Proposed formulae of peaks on CAD spectra of [TPGS+H+Ag] ²⁺ in Figure 5.6le							
Charge state	Proposed Formula	Theoretical m/z	Experimental m/z	Error (ppm)	Experimental m/z Internally calibrated	Error (ppm)	Proposed cleavage site
2	*C ₈₇ H ₁₆₂ O ₃₂ HAg	913.50837	913.50793	-0.48	913.50837	---	M
1	*C ₅₄ H ₁₀₉ O ₂₈ AgH	1313.62291	1313.62381	0.69	1313.62293	---	e
1	C ₅₂ H ₁₀₅ O ₂₇ AgH	1269.59669	1269.59705	0.28	1269.59677	0.06	e
1	C ₅₀ H ₁₀₁ O ₂₆ AgH	1225.57048	1225.57137	0.73	1225.57079	0.25	e
1	C ₄₈ H ₉₇ O ₂₅ AgH	1181.54426	1181.54421	-0.04	1181.54431	0.04	e
1	C ₄₆ H ₉₃ O ₂₄ AgH	1137.51805	1137.5179	-0.13	1137.51791	-0.12	e

1	C ₄₄ H ₈₉ O ₂₃ AgH	1093.49183	1093.49153	-0.28	1093.49176	-0.07	e
1	C ₄₂ H ₈₅ O ₂₂ AgH	1049.46562	1049.4653	-0.30	1049.46558	-0.04	e
1	C ₄₀ H ₈₁ O ₂₁ AgH	1005.43940	1005.43902	-0.38	1005.4394	0.00	e
1	C ₃₈ H ₇₇ O ₂₀ AgH	961.41319	961.41259	-0.62	961.41319	0.00	e
2	C ₅₈ H ₁₁₃ O ₃₀ Ag	698.31783	698.31698	-1.22	698.31779	-0.06	c
1	C ₄₁ H ₆₉ O ₈	689.49836	689.49773	-0.91	689.4987	0.49	h + 4 C ₂ H ₄ O
1	*C ₃₇ H ₆₁ O ₆	601.44627	601.44523	-1.72	557.42005	---	h + 2C ₂ H ₄ O
1	C ₃₅ H ₅₇ O ₅	557.42005	557.41911	-1.69	601.44625	-0.02	h + C ₂ H ₄ O
1	*C ₈₁ H ₁₄₉ O ₂₉ HAg	1693.93082	1693.9328	1.17	1693.9308	---	M-3 C ₂ H ₄ O
1	C ₇₉ H ₁₄₅ O ₂₈ HAg	1649.90461	1649.90764	1.84	1649.90493	0.20	M-4 C ₂ H ₄ O
1	C ₇₇ H ₁₄₁ O ₂₇ HAg	1605.87839	1605.88024	1.15	1605.87886	0.29	M-5 C ₂ H ₄ O
1	C ₇₅ H ₁₃₇ O ₂₆ HAg	1561.85218	1561.8542	1.30	1561.85226	0.05	M-6 C ₂ H ₄ O
1	C ₇₃ H ₁₃₃ O ₂₅ HAg	1517.82596	1517.82769	1.14	1517.82613	0.11	M-7 C ₂ H ₄ O
1	C ₇₁ H ₁₂₉ O ₂₄ HAg	1473.79975	1473.80143	1.14	1473.79986	0.08	M-8 C ₂ H ₄ O
1	C ₆₉ H ₁₂₅ O ₂₃ HAg	1429.77353	1429.77489	0.95	1429.77385	0.22	M-9 C ₂ H ₄ O
1	C ₆₇ H ₁₂₁ O ₂₂ HAg	1385.74732	1385.74828	0.70	1385.74741	0.07	M-10 C ₂ H ₄ O
1	C ₆₅ H ₁₁₇ O ₂₁ HAg	1341.72110	1341.72192	0.61	1341.72111	0.01	M-11 C ₂ H ₄ O
1	C ₆₃ H ₁₁₃ O ₂₀ HAg	1297.69489	1297.69536	0.37	1297.69516	0.21	M-12 C ₂ H ₄ O
1	C ₆₁ H ₁₀₉ O ₁₉ HAg	1253.66867	1253.66886	0.15	1253.66878	0.09	M-13 C ₂ H ₄ O
average				0.18		0.09	
SD				0.95		0.14	

* Peaks used as calibrants

Table D.6 Mass list of proposed peaks on the ECD spectra of $[M+2H]^{2+}$, $[M+H+Li]^{2+}$, $[M+H+Na]^{2+}$, $[M+H+K]^{2+}$, and $[M+H+Ag]^{2+}$ in Figure 5.6II

Proposed formulae of peaks on ECD spectra of $[TPGS+2H]^{2+}$ in Figure 5.6IIa							
Charge state	Proposed Formula	Theoretical m/z	Experimental m/z	Error (ppm)	Experimental m/z Internally calibrated	Error (ppm)	Proposed cleavage site
2	* $C_{87}H_{162}O_{32}H_2$	860.55974	860.55851	-1.43	860.55967	---	M
1	* $C_{87}H_{162}O_{32}H$	1720.11220	1720.11354	0.78	1720.11211	---	M-H
1	$C_{52}H_{107}O_{27}$	1163.69942	1163.69863	-0.68	1163.69938	-0.03	e
1	$C_{50}H_{103}O_{26}$	1119.67321	1119.67267	-0.48	1119.67351	0.27	e
1	$C_{48}H_{99}O_{25}$	1075.64699	1075.64633	-0.61	1075.64708	0.08	e
1	* $C_{46}H_{95}O_{24}$	1031.62078	1031.61985	-0.90	1031.62091	---	e
1	$C_{44}H_{91}O_{23}$	987.59456	987.59354	-1.03	987.59466	0.10	e
1	$C_{42}H_{87}O_{22}$	943.56835	943.56718	-1.23	943.56839	0.05	e
1	$C_{40}H_{83}O_{21}$	899.54213	899.54111	-1.13	899.54234	0.23	e
1	$C_{38}H_{79}O_{20}$	855.51592	855.51486	-1.23	855.51581	-0.12	e
1	$C_{36}H_{75}O_{19}$	811.48970	811.48858	-1.38	811.48991	0.26	e
1	$C_{34}H_{71}O_{18}$	767.46349	767.46228	-1.57	767.46363	0.19	e
1	$C_{32}H_{64}O_{16}H$	705.42672	705.42557	-1.62	705.42641	-0.43	f
1	$C_{30}H_{60}O_{15}H$	661.40050	661.39921	-1.95	661.40062	0.18	f
1	$C_{28}H_{56}O_{14}H$	617.37429	617.37312	-1.89	617.37428	-0.01	f
1	$C_{26}H_{52}O_{13}H$	573.34807	573.34704	-1.80	573.34786	-0.37	f
1	$C_{24}H_{48}O_{12}H$	529.32186	529.32058	-2.41	529.32213	0.52	f
1	$C_{22}H_{44}O_{11}H$	485.29564	485.29474	-2.92	485.29516	-0.99	f
1	$C_{20}H_{40}O_{10}H$	441.26943	441.26874	-2.82	441.26969	0.60	f
1	* $C_{29}H_{50}O_2$	430.38053	430.37960	-2.16	430.38053	---	g
1	$C_{58}H_{113}O_{29}$	1273.73620	1273.73581	-0.31	1273.73638	0.14	c?
average				-1.37		0.04	
SD				0.87		0.37	
Proposed formulae of peaks on ECD spectra of $[TPGS+Li+H]^{2+}$ in Figure 5.6IIb							
Charge state	Proposed Formula	Theoretical m/z	Experimental m/z	Error (ppm)	Experimental m/z Internally calibrated	Error (ppm)	Proposed cleavage site
2	* $C_{87}H_{162}O_{32}HLi$	863.56383	863.56287	-1.11	863.56385	---	M
1	* $C_{87}H_{162}O_{32}Li$	1726.12038	1726.12375	1.95	1726.1204	---	M-H

1	*C ₅₂ H ₁₀₄ O ₂₆ Li	1151.6971 5	1151.69689	-0.23	1151.69712	---	f
1	C ₅₀ H ₁₀₀ O ₂₅ Li	1107.6709 4	1107.67076	-0.16	1107.67114	0.1 9	f
1	C ₄₈ H ₉₆ O ₂₄ Li	1063.6447 2	1063.64430	-0.39	1063.64483	0.1 0	f
1	C ₄₆ H ₉₂ O ₂₃ Li	1019.6185 1	1019.61805	-0.45	1019.61871	0.2 0	f
1	C ₄₄ H ₈₈ O ₂₂ Li	975.59229	975.59196	-0.34	975.59273	0.4 5	f
1	C ₄₂ H ₈₄ O ₂₁ Li	931.56608	931.56515	-0.99	931.56602	- 0.0 6	f
1	C ₄₀ H ₈₀ O ₂₀ Li	887.53986	887.53886	-1.13	887.5398	- 0.0 7	f
1	C ₃₈ H ₇₆ O ₁₉ Li	843.51365	843.51260	-1.24	843.5136	- 0.0 5	f
1	C ₃₆ H ₇₂ O ₁₈ Li	799.48743	799.48647	-1.20	799.48752	0.1 1	f
1	*C ₃₂ H ₆₄ O ₁₆ Li	755.46122	755.46013	-1.44	755.46121	---	f
1	C ₅₈ H ₁₁₄ O ₃₀ Li	1297.7550 7	1297.75593	0.66	1297.75551	0.3 4	c
1	C ₅₄ H ₁₁₀ O ₂₈ Li	1213.7339 3	1213.73418	0.21	1213.73415	0.1 8	e
1	C ₈₆ H ₁₆₁ LiO ₃₀	1681.1229 0	1681.12617	1.95	1681.1232	0.1 8	??
average				-0.26		0.1 4	
SD				0.07		0.1 6	
Proposed formulae of peaks on ECD spectra of [TPGS+H+Na] ²⁺ in Figure 5.6IId							
Charge state	Proposed Formula	Theoretical <i>m/z</i>	Experimental <i>m/z</i>	Error (ppm)	Experimental <i>m/z</i> Internally calibrated	Error (ppm)	Proposed cleavage site
2	*C ₈₇ H ₁₆₂ O ₃₂ Na H	871.55071	871.54986	-0.98	871.5507	---	M
1	*C ₈₇ H ₁₆₂ O ₃₂ Na	1742.09414	1742.0974 8	1.91	1742.09414	---	M-H
1	*C ₅₂ H ₁₀₄ O ₂₆ Na	1167.67080	1167.6709 9	0.16	1167.67079	---	f
1	C ₅₀ H ₁₀₀ O ₂₅ Na	1123.64459	1123.6442 6	-0.29	1123.6445	-0.08	f
1	C ₄₈ H ₉₆ O ₂₄ Na	1079.61837	1079.6183 1	-0.06	1079.6185	0.12	f
1	C ₄₆ H ₉₂ O ₂₃ Na	1035.59216	1035.5918 3	-0.31	1035.5923	0.14	f
1	C ₄₄ H ₈₈ O ₂₂ Na	991.56594	991.56553	-0.41	991.56611	0.17	f
1	C ₄₂ H ₈₄ O ₂₁ Na	947.53973	947.53930	-0.45	947.5399	0.18	f
1	*C ₄₀ H ₈₀ O ₂₀ Na	903.51351	903.51299	-0.58	903.51352	---	f
average				-0.11		0.11	
SD				0.82		0.11	
Proposed formulae of peaks on ECD spectra of [TPGS+H+K] ²⁺ in Figure 5.6IIId							
Charge state	Proposed Formula	Theoretical <i>m/z</i>	Experimental <i>m/z</i>	Error (ppm)			Proposed

							cleavage site
2	C ₈₇ H ₁₆₂ O ₃₂ HK	879.53768	879.53729	-0.44			M
1	C ₈₇ H ₁₆₂ O ₃₂ K	1758.06808	1758.06931	0.70			M-H
1	C ₄₈ H ₉₆ O ₂₄ Na	1095.59231	1095.59148	-0.76			f
1	C ₄₆ H ₉₂ O ₂₃ Na	1051.5661	1051.56648	0.37			f
1	C ₄₄ H ₈₈ O ₂₂ Na	1007.53988	1007.54187	1.98			f
1	C ₄₂ H ₈₄ O ₂₁ Na	963.513665	963.51399	0.34			f
average				0.37			
SD				0.96			
Proposed formulae of peaks on ECD spectra of [TPGS+Ag+H] ²⁺ in Figure 5.6Ile							
Charge state	Proposed Formula	Theoretical <i>m/z</i>	Experimental <i>m/z</i>	Error (ppm)			Proposed cleavage site
2	C ₈₇ H ₁₆₂ O ₃₂ HA _g	913.50837	913.50866	0.32			M
1	C ₈₇ H ₁₆₂ O ₃₂ H	1720.11220	1720.11513	1.70			M-Ag
1	C ₈₇ H ₁₆₂ O ₃₂ Ag	1826.00947	1826.01296	1.91			M-Li
average				1.31			
SD				0.86			

* Peaks used as calibrants

Appendix E. (Supporting information for Chapter 6)

Figure E.1 CAD spectra of chlorophyll-*a* under different collision energies

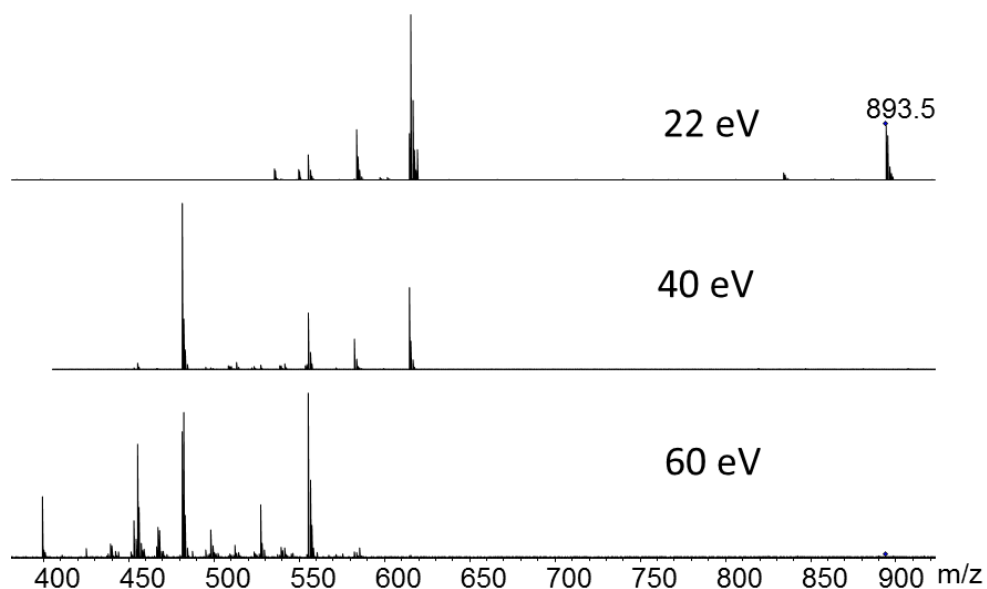


Figure E.2 The expansion of peaks at m/z 455.2081, m/z 541.2085 and m/z 833.5215

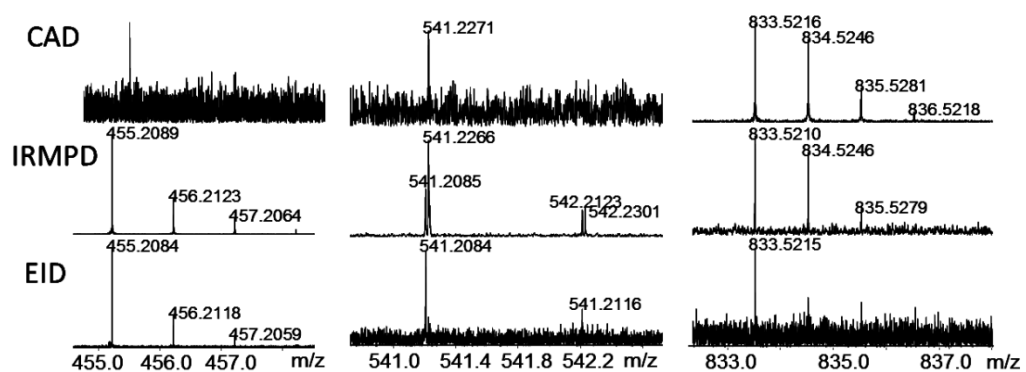


Table E.1 Peak list of Figure 6.2

Proposed formula	Theoretical mass	Charge state	EID		CAD		IRMPD	
			<i>m/z</i>	relative intensity %	<i>m/z</i>	relative intensity %	<i>m/z</i>	relative intensity %
C ₅₅ H ₇₃ O ₅ N ₄ Mg*	893.5426	1	893.5426	100	893.5426	18.29	893.5426	27.00
C ₅₃ H ₆₉ O ₃ N ₄ Mg	833.5215	1	833.5215	0.20	833.5216	2.47	833.5208	1.50
unidentified		1	739.5932	0.25	739.5932	0.06	739.5933	0.79
unidentified		2					728.6087	0.88
unidentified		2					714.5935	1.40
unidentified		1			666.5567	0.80		
unknown		-----			619.2037	15.56	619.2037	22.98
C ₃₅ H ₃₅ O ₅ N ₄ Mg	615.2452	1	615.2453	4.73	615.2454	100	615.2456	68.13
C ₃₅ H ₃₄ O ₅ N ₄ Mg*	614.2374	1	614.2374	9.35	614.2374	24.48	614.2374	28.38
C ₃₄ H ₃₃ O ₄ N ₄ Mg	601.2296	1			601.2294	1.79		
C ₃₄ H ₃₁ O ₄ N ₄ Mg*	583.2190	1	583.2190	6.70	583.2193	25.04	583.2191	80.30
C ₃₄ H ₃₀ O ₄ N ₄ Mg	582.2112	1	582.2112	2.15	582.2114	0.65	582.2113	2.26
C ₃₃ H ₃₁ O ₃ N ₄ Mg	555.2241	1	555.2240	10.12	555.2242	14.40	555.2243	100.00
unidentified		2			549.4544	6.99	549.4544	39.20
C ₃₂ H ₂₉ O ₃ N ₄ Mg	541.2085	1	541.2084	0.23			541.2085	1.93
C ₃₃ H ₃₁ O ₂ N ₄ Mg	539.2292	1	539.2292	0.48	539.2290	2.12	539.2294	19.50
C ₃₃ H ₃₀ O ₂ N ₄ Mg	538.2214	1	538.2213	0.97			538.2216	0.45
unidentified		2			535.4388	7.33	535.4387	23.13

C ₃₂ H ₃₁ O ₂ N ₄ Mg	527.2292	1	527.2292	0.92			527.2294	15.78
C ₃₁ H ₂₈ O ₂ N ₄ Mg	512.2057	1	512.2057	0.19			512.2058	6.66
C ₃₂ H ₃₀ ON ₄ Mg	510.2265	1	510.2266	0.08			510.2268	2.30
C ₃₂ H ₂₉ ON ₄ Mg	509.2186	1	509.2184	0.18			509.2189	3.23
C ₃₁ H ₂₅ O ₂ N ₄ Mg	509.1822	1	509.1823	0.36				
C ₃₂ H ₂₈ ON ₄ Mg	508.2108	1	508.2108	0.83			508.2110	0.33
C ₃₁ H ₃₀ ON ₄ Mg	498.2265	1	498.2264	0.59			498.2267	10.83
C ₃₀ H ₂₆ O ₂ N ₄ Mg	498.1901	1	498.1903	0.21			498.1903	6.77
C ₃₁ H ₂₇ ON ₄ Mg	495.2030	1	495.2030	0.23			495.2035	1.87
C ₃₀ H ₂₆ ON ₄ Mg	482.1952	1	482.1953	0.74			482.1952	6.72
C ₃₁ H ₂₉ N ₄ Mg	481.2237	1					481.2237	1.85
C ₃₀ H ₂₅ ON ₄ Mg*	481.1873	1	481.1873	4.37	481.1872	0.81	481.1878	1.92
C ₂₉ H ₂₆ ON ₄ Mg	470.1952	1					470.1952	1.81
C ₃₀ H ₂₈ N ₄ Mg	468.2159	1					468.216	1.00
C ₃₀ H ₂₇ N ₄ Mg	467.2081	1	467.2081	0.16			467.2081	1.41
C ₂₉ H ₂₃ ON ₄ Mg	467.1717	1	467.1717	0.94			467.1718	0.53
C ₃₀ H ₂₆ N ₄ Mg	466.2002	1	466.2005	0.06			466.2004	0.45
C ₂₉ H ₂₂ ON ₄ Mg	466.1639	1	466.1638	0.28			466.1638	0.27
C ₃₀ H ₂₅ N ₄ Mg	465.1924	1					465.1924	0.29
C ₂₉ H ₂₁ ON ₄ Mg	465.1560	1	465.1560	0.17			465.1561	0.21
C ₂₉ H ₂₇ N ₄ Mg□	455.2081	1	455.2081	1.82			455.2087	15.36

C ₂₉ H ₂₆ N ₄ Mg	454.2002	1	454.2003	0.20	454.2003	3.96
C ₂₉ H ₂₅ N ₄ Mg	453.1924	1	453.1924	0.42	453.1924	4.30
C ₂₈ H ₂₁ ON ₄ Mg	453.156	1	453.156	0.71	453.1561	2.83
C ₂₉ H ₂₄ N ₄ Mg	452.1846	1	452.1847	0.10	452.1845	4.64
C ₂₈ H ₂₀ ON ₄ Mg	452.1482	1	452.1483	0.33		
C ₂₉ H ₂₃ N ₄ Mg	451.1768	1	451.1766	0.10		
C ₂₈ H ₁₉ ON ₄ Mg	451.1404	1	451.1404	0.33		
C ₂₈ H ₂₅ N ₄ Mg	441.1924	1	441.1925	0.16		
C ₂₈ H ₂₄ N ₄ Mg	440.1846	1	440.1847	0.16	440.1846	1.16
C ₂₈ H ₂₃ N ₄ Mg	439.1768	1	439.1767	0.44	439.1768	0.61
C ₂₇ H ₁₉ ON ₄ Mg	439.1404	1	439.1404	0.11		
C ₂₈ H ₂₂ N ₄ Mg	438.1689	1	438.1689	0.29	438.1689	0.71
C ₂₇ H ₁₈ ON ₄ Mg	438.1326	1	438.1327	0.09		
C ₂₈ H ₂₁ N ₄ Mg	437.1611	1	437.1611	0.27	437.161	0.35
C ₂₇ H ₁₇ ON ₄ Mg	437.1247	1	437.1247	0.20		
C ₂₈ H ₂₀ N ₄ Mg	436.1533	1	436.1532	0.12		
C ₂₇ H ₁₆ ON ₄ Mg	436.1169	1	436.1169	0.09		
C ₂₈ H ₁₉ N ₄ Mg	435.1455	1	435.1455	0.12		
C ₂₇ H ₂₂ N ₄ Mg	426.1689	1	426.169	0.13	426.1688	3.98
C ₂₇ H ₂₁ N ₄ Mg	425.1611	1	425.1611	0.38	425.1610	6.07
C ₂₇ H ₂₀ N ₄ Mg	424.1533	1	424.1533	0.26	424.1532	1.36

C ₂₇ H ₁₉ N ₄ Mg	423.1455	1	423.1455	0.39			423.1453	0.52
C ₂₇ H ₁₈ N ₄ Mg	422.1376	1	422.1375	0.23				
C ₂₇ H ₁₇ N ₄ Mg	421.1298	1	421.1298	0.19				
C ₂₇ H ₁₆ N ₄ Mg	420.1220	1	420.1222	0.09				
C ₂₆ H ₁₉ N ₄ Mg	411.1455	1	411.1455	0.14			411.1453	2.92
C ₂₆ H ₁₈ N ₄ Mg	410.1376	1	410.1377	0.19			410.1375	0.34
C ₂₆ H ₁₇ N ₄ Mg	409.1298	1	409.1299	0.27			409.1297	0.24
C ₂₆ H ₁₆ N ₄ Mg	408.1220	1	408.1220	0.18				
C ₂₆ H ₁₅ N ₄ Mg	407.1142	1	407.1141	0.17				
C ₂₆ H ₁₄ N ₄ Mg	406.1063	1	406.1064	0.16				
unidentified		1	399.2957	0.12	399.2954	0.76	399.2954	1.76
unidentified		2			385.2784	0.89	385.2785	1.66
C ₂₇ H ₁₈ ON ₄ Mg	438.1326	1	438.1327	0.09				
C ₂₈ H ₂₁ N ₄ Mg	437.1611	1	437.1611	0.27			437.161	0.35
C ₂₇ H ₁₇ ON ₄ Mg	437.1247	1	437.1247	0.20				
C ₂₈ H ₂₀ N ₄ Mg	436.1533	1	436.1532	0.12				
C ₂₇ H ₁₆ ON ₄ Mg	436.1169	1	436.1169	0.09				
C ₂₈ H ₁₉ N ₄ Mg	435.1455	1	435.1455	0.12				
C ₂₇ H ₂₂ N ₄ Mg	426.1689	1	426.169	0.13			426.1688	3.98
C ₂₇ H ₂₁ N ₄ Mg	425.1611	1	425.1611	0.38			425.1610	6.07
C ₂₇ H ₂₀ N ₄ Mg	424.1533	1	424.1533	0.26			424.1532	1.36
C ₂₇ H ₁₉ N ₄ Mg	423.1455	1	423.1455	0.39			423.1453	0.52

C ₂₇ H ₁₈ N ₄ Mg	422.1376	1	422.1375	0.23				
C ₂₇ H ₁₇ N ₄ Mg	421.1298	1	421.1298	0.19				
C ₂₇ H ₁₆ N ₄ Mg	420.1220	1	420.1222	0.09				
C ₂₆ H ₁₉ N ₄ Mg	411.1455	1	411.1455	0.14			411.1453	2.92
C ₂₆ H ₁₈ N ₄ Mg	410.1376	1	410.1377	0.19			410.1375	0.34
C ₂₆ H ₁₇ N ₄ Mg	409.1298	1	409.1299	0.27			409.1297	0.24
C ₂₆ H ₁₆ N ₄ Mg	408.1220	1	408.1220	0.18				
C ₂₆ H ₁₅ N ₄ Mg	407.1142	1	407.1141	0.17				
C ₂₆ H ₁₄ N ₄ Mg	406.1063	1	406.1064	0.16				
unidentified		1	399.2957	0.12	399.2954	0.76	399.2954	1.76
unidentified		2			385.2784	0.89	385.2785	1.66

* Peaks used as internal calibrants

Table E.2 Summary of several higher intensity fragments

Proposed formula	Theoretical mass	EID ion (m/z) Externally calibrated	Error (ppm)	EID ion (m/z) Internally calibrated	Error (ppm)	IRMPD ion (m/z) Externally calibrated	Error (ppm)	IRMPD ion (m/z) Internally calibrated	Error (ppm)
$C_{32}H_{31}O_2N_4Mg$	527.2292	527.2297	-0.95	527.2292	0	527.2301	-1.71	527.2294	-0.38
$C_{31}H_{30}ON_4Mg$	498.2265	498.2268	-0.60	498.2264	0.20	498.2273	-1.61	498.2267	-0.40
$C_{30}H_{26}O_2N_4Mg$	498.1901	498.1903	-0.40	498.1899	0.40	498.1913	-2.41	498.1903	-0.40
$C_{31}H_{29}N_4Mg$	481.2237					481.2249	-2.49	481.2237	0.00
$C_{29}H_{27}N_4Mg^*$	455.2081	455.2083	-0.44	455.2081	---	455.2091	-2.20	455.2087	---
Average			-0.60		0.3		-2.08		-0.30
SD (σ)			0.25		0.14		0.41		0.20

* Peak used as internal calibrant

Appendix F. (Supporting information for Chapter 7)

Table F.1 Peak list of Figure 7.4

Proposed formula	Theoretical mass	EID			CAD			IRMPD		
		<i>m/z</i>	Error	relative intensity %	<i>m/z</i>	Error	relative intensity %	<i>m/z</i>	Error	relative intensity %
C ₅₅ H ₇₅ O ₅ N ₄ *	871.5732	871.57322		36.03	871.57222	-1.12	17	871.57309		65.70
C ₃₅ H ₃₇ O ₅ N ₄	593.27585	593.27583	0.03	8.9	593.27563	-0.37	100	593.27587	0.03	85.07
C ₃₅ H ₃₆ O ₅ N ₄ *	592.26802	592.26796	0.10	1.85	592.26781	-0.35	30.15	592.26801		2.53
C ₃₄ H ₃₃ O ₄ N ₄	561.24963	561.24971	0.14	0.52	561.24839	-2.21	2.18	561.24965	0.04	5.45
C ₃₄ H ₃₂ O ₄ N ₄	560.24181							560.24181	0.00	0.49
C ₃₃ H ₃₃ N ₄ O ₃	533.25471	533.25467	0.08	7.69	533.25452	-0.36	74.3	533.25467	-0.08	100.00
C ₃₃ H ₃₁ O ₂ N ₄	515.24414							515.2441	-0.08	1.33
C ₃₂ H ₃₁ O ₃ N ₄	519.23907	519.23874	0.64	0.89						
C ₃₃ H ₃₃ O ₂ N ₄	517.2598							517.25973	-0.14	3.92
C ₃₂ H ₃₂ O ₂ N ₄	504.25198							504.25193	-0.10	6.66
C ₃₂ H ₃₁ O ₂ N ₄	503.24415							503.24425	0.20	0.99
C ₃₂ H ₃₃ ON ₄	489.26489							489.26485	-0.08	3.66

C ₃₂ H ₃₂ ON ₄	488.25706				488.25703	-0.06	8.17
C ₃₁ H ₂₉ O ₂ N ₄	489.2285				489.22851	0.02	3.07
C ₃₂ H ₃₁ ON ₄	487.24924				487.24918	-0.12	2.94
C ₃₁ H ₃₂ ON ₄	476.25706				476.25704	-0.04	15.04
C ₃₁ H ₂₉ ON ₄	473.23359				473.23356	-0.06	10.09
C ₃₀ H ₂₉ ON ₄	461.23359	461.23349	0.22	0.73	461.23358	-0.02	38.18
C ₃₀ H ₂₈ ON ₄	460.22576	460.22592	-0.35	0.62	460.22577	0.02	6.41
C ₃₀ H ₂₇ ON ₄	459.21794				459.2179	-0.09	2.75
C ₃₁ H ₃₃ N ₄	461.26997				461.26996	-0.02	2.65
C ₃₁ H ₃₁ N ₄	459.25432				459.25431	-0.02	1.64
C ₂₉ H ₂₈ ON ₄	448.22576				448.22569	-0.16	5.72
C ₂₉ H ₂₇ ON ₄	447.21794				447.21786	-0.18	2.43
C ₂₉ H ₂₅ ON ₄	445.20229				445.20226	-0.07	3.79
C ₂₉ H ₂₆ ON ₄	446.21011				446.21016	0.11	1.96
C ₃₀ H ₂₉ N ₄	445.23867				445.23869	0.04	2.92
C ₂₉ H ₂₄ ON ₄	444.19446				444.19442	-0.09	1.05
C ₂₉ H ₂₃ ON ₄	443.18664				443.18679	0.34	0.67

$C_{30}H_{28}N_4$	444.23085					444.23083	-0.05	1.12
$C_{29}H_{29}N_4^*$	433.23867	433.23884	-0.39	0.86		433.23868		25.58
$C_{28}H_{25}ON_4$	433.20229					433.20231	0.05	4.62
$C_{29}H_{28}N_4$	432.23085					432.23088	0.07	1.51
$C_{28}H_{24}ON_4$	432.19446					432.1944	-0.14	1.49
$C_{29}H_{27}N_4$	431.22302					431.22304	0.05	3.42
$C_{28}H_{23}ON_4$	431.18664					431.18662	-0.05	3.12
$C_{28}H_{26}N_4$	418.2152					418.2151	-0.24	5.56
$C_{28}H_{25}N_4$	417.20737					417.20734	-0.07	7.11
$C_{27}H_{21}N_4O$	417.17099					417.17082	-0.41	1.05
$C_{28}H_{24}N_4$	416.19955					416.19952	-0.07	2.11
$C_{27}H_{19}N_4O$	415.15534					415.15509	-0.60	0.70
$C_{27}H_{24}N_4$	404.19955					404.19948	-0.17	4.85
$C_{27}H_{23}N_4$	403.19172					403.19168	-0.10	13.62
$C_{27}H_{22}N_4$	402.18391					402.1839	-0.02	2.88
$C_{27}H_{21}N_4$	401.17607					401.17585	-0.55	0.62
$C_{26}H_{17}N_4O$	401.13969					401.13973	0.10	0.50

$C_{26}H_{21}N_4$	389.17607		389.17593	-0.36	6.49
$C_{26}H_{23}N_4$	391.19172		391.19179	0.18	1.25
$C_{26}H_{20}N_4$	388.16825		388.16787	-0.98	4.80
$C_{26}H_{19}N_4^*$	387.16042		387.16042		4.29
$C_{25}H_{19}N_4$	375.16042		375.16028	-0.37	1.04
$C_{25}H_{17}N_4$	373.14477		373.14442	-0.94	3.37
$C_{25}H_{18}N_4$	374.1526		374.15232	-0.75	2.15
$C_{26}H_{18}N_3$	372.14952		372.14947	-0.13	0.65
$C_{25}H_{16}N_4$	372.13695		372.1367	-0.67	0.97
$C_{25}H_{17}N_3$	371.1417		371.14162	-0.22	0.63
$C_{25}H_{18}N_3$	360.14952		360.14896	-1.55	0.53
$C_{24}H_{15}N_4$	359.12912		359.12876	-1.00	0.86
$C_{24}H_{16}N_3$	346.13387		346.13353	-0.98	0.57
$C_{21}H_{41}O_3$	341.30502		341.30471	-0.91	1.24
$C_{23}H_{18}N_3$	337.15735		337.15674	-1.81	0.51
$C_{23}H_{18}N_3$	336.14952		336.14916	-1.07	0.59
$C_{22}H_{18}N_3$	324.14952		324.14919	-1.02	0.68

C ₂₂ H ₁₆ N ₃	322.13387				322.13353	-1.06	0.85
C ₁₉ H ₁₉ O ₄ H	312.13561	312.13561	0.00	100			
C ₂₁ H ₁₈ N ₃	312.14952				312.14925	-0.86	0.70
C ₂₁ H ₁₇ N ₃	311.1417				311.14136	-1.09	0.78
C ₂₁ H ₁₆ N ₃	310.13387				310.13359	-0.90	0.81
C ₂₃ H ₂₀ N	310.15903				310.15889	-0.45	0.38
C ₂₁ H ₁₅ N ₃	309.12605				309.12567	-1.23	0.58
C ₂₁ H ₁₄ N ₃	308.11822				308.11743	-2.56	0.43
C ₂₀ H ₁₆ N ₃	298.13387				298.13314	-2.45	0.76
C ₁₉ H ₂₀ O ₃	296.1407	296.1407	0.00	3.19			
C ₂₀ H ₁₄ N ₃	296.11822				296.11789	-1.11	0.68
C ₁₉ H ₁₄ N ₃	284.11822				284.11806	-0.56	0.36
C ₁₆ H ₁₄ O ₃	254.09375	254.09374	0.04	9.8			
C ₁₉ H ₂₅	253.19508	253.19505	0.12	0.67			
C ₁₆ H ₁₃ O ₃	253.08592	253.08591	-0.04	0.95			
average			0.03		0.74		0.41
SD			0.10		0.81		0.56

* Peaks used as internal calibrants

Figure F.1 CAD spectra of pheophytin-a under different collision energies

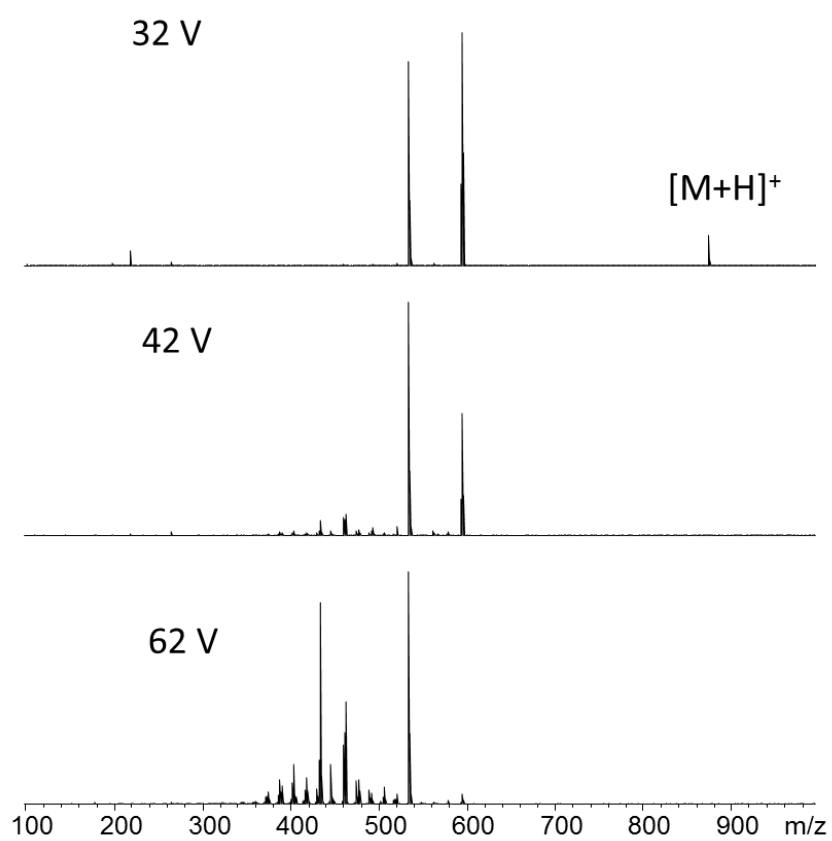
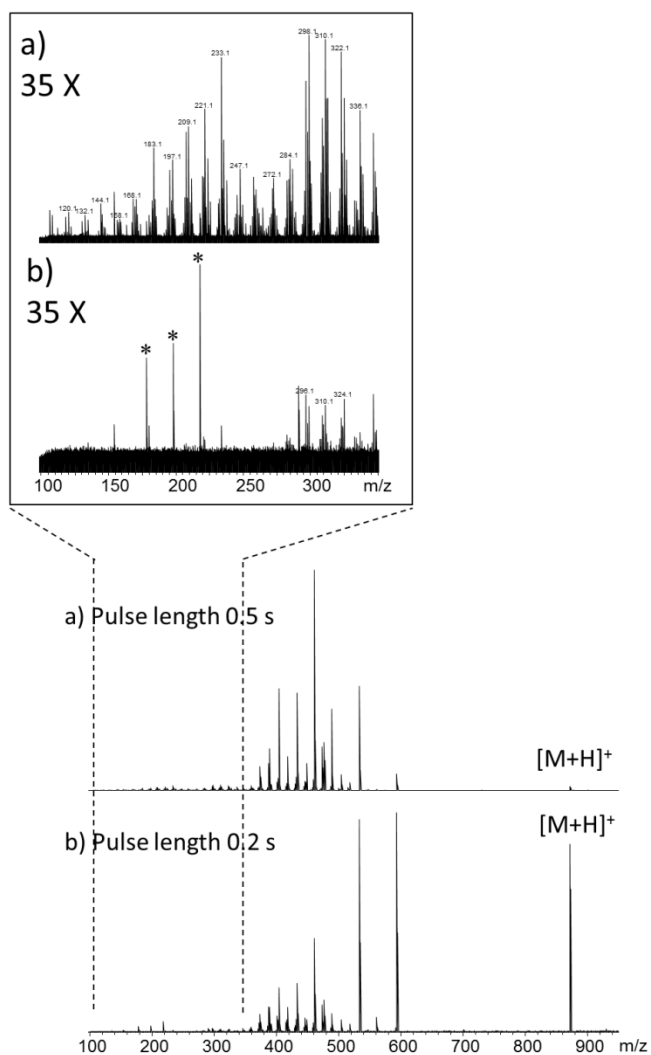


Figure F.2 IRMPD spectra of pheophytin-a of different pulse length a) 0.5 s and b) 0.2 s. Insets in the square are expanded regions from m/z 100-350. Peaks with asterisk are harmonics or noise



Appendix G. (Supporting information for Chapter 8)

Table G.1 Peak assignment in the CAD spectrum of p65 in Figure 8.2

Charge state	ions	Theoretical m/z	Experimental m/z	Error/ppm
1	b3+126.03	424.16917	424.17786	20.48
1	b4+126.03	552.22775	552.23347	10.36
1	b5+126.03	623.26486	623.26988	8.05
1	b6+126.03	710.29689	710.29904	3.02
1	b3+144.04	442.17974	442.18815	19.03
1	b4+144.04	570.23832	570.24373	9.49
1	b5+144.04	641.27543	641.27924	5.95
1	b6+144.04	728.30746	728.30907	2.22
3	y17	710.07349	710.06316	-14.55
4	y23	737.91453	737.90389	-14.42
4	y24	766.67126	766.65796	-17.35
5	y26	656.75339	656.74239	-16.75
5	y28	699.16933	699.15795	-16.28
5	y30	754.39881	754.38601	-16.97

Curriculum Vitae

Juan Wei

EDUCATION

Oct. 2011 - Oct. 2014 Department of Chemistry, the University of Warwick, UK

PhD

Sep. 2008 - Mar. 2011 College of Pharmacy, Shanghai Jiao Tong University, China

Master degree of Medicine

Sep. 2004 - Jun. 2008 Department of Pharmacy, Wuhan University, China

Bachelor degree of Science

PUBLICATIONS

1. **Wei, J.**, Antzutkin, O. N., Iuga, D., Barrow, M. P., Dupree, R., Brown, S. P., O'Connor, P. B. Using isotopic fine structure mass spectrometry to quantify the ^{17}O enrichment ratio in $\text{A}\beta_{37-42}$ ($\text{GG}_{38}(^{17}\text{O})\text{VVIA}$) and $\text{A}\beta_{37-42}$ ($\text{GGV}_{39}(^{15}\text{N})\text{VIA}$) mixture, in preparation
2. **Wei, J.**, O'Connor, P. B. Extensive fragmentation of pheophytin-a by infrared multiphoton dissociation, in preparation
3. **Wei, J.**, Antzutkin, O. N., Filippov, A. V., Iuga, D., Barrow, M. P., Dupree, R., Brown, S. P., O'Connor, P. B. Amyloid hydrogen bonding polymorphism evaluated by $^{15}\text{N}\{^{17}\text{O}\}$ REAPDOR solid-state NMR and ultra-high resolution FTICR MS, submitted
4. **Wei, J.**, Bristow, A. W. T., O'Connor, P. B. The competitive influence of Li^+ , Na^+ , K^+ , Ag^+ , and H^+ on the fragmentation of a PEGylated polymeric excipient, *J. Am. Soc. Mass. Spectrom.*, 2014, accepted
5. **Wei, J.**, Bristow, A.W.T., McBride, E., Kilgour, D.P.A., O'Connor, P.B. D- α -tocopheryl polyethylene glycol 1000 succinate: A view from FTICR MS and tandem MS, *Anal. Chem.*, 2014, 86(3):1567-1574
6. **Wei J.**, Li H. L., Barrow M., O'Connor B. P.. Structural characterization of chlorophyll-a by high resolution tandem mass spectrometry, *J. Am. Soc. Mass. Spectrom.*, 2013, 24: 753-760
7. **Wei J.**, Gu X., Wang Y., Wu Y, Yan C.. Two-dimensional separation system by on-line hyphenation of capillary isoelectric focusing with pressurized capillary electrochromatography for peptide and protein mapping, *Electrophoresis*, 2011, 32(2):230-237
8. **Wei J.**, Gu X., Wang Y., Yan C.. Off-line two-dimensional separation system

- cIEF/pCEC for peptides separation, *Chinese J. Anal. Chem*, 2011, 39(2):45-51
9. Mei, J., Tian Y. P., He W., Xiao Y. X., **Wei J.**, Feng Y., Q.. Preparation approaches of the coated capillaries with liposomes in capillary electrophoresis, *J. Chromatogr. A*, 2010, 1217:6979-6986
10. Wu Y., Zhang X. H., **Wei J.**, Xue Y., Bahatibieke M., Wang Y., Yan C.. Recent advances and applications of CEC and pCEC, *Chinese J. Chromatogr.*, 2009, 27(5):609-620

SELECTED CONFERENCE PRESENTATIONS

- The 62nd ASMS Conference on Mass Spectrometry, 15th-19th June 2014, Baltimore, USA, **Oral Presentation**
- 11th European Fourier Transform Mass Spectrometry Conference, 22nd-25th April 2014, Paris, France, **Oral Presentation**
- 11th Uppsala Conference on Electron Capture and Transfer Dissociation, 30th March-2nd April 2014, Austria, Poster Presentation
- 21st Annual Meeting of the BioEnvironmental Polymer Society, 18th-20th September 2013, the University of Warwick, UK, Poster Presentation
- The BMSS Annual Meeting 2013, 9th-11th September 2013, Eastbourne, UK, **Oral Presentation**
- The 61st ASMS Conference on Mass Spectrometry, 9th-13th June 2013, Minneapolis, USA, **Oral presentation**
- The Warwick Mass Spectrometry 80/60 Conference, 10th-11th December 2012, Warwick, UK, Poster Presentation
- The 2012 Ardgour Symposium, 21st-24th September 2012, Scotland, UK, **Oral Presentation**
- The BMSS Annual Meeting 2012, 17th-18th April 2012, AstraZeneca, UK, Poster Presentation
- 10th European Fourier Transform Mass Spectrometry Conference, 1st-5th April 2012, the University of Warwick, UK, Poster Presentation